ICRR ANNUAL REPORT 2022

INSTITUTE

FOR

COSMIC RAY RESEARCH

THE UNIVERSITY OF TOKYO

ANNUAL REPORT
(APRIL 2022 – MARCH 2023)

5-1-5, Kashiwanoha, Kashiwa, Chiba 277-8582, Japan

Telephone: (81) 4-7136-3102
Facsimile: (81) 4-7136-3115
WWW URL: http://www.icrr.u-tokyo.ac.jp/

TABLE OF CONTENTS

PREFACE

This report summarizes the scientific activities of the Institute for Cosmic Ray Research (ICRR) of The University of Tokyo in the Japanese FY (JFY) 2022.

ICRR is an inter-university research institute for studies of cosmic rays. The headquarters of ICRR is located in Kashiwa, Chiba prefecture, Japan. In order to promote various cosmic-ray-related studies efficiently, ICRR has three research divisions; Neutrino and Astroparticle division, High Energy Cosmic Ray division, and Astrophysics and Gravity division. ICRR have four observatories in Japan; Kamioka Observatory and KAGRA Observatory (Kamioka underground, Gifu prefecture), Norikura Observatory (2770 meters above sea level, Mt. Norikura, Gifu prefecture), and Akeno Observatory (Yamanashi prefecture), together with 1 research center; Research Center for Cosmic Neutrinos (Kashiwa, Chiba prefecture). In addition, there are three major experimental facilities outside of Japan. They are located in Utah in USA, Yangbajing in Tibet, China and the La Palma island in Spain.

Many researchers from various Japanese institutions as well as those from overseas are involved in the research programs of ICRR. It should be noted that most of the scientific outputs from ICRR are the results of the collaborative efforts by many researchers from various institutions. In order to produce outstanding results, it is very important to carry out an experiment by an international collaboration composed of top-level researchers all over the world. Hence, all of the experimental collaborations that ICRR is involved are international ones. With these activities, ICRR has been selected as one of the institutions of the "International Joint Usage/Research Center" program by Ministry of Education, Culture, Sports, Science and Technology -Japan (MEXT) in November 2018.

Since JFY 2020, our inter-university research activities have been deeply affected by the COVID-19 pandemic. Still, even during the pandemic, ICRR has carried out various research actibities, such as continuous operation of the detectors, as described in this report. And in JFY 2022, our activities gradually returned to normal and manual operations required for the scientific research have been increasing at the observational sites.

We hope that this report is useful for the understanding of the current research activities of ICRR. Finally, we appreciate the strong support of our colleagues in this research field, The University of Tokyo and MEXT. They are indispensable for the continuing, and exciting scientific outcome of ICRR.

Masayuki Nakahata,
Director,
Institute for Cosmic Ray Research,
The University of Tokyo

The ICRR building at Kashiwa, Chiba, Japan.

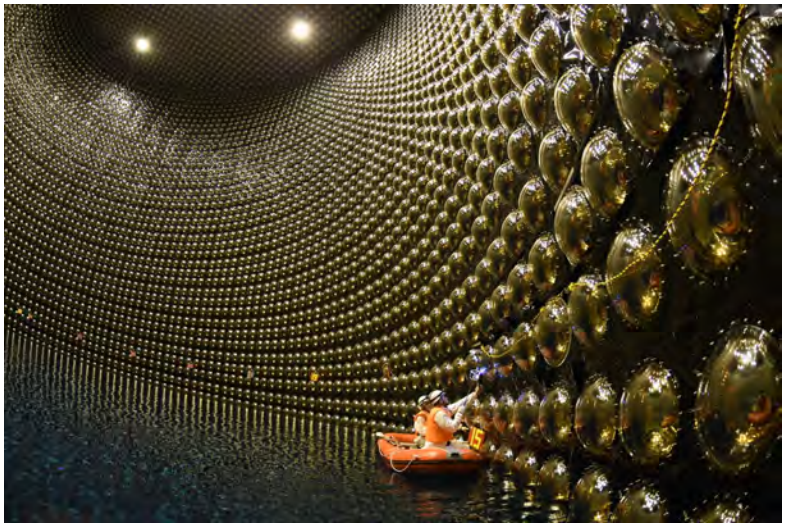

The Super-Kamiokande detector (the photo was taken during refurbishment work in 2018).

The ceiling part of the Hyper-Kamiokande main cavern under excavation. (March 2023)

The first Large Size Telescope of CTA installed at Observatory Roque de los Muchachos inaugurated on October 10 2018.

Tibet-III air shower array (37000 m^2) at Yangbajing, Tibet (4300 m in altitude).

Air fluorescence telescopes (left) and a scintillator surface detector (right) of the Telescope Array experiment in Utah, USA to explore the origin of extremely high energy cosmic rays.

KAGRA's (left) 3km-long arm tunnel and (right) a sapphire mirror installed in a cryogenic suspension system.

Online public lecture co-organized with the Institute for the Physics and Mathematics of the Universe (Kavli IPMU).

Organization

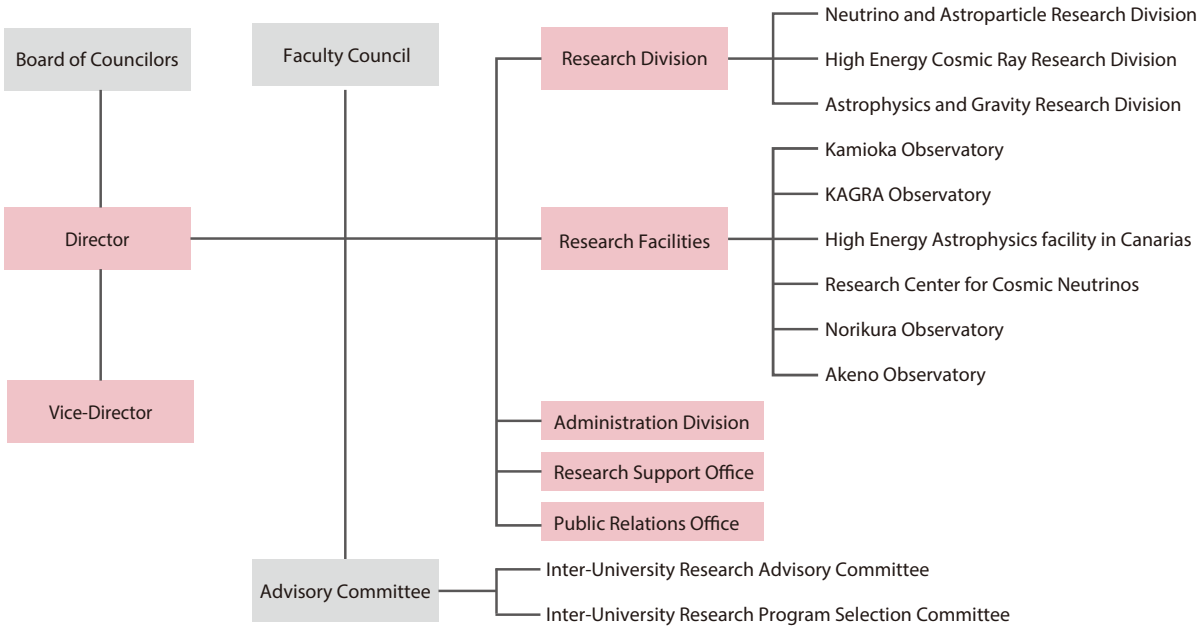

Number of Staff Members (As of May 1, 2022)

	Scientific Staff	Technical Staff	Research Fellows	Administrators and Secretaries	Total
Neutrino and Astroparticle Div.	24	6	1	19	50
High Energy Cosmic Ray Div.	22	12	10	3	47
Astrophysics and Gravity Div.	17	14	6	8	45
Administration	0	0	0	22	22
Total	63	32	17	52	164

FY 2015-2022 Budget

	2015	2016	2017	2018	2019	2020	2021	2022
Personnel expenses	684 000	683 000	779 000	823 000	872 000	898 000	898 000	1 048 000
Non-personnel expenses	1 595 000	1 288 000	1 514 000	1 729 000	1 611 000	1 173 000	2 078 000	1 990 000
Total	2 279 000	1 971 000	2 293 000	2 552 000	2 483 000	2 071 000	2 976 000	3 038 000

(in 1 000 yen)

RESEARCH DIVISIONS

Neutrino and Astroparticle Division

Overview
Super-Kamiokande
T2K Experiment
XMASS Experiment
Hyper-Kamiokande

High Energy Cosmic Ray Division

Overview
Cherenkov Cosmic Gamma-Ray Group
TA: Telescope Array Experiment
Tibet ASγ Experiment
ALPACA Project
High Energy Astrophysics Group
Other Activities

Astrophysics and Gravity Division

Overview
Gravitational Wave Group
KAGRA Project
Observational Cosmology Group
Theory Group
Particle Phenomenology
Particle Cosmology

NEUTRINO AND ASTROPARTICLE DIVISION

Overview

This division aims to study particle physics with prime interests in physics of neutrinos and proton decay, and astroparticle physics with the use of underground experimental facilities.

The Super-Kamiokande (SK) detector is a 50 kton water Cherenkov detector using 11,129 50 cm-diameter photomultipliers (PMTs) for its inner detector and 1,885 20 cm-diameter PMTs for its outer detector. The data taking of SK started in April 1996 and 20th anniversary was celebrated in 2016. The neutrino oscillations in atmospheric neutrinos were discovered in 1998 and thereby it was demonstrated that neutrinos have a finite mass. In 2001, the accurate measurements of the ^{8}B solar neutrino flux by SK and SNO discovered that neutrino oscillations are the solution of the solar neutrino problem beyond doubt. These findings became the research achievement for which the Nobel Prize in Physics was awarded in 2015. After the epoch-making discoveries, precise measurements of atmospheric neutrinos and solar neutrinos have been performed and they unraveled various phenomena of neutrino oscillations. The evidence of tau neutrino appearance in atmospheric neutrinos was confirmed in 2013 and atmospheric neutrino anomaly has been finally concluded. The indication of day-night asymmetry of the solar neutrino flux, which is expected from the matter effect of neutrino oscillations, was reported in 2014. At present, the most interesting subjects in those observations are the determination of neutrino mass hierarchy using atmospheric neutrinos and the consistency check of solar(ν_e) and reactor($\bar{\nu}_e$) oscillations.

A high intensity neutrino beam experiment using the J-PARC accelerator (T2K) was started in 2009. The T2K experiment uses the SK detector as the far detector. Search for leptonic *CP* violation and the high precision measurement of oscillation parameters are main physics subjects in T2K. An indication of electron neutrino appearance was found in June 2011, and later the electron appearance has been established with greatly improved significance. Since 2014, anti-neutrino beam data also have been taken in order to search for *CP* violation. T2K later reported the exclusion of the conservation of *CP* symmetry in neutrino oscillations at more than 95% CL.

The search for nucleon decay is another important subject at SK because it gives a direct evidence for the Grand Unified Theories (GUTs). SK gives the current best limit which strongly constrains various GUT models.

If a supernova happens in our galaxy, thousands of neutrino interactions are expected at SK and they will reveal detailed mechanism of the supernova explosion. SK is the only detector in the world which can identify the direction of the supernova neutrinos. So, SK has been operated almost all the time with small dead time and if a supernova is observed at SK, we will send burst information to astronomers as soon as it is detected. In addition, SK aims to observe supernova relic neutrinos, which is an accumulated supernova burst neutrinos from the beginning of the universe. For this purpose, it is planned to add 0.1% of gadolinium into the Super-K tank (called SK-Gd project) in order to tag neutrons for $\bar{\nu}_e$ detection. A feasibility study for the SK-Gd project is being performed using a 200 ton tank which mimics the Super-K detector. Refurbishment of the Super-K tank and upgrade of the water circulation system were conducted in 2018, 0.01% gadolinium was dissolved in the detector water in the summer of 2020, and further additions in the summer of 2022 achieved 0.03% gadolinium concentration.

Another activity of the Neutrino and Astroparticle division is a multi-purpose experiment using liquid xenon aiming at the detection of cold dark matter, neutrino absolute mass using neutrinoless double beta decay, and low energy solar neutrinos. A 800 kg liquid xenon detector was constructed in an experimental hall near the SK site. Data taking continued for more than five years and completed in February 2019. Searches for dark matter interactions and rare phenomena in liquid xenon are being conducted.

The Hyper-Kamiokande (Hyper-K or HK) experiment is proposed as a joint project of the University of Tokyo and KEK by combining a next generation underground water Cherenkov detector and upgraded J-PARC neutrino beam. The Hyper-K detector is an order of magnitude larger in detector fiducial mass than Super-K and has discovery potential of leptonic *CP* violation and proton decays. The project has officially started by receiving its first Japanese funding in the beginning of 2020. Its construction schedule includes 5 years of the cavern excavation, 2 years of instrumentation, and data taking commencement in 2027. In parallel, the J-PARC beam delivered to the detector will be upgraded from 0.5 to 1.3 MW over the same time period.

SUPER-KAMIOKANDE

[Spokesperson : Masayuki Nakahata
(Kamioka Observatory, ICRR, The University of Tokyo)]

Atmospheric neutrinos

Atmospheric neutrinos are produced from the decays of secondary particles produced in the collision of primary cosmic rays with nuclei in the atmosphere. Atmospheric neutrinos have several remarkable features:

- The flavor ratio, $(\nu_\mu + \bar{\nu}_\mu)/(\nu_e + \bar{\nu}_e)$ is 2 (> 2 for above few GeV)
- Zenith angle distribution is up/down symmetry above a few GeV.

These features are realized without neutrino oscillations, and provide a useful constraint in the study of these neutrinos. Super-Kamiokande has been observing atmospheric neutrinos since 1996 and has accordingly made several important measurements with them, including the discovery of neutrino oscillations [1].

Starting in summer of 2020 SK was operated with a 0.01% concentration of Gd dissolved into the detector water. This period of the detector, SK6, lasted until 2022, when the concentration was increased to 0.01% marking the start of the SK7 period. Figure 1 shows the atmospheric neutrino data taken with Gd-loaded water in SK7 in comparison to data taken from SK6. There is no large charge in the detector's ability to observe atmospheric neutrinos and the SK7 data are judged to be of similarly high quality as those in previous Gd-loaded and pure-water periods.

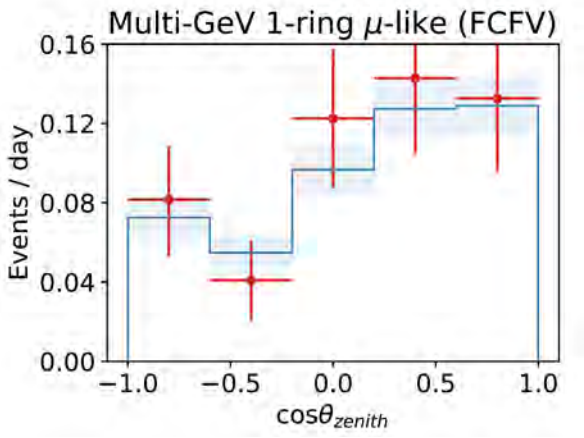

Fig. 1. Comparison of the atmospheric neutrino event rate in SK6 and SK7 for the multi-GeV μ-like sample.

Three flavor oscillations and the neutrino mass hierarchy

The SK atmospheric neutrino data are described at leading order by two-flavor $\nu_\mu \rightarrow \nu_\tau$ oscillations with maximal mixing (θ_{23}=π/4). However, sub-leading contributions via $\nu_\mu \rightarrow \nu_e$ oscillations induced by the mixing angle θ_{13} as well as the "solar" mixing parameters ($\Delta m^2_{12}, \theta_{12}$) provide the ability to probe currently unknown aspects of the standard neutrino oscillation paradigm, such as the existence of leptonic *CP* violation and the neutrino mass ordering (hierarchy). Understanding these open questions may bring important insight into larger questions, such as the origin and evolution of today's matter-dominated universe.

Several sub-leading oscillation effects are expected to appear in atmospheric neutrinos:

- Resonant enhancement of $\nu_\mu \rightarrow \nu_e$ oscillations due to the effects of matter is expected to occur at energies between 2 and 10 GeV and will manifest as an excess of upward-going electron-like events (e-like) in the atmospheric sample.
- This enhancement exists for either ν_e or $\bar{\nu}_e$ depending on the mass hierarchy. Therefore the mass hierarchy can be probed by understanding the relative amount of neutrino and antineutrino interactions in the detector.
- The combination of the solar oscillation parameters and the octant of $\sin^2\theta_{23}$ may enhance or suppress the event rate and, to some extent, alter the spectral shape of Sub-GeV electron-like data due to the $\nu_\mu \leftrightarrow \nu_e$ oscillations they induce.
- The standard oscillation paradigm includes a *CP*-violating factor, δ_{cp}, which is expected to induce several sub-dominant oscillation effects in many of the SK atmospheric neutrino samples, even if CP is conserved.

Super-Kamiokande has studied the effects of these oscillations on atmospheric neutrino data separated into fully-contained (FC) events, partially-contained (PC) events, and upward-going muon (UPMU) topologies. Fully-contained events are characterized by a primary interaction vertex that is located inside the fiducial volume of the detector and whose visible particles stop within the inner detector. On the other hand, though the primary vertex position of PC events is within the fiducial volume, they are characterized by having at least one charged particle escaping the inner detector and depositing light in the outer detector. In most cases the escaping particle is a muon. Upward-going muons originate from high energy muon-neutrino interactions in the rock surrounding the detector. Since all other particles are lost to interactions in the rock, only the muon is penetrating enough to reach the detector and be identified. The FC sample is separated into electron-like and muon-like (μ-like) subsamples by applying a particle identification algorithm to the most energetic Cherenkov ring of each event. Since PC and upward-going events are predominantly produced by muon neutrinos, no particle identification is applied. Though SK cannot distinguish on an event-by-event basis neutrino and antineutrino interactions, statistical separation of multi-GeV electron-like subsamples is performed to improve sensitivity to the mass hierarchy. A likelihood method designed to enhance the kinematic differences between neutrino and antineutrino interactions is applied to separate events into ν_e-like and $\bar{\nu}_e$-like subsamples.

Since the start of SK4 SK has had the ability to identify neutrons, albeit with a limited efficiency of 25%. In 2020 atmospheric neutrino events from this data set were separated into neutrino-like and antineutrino-like samples taking advantage of the fact that the former are expected to produce fewer neutrons on average than the latter. Further, a novel event selection based on a boosted decision tree was introduced to improve the classification of multi-ring events in all data periods. Using these new event selections all SK data until the end of the SK5 period (2020) were analyzed to update the analysis presented in [2, 3]. In addition, the fiducial volume used in the current analysis has been expanded by 20%. With these improvements the analysis found a preference for the normal mass ordering (NO) of of between 78% and 96.7% over the range of oscillation parameter values allowed at the 90% confidence level. This result is similar to that of the publication,

whose preference was 81.9% to 96.7% over its allowed range. The updated analysis shows no strong preference for the octant of $\sin^2\theta_{23}$ and has a weak preference for a non-zero CP-violating phase. Combining these data with a model of the T2K experiment's Run 1-9 result, difference between the inverted mass ordering (IO) and NO best χ^2 strengthens to 8.54 units. These results are summarized in Table 1 and in Figure 2.

Though there is a significant body of evidence for the existence of dark matter in the universe, its nature remains largely unknown. Indeed, despite considerable effort by direct detection experiments to observe the interactions of dark matter particles with detector nuclei or electrons, so far no evidence of such interactions has been found. As such experiments are primarily sensitive to dark matter masses in the GeV/c^2 to TeV/c^2 range, alternative scenarios supporting lower mass dark matter are gaining traction. In some scenarios the light dark matter particles may be boosted to relativistic energies by interaction with cosmic rays, thereby gaining sufficient energy to be detected via a subsequent scattering with nuclei (or electrons) in a detector. In Super-K, such interactions may be energetic enough for the outgoing particles to produce Cherenkov radiation. Since dark matter is expected to cluster near the galactic center, the boosting process will dominantly produce dark matter arriving at Super-K from that direction.

A search for this boosted dark matter signal was performed using the full data set from the first four runs of Super-K, corresponding to a 370 kton–year exposure. To probe the dark-matter-nucleon interaction cross section, the analysis search for free protons as the signal of this process. No evidence for these interactions was seen and the data were found to be consistent with atmospheric neutrino backgrounds. However, due to Super-K's ability to resolve the direction of the scattered particles and its large detection volume, limits more than ten times more stringent than previous measurements were obtained for dark matter masses between 1 to 1,000 MeV/c^2 (Figure 3). These results were published in Ref [4].

Bibliography

[1] Y. Fukuda *et al.* [Super-Kamiokande Collaboration], Phys. Rev. Lett. **81**, 1562 (1998).

[2] R. Wendell *et al.* [Super-Kamiokande Collaboration], Phys. Rev. D **81**, 092004 (2010).

[3] K. Abe *et al.* [Super-Kamiokande Collaboration], Phys. Rev. D **97**, no. 7, 072001 (2018).

[4] K. Abe *et al.* [Super-Kamiokande Collaboration], Phys. Rev. Lett **130**, no. 3, 031802, (2023)

Solar Neutrinos

Introduction

Solar neutrinos constitute by far the largest component of neutrino flux on the Earth among those produced from natural sources. Most of solar neutrinos are produced by proton-proton fusion, $p+p \rightarrow d+e^+ + \nu_e$, and its subsequent fusion reactions (pp-chain)[1]. They are categorized into the *pp*, *pep*, ^{7}Be, ^{8}B and *hep* neutrinos. Among these, Super-Kamiokande is sensitive to ^{8}B and *hep* neutrinos, which have relatively higher energy that extends up to $\sim$20 MeV.

Past observations of solar neutrino flux by Super-Kamiokande (SK) [1] and the Sudbury Neutrino Observatory (SNO) [2] led to the discovery of solar neutrino flavor conversion. Our current interest for solar neutrino measurements with the SK detector [3] is to make a precision test of the neutrino flavor conversion through the Mikheyev-Smirnov-Wolfenstein (MSW) effect [4, 5]. The MSW effect leads to a resonant conversion of the solar neutrinos within the Sun and results in an about 30% level of the survival probability above $\sim$5 MeV. The survival probability of lower energy neutrinos are described by the vacuum oscillation probability of $\sim 50\%$, and the transition region between the two lies at a few MeV region. This transition from the matter dominant oscillation to the vacuum dominant oscillation is often called as the "up-turn" of the solar neutrino spectrum. Current experimental data is not enough to directly demonstrate this "up-turn" because of the experimental sensitivity as well as the statics.

SK aims to directly test the "Spectrum up-turn" by precisely measuring energy spectrum of ^{8}B solar neutrino in this transition region. This measurement is important not only to test the MSW effect but also to test several alternative theoretical models, such as sterile neutrinos [6, 7], mass-varying neutrinos [8], non-standard interactions [9, 10] and so on.

The matter effect can also be tested with the matter in the interior of the Earth. Electron flavor neutrinos are regenerated due to the matter effect of the Earth, making the neutrino flux in night is larger than that in day by about a few % level depending on the neutrino oscillation parameters.

In this article, we report results of solar neutrino measurements using the data taken through the end the fourth SK data taking phase (SK-IV) in May 2018, with an analysis method improved from our previous publication [11]. The total live-time used for this analysis is 5,805 days, with 2970 days from the SK-IV phase.

In addition to the standard neutrino oscillation analysis, we report the results of searching for solar electron anti-neutrinos due to spin-flavor precession in the Sun [12]. Finally, we briefly report the status of solar neutrino observation in the SK detector after loading the Gadolinium [13].

Analysis

For precisely measuring the energy spectrum of recoil electrons, the energy scale should be reduced and the removal of background events is essential. For that purpose, the detector simulation was improved with more accurate modeling of the PMT timing response and the non-uniformity of the water quality. For example, the energy reconstruction method was improved with a correction for the PMT gain drift and with a new correction of the energy scale non-uniformity. The correction for the gain drift was first introduced in 2017 and then refined in this analysis with an improved correction for the dark noise contribution. Furthermore, the correction for the PMT angular response was improved with more realistic simulation of the PMT response and arrangement. By introducing those improvements, the standard variation of the energy

*[1] with a subdominant ($\sim$1%) contribution from the CNO cycle

Fit	Hierarchy	$\sin^2\theta_{23}$	$\lvert\Delta m^2_{32,31}\rvert$ [$\times 10^{-3}$ eV^2]	δ_{CP}	$\delta\chi^2$ (IO-NO)
SK only	NH	0.49	2.40	4.71	
	IH	0.49	2.40	4.71	5.69
SK+T2K Model	NH	0.51	2.40	-1.75	
	IH	0.53	2.40	-1.57	8.54

Table 1. Best fit oscillation parameters obtained by the three flavor oscillation analysis. Fits are conducted for both the normal (NH) and inverted (IH) hierarchy assumptions The fit was performed assuming $\sin^2\theta_{13}$=0.0218, which is taken from the PDG.

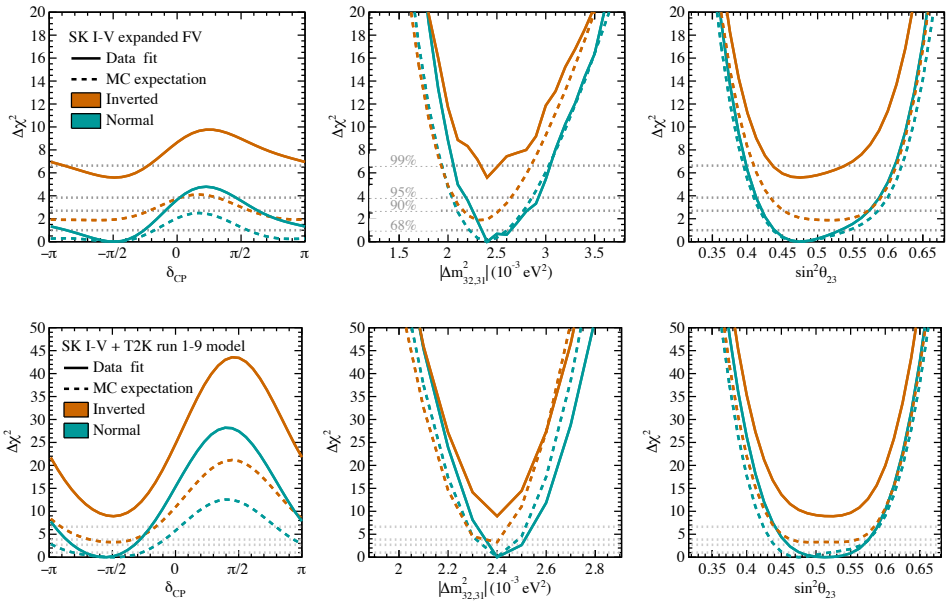

Fig. 2. Measured $\Delta\chi^2$ distributions for the $\Delta m^2_{23,31}$, $\sin^2\theta_{23}$, and δ_{cp} oscillation parameters for the Super-K only fit (top) and Super-K combined with a model of the T2K Run1-9 result. These are the results of a fit with $\sin^2\theta_{13}$ constrained to the preferred value from reactor measurements.

scale variation was reduced down to $\pm 0.5\%$, which is three times smaller than that previously estimated.

In addition to the energy scale improvements, the rejection method for the spallation backgrounds is also improved by tagging neutrons in the hadronic shower induced by cosmic muons. By applying this cut to the data sample, the signal efficiency improved about 12% while keeping the removal efficiency of muon spallation events about 90% [14].

^{8}B solar neutrino flux measurement

The SK detector observes solar neutrinos via elastic scatterings with electrons in pure water. The direction of a recoiled electron is highly correlated with the direction of the incident neutrino. Figure 4 shows the distribution of $\cos\theta_{\rm Sun}$ for solar neutrino candidates observed during the SK-IV phase. With the 2970 days of data in SK-IV, more than 60,000 events are observed over the background. Adding the solar neutrino events observed in other phases, the total number of the solar neutrino events is more than 100,000. Based on this data, the ^{8}B solar neutrino flux is determined to be $(2.35 \pm 0.04) \times 10^6$ /cm^2/sec assuming a pure electron neutrino flavor content. The ratio between the SK result and the SNO NC current flux (5.25×10^6 /cm^2/sec) [15] is found to be 0.447 ± 0.008.

The solar activity cycle is the 11 years periodic change of sunspots releasing the magnetic flux at the surface of the Sun. The number of the sunspots strongly correlated with the solar activity cycle. The solar neutrino data set which is used for this analysis spans more than 21 years and covers about two solar activity cycles. Figure 5 shows the SK yearly flux measured throughout the different phases of SK together with the corresponding sunspot number (Source: WDC–SILSO, Royal Observatory of Belgium, Brussels [16]). The χ^2 between observed data and no time dependence hypothesis is calculated with the total experimental uncertainties as $\chi^2 = 23.25/22$ d.o.f., which corresponds to a probability of 38.8%. The SK solar rate measurements are fully consistent with a constant solar neutrino flux emitted by the Sun.

Energy spectrum analysis

Analysis of solar neutrino energy spectrum was done using all the data from SK-I to SK-IV [1, 17, 18, 11]. The data quality for SK-IV was significantly improved thanks to the new front-end electronics for SK-IV [19], the upgraded

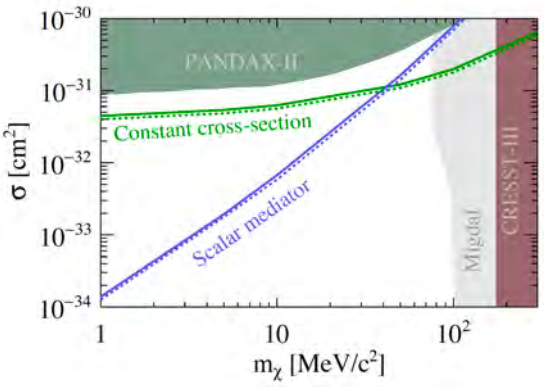

Fig. 3. Limits on the dark-matter-nucleon interaction cross section as a function of dark matter mass. Super-K's results are shown in green and blue assuming a constant cross section and that produced by a scalar mediator, respectively. The 90% confidence level upper limits from the data are shown as solid lines, while the dashed lines depict the expected sensitivity [4].

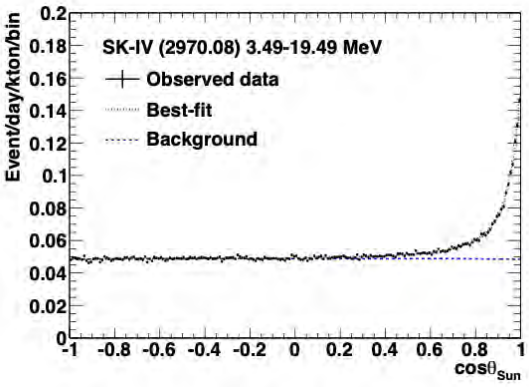

Fig. 4. The solar angle distribution in SK-IV. The horizontal axis shows the cosine of the solar angle $\cos\theta_{\rm Sun}$ and the vertical axis shows the number of the observed events. The black points shows the observed data, and the red (blue) histogram shows the best-fit (background) shape.

water circulation system and the upgraded calibration methods [20]. Owing to these upgrades, SK has achieved the lowest background (induced by radioisotopes in pure water, especially ^{214}Bi) among all the SK phases [21]. The energy threshold in SK-IV have been lowered to 3.49 MeV in recoil electron kinetic energy (SK-I: 4.49 MeV, SK-III: 3.99 MeV) and this enabled SK to measure the solar neutrino energy spectrum with higher sensitivity. In addition, in May 2015, the trigger threshold was changed from 34 observed PMT signals within 200 nsec to 31 hits [22, 23]. Because of this lower threshold, the detection efficiency between 3.49 MeV and 3.99 MeV was improved from ∼86% to ∼100%. This improvement led to further reduction of the statistical uncertainty below 4.99 MeV in SK-IV.

Figure 6 shows the energy spectra obtained from SK-I, -II, -III and -IV, overlaid with the best-fits with generic polynomial and exponential functions, and the predictions assuming the current oscillation parameters described in the next section. Figure 7 shows the combined energy spectrum from SK-I to SK-IV with the predictions. Note that all SK the phases are combined without regard to energy resolution or systematic uncertainties in Figure 7, but those uncertainties are taken into account in the χ^2 calculation between the data and the prediction. Comparing χ^2 between the data (black) and the predictions (green or blue), the energy spectrum of SK is consistent within $\sim 1\sigma$ with the MSW up-turn with both the SK+SNO best fit parameters (green in Fig. 9) and the KamLAND best-fit parameters (blue in Fig. 9). The data also slightly disfavors the flat oscillation probability by $\sim 1\sigma$ significance.

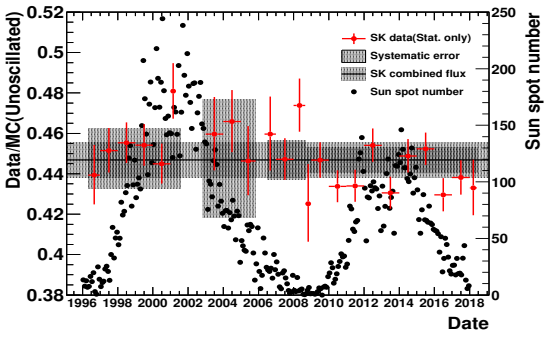

Fig. 5. The ratio of ^{8}B solar neutrino flux in SK over the SNO's NC current flux from 1996 to 2018. The red points show the yearly flux measured by SK (statistical uncertainty only), the gray bands show the systematic uncertainties for each SK phase, the black-horizontal line shows the combined measured flux with the uncertainty drawn as the red horizontal band. The back points show the sunspot number provided from [16].

Day-night asymmetry

The day-night asymmetry of the solar neutrino flux for the full SK-IV data set was extracted with the same method described in Ref. [24]. Here, the day-night asymmetry is defined as,

$$A_{D/N} = \frac{\Phi_{\rm day} - \Phi_{\rm night}}{0.5(\Phi_{\rm day} + \Phi_{\rm night})},$$

where $\Phi_{\rm day(night)}$ is the observed solar neutrino flux during day(night). Figure 8 shows the result of a day-night asymmetry amplitude fit as a function of Δm^2_{21} for the solar neutrino sample at $3.5 < E_{\rm kin} < 19.5$ MeV. The fitted day-night asymmetry, $A^{\rm Fit}_{D/N}$, assuming the SK+SNO best fit oscillation parameters (green in Fig. 9) was obtained as,

$$A^{\rm Fit}_{D/N} = (-2.1 \pm 1.1({\rm stat.}))\% \quad (3.5 < E < 19.5\ {\rm MeV}).$$

Oscillation parameter extraction

The oscillation parameters were extracted using the results from the solar neutrino measurements at SK and SNO [15], as well as the reactor antineutrino measurement by KamLAND [25, 26]. Figure 9 shows the allowed parameter region from the SK+SNO data as well as the KamLAND data. SK significantly contributes to the measurement of the solar angle θ_{12}. From the SK+SNO data, the mixing angle is

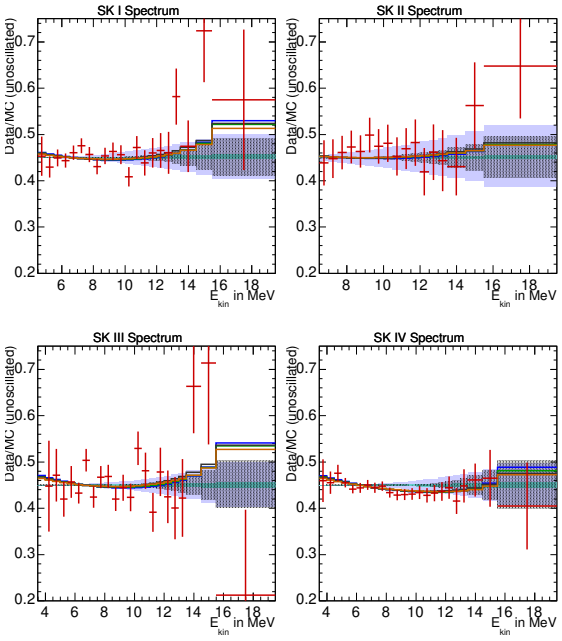

Fig. 6. SK-I, II, III and IV recoil electron spectra divided by the unoscillated expectation. The green (blue) line represents the best–fit to SK data using the oscillation parameters from the fit to SK and SNO (KamLAND) data. The orange (black) line is the best-fit to SK data of a general exponential or quadratic (cubic) P_{ee} survival probability. Error bars on the data points give the statistical plus systematic energy-uncorrelated uncertainties while the shaded purple, red, and green histograms give the energy-correlated systematic uncertainties arising from energy scale, energy resolution, and neutrino energy spectrum shift.

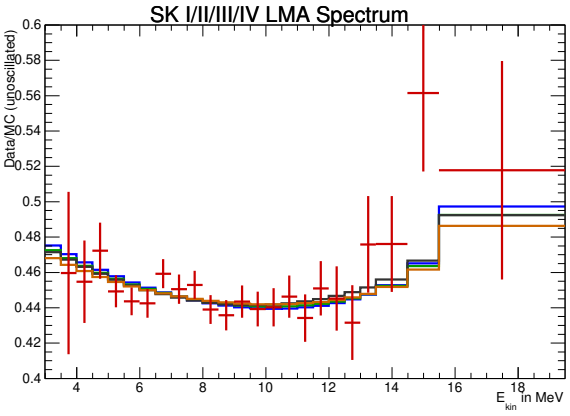

Fig. 7. The energy spectrum combining SK-I through SK-IV as a function of the recoil electron energy. The red points show the ratio of the data to the expected flux using a non-oscillated ^{8}B solar neutrino spectrum. The green (blue) curve shows the expected energy spectrum assuming the MSW effect inputting oscillation parameters of SK and SNO (KamLAND). The orange (black) line is the best-fit to SK data of a general exponential or quadratic (cubic) P_{ee} survival probability.

determined to be $\sin^2\theta_{12} = 0.306 \pm 0.014$ and the mass difference is determined to be $\Delta m^2_{21} = 6.11^{+1.21}_{-0.68} \times 10^{-5}$ eV^2 as shown in Fig. 9. The SK+SNO fit results favors a lower Δm^2_{21} value compared to the KamLAND best fit value of

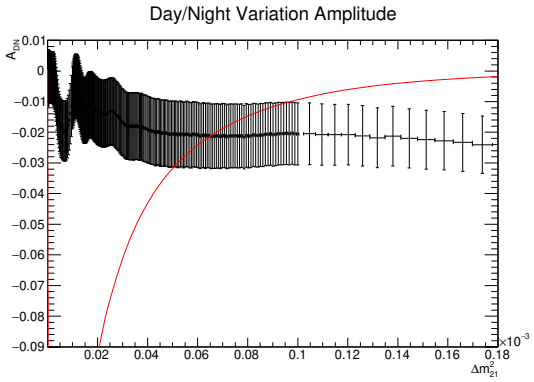

Fig. 8. Result of the day-night asymmetry amplitude fit as a function of the input Δm^2_{21} value. The black points show the data fit results with the statistical uncertainties, while the red curve show the expectation.

$\Delta m^2_{21} = 7.54^{+0.19}_{-0.18} \times 10^{-5}$ eV^2. Currently, the SK+SNO data disfavors the KamLAND best fit value at $\sim 1.4\sigma$, while it was $\sim 2\sigma$ in the previous analysis. Adding the KamLAND result, the oscillation parameters are determined to be $\sin^2\theta_{12} = 0.306^{+0.013}_{-0.012}$ and $\Delta m^2_{21} = 7.51^{+0.19}_{-0.18} \times 10^{-5}$ eV^2.

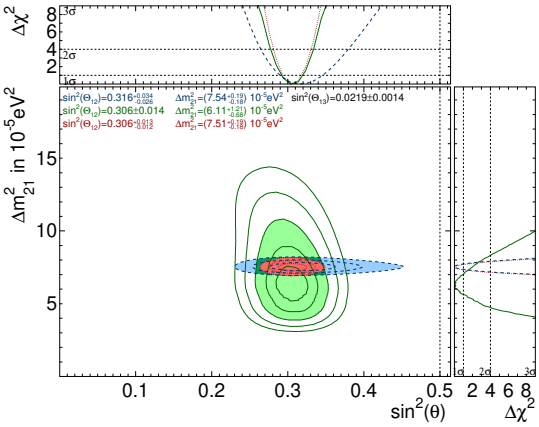

Fig. 9. The allowed contours for Δm^2_{21} vs. $\sin^2\theta_{12}$ from solar neutrino data at SK and SNO (green solid line). The allowed contour from KamLAND is also shown in blue. The combined allowed region is shown in red.

Solar neutrino observation after Gd-loading

As reported in the later section, the Gadolinium was loaded into the Super-Kamiokande's pure water [13] to enhance detector's sensitivity to supernova relic neutrinos by tagging neutrons originated from the inverse beta decay of electron anti-neutrino interactions. The first Gd loading was conducted in 2020 July and the second was done in 2022 June.

In order to validate the detector performance, calibration data were taken after loading Gadolinium and compared with

the results in pure water phase. For example, Figure 10 shows the reconstructed electron kinetic energy with the DT calibration device [27] before and after the Gd loading. The differences of the peak position and resolution between SK-V (pure water) and SK-VI (Gd concentration 0.011%) are less than $\pm 1\%$. Hence, the detector's energy scale is enough to continue to observe the solar neutrinos in the MeV region.

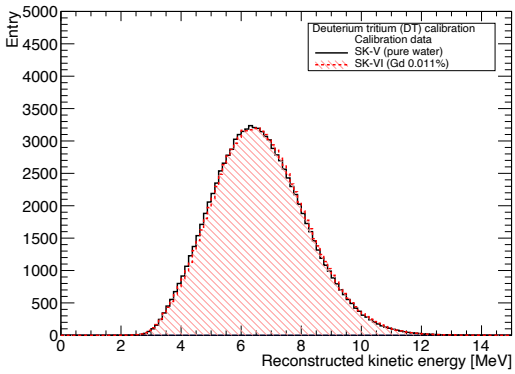

Fig. 10. The comparison of energy distribution between SK-V (pure water) and SK-VI (Gd concentration 0.011%). The calibration data was taken at the center position of the SK detector.

Figure 11 shows the typical distributions of $\cos\theta_{\rm Sun}$ before and after the Gd-loading. The peak of solar neutrinos around $\cos\theta_{\rm Sun} = 1$ is clearly observed even through we added the Gd into pure water. Figure 11 also demonstrates that no additional background exist in the energy range above 6.49 MeV even after the second Gd-loading. The background events below that level is under investigation since the detection efficiency for such events is different from that evaluated in pure water phase mentioned in the previous section. Based on the DT calibration and $\cos\theta_{\rm Sun}$ distribution, the SK detector can continue to conduct the solar neutrino observation using Gd-loaded water.

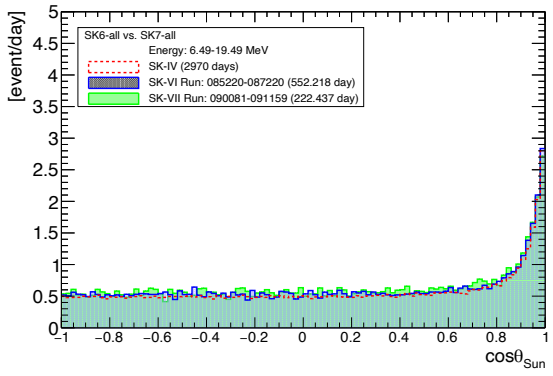

Fig. 11. The comparison of the cosine theta distribution between 6.49 and 19.49 MeV before and after the Gd-loading. The phases of SK-IV (red) was operated by filling pure water while SK-VI (blue) and SK-VII (light green) were operated by adding Gd into the detector's pure water. Even after dissolving additional Gd in the second Gd-loading, the background rate is unchanged because of developing ultra-low radio-purity Gd powder.

Summary and outlook

In summary, Super-Kamiokande has precisely measured the ^{8}B solar neutrino flux, its time variation and recoil electron spectrum. Using 5,805 days of data, more than 100,000 solar neutrino interactions were extracted over the background. No significant correlation between the observed solar neutrino flux and the sunspot number was found with more than 21 years of continuous observation of the solar neutrino flux. The measured energy spectrum of ^{8}B solar neutrino is consistent within $\sim 1\sigma$ with the MSW up-turn with both the solar best-fit parameters and the KamLAND best-fit parameters. The previously existed $\sim 2\sigma$ tension between the solar and KamLAND best fit Δm^2_{21} values was reduced to $\sim 1.4\sigma$ in this analysis. Combining the solar neutrino oscillation analyses by SK, SNO and KamLAND, the oscillation parameters are determined as $\Delta m^2_{21} = 7.51^{+0.19}_{-0.18} \times 10^{-5}$ eV^2 and $\sin^2\theta_{12} = 0.306^{+0.013}_{-0.012}$.

The Super-Kamiokande detector was recently upgraded by dissolving Gadolinium (Gd), and started a new phase of observation as SK-Gd. In order not to cause significant harm to the solar neutrino observation, ultra-pure $Gd_2(SO_4)_3$ powder with extremely low radio-impurity was newly developed and dissolved into the SK detector. Furthermore, the calibration data after the Gd-loading has been taken Enhanced neutron detection capability with Gd can be used to further reduce the cosmic-ray spallation backgrounds. We aim to further improve our solar neutrino measurements with additional data and analysis improvements in the SK-Gd era.

Bibliography

[1] J. Hosaka *et al.*, Phys. Rev. D **73**, 112001 (2006).

[2] Q.R. Ahmad *et al.*, Phys. Rev. Lett. **87**, 071301 (2001).

[3] Y. Fukuda *et al.*, Nucl. Instrum. Meth. A **501**, 418 (2003).

[4] S.P. Mikheyev and A. Y. Smirnov, Sov. Jour. Nucl. Phys. **42**, 913 (1985).

[5] L. Wolfenstein, Phys. Rev. D **17**, 2369 (1978).

[6] P.C. de Holanda and Y. Smirnov, Phys. Rev. D **69**, 113002 (2004).

[7] P.C. de Holanda and Y. Smirnov, Phys. Rev. D **83**, 113011 (2011).

[8] V. Barger *et al.*, Phys. Rev. Lett. **95**, 211802 (2005).

[9] A. Friedland *et al.*, Phys. Rev. B **594**, 347 (2004).

[10] O.G. Miranda *et al.*, J. High Energy Phys. **10** 008 (2006)

[11] K. Abe *et al.*, Phys. Rev. D **94**, 052010 (2016).

[12] K. Abe *et al.*, Astropart. phys. **139**, 102702 (2022).

[13] K. Abe *et al.*, Nucl. Instrum. Meth. A **1027**, 166248 (2022).

[14] S. Locke *et al.*, arXiv:2112.00092 [hep-ex].

[15] B. Aharmin *et al.*, Phys. Rev. C **88**, 025501 (2013).

[16] WDC-SILSO, Royal Observatory of Belgium, Brussels. http://www.sidc.be/silso/datafiles

[17] J.P. Cravens *et al.*, Phys. Rev. D **78**, 032002 (2008).

[18] K. Abe *et al.*, Phys. Rev. D **83**, 052010 (2011).

[19] H. Nishino *et al.*, Nucl. Instrum. Meth. A **610**, 710 (2009).

[20] K. Abe *et al.*, Nucl. Instrum. Meth. A **737**, 253 (2014).

[21] Y. Nakano, J. Phys. Conf. Ser. **888**, 012191 (2017).

[22] S. Yamada *et al.*, IEEE Trans. Nucl. Sci. **57**, 428 (2010).

[23] Y. Nakano, PhD thesis, The Univ. of Tokyo (2016).

[24] A. Renshaw *et al.*, Phys. Rev. Lett. **112**, 091805 (2014).

[25] S. Abe *et al.*, Phys. Rev. Lett. **100**, 221803 (2008).

[26] A. Gando *et al.*, Phys. Rev. D **88**, 033001 (2013).

[27] E. Blaufuss *et al.*, Nucl. Instrum. Meth. A **458**. 636 (2001).

Searches for nucleon decays

Among many physics models beyond the Standard Model (SM) of particle physics, Grand Unified Theories (GUTs) are promising models that can explain several features of the SM including the quantized hypercharge. One of the remarkable predictions of the GUTs is the decay of protons or bound neutrons, which are stable particles within the SM. Super-Kamiokande is the most sensitive experiment for these phenomena and has been looking for them since its beginning in 1996.

However, the minimal SU(5)-based Grand Unification was ruled out by a search for the proton decay, $p \to e^+\pi^0$ [1]. This SU(5) model was also rejected by the fact that there is no precise agreement at the GUT scale in the strength of the three gauge coupling constants extrapolated from precise measurements of these constants at LEP [2]. To avoid these experimental constraints, it is needed to lift up the GUT scale and make the proton's lifetime longer than the experimental limit by introducing some extra particles between the electroweak scale and the GUT scale. This addition of the extra degrees of freedom will also modify the renormalization group equations of the three coupling constants and allow these constants to meet at the GUT scale.

One such extension to the SM is the super-symmetry (SUSY), which introduces a super-partner for each SM particle. SUSY GUTs, which are combinations of SUSY and GUTs, typically predict short lifetime for proton decay modes involving kaons including $p \to \bar{\nu}K^+$ and $p \to \mu^+K^0$ [3, 4] as well as suppressing the $p \to e^+\pi^0$ decay within the current experimental limit. This year, a new result of a search for the $p \to \mu^+K^0$ mode has been published [5], which is briefly discussed in this report.

This $p \to \mu^+K^0$ decay was searched for analyzing the data from the SK-I, II, III periods (199 kton·year) in the previous publication [6], and the lower limit of the partial lifetime was reported as 1.6×10^{33} years. This limit has been updated with a new analysis using the SK-IV dataset, which results in a total exposure of 372 kton·year. In this analysis, an improved event reconstruction, called *fiTQun* [7], and a neutron tagging method [8] are newly employed for the SK-IV data.

To search for the proton decay, $p \to \mu^+K^0$, in SK, we apply a set of event selection cuts to the data. The event selection used in the new SK-IV analysis is outlined in this paragraph whilst readers who are interested in the details are directed to Ref. [5]. In the new SK-IV analysis, there are five event selection categories defined to pick up the five kaon decay modes, $K^0_S \to 2\pi^0$, $\pi^+\pi^-$ and $K^0_L \to \ell^\pm\pi^\mp\nu$, $\pi^+\pi^-\pi^0$, $3\pi^0$, where $\ell^\pm$ is either $e^\pm$ or $\mu^\pm$ throughout this article. In all these five categories, proton decay events are extracted when they are matched criteria suited for the event topologies of $p \to \mu^+K^0$ followed by the five K^0 decays. These criteria are defined by combining the number or the momenta of the Cherenkov rings, the patterns of the rings, which differ among e, μ and $\pi^\pm$, and so on. For the K^0_S decays, the kaon is identified using the invariant mass of the two decay pions. Distributions of the reconstructed invariant mass of the K^0_S are shown in Figure 12. It can be seen that the invariant mass of the K^0_S is nicely reconstructed in both categories. A K^0_L has a relatively long

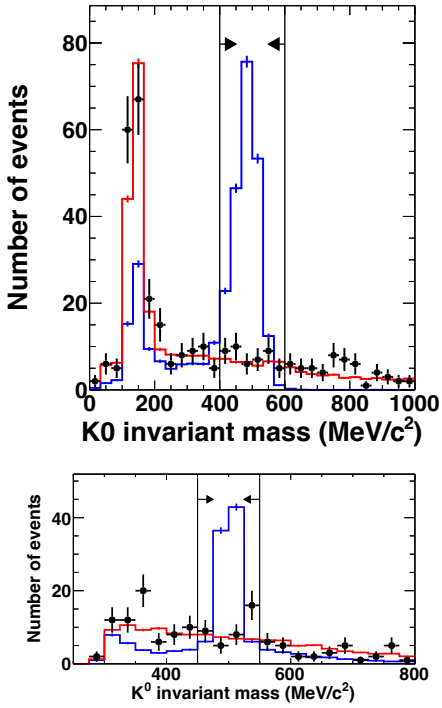

Fig. 12. Reconstructed invariant mass of K^0_S for the $K^0_S \to 2\pi^0$ selection (top) and the $K^0_S \to \pi^+\pi^-$ selection (bottom). The blue, red, and black histograms show the distributions for the $p \to \mu^+K^0_S$ process, the atmospheric neutrino events, and the data, respectively. These plots are drawn before applying the cuts on the invariant mass.

lifetime of 51 ns and decays at a position a few meters away from the original proton decay vertex. This makes it difficult to detect all the decay products and reconstruct the mass of the K^0_L precisely. Hence, the K^0_L is identified by using the de-

cay vertex of K_L^0 separated from the primary vertex instead of its reconstructed invariant mass. The variable that was actually used was called *vertex separation*, $v_{\rm sep}$, and its definition is shown in Figure 13. A distribution of $v_{\rm sep}$ for the three K_L^0 categories is shown in Figure 14. The $p \to \mu^+ K_L^0$ signal forms a peak shifted by 0.5 m in the positive direction whereas the atmospheric neutrino sample shows a peak that sits at zero. Using this feature of the signal, we selected the events with $v_{\rm sep} > 1.5$ m as final samples for all three K_L^0 categories.

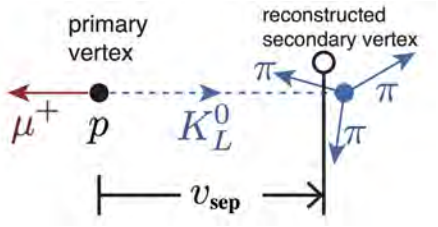

Fig. 13. Definition of the vertex separation, $v_{\rm sep}$. This variable is defined using the direction of the muon and the position of the second vertex.

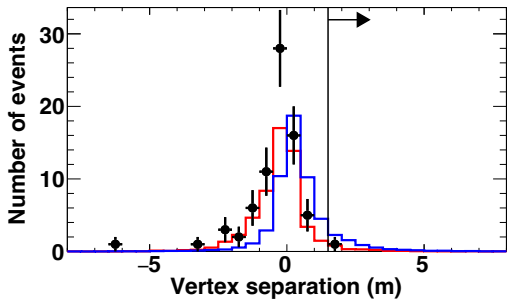

Fig. 14. Vertex separation distribution for the K_L^0 selection categories. The events in the three selections for $K_L^0 \to \pi^\pm \ell^\mp \nu$, $\pi^+\pi^-\pi^0$, $3\pi^0$ are included. The blue, red, and black histograms show the distributions for the $p \to \mu^+ K_L^0$ process, the atmospheric neutrino events, and the data, respectively. These plots are drawn after applying all the cuts except the vertex separation.

After applying the abovementioned event selection criteria for the five kaon decay modes, the selection efficiency, the predictions of the background yields, and the number of data events that are actually observed are obtained in Table 2. A Bayesian analysis combining SK-I, II, III, and new SK-IV resulted in a lower limit of the partial lifetime of 3.6×10^{33} years at 90% confidence level, which is the most stringent limit of this decay mode ever.

In addition to the published proton decay mode, $p \to \mu^+ K^0$, there are several searches for other nucleon decay modes ongoing within the analysis group. Two sets of analyses searching for proton decays into a charged lepton and mesons, $p \to \ell^+ \eta^0$ and $p \to \ell^+ \pi^0 \pi^0$, have been finalized and papers are being prepared to make these results public. Besides, analyses searching for nucleon decays involving a neutrino, $p \to \bar{\nu}\pi^+$ and $n \to \bar{\nu}\pi^0$, $\bar{\nu}\eta^0$ are started. These aim to look at the data within 1-2 years.

Fig. 15. In the LAB-E cavern, the 200-ton tank (a) with currently 240 photo-multipliers installed, the Gd pre-mixing and pre-treatment 15-ton tank (b), the selective filtration system (d), Gd removal resins (c) for test and a device to measure the water transparency (e) have been installed.

Bibliography

[1] A. Takenaka *et al.*, Super-Kamiokande Collaboration, Phys. Rev. D **102**, 112011 (2020)

[2] U. Amaldi *et al.*, Phys. Lett. B **260** 447, (1991)

[3] K. S. Babu *et al.*, Phys. Lett. B **423**, 337 (1998)

[4] K. S. Babu *et al.*, Nucl. Phys. B **566**, 33 (2000)

[5] R. Matsumoto *et al.*, Super-Kamiokande Collaboration, Phys. Rev. D **106** 072003 (2020)

[6] C. Regis *et al.*, Phys. Rev. D **86**, 012006 (2012)

[7] M. Jiang *et al.*, Super-Kamiokande Collaboration, Prog. Theor. Exp. Phys. **2019**, 053F01 (2019)

[8] K. Abe *et al.*, Super-Kamiokande Collaboration, Journal of Instrumentation **17**, 10029 (2022)

EGADS: From R&D for the gadolinium project to standalone Supernova monitor

As mentioned above, although at SK a few SRN events a year are expected, SRNs have not been detected yet because of the large backgrounds that constrain our search. The observation of SRNs in general or neutrinos from distant supernovae in particular, would give us some information about the universe, for example the core collapse rate from SRNs, and about the neutrino itself too, for example its lifetime. The main signal from SRN is expected to be the inverse beta decay reaction ($\bar{\nu}_e + p \to e^+ + n$), in which a positron and a neutron are produced, the delayed coincidence between the positron interaction and the neutron capture should allow to reduce the background affecting this analysis.

Before Gd loading in 2020, the SK detector had a poor neutron detection efficiency. It was then proposed to add 0.2% of gadolinium (Gd) sulfate by mass into SK in order to achieve a high neutron detection efficiency. Since Gd has a neutron capture cross section of 49.000 barns (about 5 orders of magnitude larger than that of protons) and emits a gamma cascade

Table 2. Summary of the event selection in the $p \to \mu^+ K^0$ search. The uncertainties are the quadratic sums of the MC statistical uncertainties and the systematic uncertainties. The lower limit (SK-I+SK-II+SK-III+SK-IV combined) is smaller than that from only the SK-IV data due to two candidates in the $K^0_S \to 2\pi^0$ selection in the SK-II data with the background expectation of 0.20 events [6].

Search mode	Efficiency (%)	Background (events)	Candidates (events)	Lower limit (10^{33} years)
$K^0_S \to 2\pi^0$	9.9 ± 1.0	0.3 ± 0.1	0	2.8
$K^0_S \to \pi^+\pi^-$	5.2 ± 0.6	0.8 ± 0.2	0	1.5
$K^0_L \to \pi^\pm \ell^\mp \nu$	1.4 ± 0.3	1.7 ± 0.5	1	0.3
$K^0_L \to 3\pi^0$	0.37 ± 0.05	0.12 ± 0.06	0	0.1
$K^0_L \to \pi^+\pi^-\pi^0$	0.18 ± 0.04	0.16 ± 0.07	0	0.05
SK-IV combined (199 kton·years)				4.5
SK-I+SK-II+SK-III+SK-IV combined (372 kton·years)				3.6

of 8 MeV, neutrons could be easily detected at SK (in space, vertices within tens of cm and in time, with the neutron capture delayed about 30 μsec).

EGADS (Evaluating Gadolinium's Action on Detector Systems) project was funded in 2009. The main motivation of EGADS was to show that by adding Gd, SK will be able to detect anti-neutrinos using the delayed coincidence technique, while keeping all its capabilities in the other analyses like solar and atmospheric neutrinos. Since then, a new hall near the SK detector has been excavated and a 200-ton tank with its ancillary equipment has been installed, see Fig.15, to mimic the conditions at SK. The selective water filtration system filters out water impurities while keeping the Gd in the water.

EGADS has been renamed as Employing Gadolinium to Autonomously Detect Supernovas after the installation of the new QBee electronics in 2017, following the Super-Kamiokande collaboration approbation of the SK Gd loading.

Water system operations

From January 2010 to July 2011 we circulated pure water through the 200-ton tank and proved that our water system is stable and achieves a high water quality. In 2013, from February 6th to April 20th, the 200-ton tank has been step wise loaded with Gd sulfate until the final 0.2% concentration was reached. Two values are monitored at three different depths: the Cerenkov light left after travelling 15 m (LL15) in water and the Gd concentration. Both values confirmed that we can achieve and maintain a good water quality and that Gd sulfate homogeneously and quickly dissolves in the 200-ton tank.

In summer 2013, we installed 240 photo-multipliers and the data taking started from September without Gd and with a DAQ based on old SK ATM modules. In April 2015, the target concentration of 0.2% $Gd_2(SO_4)_3$ was achieved. Figure 16 shows the time variation of LL15. The blue band in the figure shows typical values for SK-III and SK-IV. As shown in the figure, the transparency of 0.2% $Gd_2(SO_4)_3$ water is within the SK range. In addition to the good water transparency, no Gd loss has been detected since the EGADS detector reached the final concentration until it was emptied again after about 2 years and 5 months, in October 2017.

Detailed studies have evaluated the impact on current analyses at SK. These studies show that current analyses will be basically unharmed after adding Gd in SK and all other tests and studies conducted have shown no showstoppers. As a consequence, the SK collaboration decided in spring 2015 to approve the SuperK-Gd project. The results of these analysis were published in [1].

In order to test the Gd-loading in SK, the detector was refilled with pure-water in November 2017, and loaded with 0.02% $Gd_2(SO_4)_3$ in the end of March 2018. This loading was performed using only the pre-treatment and the fast re-circulation systems, with one pass, similar to what is expected for SK 0.02% loading.

Since then, different configurations of the water system have been tested in order to determine what is needed to ensure high water transparency in SK without band-pass system. Figure 17 shows the time variation of LL15 since this loading until May 2020. From March 2018 to June 2018 a slow but continuous decrease of the water transparency has been observed ith the fast re-circulation system only. From June 2018 to August 2018 the use of the band-pass system allowed to recover high water transparency. There-after the fast-re-circulation system only has been used.

In May 2019, the water system was stopped for about one week due to electrical damage following a power-cut. This led to a reduction of the water transparency. After restarting, the water transparency was recovered. On September 2019 the water flow was modified so that only half of the flow pass through the special cation exchange resin. The water transparency remained stable and high. Finally, in November 2020, in order to simulate the future additional Gd loading in Super-Kamiokande, EGADS was loaded from 0.01% to 0.03% Gd concentration.

Ion exchange resin tests

Impurities in water Cerenkov detector's water can be removed using anion and cation resins as a standard method.

In case of Gd-loaded water, standard cation exchange resins are expected to also remove Gd. Hence, a special cation exchange resin has been developed and installed in EGADS, in addition to the usual anion exchange resin. The installation was done in January-February 2019 (in January, the new cation exchange resin was used alone, leading a water transparency drop). As showed in Figure 17, we observed an improvement of the water transparency compared than with only anion exchange resin. This increase was enhanced following the replacement of the TOC and UV lamps in March 2019, which stresses the importance of the ionization lamps for the

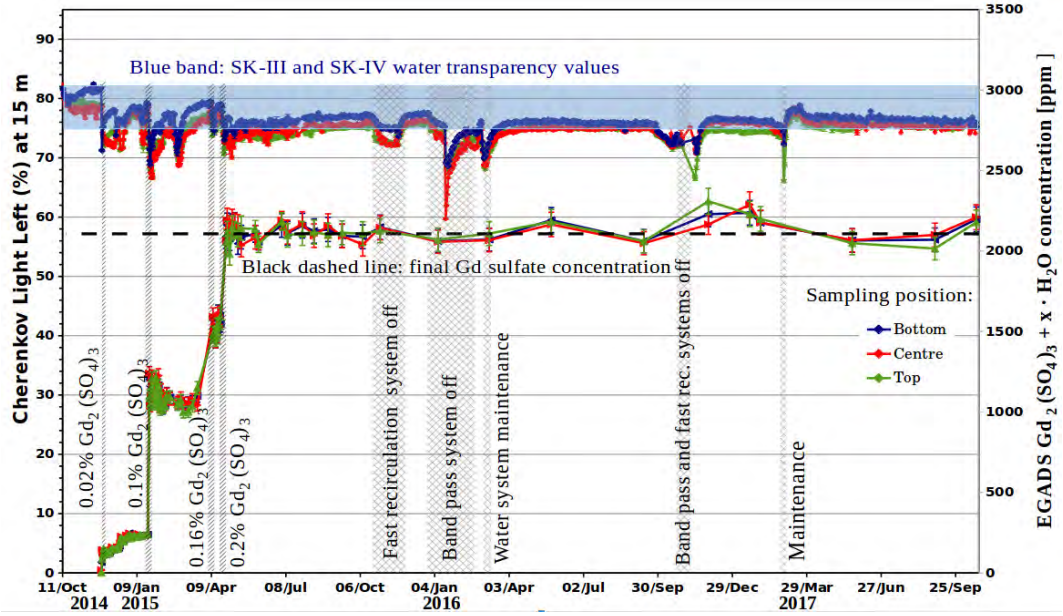

Fig. 16. Cerenkov light left at 15 m for Gd loaded water in EGADS until September 2017. The horizontal blue band are the typical values for SK-III and SK-IV. The vertical lines shows the injection dates where we also indicate the concentration (% in mass) in the 200-ton tank. The black dashed line shows the final expected concentration.

water transparency.

In 2020, we learned the AmberJet 4400 anion exchange resin will be discontinued soon by its manufacturer. In order to replace it we started to test several other resin substitute candidates. In May 2021, we started to test AmberJet 4002 which allowed to quite a high water transparency. The initial drops following the installation of this new resin were due to a too short resin flushing period.

From November 2021, we learned the AmberJet 1020 (Gd) special cation resin was also going to be discontinued by its manufacturer. A substitute candidate, Amberlite IR120B (Gd), was installed in the water system in December 2021. Data after one year and half shows acceptable results, though not as good as the AmberJet 1020 (Gd).

DAQ operations

In June 2017, EGADS electronics have been upgraded from the ATM electronics to SK's QBee electronics, the DAQ system was also upgraded to use these new electronics. Thanks to this upgrade, the stability of the DAQ has been greatly improved, specially at high rate. Several SN tests were performed, and demonstrated that EGADS is able to detect and process a 10 second long burst of more than 100k Hz without trouble. This is much more than what is expected from a very close galactic SN burst: in case of Betelgeuse, about 25k events are expected according to Nakazato's model.

We developed an online fitter, HEIMDALL, based on SK WIT. It is able to reconstruct all the events online during a SN burst and then provides an alarm within few seconds. HEIMDALL is looking for IBD candidates, therefore taking advantage of the delayed coincidence to reduce the background. Thanks to this, EGADS is able to look for SN in the far end of our galaxy. This enable us to instantly and autonomously detect a galactic SN and report to local experts and neutrino and astronomy community.

Bibliography

[1] Marti, Ll. et al., NIM-A 959, 163549 (2020)

SK-Gd

In SK-Gd project, the sensitivity of anti-electron neutrino observation has been improved significantly by detecting neutrons with gadolinium (Gd) (specifically, gadolinium sulfate octahydrate ($Gd_2(SO_4)_3 \cdot 8H_2O$)). Already in 2020, 0.01% Gd (about 13 tons in total weight of $Gd_2(SO_4)_3 \cdot 8H_2O$) has been introduced, achieving about 50% neutrino capture efficiency [1]. As a next step, we have increased Gd concentration to 0.03% during June - July 2022 to achieve 75% neutron capture efficiency. In order to achieve the goal, we needed to dissolve twice as much $Gd_2(SO_4)_3 \cdot 8H_2O$ in a month as we did in 2020.

The second loading in 2022

For the second loading, We doubled the amount of powder and water compared to the previous load to improve the loading speed by a factor of two. For that purpose, tank plumbing modifications were made to improve flow in the dissolving tank.

In the previous Gd loading, the dissolving tank has only one pipe inside at the edge of it. This pipe is bent 90 degrees at the bottom of the tank to make a vortex inside the tank. If the vortex is not strong enough, the powder tends to stagnate at the bottom of the dissolving tank without returning to the shear mixer. For the second Gd loading, since the amount of

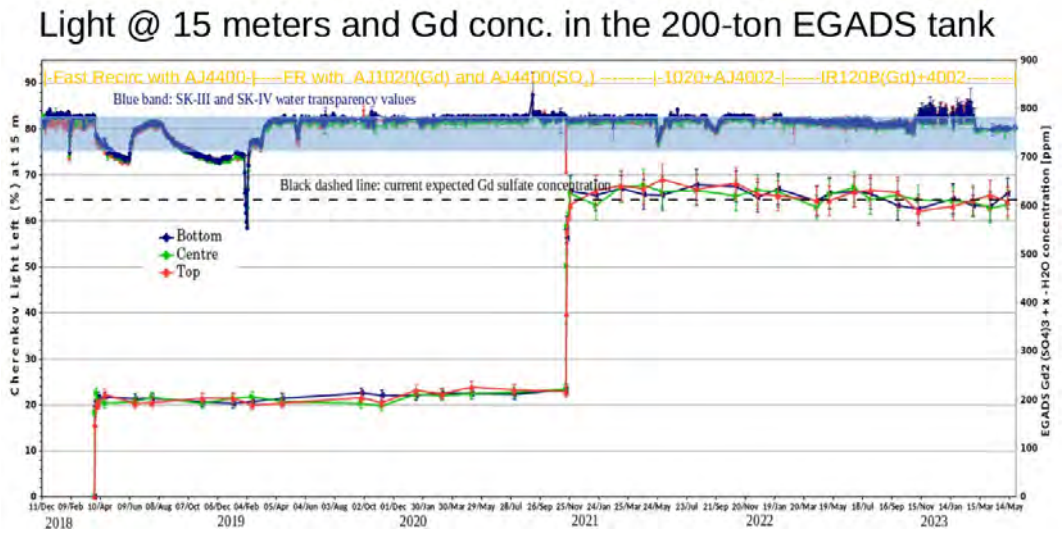

Fig. 17. Cerenkov light left at 15 m for Gd loaded water in EGADS since December 2018. The horizontal blue band are the typical values for SK-III and SK-IV. The vertical lines shows the injection dates where we also indicate the concentration (% in mass) in the 200-ton tank. The black dashed line shows the final expected concentration.

water in the dissolving tank doubled, it was more difficult to make a vortex inside the tank. Therefore, we added two more pipes for the circulation as shown in the Figure 18 The pipe just in front of the exit port efficiently returns the powder to the shear mixer. This line was used at the first ∼5 minutes of each dissolving process (20 min). After that, it is then partially closed, and the other two lines with 90-degree bends are opened to make a vortex for the remaining 15 minutes.

There was another modification in the purification system. In the pre-treatment system, which purifies the Gd water after the dissolving system before the injection to the main circulation line, a cation exchange resin tank is installed to remove impurities present in positive ions especially Ra, which is a radioactive impurity (RI). Before and after the first Gd-loading, the cation exchange resin AMBERJET™1020(Gd) was sampled and measured with the high-purity Ge detector. It was confirmed that the Ra was captured by AMBERJET™1020(Gd). Even though the remaining ion exchange capacity of the resin was confirmed to be still fine, RI such as Rn should come out as the adsorbed Ra decays. Therefore, this resin was replaced with AMBERLITE™IR120B (successor of AMBERJET™1020(Gd)) before the second Gd-loading.

The $Gd_2(SO_4)_3 \cdot 8H_2O$ for SK-Gd needed to meet requirements for impurities described in [2] in order to continue solar neutrinos and supernova relic neutrino (SRN) searches in SK with a similar background rate in SK-IV (pure-water phase) even after loading to the final target concentration of 0.1% Gd. New chemical processing procedures were developed which is can be found in [2]. We performed trace analysis for U, Th, and Ra using ICP-MS and Ge detectors for all production lots to confirm that the requirements were met. The second loading started on June 1st and ended on July 4th of 2022. During the second loading, 27.3 tons of powder was dissolved into the detector without any troubles. The powder contained an average of 4.5% additional water left over from processing.

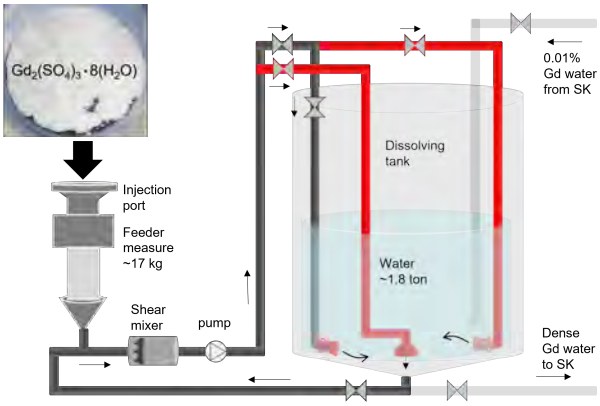

Fig. 18. Modified dissolving system for the second loading.

Therefore, the mass of $Gd_2(SO_4)_3 \cdot 8H_2O$ itself is 26.1 tons. This amount (plus Gd from the first loading) should yield a Gd concentration in the SK tank of 0.033%. Monitoring of the water transparency has confirmed that the transparency had been recovered about two months after the end of the second loading. From the measurements of Gd concentration, it was confirmed that the Gd concentration is uniform in the tank and the neutron capture efficiency by Gd increased by 1.5 times as expected.

Results from the first phase of SK-Gd

Supernova relic neutrinos (SRN) are neutrinos flying like background radiation originating from numerous supernova explosions that have occurred since the beginning of the universe. Observation of SRN will be a key to describe an average picture of a supernova explosion, but it has not been discovered yet. The SRN is the expected to be the main com-

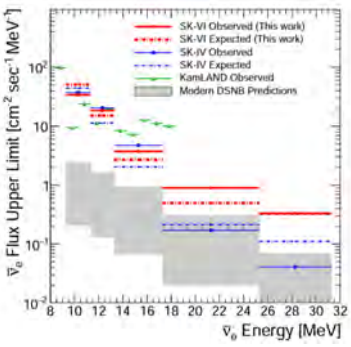

Fig. 19. Upper limits on the anti ν_e flux, obtained by the this study [3]. The red, blue and green lines show SK-VI (This work), SK-IV [4], and KamLAND [5] respectively. The gray-shaded region represents the range of the modern theoretical expectation.

ponent of the anti-electron neutrino that reaches the earth in the energy range of 10-30 MeV while reactor neutrinos dominate in 10 MeV or less, and atmospheric neutrinos dominate in 30 MeV or more.

SRN search was performed for the first SK-Gd (= SK-VI) data between 2020 August and 2022 May, with 0.01% Gd mass concentration. We have developed a new method for tagging neutrons using the signal of neutron capture on Gd in this analysis. The total efficiency of neutron tagging is estimated as 35.6±2%. This is about twice as high compared to that of the pure water phase, while keeping a low-misidentification probability. For five separate energy bins between 9.3 and 31.3 MeV, no significant excess is found above the expected backgrounds at greater than 90%C.L. level. Figure19 shows the upper limits on the anti nue flux. The figure shows the sensitivity of this work with live time of 552.2 days is already comparable to the previous SK-IV search[4] with a live time of 2970 days, which is the world's best above 13.3 MeV.

Bibliography

[1] K. Abe et al., Nucl. Instrum. Meth. A, 1027, 166248 (2022), arXiv:2109.00360

[2] K. Hosokawa et al., PTEP, 2023, 1, January 2023, 013H01

[3] K.Abe et al., ApJ Letters, 951, L27 (2023) July 10

[4] K.Abe et al., 2021, PhRvD, 104, 122002

[5] S.Abe et al., 2022,ApJ, 925, 14

T2K EXPERIMENT

[Spokesperson : Ken Sakashita]
KEK

The Tokai to Kamioka (T2K) experiment [1] is a long baseline neutrino oscillation experiment: a man-made beam of neutrinos is used to do precise studies of the oscillations of neutrinos. Accelerated protons are used to produce the neutrinos in the J-PARC center in the Ibaraki prefecture, which then travel 295 km to reach the Super-Kamiokande (Super-K) detector in the Gifu prefecture where they can be detected after oscillations. A complex of near detectors located 280 meters away from the proton target is used to monitor the neutrino beam, and constrain systematic uncertainties on the neutrino fluxes and interactions. T2K was the first long-baseline experiment to use the off-axis beam technique [2]: the beam is not aimed directly at Super-K, but in a direction making a 2.5° angle with the far detector direction. This gives increased sensitivity to neutrino oscillations while reducing the backgrounds by producing a narrow band neutrino beam centered on the energy corresponding to the first maximum of the $\nu_\mu \to \nu_e$ oscillation probability.

T2K realized the first observation of the appearance of a flavor of neutrinos through oscillation by detecting electron neutrinos in a beam of neutrinos produced in the muon flavor [3]. After achieving this milestone, the experiment has been using its ability to produce a beam of either neutrinos or anti-neutrinos to compare the oscillations of neutrinos and their antiparticles. This allows to study the main remaining open questions in neutrino oscillations (CP symmetry and ordering of the neutrino mass states) by looking at the differences between the oscillations $\nu_\mu \to \nu_e$ and $\bar{\nu}_\mu \to \bar{\nu}_e$. At the same time, T2K's physics goals include the precise measurement of the neutrino oscillation parameters θ_{23} and Δm^2_{32} through a precise study of the pattern of the disappearance of the muon neutrinos in conjunction with the data used to study the oscillation to the electron flavor. The experiment additionally performs searches for physics beyond the standard model, such as oscillations due to sterile neutrinos and CPT violation. Finally, the near detectors are used to perform a wide range of neutrino and anti-neutrino cross-section measurements.

In J-PARC, protons are accelerated to 30 GeV by a series of three accelerators, and hit a 1.9 interaction-length graphite target. The collisions produce hadrons, in particular charged pions and kaons, which are focused by three electromagnetic horns. The hadrons then go through a 96 m-long decay tunnel where they decay in flight into neutrinos. A beam dump at the end of the decay tunnel stops the remaining hadrons, while high energy muons (5 GeV/c or higher) can pass through this beam dump and are measured to provide a first, indirect monitoring of the neutrino beam. The horns can be used either with a positive current (ν-mode), in which case the beam is mainly made of ν_μ, or with a negative current ($\bar{\nu}$-mode) which gives a mainly $\bar{\nu}_\mu$ beam.

The near detectors are separated into two groups. On the axis of the beam, the INGRID detector, made of fourteen identical modules is used to monitor the beam direction and rate stabilities. Each module is made of a succession of iron plates to provide large target mass (7.1 tons per module) alternating with scintillator planes for detection. Using the number of events reconstructed in each module, the beam direction can be measured daily with better than 0.4 mrad accuracy. Located in the direction of Super-K, the off-axis detector ND280 is made of several detectors located inside a 0.2T magnet. The higher precision of those off-axis detectors allows to do more

detailed measurements of the unoscillated neutrino beam. In neutrino oscillation analyses, the ND280 is used to provide information on the ν_μ and $\bar{\nu}_\mu$ unoscillated spectra directed at SK, constrain the dominant backgrounds, and constrain the combination of flux and interaction cross sections.

The far detector, Super-K, is a 50 kton water Cherenkov detector, shielded from atmospheric muons by 1000 m of rock, or 2700 meters-water-equivalent (m.w.e.) mean overburden. To select events corresponding to the T2K beam, Super-K is synchronized via GPS to the J-PARC beamline. Hit information within $\pm 500 \mu s$ from the beam arrival timing is used for T2K data analysis. Events are reconstructed by detecting Cherenkov rings from charged particles produced by neutrino interactions. These events are separated into muon-like and electron-like events based on the light pattern of this ring, and additional selection cuts are applied to produce samples enriched in certain interaction modes. In 2020, Gadolinium was dissolved into the Super-Kamiokande detector at 0.01%, and the new phase of Super-K, SK-Gd, was started [4]. Additional gadolinium was loaded to Super-K in 2022, and the detector is currently operational with 0.03% gadolinium concentration. Additions of gadolinium significantly increased neutron detection capability, which will benefit T2K's neutrino interaction and oscillation measurements as well.

To study neutrino oscillations, the data observed at the far detector are compared to the predictions of the three-flavor oscillation model for different values of the oscillation parameters. To this end, a model of the experiment is constructed: the fluxes of the different flavors of neutrinos reaching the detectors are predicted by a series of simulations, and the interactions of ν and $\bar{\nu}$ in the detectors are simulated using the NEUT Monte Carlo event generator [5]. First, the flux and properties of the proton beam reaching the target are measured by the proton beam line monitors. Interactions of the protons in the graphite target and production of secondary hadrons are then simulated using the FLUKA package [6]. Measurements from hadron production experiments, in particular NA61/SHINE [7], are used to tune this part of the simulation and the out-of-target interactions. The propagation and decay-in-flight of the hadrons in the decay tunnel are then simulated using the GEANT3 and GCALOR [8] packages. The predictions from this model are compared to the data observed in the near detectors to tune the predictions for the far detector by constraining the model parameters. The result of this near detector fit provides the initial values and uncertainties of the flux and interaction model parameters used in the far detector analysis to measure parameters describing neutrino oscillations.

T2K started collecting physics data in January 2010. Up to run 10 was taken with the pure-water phase of the Super-K detector. Run 11 was the first data taken with gadolinium dissolved in Super-K water at 0.01% Gd concentration. From the run 11 data, evidence for the signal corresponding to the capture of neutrons on gadolinium was seen: an excess of low energy events is seen after the trigger. The number of events in this excess follows an exponential decrease in time, with a time constant compatible with the expected capture time on gadolinium (Fig 20).

After the run 11 data taking, a long shutdown to upgrade

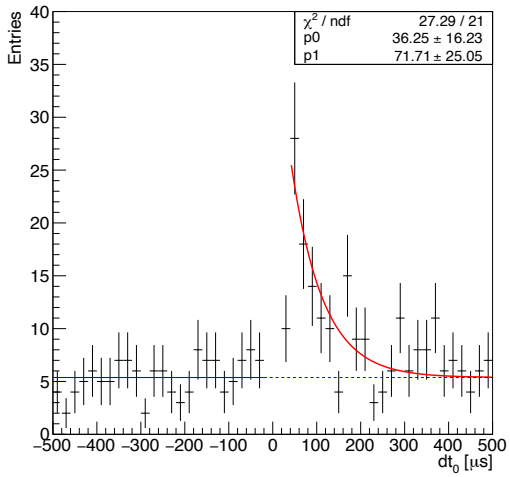

Fig. 20. Number of low energy events seen in run 11 as a function of time since beam trigger (dt$_0$). An exponential fit is performed: $n(t) = \mathrm{p0} \times e^{-t/\mathrm{p1}} + (\mathrm{const.})$, and the time constant obtained is compatible with the expected capture time at the current Gd concentration (115μs).

the accelerator used to produce the neutrino beam took place. After the upgrade, the experiment took a short period of beam data, run 12, which unfortunately lasted only a few days due to troubles at the accelerator. Nevertheless, the record beam power of about 550 kW was achieved and beam-induced neutrino interactions were successfully observed at the far detector during run 12.

The details of the data that have been collected at the far detector can be found in Table 3. Over the whole period, the event rates and the beam direction were found to be consistent with the expectations and stable by the measurements of the muon monitor and the on-axis near detector. In particular, the beam direction remained stable well within the $\pm$1mrad target.

An upgrade of the off-axis near detectors is also ongoing. A new set of detectors to replace the π^0 detector part of the current ND280 is being constructed and commissioned. Those new detectors will give improved ability to study neutrino interactions, with a larger efficiency for high-angle events, lower threshold to detect protons, and the ability to reconstruct neutron energy.

In addition, a joint analysis of T2K beam data and Super-K's atmospheric neutrino data, and also another joint analysis with T2K and NOvA experiments are both in progress. In particular significant progress on the joint analysis with the Super-K's atmospheric neutrino data was made during FY2022. It is expected that the sensitivity will improve thanks to the cancellation of many systematic uncertainties, such as the Super-K detector response, flux, and cross-section between the two measurements. Its first result is expected to be released soon.

Table 3. T2K data taking periods and integrated numbers of protons on target (POT) used in the far detector analysis.

Run Period	Dates	$\times 10^{20}$ POT ν	$\bar{\nu}$
Run 1	Jan.2010 - Jun.2010	0.32	–
Run 2	Nov.2010 - Mar.2011	1.11	–
Run 3	Mar.2012 - Jun.2012	1.60	–
Run 4	Oct.2012 - May.2013	3.60	–
Run 5	May.2014 - Jun.2014	0.24	0.51
Run 6	Oct.2014 - Jun.2015	0.19	3.55
Run 7	Feb.2016 - May.2016	0.48	3.50
Run 8	Oct.2016 - Apr.2017	7.17	–
Run 9	Oct.2017 - May.2018	0.20	8.79
Run 10	Oct.2019 - Feb.2020	4.73	–
Run 11	Mar.2021 - Apr.2021	1.76	–
Run 12	Apr.2023 - Apr.2023	0.09	–
Total	**Jan.2010 - Apr.2023**	**21.51**	**16.35**

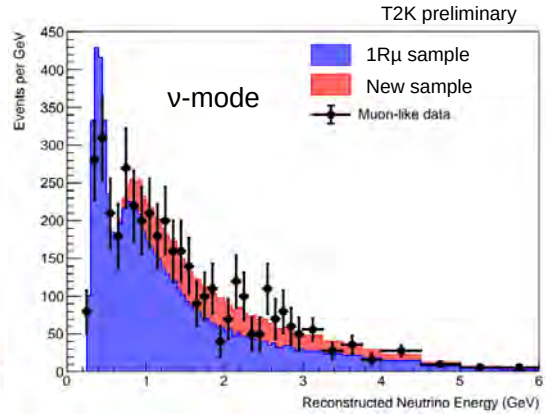

Fig. 21. Reconstructed neutrino energy distributions of the combined 1-Ring ν_μ and multi-ring ν_μ samples. The blue(red) filled histogram shows the contribution of the single-(multi-)ring sample. The black point shows the observed data.

New oscillation analysis results with new multi-ring event sample at the Super-K detector

The T2K experiment released a new result of neutrino oscillation parameter measurements and search for CP-violation in the lepton sector at the Neutrino 2022 conference [9]. This analysis uses an Super-K dataset collected up to the end of Feb. 2020. This corresponds to an exposure of 19.66 $\times 10^{20}$ protons on target (POT) in neutrino mode and 16.35 × $\times 10^{20}$ in antineutrino mode, which adds 4.73 $\times 10^{20}$ of POT in the neutrino mode compared to the oscillation analysis results released before 2021 [10, 11]. Initial oscillation analyses with this additional beam exposure were conducted and released in Refs. [12, 13]. For this analysis presented in this report, further significant improvements were made on most parts of the analysis. Flux prediction was improved by using the new hadron production data taken by NA61/SHINE experiment using a replica target [14]. The near detector analysis was improved by tagging protons from CC-0π as well as tagging photons at the electromagnetic calorimeter to make samples dominated by DIS and CC-1π^0 interactions. Neutrino interaction models were also improved with improved modeling of CC-QE and CC-2p2h interactions based on the spectrum function model, together with improved modeling of the other interaction modes. Finally, multi-ring samples at Super-K are included in the T2K oscillation studies for the first time.

Previous oscillation analyses at T2K only used events with a single reconstructed Cherenkov ring at Super-K. As described above, multi-ring events from the ν_μ sample were newly introduced to this oscillation analysis. Figure 21 shows reconstructed neutrino energy distributions of the new combined ν_μ sample overlaid with the observed data. Although the new multi-ring sample has energy slightly above the oscillation maximum, it is still sensitive to the oscillation and adds up statistics of the neutrino mode ν_μ sample by about 30%. The multi-ring sample also serves as an important control sample for the prediction of CC-nonQE interactions.

Oscillation parameters were extracted by simultaneously fitting the six data samples; (ν-mode) single electron-like ring, single electron-like ring with decay-electron, single muon-like ring, multiple muon-like ring, ($\bar{\nu}$-mode) single electron-like ring and single μ-like ring samples. Figure 22 shows the allowed region in the $\Delta m^2_{32(31)}$ vs. $\sin^2\theta_{23}$ plane. The best-fit point is in the upper θ_{23} octant and prefers the normal mass ordering.

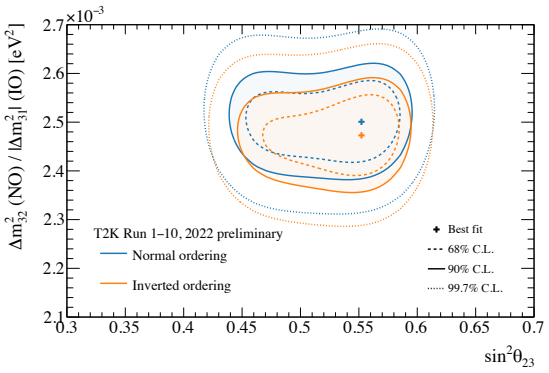

Fig. 22. The allowed regions in the $\Delta m^2_{32(31)}$ vs. $\sin^2\theta_{23}$ plane. The contours are drawn with a fixed $\Delta\chi^2$ value for each confidence level (C.L.). The value of θ_{13} is constrained to be $\sin^2(2\theta_{13}) = 0.0861 \pm 0.0027$ based on the reactor measurements.

Figure 23 shows distributions of reconstructed neutrino energy from the electron-like sample taken with the neutrino and antineutrino mode beams. Constraints on the δ_{CP} evaluated by both frequentist and Bayesian approaches are shown in Fig. 24. In both approaches, CP-conserving values of $\delta_{CP} = 0$ and $\delta_{CP} = \pi$ are outside of the 90% C.L. intervals.

Bibliography

[1] K. Abe *et al.* (T2K Collaboration), Nucl. Instrum. Meth. A **659**, 106 (2011).

[2] D. Beavis, A. Carroll, I. Chiang, *et al.*, Long Baseline Neutrino Oscillation Experiment at the AGS (Proposal E889), 1995. Physics Design Report, BNL 52459.

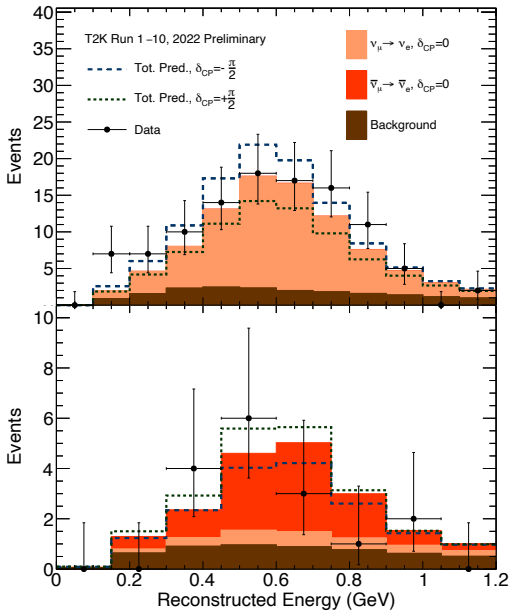

Fig. 23. Reconstructed neutrino energy distributions for the electron–like ring samples. The top and bottom panels show distributions for the neutrino-mode and antineutrino-mode beam data, respectively. The filled histogram shows the predictions with different δ_{CP} values. The black point shows the observed data.

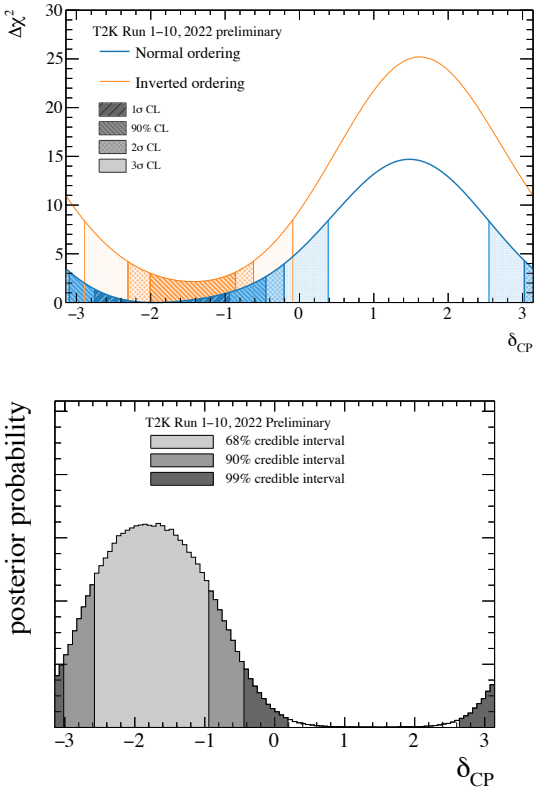

Fig. 24. Constraints on the δ_{CP} parameters from T2K Run 1-10 data. The top panel shows the result from the frequentist approach with the Feldman-Cousins method, while the bottom panel shows the result from the Bayesian approach. The value of θ_{13} is constrained to be $\sin^2(2\theta_{13}) = 0.0861 \pm 0.0027$ based on the reactor measurements.

[3] K. Abe *et al.* (T2K Collaboration), Phys. Rev. Lett. **112**, 061802 (2014).

[4] K. Abe *et al.* (Super-Kamiokande Collaboration), Nucl. Instrum. Meth. A **1027**, 166248 (2022).

[5] Y. Hayato, Acta Phys. Pol. B **40**, 2477 (2009).

[6] T. Bhlen *et al.*, Nucl. Data Sheets **120**, 211 (2014).

[7] N. Abgrall et al. (NA61/SHINE Collaboration), Eur. Phys. J. C **76**, 84 (2016).

[8] C. Zeitnitz and T. A. Gabriel, Proceedings of International Conference on Calorimetry in High Energy Physics (World Scientific, Corpus Christi, Texas, 1992), ISBN 9789810213039, pp. 394-404.

[9] Christophe Bronner, "Recent results from T2K", Zenodo https://doi.org/10.5281/zenodo.6683821 (June 2022).

[10] K. Abe *et al.* (T2K Collaboration), Nature, 2020, 580(7803), pp. 339–344

[11] K. Abe *et al.* (T2K Collaboration), Phys. Rev. D **103**, 112008 (2021)

[12] M. A. Ramírez *et al.* (T2K Collaboration), [arXiv:2303.03222 [hep-ex]].

[13] M. A. Ramírez *et al.* (T2K Collaboration), [arXiv:2305.09916 [hep-ex]].

[14] N. Abgrall *et al.* (NA61/SHINE Collaboration), Eur. Phys. J. C **79**, no.2, 100 (2019).

XMASS EXPERIMENT

[Spokesperson : Shigetaka Moriyama]

Kamioka Observatory, ICRR, the University of Tokyo

Introduction

The XMASS project was designed to detect dark matter, neutrinoless double beta decay, and ^{7}Be/pp solar neutrinos using highly-purified liquid xenon (LXe) scintillator in an ultra-low radioactivity environment [1]. The advantages of using LXe are a large amount of scintillation light yield, scalability of the size of the detector mass, easy purification to reduce internal radioactive backgrounds (BGs), and shielding ability against radiation from outside the detector due to a high atomic number ($Z = 54$) [2]. A breakthrough technology was developed to purify liquid xenon from the radioactive contaminant of ^{85}Kr found in commercial gas xenon [3]. This makes liquid xenon detectors suitable for rare event searches. The detector containing ~830 kg of LXe, was constructed in September 2010. Commissioning data was taken from December 2010 to May 2012. Based on commission-

ing data results were published on DM searches [4, 5, 6], solar axions [7], and two-neutrino double electron capture on ^{124}Xe [8]. We also studied the possibility of detecting galactic supernova neutrinos via coherent elastic neutrino-nucleus scattering [9].

Analyzing the commissioning data we found that a majority of events at low energy originated from radioactive contamination in the aluminum seal of the photomultiplier tube (PMT) window. In order to minimize the impact of this BG, the detector was refurbished. The contaminated seals were covered with copper rings and plates to stop scintillation lights and radiation caused by this contamination to reach the inner detector volume. The PMT windows were cleaned with nitric acid, and copper parts were electropolished in order to remove possible surface contamination. After a year of detector refurbishment, data-taking resumed in November 2013 with background significantly reduced and continued for more than five years. We completed data taking in February 2019. Results were published from searches for annual modulation from dark matter [10, 11], solar Kaluza-Klein axions [12], two-neutrino double electron capture on ^{124}Xe [13], dark matter through elastic-scattering [14], hidden photons [15], inelastic-scattering off ^{129}Xe [16], sub-GeV dark matter [17], exotic neutrino-electron interactions [18], events coincident with the arrival of gravitational waves [19], and for neutrinoless quadruple beta decay of ^{136}Xe [20].

In the following sections, we briefly introduce the XMASS-I detector and report the latest physics results from XMASS data collected after the refurbishment.

The XMASS-I detector

XMASS-I was a single-phase LXe scintillator detector located underground (2700 m water equivalent) at the Kamioka Observatory [21]. Figures 25 and 26 show a schematic drawing of the XMASS-I detector and a picture during the refurbishment work, respectively. It contained ∼830 kg of LXe in its active region. The active volume is viewed by 630 hexagonal and 12 cylindrical Hamamatsu R10789 PMTs arranged on an 80 cm diameter pentakis-dodecahedron support structure. These PMTs were developed to achieve low background requirements [22]. The largest contributions to the reduction of radioactivity came from the PMTs' stem and its dynode support. The glass stem was exchanged for a the Kovar alloy one, and the ceramic support was changed to a quartz one. The R10789 is the first model of Hamamatsu Photonics K. K. that adopted these materials for low background purposes and provided a groundbreaking step for further reductions of radioactivity in PMTs. A total photocathode coverage of more than 62% of the inner surface was achieved in XMASS. The almost spherical array of PMTs was supported in a double-walled vessel made of oxygen-free high conductivity copper [23]. The waveforms of each PMT were recorded with CAEN V1751 waveform digitizers with a 1 GHz sampling rate and 10 bit resolution. The detector was calibrated regularly with a ^{57}Co source inserted along its central vertical axis and an external ^{60}Co source. From the data taken with the ^{57}Co source at the center of the detector volume, the photoelectron (PE) yield was determined to be ∼14 PE/keV. Two different energy scales were used: keV$_{ee}$ represents an electron equivalent energy, and keV$_{nr}$ denotes the nuclear recoil energy. The scintillation decay time constant was investigated in liquid xenon with the XMASS detector. The results were summarized in [24] and [25].

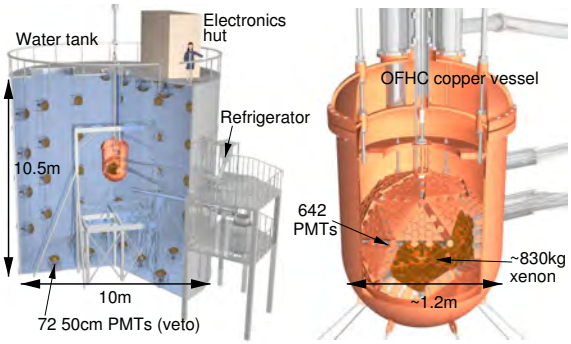

Fig. 25. Schematic drawing of the XMASS-I detector.

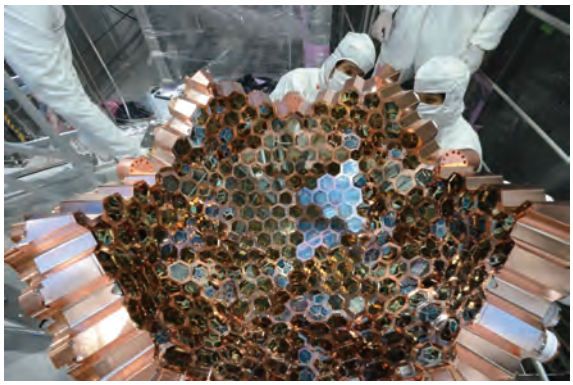

Fig. 26. The XMASS detector (the photo was taken during the refurbishment work in 2013).

In order to shield the LXe detector from external gammas, neutrons, and muon-induced BGs, the copper vessel was placed at the center of a ϕ10 m$\times$ 10.5 m cylindrical tank filled with pure water. This water tank was equipped with 72 Hamamatsu R3600 20-inch PMTs to provide both an active muon veto and a passive shield against external BGs. XMASS-I was the first direct detection dark matter experiment equipped with such an active water Cherenkov shield. The LXe and water Cherenkov detectors were called the Inner Detector (ID) and the Outer Detector (OD), respectively.

It is also worth noting that there were some important technical studies related to pulse-shape discrimination between nuclear recoils and electron recoils [26], radon removal using charcoal filters [27], scintillation performance of liquid xenon at room temperature [28], a ^{220}Rn calibration source [29], and 3-inch low background photomultiplier tubes [30] for future applications.

Search for neutrinoless quadruple beta decay of ^{136}Xe in XMASS-I [20]

Despite the great success of the standard model (SM) in particle physics, the nature of the neutrino is not yet under-

stood thoroughly. If the neutrino is a Majorana particle, processes that violate the lepton number (L) by two ($\Delta L = 2$) can occur. The neutrinoless double beta decay ($0\nu\beta\beta$) is one of the $\Delta L = 2$ processes beyond the SM. Observing the $0\nu\beta\beta$ would tell us the Majorana nature of the neutrino. It is also linked to the seesaw mechanism, which explains the extremely light neutrino mass and baryon number asymmetry in the universe via leptogenesis. Although a number of $0\nu\beta\beta$ experiments using a variety of candidate nuclei have been performed, no evidence has been achieved so far.

On the other hand, Heeck and Rodejohann proposed that even if the neutrino is a Dirac particle, a decay that violates L by four ($\Delta L = 4$) can occur by adding three right-handed neutrinos in the SM. This $\Delta L = 4$ process is naturally linked to the light Dirac mass terms of neutrino, CP violation and leptogenesis. The neutrinoless quadruple beta decay ($0\nu4\beta$)

$$(A, Z) \rightarrow (A, Z+4) + 4e^{-}, \tag{1}$$

is one of the $\Delta L = 4$ processes. Here A and Z are the atomic mass and atomic numbers, respectively. It is theoretically predicted that only three candidate nuclei, ^{150}Nd, ^{136}Xe, and ^{96}Zr, can undergo this process; there is no experimental search with either ^{136}Xe or ^{96}Zr $0\nu4\beta$ decay so far. The Q-value of the ^{136}Xe $0\nu4\beta$ ($Q_{0\nu4\beta}$) is 79 keV.

In a neutrinoless quadruple beta decay of ^{136}Xe, four β-rays with a total energy of 79 keV are emitted simultaneously. Since these β-rays are expected to deposit all their energy in the liquid xenon at each decay, a monochromatic peak is expected in the energy spectrum. The scintillation yield from the four electrons and the detector response were simulated by the XMASS Monte Carlo simulation based on Geant4. The expected peak energy reconstructed from the observed light is found at an energy 4% higher than 79 keV. This is because the energy of each electron is lower than 79 keV and the scintillation efficiency of liquid xenon is higher for the low energy electrons.

A search for the $0\nu4\beta$ decay was carried out with the data accumulated from November 2013 to July 2016. During this period, the detector condition, specifically the temperature and pressure of LXe, was kept stable. The data set was divided into four subsets (subset 1–4) depending on the Xe gas circulation status and the BG rate due to the neutron activation.

The data went through several event selections. First, the event is triggered only by ID. Then the event should have both the time difference from the previous event more than 10 ms and the root mean square of the hit timing in the event less than 100 ns. For the rejection of external γ-rays, we apply the fiducial volume selection using the position reconstruction of the events' vertices. The events whose vertices were reconstructed inside the fiducial volume within 30 cm radius, were selected. The internal BG of ^{222}Rn daughter nuclei were quantified by counting ^{214}Bi events taking the coincidences of ^{214}Bi-^{214}Po chain-decays. This provided ^{214}Bi samples with 0.4% of non-^{214}Bi events due to the accidental coincidence.

Further event selections were applied to estimate the abundance of other BG and the signal. A small fraction of scintillation light from α events would leak into the sensitive region via small gaps of the detector structure and would be detected by the PMTs. These events can be removed using the scintillation time constant obtained by the fitting of the summed-up waveforms with an exponential function. The events which survived the α-event reduction were further classified into β-depleted and β-enriched samples using the particle identification selection. The particle identification uses the difference of the scintillation time profiles between β-rays and γ-rays.

By fitting the energy spectra of the β-depleted, β-enriched, and ^{214}Bi samples simultaneously, we estimated the abundance of the signal and the BG. To estimate the activities of the BG, the energy range of the fit was set from 30 to 200 keV$_{ee}$ with the energy bin's width 2 keV$_{ee}$. As a result, no significant signal excess over the expected BG was found as shown in Fig 27. The calculated 90% CL lower limit is 3.7×10^{24} years for the neutrinoless quadruple beta decay of ^{136}Xe. This is the first experimental constraint on the neutrinoless quadruple beta decay of ^{136}Xe.

Bibliography

[1] Y. Suzuki *et al.*, hep-ph/0008296.

[2] K. Abe *et al.* (XMASS Collaboration), Astropart. Phys. **35** (2012) 609.

[3] K. Abe *et al.* (XMASS Collaboration), Astropart. Phys. **31** (2009) 290.

[4] K. Abe *et al.* (XMASS Collaboration), Phys. Lett. B **719** (2013) 78.

[5] H. Uchida *et al.* (XMASS Collaboration), Prog. Theor. Exp. Phys. (2014) 063C01.

[6] K. Abe *et al.* (XMASS Collaboration), Phys. Rev. Lett. **113** (2014) 121301.

[7] K. Abe *et al.* (XMASS Collaboration), Phys. Lett. B **724** (2013) 46.

[8] K. Abe *et al.* (XMASS Collaboration), Phys. Lett. B **759** (2016) 64.

[9] K. Abe *et al.* (XMASS Collaboration), Astropart. Phys. **89** (2017) 51.

[10] K. Abe *et al.* (XMASS Collaboration), Phys. Lett. B **759** (2016) 272.

[11] K. Abe *et al.* (XMASS Collaboration), Phys. Rev. D **97** (2018) 102006.

[12] N. Oka *et al.* (XMASS Collaboration), Prog. Theor. Exp. Phys. **2017** (2017) 103C01.

[13] K. Abe *et al.* (XMASS Collaboration), Prog. Theor. Exp. Phys. **2018** (2018) 053D03.

[14] K. Abe *et al.* (XMASS Collaboration), Phys. Lett. B **789** (2019) 45.

[15] K. Abe *et al.* (XMASS Collaboration), Phys. Lett. B **787** (2018) 153.

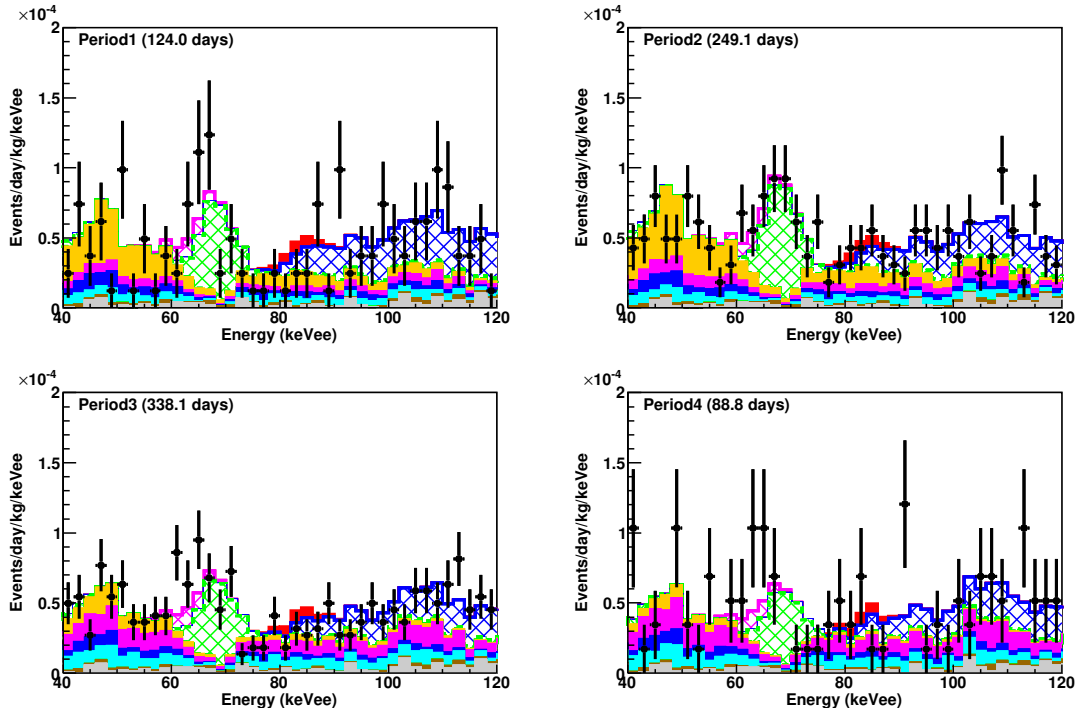

Fig. 27. Energy spectra for β-depleted samples for the four subsets. The data are shown as black points with statistical error bars. Signal (90% CL lower limit of the half life, red filled), ^{126}Xe two neutrino double electron capture (magenta hatched), ^{125}I (green hatched), ^{133}Xe (blue hatched) ^{14}C (orange filled), ^{39}Ar (magenta filled), ^{85}Kr(blue filled), ^{214}Pb (cyan filled), ^{136}Xe 2ν double beta(brown filled), and external γ-rays (gray filled) backgrounds are shown as stacking histograms. Here, we show an enlarged view of the signal region for the convenience.

[16] T. Suzuki *et al.* (XMASS Collaboration), Astropart. Phys. **110** (2019) 1.

[17] M. Kobayashi *et al.* (XMASS Collaboration), Phys. Lett. B **795** (2019) 308.

[18] K. Abe *et al.* (XMASS Collaboration), Phys. Lett. B **809** (2020) 135741.

[19] K. Abe *et al.* (XMASS Collaboration), Astropart. Phys. **129** (2021) 102568.

[20] K. Abe *et al.* (XMASS Collaboration), Phys. Lett. B **833** (2022) 137355.

[21] K. Abe *et al.* (XMASS Collaboration), Nucl. Instrum. Meth. A **716** (2013) 78.

[22] K. Abe *et al.* (XMASS Collaboration), Nucl. Instrum. Meth. A **922** (2019) 171.

[23] K. Abe *et al.* (XMASS Collaboration), Nucl. Instrum. Meth. A **884** (2018) 157.

[24] H. Takiya *et al.* (XMASS Collaboration), Nucl. Instrum. Meth. A **834** (2016) 192.

[25] K. Abe *et al.* (XMASS Collaboration), JINST **13** (2018) P12032.

[26] K. Abe *et al.* (XMASS Collaboration), Nucl. Instrum. Meth. A **659** (2011) 161.

[27] K. Abe *et al.* (XMASS Collaboration), Nucl. Instrum. Meth. A **661** (2012) 50.

[28] K. Abe *et al.* (XMASS Collaboration), Nucl. Instrum. Meth. A **594** (2008) 148.

[29] M. Kobayashi, M. Yamashita, A. Takeda, K. Kishimoto, S. Moriyama, Journal of Physics: Conference Series 718 (2016) 042069 (TAUP2015).

[30] K. Abe *et al.* (XMASS Collaboration), JINST **15** (2020) P09027.

XENON EXPERIMENT

XENON ICRR group
[Principal investigator : Shigetaka Moriyama]
Kamioka Observatory, ICRR, the University of Tokyo

Introduction

The XENONnT experiment [1] is the most sensitive direct dark matter search experiment conducted at LNGS in Italy. The XENON collaboration includes about 180 collaborators from 27 institutions in 12 countries. From Japan, the University of Tokyo (ICRR and Kavli IPMU), Nagoya University, and Kobe University participate since 2017. The XENON group uses liquid xenon and employs a time projection chamber (TPC) shown in Fig. 28, characterized by its ability to discriminate between nuclear and electron recoil. The Japanese group is making a significant contribution toward the discovery of DM particles based on a purification technology for liquid xenon developed in XMASS and the neutron detection technology developed for Super-Kamiokande. The XENON collaboration completed XENONnT detector construction in 2020 and started data taking in 2021. Japan also participated in the data analysis of the predecessor XENON1T experiment, from which the XENON collaboration reported a significant 3.3σ excess of electron recoil events over the background in 2020 [2]. Since this could be interpreted as a signal of axions produced in the Sun, the ICRR members, who have also searched for solar axions in XMASS [3], contributed to interpreting the data.

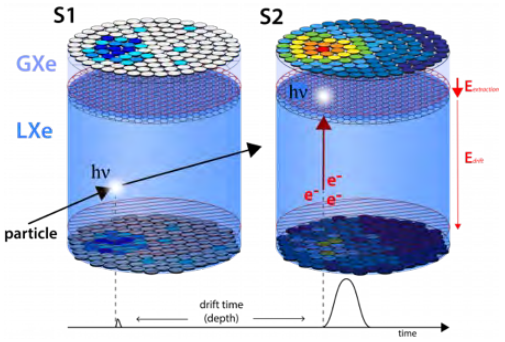

Fig. 28. Principle of operation of liquid xenon time projection chamber (TPC). The interaction of dark matter produces scintillation light S1, and electrons drifted by an electric field give a delayed signal S2; the observed pattern of S2 can identify the planar location of the interaction, and the time difference between S1 and S2 provides depth information. The ratio of S1 to S2 also holds information about the type of particle that caused the interaction. Figure from the XENON collaboration.

In this year, a blinded analysis of low-energy electronic recoil data from the first science run of the XENONnT dark matter experiment was reported [4]. The XENONnT detector has the increased 5.9 ton liquid xenon target and the lowerst background ever achieved in a dark matter detector, which is $\sim$5 times lower than in XENON1T. With an exposure of 1.16 ton-years, we observe no excess above background and set stringent new limits on solar axions, an enhanced neutrino magnetic moment, and bosonic dark matter. Details are shown in the section below.

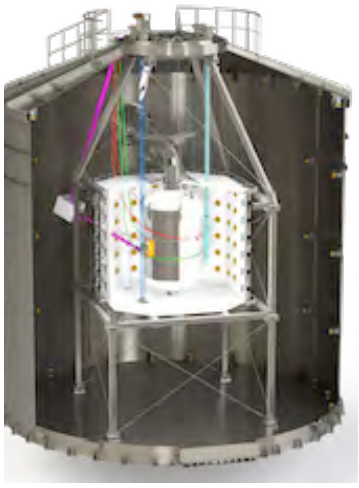

Fig. 29. Overview of the XENONnT detector. The white part is the neutron veto detector. The liquid xenon TPC is at the center, surrounded by the white reflective material, and 120 photomultiplier tubes are used to detect the Cherenkov lights produced by gamma rays when neutrons are captured by gadolinium or other nuclei and used to identify the neutrons. The water tank is 10 m in diameter and 10 m in height, and 0.2% of gadolinium will be added to the entire system. Figure from the XENON collaboration.

There are some other publications describing application and modeling of an online distillation method to reduce krypton and argon in XENON1T [5], emission of single and few electrons in XENON1T and limits on light dark matter [6], double-weak decays of ^{124}Xe and ^{136}Xe in the XENON1T and XENONnT experiments [7], an approximate likelihood for nuclear recoil searches with XENON1T data [8], and a next-generation liquid xenon observatory for dark matter and neutrino physics [9].

Neutron background tagging utilizing SK-Gd technology

Background reduction is critical in rare event searches, and there are two primary background sources important in XENONnT: one is radon in liquid xenon, and the other is neutrons emitted from instrument components. The Japanese group is contributing to the realization and operation of a neutron veto detector that tags these neutrons and reduces the background by event basis, using the gadolinium-doped water Cherenkov detector technology developed at Kamioka for Super-Kamiokande [10]. Figure 29 shows a full view of the XENONnT detector, which is entirely housed in a water tank with a white reflective material optically isolating the neutron veto immediately surrounding the liquid xenon TPC at its center. The neutron veto is equipped with 120 PMTs. By adding 0.2% of Gd to the water in the whole tank, neutrons emitted from the detector components are expected to be captured by Gd with a high probability if they reach the neutron veto after recoiling from xenon nuclei in the TPC. After capturing the

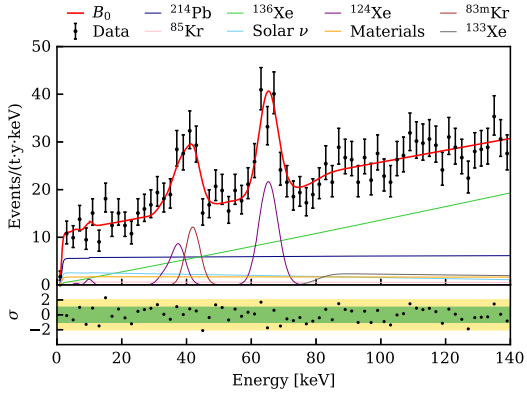

Fig. 30. Fit to SR0 data using the background model B_0. The fit result of B_0 is the red line. Figure from Ref. [4].

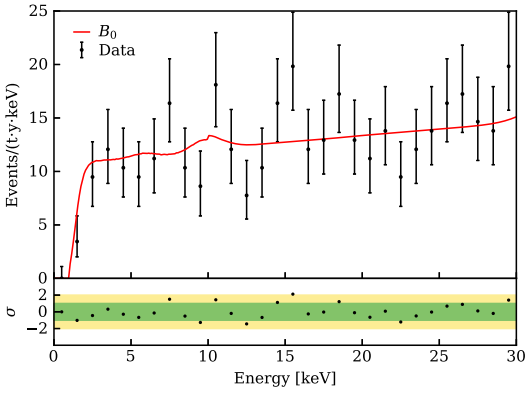

Fig. 31. Data and best-fit B_0 model below 30 keV. No significant excess above the background was found. Figure from Ref. [4].

neutron on Gd, we expect PMTs in the neutron veto detector to observe Cherenkov light caused by gamma rays emitted from the Gd nucleus that captured the neutron. This enables us to tag neutrons that cause background for the WIMP search and thus maximize the experiment's sensitivity. XENONnT aims to tag approximately 87% of such neutron events that are otherwise indistinguishable from dark matter events. During the construction period, the neutron veto detector was completed. With the help of the Super-Kamiokande collaboration, about 2.6 tons of the purest grade of gadolinium sulfate was obtained in Japan and delivered to LNGS [11]. The Super-Kamiokande collaboration also helped us to design the water plant for our application. In 2021, the installation of a gadolinium-loaded water purification plant was completed, and in 2022, commissioning tests of the plant started using pure water and Gd-loaded water. They were successful and the performance is being optimized. At present, the neutron veto operates with pure water. The gadolinium loading into the water in the tank is being prepared.

Search for New Physics in Electronic Recoil Data from XENONnT [4]

In 2020 an unexpected excess of electronic recoil (ER) events below ∼7 keV was reported in the XENON1T dark matter (DM) experiment [2]. The excess was compatible with decays from trace amounts of tritium but the presence of which we were unable to confirm or exclude at the time. The result was also interpreted as physics beyond the standard model such as solar axions, bosonic DM, solar neutrinos with enhanced magnetic moment, and many other models.

Since tritium was a potential explanation for the XENON1T excess, a number of measures were taken to minimize the possibility of introducing it into XENONnT in the form of tritiated hydrogen (HT) and tritiated water. The science run 0 (SR0) dataset was collected from July 6, 2021, to November 10, 2021, with a total live time of 97.1 days. In this analysis, we consider ER interactions only. Using the ^{220}Rn calibration as a reference, the ER signal region in S1-S2 space was blinded below 20 keV in the SR0 dataset. A fiducial mass of (4.37 ± 0.14) tons is used for this analysis, yielding a total exposure of 1.16 ton $\times$ years. We consider three categories of potential BSM signals in this search: (a) solar axions, (b) solar neutrinos with an enhanced magnetic moment, and (c) bosonic DM, which primarily includes axionlike particles and dark photon DM.

In order to further explore the possibility of tritium as an explanation for the XENON1T excess, we operated XENONnT in a different mode for 14.3 days bypassing the getter purifying the GXe volume of the cryostat after the SR0 data was collected. This "tritium-enhanced" dataset, when unblinded, showed no evidence for a tritiumlike excess. Based on this null result, combined with the aforementioned reduction measures, tritium is not included in the background model.

The low-energy ER background in XENON1T was dominated by ^{214}Pb. For XENONnT, in addition to an extensive material radioassay campaign, a new high-flow radon removal system was developed to further reduce this background. We consider nine components in the background model B_0: ^{214}Pb, ^{85}Kr, gamma rays from detector materials, ^{136}Xe, electron scattering caused by solar neutrinos, ^{124}Xe, accidental coincidences, ^{133}Xe, and ^{83m}Kr. Having successfully reduced some of the background sources above, the two-neutrino double-beta ($2\nu\beta\beta$) decay of ^{136}Xe becomes an important background in this analysis, overtaking ^{214}Pb as the dominant component above 40 keV. The double-electron capture (2νECEC) decay rate of ^{124}Xe is left unconstrained in B_0. The last background component, accidental coincidences, is the only non-ER background in B_0. After all aspects of the analysis had been fixed and a good agreement between the background model and data above 20 keV was found (p-value ∼0.2), the region between $\pm 2\sigma$ quantile of ER events in S2 was unblinded. We performed a fit in reconstructed energy space using an unbinned maximum likelihood. The best fit of B_0 is illustrated in Figs 30 and 31. The SR0 dataset agrees well with B_0, and no excess above the background is found. The efficiency-corrected average ER background rate within (1, 30) keV is measured to be $(15.8 \pm 1.3_{\text{stat}})$ events/(t y keV), a factor of ∼5 lower than the rate in XENON1T. This is the

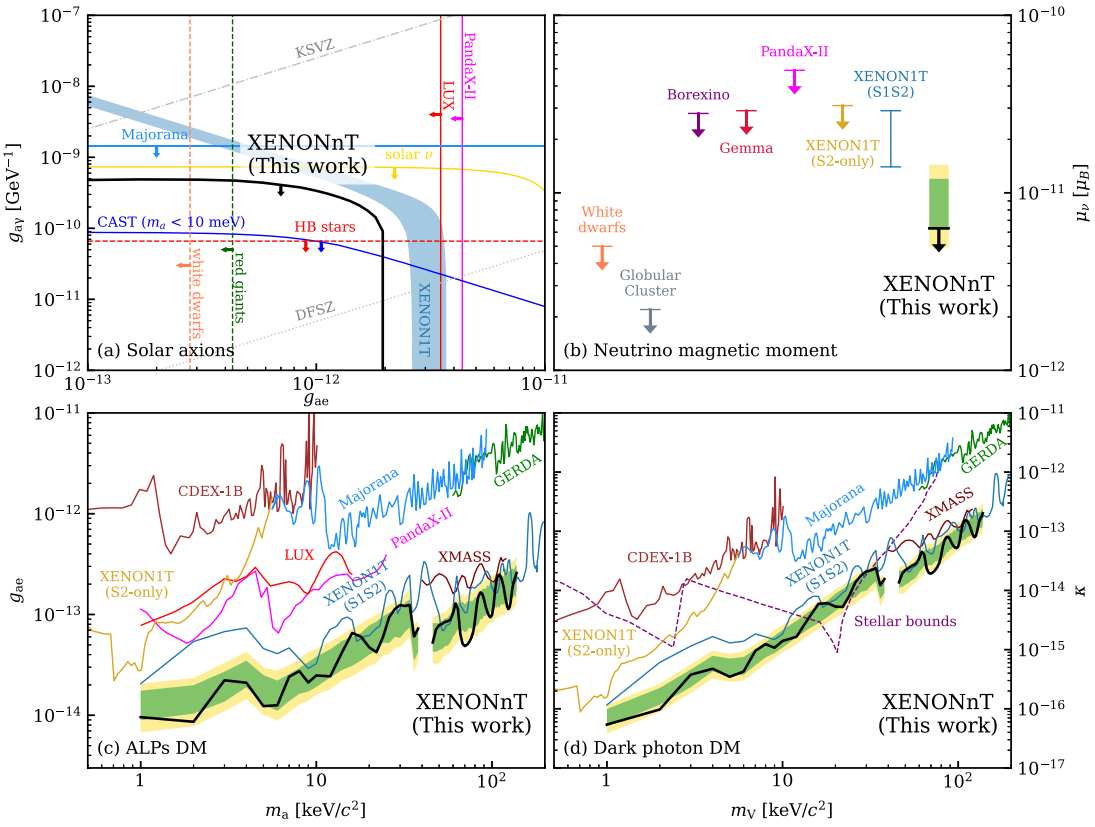

Fig. 32. 90% C.L. upper limit on different new physics models. Constraints on the axion-electron g_{ae} and axion-photon $g_{a\gamma}$ couplings from a search for solar axions are shown in (a). Constraints on solar neutrinos with an enhanced magnetic moment (b), ALP DM (c), and dark photon DM (d) are shown together with the 1σ (green) and 2σ (yellow) sensitivity bands estimated with the background-only fit. Figures from Ref. [4].

lowest background rate ever achieved at these energies among dark matter direct detection experiments.

Figure 32 shows the 90% confidence level (C.L.) upper limit on solar axions, bosonic DM models, and solar neutrinos with an enhanced magnetic moment together with sensitivity bands estimated from the background-only fit. We also searched for a tritium component on top of the background model B_0. The best-fit rate of tritium is 0 and the upper limit (90% C.L.) is 15 events/(t yr). The blind analysis shows no excess above the background, excluding our previous BSM interpretations of the XENON1T excess.

Bibliography

[1] E. Aprile *et al.* (XENON collaboration), JCAP 11 (2020) 031.

[2] E. Aprile *et al.* (XENON collaboration), Phys. Rev. D **102**, 072004 (2020).

[3] K. Abe *et al.* (XMASS collaboration), Phys. Lett. B 724 (2013) 46.

[4] E. Aprile *et al.* (XENON collaboration), Phys. Rev. Lett. 129, 161805 (2022).

[5] E. Aprile *et al.* (XENON collaboration), PTEP 2022 053H01 (2022) pp1-21.

[6] E. Aprile *et al.* (XENON collaboration), Phys. Rev. D 106 022001 (2022) pp022001-1-022001-21.

[7] E. Aprile *et al.* (XENON collaboration), Phys. Rev. C 106 024328 (2022) pp024328-1-024328-19.

[8] E. Aprile *et al.* (XENON collaboration), Eur. Phys. J. C 82:989 (2022) pp1-10.

[9] J. Aalbers *et al.*, J. Phys. G: Nucl. Part. Phys. 50 013001 (2023).

[10] L. Marti, *et al.* (Super-Kamikande collaboration), Nucl. Instrum. Meth. A, 959, 163549 (2020); K. Abe *et al.* (Super-Kamiokande collaboration), Nucl. Instr. Meth. A, 1027 (2022) 166248.

[11] E. Aplile *et al.* (XENON collaboration), Eur. Phys. J. C (2022) 82:599.

HYPER-KAMIOKANDE

[Co-Spokespersons: Masato Shiozawa[1], Francesca Di Lodovico[2]]
1: Kamioka Observatory, ICRR, The University of Tokyo
2: Department of Physics King's College London

Introduction

The Hyper-Kamiokande (Hyper-K or HK) project [1] is the world-leading international scientific research project hosted by the university of Tokyo and High Energy Accelerator Research Organization (KEK) consisting of a next generation underground water Cherenkov detector and upgraded Japan Proton Accelerator Research Complex (J-PARC) neutrino beam. The supplementary budget for FY2019 including the first-year construction budget for Hyper-K project was approved by the Japanese Diet on January 2020 and the Hyper-K project has officially started.

Figure 33 shows a schematic drawing of the Hyper-K cylindrical detector. The detector is filled with 0.260 million metric tons of ultra pure water, which serves an order of magnitude larger fiducial mass of 0.188 million metric tons than Super-K, equipped with newly developed high-sensitivity photosensors, and a high-intensity neutrino beam produced by an upgraded J-PARC accelerator facility. It provides an enormous potential to discover leptonic charge-parity (CP) violation by observing neutrino and anti-neutrino beams from J-PARC, investigate the Grand Unified Theory by exploring proton decay, and determine the neutrino mass ordering by observing atmospheric neutrinos combining beam data. Hyper-K will also have far better capabilities to observe solar neutrinos and neutrinos from other astronomical sources than those of predecessor experiments.

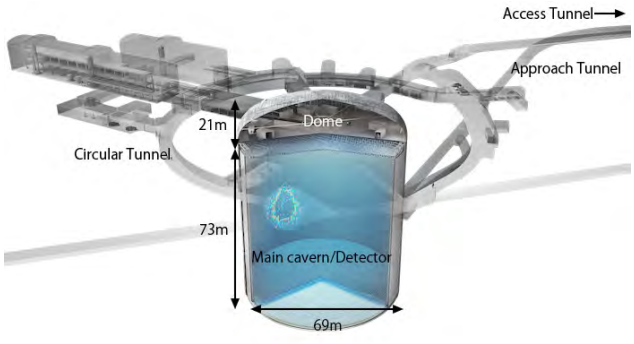

Fig. 33. Schematic view of the Hyper-K water tank and approach tunnel.

The Hyper-K international collaboration consists of about 560 researchers from 101 institutes in 20 countries. The detector technology has been developed based upon the successful Super-K experiment and feasibility studies have been completed by international group. The Hyper-K operation plans to start in 2027.

Hyper-K will have capability to measure the magnitude of the CP violation with high precision, which could explain the baryon asymmetry in the Universe. Figure 34 shows an expected significance of the CP violation discovery by ten years operation. With expected systematic error improvement, Hyper-K covers the 60% of the parameter space with 5σ or more as red dotted line shows in the figure. More than 8σ significance will be expected if $\delta_{CP} = -\pi/2$ as suggested by T2K [2] and NOνA [3] results.

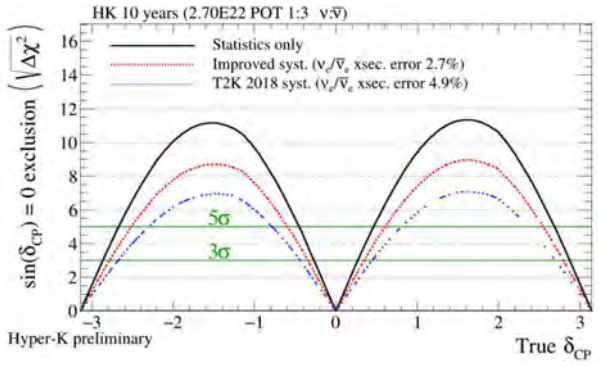

Fig. 34. Significance of the leptonic CP violation discovery with a 10-year observation in Hyper-K (HK) as a function of the unknown CP phase assuming the normal neutrino mass hierarchy. Red dotted line shows the result with expected systematic error improvement, blue dotted line shows the result with achieved systematic error by T2K 2018 and black line shows the result with only statistical error.

A proton decay $p \to e^+\pi^0$ is an important signal favored by many Grand Unified Theory models with a prediction close to the current limit of the proton decay life time. High sensitive Hyper-K PMTs result in strong background (atmospheric neutrinos) reduction and $p \to e^+\pi^0$ search in Hyper-K is expected to be "background-free" particularly in the free-proton enhanced signal region. Figure 35 shows the 3σ discovery potential for the $p \to e^+\pi^0$ mode as a function of year. Hyper-K is an only realistic proposal which can go beyond the proton lifetime of 1×10^{35} years.

As well as the supernova burst neutrino that was successfully observed in Kamiokande at once, undiscovered supernova relic neutrinos, accumulated by past all supernovae since the beginning of the universe, are interesting events to explore the history of heavy elements and the onset of stellar formation.

Construction status

Figure 36 is schematic drawing of Hyper-K tunnels and the cavern. The excavation of the tunnel toward the Hyper-K cavern site was started from 6th May, 2021 after the completion of the entrance yard construction.

Without any serious trouble, the first part of the tunnel, 1873.5m access tunnel excavation was finished at February 2022 as scheduled.

The second part of the tunnel, the approach tunnel excavation started from March 2022. The work was finished on 23th, June 2022 by reaching the center of HK dome shown in Figure 37. We achieved a significant milestone towards the realization of the Hyper-Kamiokande project.

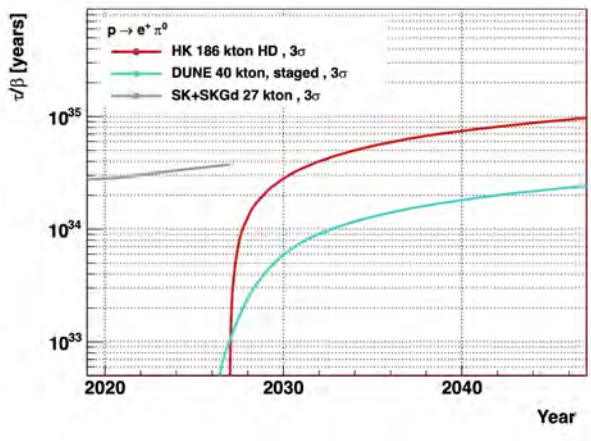

Fig. 35. The $p \to e^+\pi^0$ discovery reach in proton lifetime with 3σ significance as a function of year. It shows Hyper-K (HK) planing to start in 2027, superimposed with the ongoing Super-K (SK) and planned DUNE experiments. The DUNE project assumes 10 kton operation from 2026, toward full 40 kton by increasing 10 kton every year [4].

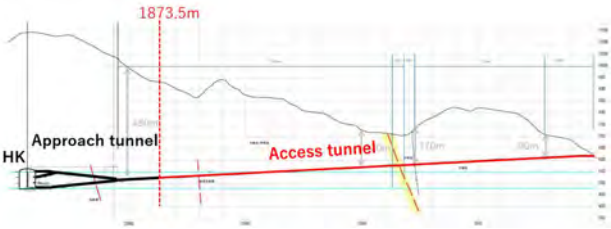

Fig. 36. Overview of the Hyper-Kamiokande excavation. The first part of tunnel is called as the access tunnel (red line). The black line after the access tunnel is the approach tunnel required for the cavern excavation.

After the approach tunnel, the excavation of Hyper-K cavern started. Figure 38 shows the ceiling of main cavern. The diameter of the cavern in the picure is 40 m, that will be extended to 69 m design diameter. After the excavation of ceiling part, the work will continue to go down to 70 m depth by end of 2024.

20-inch PMT, Delivery and inspection

Newly developed photomultiplier tubes R12860 by Hamamatsu Photonics K.K is shown in Fig. 39. The total detection efficiency of R12860 for single photon is twice higher than that of the Super-K PMT owing to 1.4 times higher quantum efficiency (about 32%) and improved photoelectron collection efficiency. The timing and charge resolutions at single photoelectron also becomes much better as 1.1 ns and 35% which can be compared with 2.1 ns and 53% of the Super-K PMT, respectively. Pressure tolerance of PMT was also improved up to the 125 m water depth, so that new PMT can be used under about 70 m depth of the detector water.

Since the start of mass production at October 2020, delivery of 400 R12860 for every month is ongoing. Total delivered number reached about 4000 by the end of FY2022 without any delay from the schedule. At the facility where delivered PMTs have been stored, inspections of the PMTs are also ongoing.

Fig. 37. The excavated access tunnel (top). The branch of approach tunnel toward top and bottom part of main cavern (middle). The center of HK dome reached on 23th, June 2022 (bottom).

The inspection consists of visual inspection for bulb and waterproof quality, signal check for signal property and noise rate, and long term stability check. The Figure 40 shows the dark room to check long term stability of 100 PMTs simultaneously. The delivery of PMTs continues until September 2026.

Electronics

The HK front-end electronics will be placed in water nearby PMTs to avoid long analog cable and its signal decay. This is another challenge of HK project. We have made a lot of efforts to develop water-tight case, high reliable front-end electronics, and communication under water. The Figure 41 and 42 shows the prototypes of 1 MPa tolerant water-tight case and signal digitizer that was newly developed and optimized to high performance HK PMT. The prototypes go

Fig. 38. The ceiling part of HK main cavern. The diameter in the picture is 40m, that will be extended to 69 m design diameter. Then the excavation will continue to go down to 70 m depth.

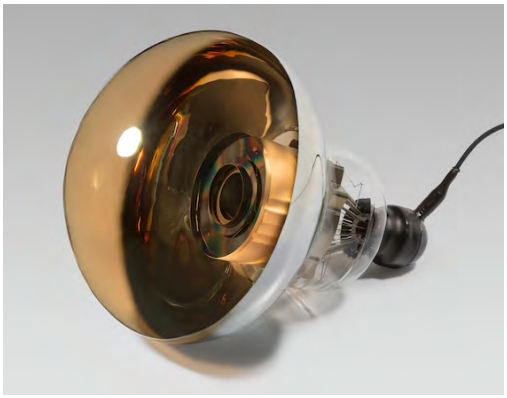

Fig. 39. New 50 cm photomultiplier tube with a box-and-line dynode (R12860, Hamamatsu Photonics K.K.).

through system test under water before starting mass production from 2024.

Bibliography

[1] "Hyper-Kamiokande Design Report," arXiv: 1805.04163.

[2] K. Abe *et al.* [T2K Collaboration], Nature 580, 339-344 (2020).

[3] P. Adamson *et al.* [NOνA Collaboration], Phys. Rev. Lett. 118, 231801.

[4] R. Acciarri *et al.* [The DUNE Collaboration], arXiv:1601.05471 [physics.ins-det].

[5] H. Sekiya [Super-K Collaboration], PoS(ICHEP2016) 982 (2016).

[6] ICRR News (2016), `http://www.icrr.u-tokyo.ac.jp/2016/06/30101400.html`.

[7] F. An *et al.* [JUNO Collaboration], J. Phys. G **43**, no. 3, 030401 (2016).

Fig. 40. Visual inspections of PMTs (top). Dark room for long term stability check of 100 PMTs (bottom).

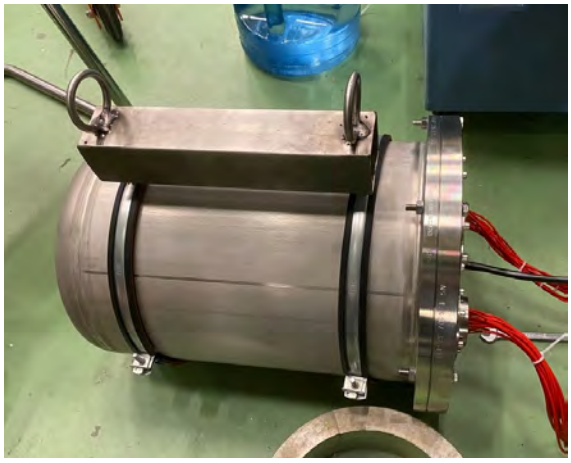

Fig. 41. Prototype of water-tight case for front-end electronics, that was designed to be 1 MPa tolerant under water.

[8] Yu-Feng LI, Presentation at "Workshop on Supernova at Hyper-Kamiokande" (2017).

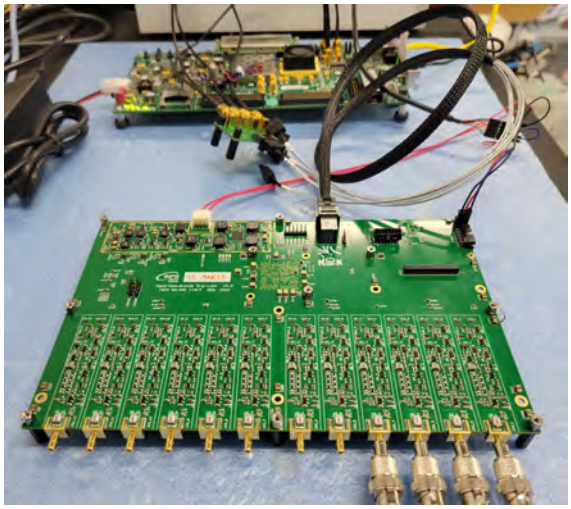

Fig. 42. Prototype of signal digitizer, that was newly developed and optimized to high performance HK PMT.

HIGH ENERGY COSMIC RAY DIVISION

Overview

There are three major experimental research activities in the High Energy Cosmic Ray Division, the study of high energy gamma rays and the development of the next generation gamma-ray telescopes by the Cherenkov Cosmic Gamma Ray group, the study of extremely high energy cosmic rays by the Telescope Array (TA) group, and the study of very high energy cosmic rays and gamma rays by the Tibet ASγ group.

Other activities, such as experiments utilizing the Akeno observatory, the Norikura observatory, the Mt. Chacaltaya observatory (jointly operated with Bolivia) are closely related to inter-university joint research programs. Also an all-sky high resolution air-shower detector (Ashra) is in partial operation on the Hawaii island. The High Energy Astrophysics group created in the fiscal year 2009 aims to explore various high energy astrophysical phenomena, through theoretical and observational approaches.

The CANGAROO telescopes had been in operation in South Australia since 1992, with a 3.8 m small telescope and then with four 10 m telescopes. The major scientific objective was the study of Very High Energy (VHE) gamma-ray sources in our galaxy in the southern hemisphere. The mission of these telescopes was completed and the CANGAROO observation site was closed in 2011.

For further development of VHE gamma-ray astronomy, the Cherenkov Cosmic Gamma Ray group is working on the design study and development and construction of the next generation international ground-based gamma-ray observatory CTA which will offer an order of magnitude better sensitivity than currently running Cherenkov telescopes, three times better angular resolution, and wider energy coverage from 20 GeV to 100 TeV or higher. The construction of the first Large-Sized Telescope (LST) was completed on the CTA-North site in La Palma in 2018. High Energy Astrophysics Facility in Canarias was established as a base for the project in April, 2019.

At the Akeno observatory, a series of air shower arrays of increasing geometrical sizes were constructed and operated to observe extremely high energy cosmic rays (EHECRs). The Akeno Giant Air Shower Array (AGASA) was operated from 1991 to January 2004 and covered the ground area of 100 km^2 as the world largest air shower array. In 13 years of operation, AGASA observed a handful of cosmic rays exceeding the theoretical energy end of the extra-galactic cosmic rays (GZK cutoff) at around 10^{20} eV.

The Telescope Array (TA), a large plastic scintillator array with air fluorescence telescopes, has been constructed in Utah, USA, which succeeds AGASA and measures the EHECRs with an order of magnitude larger aperture than that of AGASA for the further study of EHECRs. The full-scale TA is accumulating data as the largest array viewing the northern sky and observed the energy spectrum with high statistics, which is in good agreement with the GZK suppression and found evidence for anisotropy of arrival directions of EHECRs. The TAx4, which is aimed at quadrupling TA, was partially constructed by March of 2019.

An air shower experiment aiming to search for celestial gamma-ray point sources started in 1990 with Chinese physicists at Yangbajing (Tibet, 4,300 m a.s.l.). This international collaboration is called the Tibet ASγ Collaboration. An extension of the air shower array was completed in 1995 and an emulsion chamber has been combined with this air shower array since 1996 to study the primary cosmic rays around the knee energy region. After successive extensions carried out in 1999, 2002 and 2003, the total area of the air shower array amounts to 37,000 m^2. The sun's shadow in cosmic rays affected by the solar magnetic field was observed for the first time in 1992, utilizing its good angular resolution at multi-TeV energy region. The group added underground water Cherenkov muon detector to detect cosmic gamma rays above 100 TeV. The group is planning to construct a new air shower array, called ALPACA, to cover the sky in the Southern hemisphere, and started the construction of its partial array in Bolivia in 2019.

The High Energy Astrophysics group is conducting theoretical researches on fundamental processes responsible for non-thermal particle acceleration in various astrophysical environments, including first-order diffusive shock acceleration, second-order stochastic acceleration in shock downstream regions, modification of shock structure by pick-up interstellar neutrals, as well as injection processes of suprathermal particles. In addition to these theoretical works, R/D studies for radio observations of pulsars and cosmic ray air showers are also being made.

Cherenkov Cosmic Gamma-Ray Group

CTA Project (Cherenkov Telescope Array)

CTA-Japan Consortium
[Spokespersons : M. Teshima and H. Kubo]

Collaboration list:
Institute for Cosmic Ray Research, The University of Tokyo, Chiba, Japan; Department of Physics, Aoyama Gakuin University, Tokyo, Japan; Department of Physics, Hiroshima University, Hiroshima, Japan; Hiroshima Astrophysical Science Center, Hiroshima University, Hiroshima, Japan; Faculty of Science, Ibaraki University, Ibaraki, Japan; Institute of Particle and Nuclear Studies, High Energy Accelerator Research Organization (KEK), Ibaraki, Japan; Department of Physics, Konan University, Hyogo, Japan; Faculty of Medical Engineering and Technology, Kitasato University, Kanagawa, Japan; Graduate School of Science and Technol-

ogy, Kumamoto University, Kumamoto, Japan; Department of Physics, Kyoto University, Kyoto, Japan; Department of Applied Physics, University of Miyazaki, Miyazaki, Japan; Department of Physics, Nagoya University, Aichi, Japan; Solar-Terrestrial Environment Laboratory, Nagoya University, Aichi, Japan; Kobayashi-Maskawa Institute, Nagoya University, Aichi, Japan; Department of Earth and Space Science, Osaka University, Japan; Astrophysical Big Bang laboratory, RIKEN, Wako, Japan; Department of Physics, Rikkyo University, Tokyo, Japan; Department of Physics, Saitama University, Saitama, Japan; Department of Physics, Tokai University, Kanagawa, Japan; Faculty of Integrated Arts and Sciences, The University of Tokushima, Tokushima, Japan; Department of Astronomy, The University of Tokyo, Tokyo, Japan; Department of Physics, The University of Tokyo, Tokyo, Japan; Faculty of Science and Engineering, Waseda University, Tokyo, Japan; Department of Physics, Yamagata University, Yamagata, Japan; Faculty of Management Information, Yamanashi Gakuin University, Yamanashi, Japan.

CTA Project

During the past years, Very High Energy (VHE) gamma-ray astronomy has made spectacular progress and has established itself as a vital branch of astrophysics. To advance this field even further, we are constructing the Cherenkov Telescope Array (CTA) [6], the next generation VHE gamma ray observatory, in the framework of a worldwide, international collaboration. CTA is the ultimate VHE gamma-ray observatory, whose sensitivity and broad energy coverage will attain an order of magnitude improvement above those of current Imaging Atmospheric Cherenkov Telescopes (IACTs). By observing the highest energy photons known, CTA will clarify many aspects of the extreme Universe, including the origin of the highest energy cosmic rays in our Galaxy and beyond, the physics of energetic particle generation in neutron stars and black holes, as well as the star formation history of the Universe. CTA will also address critical issues in fundamental physics, such as the identity of dark matter particles and the nature of space and time.

VHE gamma rays from 100 GeV to 10 TeV can be observed with ground-based current IACTs. The history of VHE gamma ray astronomy began with the discovery of VHE gamma rays from the Crab Nebula by the Whipple Observatory in 1989. To date, the current generation IACTs featuring new technologies, such as H.E.S.S., MAGIC, and VERITAS, have discovered more than 200 Galactic and extragalactic sources of various types.

CTA is designed to achieve superior sensitivity and performance, utilizing established technologies and experiences gained from the current IACTs. The project is presently in its pre-construction (prototyping) phase, with international efforts from Japan, US, and EU countries. It will consist of several 10s of IACTs of three different sizes (Large Size Telescopes, Mid Size Telescopes, and Small Size Telescopes)(Fig. 1). With a factor of 10 increase in sensitivity (1 mCrab $\sim 10^{-14}$erg s^{-1} cm^{-2}), together with a much broader energy coverage from 20 GeV up to 300 TeV. CTA will bring forth further dramatic advances for VHE gamma-ray astronomy. The discovery of more than 1000 Galactic and extragalactic sources is anticipated with CTA.

CTA will allow us to explore numerous diverse topics in physics and astrophysics. The century-old question of the origin of cosmic rays is expected to be finally settled through detailed observations of supernova remnants and other Galactic objects along with the diffuse Galactic gamma-ray emission, which will also shed light on the physics of the interstellar medium. Observing pulsars and associated pulsar wind nebulae will clarify physical processes in the vicinity of neutron stars and extreme magnetic fields. The physics of accretion onto supermassive black holes, the long-standing puzzle of the origin of ultra-relativistic jets emanating from them, as well as their cosmological evolution, will be addressed by extensive studies of active galactic nuclei (AGN). Through dedicated observing strategies, CTA will also elucidate many aspects of the mysterious nature of gamma ray bursts (GRBs), the most energetic explosions in the Universe. Detailed studies of both AGNs and GRBs can also reveal the origin of the highest energy cosmic rays in the Universe, probe the cosmic history of star formation including the very first stars, and provide high precision tests of theories of quantum gravity. Finally, CTA will search for signatures from elementary particles constituting dark matter with the highest sensitivity yet. Realisation of the rich scientific potential of CTA is very much feasible, thanks to the positive experiences gained from the current IACTs.

The CTA-Japan consortium [1] is contributing particularly to the construction of the Large Size Telescopes (LSTs, Fig. 2) and is involved in their development. The LST covers the low energy domain from 20 GeV to 3 TeV and is especially important for studies of high redshift AGNs and GRBs. The diameter and area of the mirror are 23 m and 400 m^2, respectively, in order to achieve the lowest possible energy threshold of 20 GeV. All optical elements and detectors require high specifications, such as high reflectivity, high collection efficiency, high quantum efficiency, ultra-fast digitization of signals, and so on. For this purpose, CTA-Japan has developed high quantum efficiency photomultipliers and ultrafast readout electronics (Fig. 3), and high precision segmented mirrors (Fig. 4). On the strength of their experiences gained from the construction of the MAGIC telescope, Max-Planck-Institute for Physics in Munich is responsible for the design of the 23-m diameter telescope structure, based on a carbon fiber tube space frame. The LSTs require very fast rotation (180 degrees in 20 seconds) to promptly observe GRBs. The first LST (LST-1) has been built in the CTA North, La Palma, Spain, in 2018, and now in the engineering run (Fig. 5). Three more LSTs will be built before 2025, then four more LSTs in the CTA South are expected to be built in the ESO site in Paranal, Chile.

The results of the commissioning of the LST-1 camera has been presented in the international conference [10]. The noise level, the charge calibration precision, the trigger rates, the DAQ performance and operation stability were well studied characterized there. Fig. 6 shows one of those results, showing the stability of noise level as a function of time and the night sky background intensity.

The Critical Design Review of LST-1 was held by CTAO

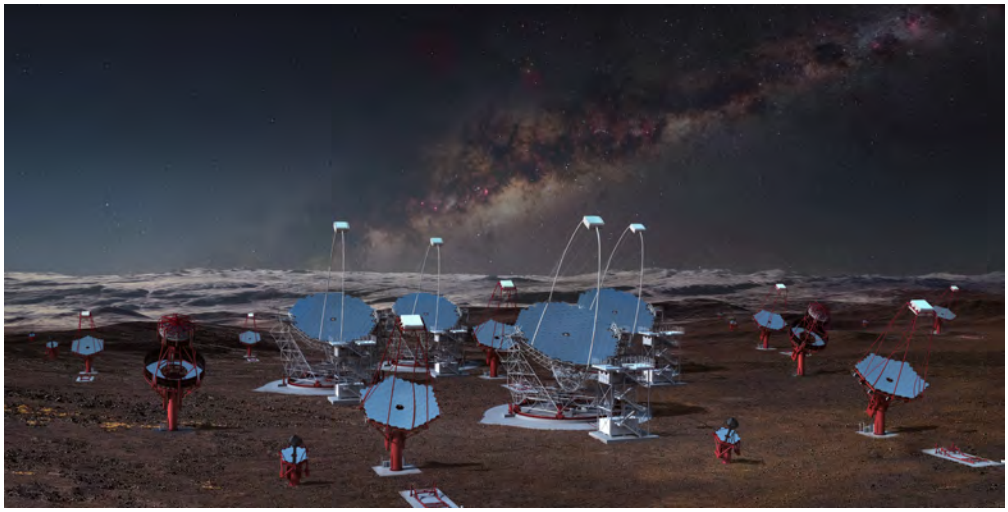

Fig. 1. Artist view of the CTA observatory. CTA consists of three types of telescopes, Large Size Telescopes (23 m diameter), Mid Size Telescopes (12 m) and Small Size Telescopes (4 m), and covers the broad energy band from 20 GeV to 300 TeV. [Credit: Gabriel Pérez Diaz (IAC)/Marc-André Besel (CTAO)/ESO/ N. Risinger (skysurvey.org)]

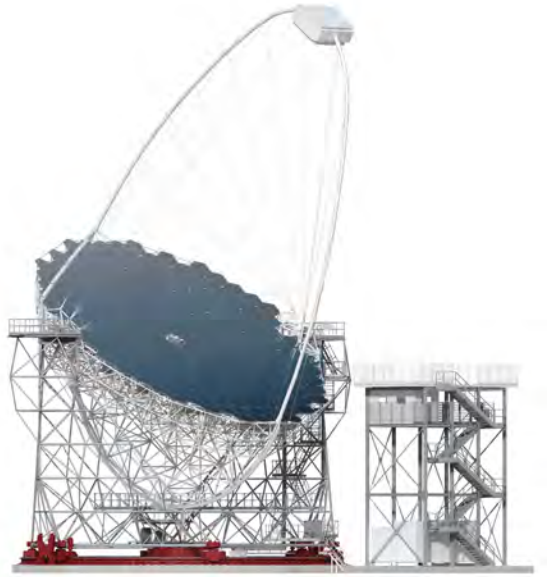

Fig. 2. Large Size Telescope (23 m diameter) designed by Max–Planck-Institute for Physics. CTA Japan is contributing to the design and and construction of the imaging camera at the focal plane, ultrafast readout electronics, and high precision segmented mirrors.

Fig. 3. Camera cluster for the Large Size Telescope (LST) developed by CTA-Japan. This cluster consists of seven high quantum efficiency photomultipliers (R11920-100), CW High Voltages, pre-amplifier, Slow Control Board, DRS4 Ultra fast waveform recording system and Trigger. The LST camera can be assembled with 265 of these clusters, cooling plates and camera housing.

Fig. 4. The high precision segmented mirrors for the Large Size Telescope (LST) developed by CTA-Japan in cooperation with Sanko Co.LTD. The mirror is made of a 60-mm thick aluminum honeycomb sandwiched by 3-mm thin glass on both sides. A surface protection coat consisting of the materials SiO_2 and HFO_2 is applied to enhance the reflectivity and to elongate the lifetime.

engineers and external experts from high energy physics. LST-1 successfully passed the review with several open items in June 2020.

The LST-1 has been regularly operated since January 2020, and has already shown an excellent performance as expected, even in a single telescope mode, through the observation of Crab Nebula, Crab Pulsar, and nearby Active Galactic Nuclei (AGN). These results certify LST-1 achieved the design performance expected by Monte Carlo simulations. The phase diagram of the Crab Pulsar observation is shown in Fig.

Fig. 5. The Large Size Telescope prototype (LST-1) constructed at Observatory de Roque de los Muchachos is now in the engineering run. The diameter of dish and mirror surface area are 23 m and 400 m^2.

7, which certifies the low threshold energy of LST-1 and also the accuracy of the recorded event timings. In July 2021, the LST collaboration issued the first telegram of reporting the detection of the AGN BL Lac with LST-1 [11]. LST-1 also detected the outburst of the recurrent symbiotic nova RS Ophiuchi in August 2021 and the results are consistent with those reported by other IACT arrays [12]. The location of the LST array in the CTA North has an overlap with MAGIC telescopes, which will allow us to perform the cross-calibration between LST and MAGIC telescopes and to operate the three telescopes together in the early phase of the construction.

On 19th September, 2021, a volcanic eruption initiated in Cumbre Vieja (El Paso) more than 20 km away in a straight line from the Roque de los Muchachos Observatory (ORM) where LST-1 is located. The LST collaboration decided to stop the LST-1 operation. The eruption continued until 25th December, 2021. After the inspection of LST-1 and the recovery works, an observation with LST-1 restarted on 21th January, 2022. We checked the optical efficiency of the telescope before and after the eruption through the analysis of muon rings. There has been no long-term effect of volcanic ash deposition (dust on our mirrors can be cleaned by rain) [13].

Construction of the second to forth LSTs (LST-2–4) has also been started. The cameras of LST-2–4 are currently in the Institute of Astrophysics in Canary islands (IAC) in Tenerife and the final integration tests are on-going (Fig. 8). Also, for the future upgrade of LST cameras, basic studies of Silicon photomultiplier (SiPM) and development of SiPM module has been started in the laboratory of ICRR.

The Cherenkov Cosmic Gamma Ray group is also operating the MAGIC Telescopes [14] on La Palma, Canary Islands (See the next subsection). This facility is used not only for scientific observations but also for technological development toward the future observatory CTA.

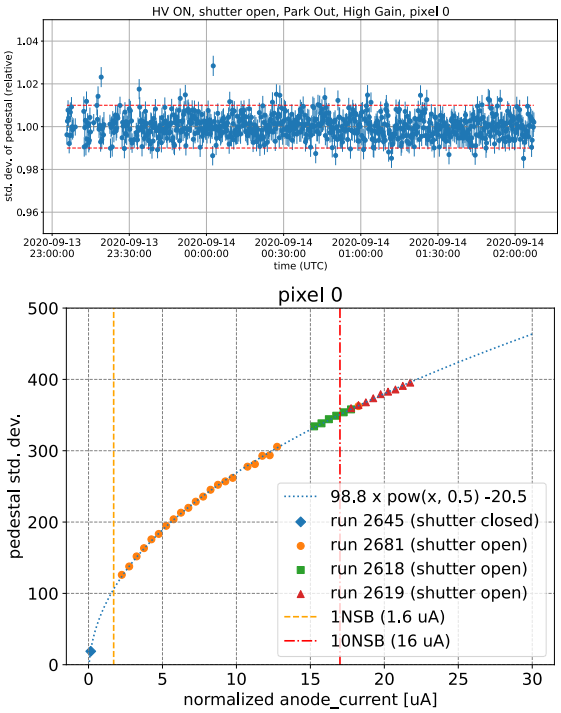

Fig. 6. (Top) Time evolution of the noise for a single pixel for three hours. Each point represents ~ 50000 events (~ 12 seconds) and error bars show standard deviation of the noise for this single pixel. (Bottom) Noise level during multiple observation runs as a function of the anode current. Orange and red dotted lines show dark night sky background (NSB) and 10 times higher than dark NSB level, respectively.

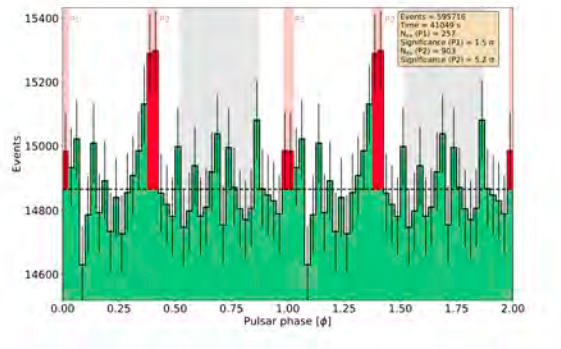

Fig. 7. Phase diagram of Crab Pulsar as measured by LST-1. The pulsar is known to emit pulses of gamma rays during phases P1 and P2. The energy threshold in this observation is estimated about 40-50 GeV.

Bibliography

[1] CTA Consortium website: http://www.cta-observatory.jp/ and http://www.cta-observatory.org/.

[2] Science with the Cherenkov Telescope Array, arXiv:1709.07997

[3] The Cherenkov Telescope Array potential for the study

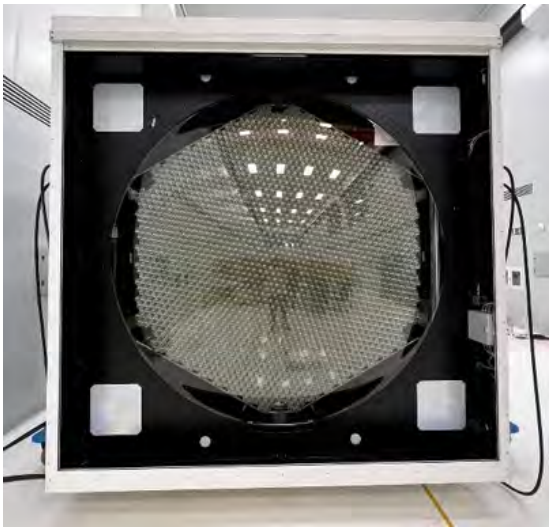

Fig. 8. The camera of the second LST (LST-2). The integration test is on going in IAC in Tenerife.

of young supernova remnants, Astropart. Phys. 62 (2015) 152-164.

[4] Introducing the CTA concept, The CTA Consortium, Astropart. Phys. 43 (2013) 3-18.

[5] Gamma-ray burst science in the era of the Cherenkov Telescope Array, S. Inoue et al., Astropart. Phys. 43 (2013) 252-275.

[6] Design Concepts for The Cherenkov Telescope Array, The CTA Consortium, Exper. Astron. 32 (2011) 193-316.

[7] Status of Very High Energy Gamma Ray Astronomy and Future Prospects, M. Teshima, The Astronomical Herald, 104 (2011) 333-342.

[8] Design Study of a CTA Large Size Telescope, Proc. of ICRC2012 at Beijing China, M. Teshima, arXiv:1111.2183.

[9] Introducing the CTA Concept, B. Acharya et al., Astroparticle Physics, 34 (2013) 3.

[10] Commissioning of the camera of the first Large Size Telescope of the Cherenkov Telescope Array, Proc. of ICRC2021 at Berlin Germany (Online), T. Saito et al., arXiv:2108.01920.

[11] Detection of very-high-energy gamma-ray emission from BL Lac with the LST-1, ATEL #14783.

[12] RS Ophiuchi nova outburst detection by the LST-1, A. Aguasca-Cabot et al., PoS (Gamma2022) 055.

[13] Status of the LST project, J. Cortina, PoS (Gamma2022) 026.

[14] MAGIC Collaboration website: `http://magic.mppmu.mpg.de/`.

Fig. 9. MAGIC Stereo System with two Cherenkov telescopes of 17 m diameters, so far achieved the threshold energy of 25 GeV with the sum trigger. It locates near the mountain top of the Roque de los Muchachos on the Canary Island of La Palma. Two telescopes are located with the distance of 85 m.

MAGIC

The MAGIC Collaboration has built in 2004 a first large atmospheric imaging Cherenkov telescope, MAGIC-I, with a mirror surface of 236 m^2 and equipped with photomultiplier tubes of optimal efficiency. In 2009, a second telescope of essentially the same characteristics was added; MAGIC-II was installed at a distance of 85 m from MAGIC-I (Fig. 9). With the accent of these instruments on large mirror surface and best light collection, cosmic gamma-rays at an energy threshold lower than any existing or planned terrestrial gamma-ray telescope have become accessible. So far achieved has been a threshold of 25 GeV. The Japanese group has joined the MAGIC collaboration since 2010, and contributed to the operation, observations and data analyses. The MAGIC telescopes are upgraded with new cameras, electronics and partially new mirrors in 2012, and are now operated with an unprecedented sensitivity by an international collaboration of about 165 scientists from 24 institutes and consortia from 12 countries.

The recent highlights from MAGIC are, (1) The first detection of the Gamma Ray Burst GRB 190114C with the ground-based gamma-ray telescope MAGIC [1], [2], [3]), (2) Observation of sub-TeV gamma rays from the IceCube 170922A [4], [5], (3) the successful observation of pulsed gamma ray signal from the Crab pulsar up to TeV regime [6]), (4) the discoveries of the most distant blazers S3 0218+35 with the redshift of 0.944 and PKS 1441+25 with the redshift of 0.939 [7], (5) the observation of the very fast flare of 1-min time scale from the blazar inside Perseus cluster, IC310 [8]) the conclusions of a 15 years joint observation campaign of the gamma-ray binary HESS J0632+057 together with the Cherenkov telescope experiments H.E.S.S. and VERITAS. (6) Detection gamma-ray emission from SNRs, γ Cygni [9] and G106.3+2.7 [10], both suggesting the acceleration of hadronic cosmic rays. These results brought new questions on the pulsar emission mechanism, cosmic rays acceleration at SNRs, the EBL energy density, and gamma ray emission mechanism from the supermassive blackholes or vicinity of them.

Gamma Ray Bursts

In January 2019, the MAGIC telescopes, for the first time, observed the TeV Gamma-Ray Burst GRB 190114C with the redshift of 0.42 [1],[2], [3]. MAGIC telescopes started observing the GRB at T_0 + 57 seconds after receiving the alert

from the SWIFT-BAT satellite. The observation shows the 100 times higher flux of gamma rays than the Crab Nebula at T_0 + 80 sec, and the resultant statistical significance of gamma-rays was more than 50 sigma. The highest-energy photon reaches above 1 TeV, and the observed spectrum after the EBL de-absorption did not show any roll-off feature in the energy spectrum [2]. This observation will require the new gamma-ray emission mechanism in the GRB to explain the TeV emission, possibly the inverse Compton emission. The light curve shows the power-law decay $t^{-1.6}$, which is surprisingly parallel to the X-ray lightcurve measured by XRT [2]. It is worth mentioning that the energetics of the TeV emission is comparable with that of the X-ray emission. The two bump structure in the spectral energy distribution can be fit consistently with the Synchroton Self-Compton model. In 2020 MAGIC published a followup paper, a constraint on Lorentz invariance violation using the data of the GRB [11].

In ICRC 2021 we have shown other two important results about long GRBs; a hint of detection from a low-luminosity GRB 201015A [13], and a clear detection from the farthest VHE GRB 201216C at $z = 1.1$ [14]. Both contributions have been led by Japanese colleagues in MAGIC Collaboration. These results show an importance of continuing GRB observations to increase the number of detections both for long and short GRB types.

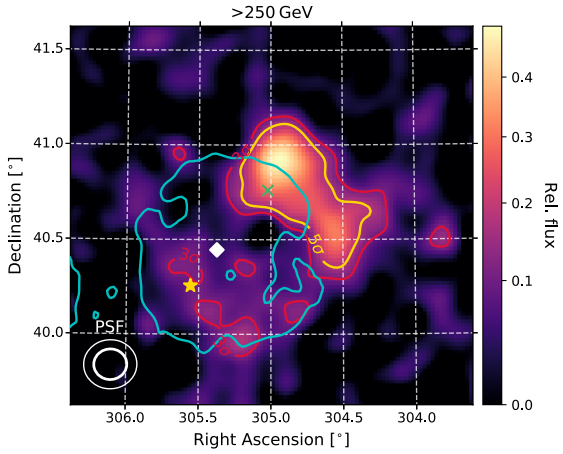

Fig. 10. Sky map in units of relative flux (excess over background) of the γ Cygni region as observed by MAGIC at Energies > 250 GeV. Regions exceeding the 3σ (5σ) local, pre-trial test statistics significance for a point source are indicated by red (yellow) contours. The cyan line is the 400 K contour of the 408 MHz observation by the Canadian Galactic Plane Survey. The white diamond gives the position of the pulsar PSR 2021+4026, the green X the position of VER J2019+407, and the yellow star the position of Sadr (γ Cyg star; mag = 2.2). The inlay in the lower left corner shows the 39 % and 68 % containment contours of the MAGIC PSF. [9]

Supernova Remnants: γ Cygni and G106.3+2.7

Supernova remnants (SNRs) continue to be considered the most plausible source of the Galactic component of cosmic rays (CRs). The arguments in favor of SNRs are often referred to collectively as the "supernova paradigm," which includes the agreement between observed Galactic CRs and the predicted CRs from SNRs in terms of total energy density and spectral particle distribution. However, a comprehensive understanding of CR acceleration by SNRs and determining whether they are indeed the primary emitters of CRs in our Milky Way galaxy requires further evidence, particularly in three key aspects: 1.) Observational confirmation of SNR's ability to accelerate CRs to PeV energies, 2.) Comprehension of the particle escape mechanism from the accelerator into the interstellar medium (ISM), and 3.) Understanding the propagation of CRs from their origin to Earth. In recent years, MAGIC observations have significantly contributed to addressing the first two issues.

Between May and November 2015, as well as between April and September 2017, MAGIC conducted observations of the γ Cygni SNR, G78.2+2.1, accumulating an effective observation time of 85 hours [9]. This SNR is believed to be the remnant of a core-collapse supernova with an age estimated at approximately 7000 years, placing it in the Sedov-Taylor phase. During this adiabatic phase, the speed of the SNR shock wave decreases, potentially enabling CRs to escape into the interstellar medium (ISM). By combining the MAGIC data with 9 years of *Fermi*-Large Area Telescope (LAT) observations, three distinct emission regions were identified in the vicinity of the SNR's radio shell (Fig. 10): emission from within the shell, emission from the surrounding ISM, and a region where the shock may be interacting with a molecular cloud. The most plausible and consistent interpretation for all three regions is a scenario in which the emission is dominated by hadrons and CRs currently escape the system. This marks the first observation of CR escape from a system that concurrently confines less energetic particles. Modeling the γ-ray emission within this scenario, we inferred the level of turbulence to be approximately $\delta B/B \approx 25\,\%$ and the time dependence of the maximum energy of the confined particles to follow $p_{\rm max} \propto t^{-2.55}$, which is steeper than the reduction resulting solely from the decrease in shock speed ($p_{\rm max} \propto t^{-1/5}$). The latter suggests that the level of turbulence must also decrease over time.

MAGIC also studied the SNR G106.3+2.7, one of the most promising PeVatron candidates [10]. Various γ-ray facilities have reported emission of 1-100 TeV from this object. In the radio band, this SNR exhibits a cometary shape, comprising a head and a tail region with distinct physical conditions. However, the specific region responsible for the 100 TeV emission as well as whether the nature of the emission is leptonic or hadronic remained uncertain. With 121.7 h of effective observation time between May 2017 and August 2019, we observed γ-ray emission that spatially coincides with the radio continuum emission at both the head and tail of the SNR G106.3+2.7 (see Fig. 11). Our results suggest that the emissions above 10 TeV detected by air shower experiments (Milagro, HAWC, Tibet ASγ, and LHAASO) originate solely from the SNR tail. Under this assumption, the multi-wavelength spectrum of the head region can be explained by either hadronic or leptonic models. In contrast, the observed spectrum in the tail can be reproduced by a hadronic model, assuming a proton spectrum with a cutoff energy of approximately 1 PeV for that region. This high-energy emission in a middle-aged SNR (4-10 kyr) can be attributed to a scenario in

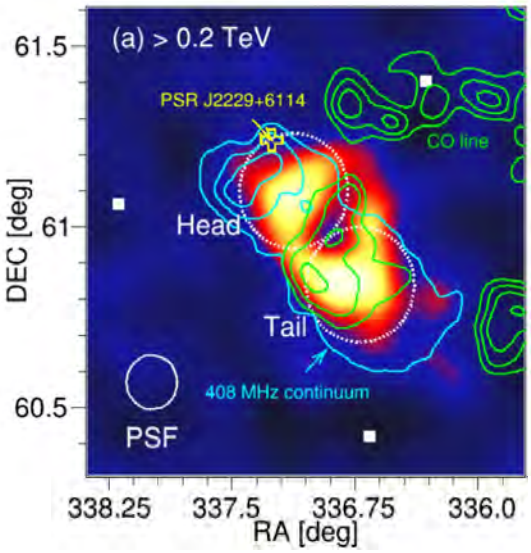

Fig. 11. Skymap of SNR G106.3+2.7 above 200 GeV. The position of PSR J2229.0+6114 is marked with the open yellow cross. The cyan contours show the radio emission of SNR G106.3+2.7 at 408 MHz by DRAO. The green contours represent 12CO (J = 1– 0) line intensity integrated over the velocity range from -6.41 to -3.94 km s^{-1}.

which protons that escaped from the SNR in the past interact with dense surrounding gases in the present. This makes this SNR the only observed possible PeV accelerator.

Recurrent Nova: RS Ophiuchi

Novae are luminous eruptions triggered by a thermonuclear runaway on a white dwarf surface when the white dwarf accretes a critical amount of matter from its stellar companion. Though novae have been revealed to be high-energy gamma-ray emitters through observations by Fermi LAT, their mechanism of the gamma-ray emission remained unclear.

RS Ophiuchi (Oph) is a symbiotic system, where a white dwarf is embedded in a red giant companion, and is well known as a recurrent nova with its recurrence time scale of $\sim$15 years. In August 2021, RS Oph was reported to be in a new burst state through optical and gamma-ray observations. In response to these alerts, MAGIC promptly started observations of RS Oph, only one day after the burst onset [15]. During the first four days after the eruption, MAGIC detected VHE gamma rays from RS Oph contemporaneous with the Fermi LAT and optical peaks at a statistical significance of 13.2σ in the energy range between 60 GeV and 250 GeV. This is the first detection of VHE gamma rays from a nova ever, which is also achieved by H.E.S.S. concurrently. The contemporaneous gamma-ray spectrum measured by Fermi LAT and MAGIC suggests a common single component between 50 MeV and 250 GeV, as shown in Fig. 12.

Though both protons and electrons may be accelerated in the nova shock and radiate gamma rays, the data strongly suggest a hadronic origin of the gamma-ray emission for the following reasons. First, the leptonic model needs an unnaturally sharp break in the intrinsic electron spectrum while the

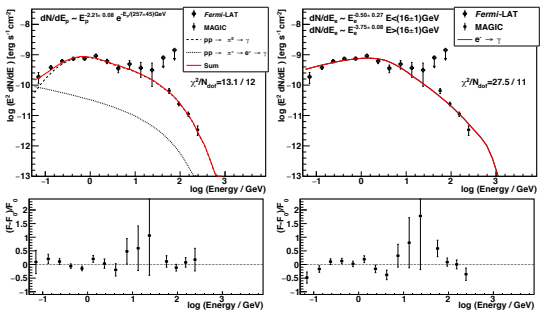

Fig. 12. Spectral energy distribution of gamma-ray emission from the 2021 outburst of RS Oph measured by Fermi LAT and MAGIC. The hadronic (*left*) and leptonic (*right*) models are tested.

hadronic model can describe the data with a natural proton distribution of a power law with an exponential cut-off. Second, the hadronic model fits the data statistically better than the leptonic model. Lastly, the data suggest an increase in the particle maximum energy over time, which is in line with the absence of fast cooling in the hadronic model, while electrons are expected to be subject to strong energy losses due to inverse Compton scattering.

The VHE gamma-ray detection of RS Oph revealed the hadronic origin of the gamma-ray emission in the nova. However, it remains to be studied if the acceleration and radiation mechanisms seen in RS Oph are common among all novae, including classical novae, or if the mechanisms are unique to recurrent symbiotic novae. To address this question, more detection of novae in the VHE gamma-ray regime is desired.

Bibliography

[1] The first detection of a GRB at sub-TeV energies; MAGIC detects the GRB190114C., ATEL # 12390.

[2] Teraelectronvolt emission from the γ-ray burst GRB 190114C, MAGIC collaboration, Nature 575, 455 (2019).

[3] Observation of inverse Compton emission from a long γ-ray burst, MAGIC collaboration et al., Nature 575, 459 (2019).

[4] First-time detection of VHE gamma rays by MAGIC from a direction consistent with the recent EHE neutrino event IceCube-170922A, ATel #10817.

[5] Multimessenger observations of a flaring blazar coincident with high-energy neutrino IceCube-170922A, Science 12 July 2018, Science.eaat1378.

[6] Phase-resolved energy spectra of the Crab pulsar in the range of 50-400 GeV measured with the MAGIC telescopes, MAGIC Collaboration, Aleksić et al., A&A 540 (2012) A69.

[7] Discovery of Very High Energy Gamma-Ray Emission from the distant FSRQ PKS 1441+25 with the MAGIC telescopes, ATEL # 7416.

[8] Black hole lightning due to particle acceleration at subhorizon scales, MAGIC collaboration, Science 346 (2014) 1080-1084.

[9] Study of the GeV to TeV morphology of the γ Cygni SNR (G 78.2+2.1) with MAGIC and Fermi-LAT. Evidence for cosmic ray escape, MAGIC collaboration et al., A&A 670, A8 (2023)

[10] MAGIC observations provide compelling evidence of hadronic multi-TeV emission from the putative PeVatron SNR G106.3+2.7, MAGIC collaboration et al., A&A 671, A12 (2023)

[11] Bounds on Lorentz Invariance Violation from MAGIC Observation of GRB 190114C, MAGIC collaboration, PRL 125 (2020) 021301.

[12] MAGIC Observations of the Nearby Short Gamma-Ray Burst GRB 160821B, MAGIC collaboration, ApJ 908 (2021) 90.

[13] Observation of a relatively low luminosity long duration GRB 201015A by the MAGIC telescopes, Y. Suda et al., PoS ICRC2021 (2021) 797.

[14] Very-high-energy gamma-ray emission from GRB 201216C detected by MAGIC, S. Fukami et al., PoS ICRC2021 (2021) 788.

[15] Proton acceleration in thermonuclear nova explosions revealed by gamma rays, MAGIC collaboration et al., Nat Astron 6 (2022) 689–697.

Other Activities

As a test bench for domestic R & D activities of future ground-based gamma-ray observatory projects, an old atmospheric Cherenkov telescope of 3 m diameter was repaired and then placed at the Akeno Observatory in November 2010. This telescope shown in Figure 13 (Akeno telescope, hereafter) is currently the only atmospheric Cherenkov telescope located in Japan [1]. We have developed an R & D imaging camera system with the Akeno telescope since 2009, the purpose of which is to make a battery-powered data acquisition system for a future mobile imaging atmospheric Cherenkov telescope array [2]. The system consists of 32 PMTs, of which detected Cherenkov light signals are read out by only four GHz-sampling analog memory ASICs.

Utilizing some central PMTs of the above system, we have also observed the optical Crab pulsar in Akeno. The purpose of this study is to investigate the efficient acceleration site of the Crab Nebula in a microscopic way with simultaneous observations of radio and optical pulses passing through the nebula plasma. We performed the first observations of the optical Crab pulsar in January 2020 after developing a dedicated pulse counting system, which were followed by further observations in 2021 and 2022 with some improvements in the system. The data taken in January 2022, which were analyzed during the 2022 academic year, revealed a 4.5σ signal at the main pulse phase of the Crab pulsar. The presence of the interpulse peak was also marginally observed in the lightcurve,

Fig. 13. Akeno atmospheric Cherenkov telescope of 3 m diameter, located in the Akeno Observatory.

suggesting that they could realistically be obtained from the optical Crab pulsar. This result indicates that the sensitivity of the Akeno telescope to the optical Crab pulsar is somewhat lower than originally anticipated. We are currently considering the future effective applications of this telescope.

Bibliography

[1] M. Ohishi et al., Proc. of 33rd Internat. Cosmic Ray Conf. (Rio de Janeiro), 587 (2013).

[2] T. Yoshikoshi et al., Proc. of 34th Internat. Cosmic Ray Conf. (The Hague), 887 (2015).

TA: Telescope Array Experiment

Spokespersons: S. Ogio[1], J.N. Matthews[2]

1 : ICRR, The Univ. of Tokyo, Kashiwa, Chiba 277-8582
2 : Dept. of Physics and Astronomy, University of Utah

Collaborating Institutions:

Chubu Univ., Kasugai, Japan; ERI, Univ. of Tokyo, Tokyo, Japan; Hiroshima City Univ., Hiroshima, Japan; Hanyang Univ., Seoul, Korea; ICRR, Univ. of Tokyo, Kashiwa, Japan; INR, Moscow, Russia; CEICO, Inst. of Phys, Czech Acad. of Sci., Prague, Czech Republic; Kanagawa Univ., Yokohama, Japan; KEK/IPNS, Tsukuba, Japan; Kochi Univ., Kochi, Japan; Kyoto Univ., Kyoto, Japan; Loyola Univ., Chicago, USA; Moscow M.V. Lomonosov State University, Moscow, Russia; NICT, Tokyo, Japan; Osaka Electro-Comm. Univ., Neyagawa, Japan; Osaka City Univ., Osaka, Japan; RIKEN, Wako, Japan; Ritsumeikan Univ., Kusatsu, Japan; Saitama

Univ., Saitama, Japan; Shibaura IT, Tokyo, Japan; Shinshu Univ., Nagano, Japan; SKKU, Suwon, Korea; Tokyo City Univ., Tokyo, Japan; Tokyo Inst. of Tech., Tokyo, Japan; Tokyo Univ. of Science, Noda, Japan; ULB, Brussels, Belgium; UNIST, Ulsan, Korea; Univ. of Nova Gorica, Nova Gorica, Slovenia; Univ. of Utah, Salt Lake City, USA; Univ. of Yamanashi, Kofu, Japan; Yonsei Univ., Seoul, Korea

1. Introduction

The Telescope Array (TA) is the largest Ultra-High Energy Cosmic Ray (UHECR) observatory in the northern hemisphere. The main aim of TA is to explore the origin and nature of UHECRs by measuring the energy spectrum, arrival direction distribution and mass composition. The TA collaboration consists of approximately 140 researchers from USA, Russia, Korea, Belgium, Czech, Slovenia and Japan.

The TA detector consists of a surface array of 507 plastic scintillator detectors (SD) and three stations of fluorescence detectors (FD). It is located in the desert, approximately 200 km south of Salt Lake City in Utah in USA. The SDs were deployed on a square grid with 1.2-km spacing, and the SD array covers an area of approximately 700 km^2. Each SD has two layers of 1.2-cm-thick scintillator with an area of 3 m^2. The full operation of SDs started in March 2008. The duty cycle is approximately 95% on average. One northern FD station at the Middle Drum (MD) site uses 14 refurbished HiRes telescopes. Two southern FD stations at the Black Rock Mesa (BRM) and Long Ridge (LR) sites were built newly each with 12 telescopes. The MD FD views 3° - 31° and the BRM and LR FDs view 3° - 33° above horizon. All three FD stations started the observation in November 2007, and have duty cycles of approximately 10%.

TA found evidence for intermediate-scale anisotropy of arrival directions of cosmic rays with greater than 5.7×10^{19} eV of energy. With enhanced statistics, it is expected to observe the structure of the hotspot along with other possible excesses and point sources along with the correlations with extreme phenomena in the nearby universe. TA proposed TAx4 project to quadruple the effective area of the TA SD aperture including the existing TA SD array by installing additional 500 newly designed SDs on a square grid with wider, 2.08-km spacing between each. The layout of TAx4 is shown in Fig. 14.

The design of SD for the TAx4 experiment is identical to the design of SD for the TA Low energy Extension(TALE) experiment, which will be described in detail later. The basic design is common to TA , but the number and arrangement of wavelength shifter fibers (WLSF), the performance of the photomultiplier tubes (PMTs), and the wireless LAN module and used protocols are different. In the TAx4 and TALE, we use a PMT with significantly improved quantum efficiency and surface uniformity. This has allowed us to reduce the total length of WLFSs by 67% while maintaining the performance of the SD as a whole. A new wireless LAN module is used for the TAx4 and TALE SDs because the one used in TA was out of production.

Detector installation for TAx4 began in 2019, and 257 SDs were deployed in February and March 2019. By this installation, the total coverage area with SDs including the original TA SD array has been increased by a factor of 2.5. The new SD array started the data acquisition in April 2019. Since the new SD array is divided into two lobes, two FD stations are required to overlook each lobe in order to increase the number of hybrid events for the measurement of $X_{\rm max}$ and to confirm the energy scale. These FD stations consist of refurbished HiRes telescopes: four telescopes at the MD site and eight telescopes at the BR site. The TAx4 FD station at the northern site was constructed and started the stable observation in June 2018. The TAx4 FDs at the southern site were constructed and started the observation in 2019. The recent status of TAx4 was reported in [1].

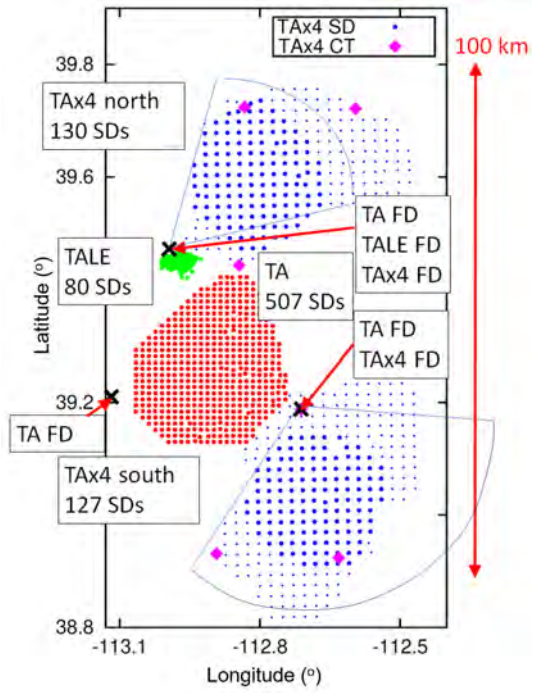

Fig. 14. The layout of the proposed TAx4. The array of 507 SDs (red filled circles on the left) is the original TA SD array. There are three TA FD stations (MD to the north, LR to the west, and BRM to the east of the TA SD array) with black cross symbols. The array of surface detectors (green) to the north of the TA SD array is the TALE SD array. The additional TAx4 500 surface detectors (blue) are located in separate lobes on the northeast and southeast sides of the TA SD array. The 257 large blue filled circles denote deployed SDs, whereas remaining blue dots denote SDs to be deployed. Additional two FD stations with refurbished HiRes telescopes for the TAx4 are located at the MD and BRM FD sites and view to the northeast and southeast as denoted each by the blue frame of the fan. Purple diamond symbols denote TAx4 communications towers.

The TA Low energy Extension (TALE) enables detailed studies of the energy spectrum and composition from $\sim10^{16.5}$ eV. The main target of TALE is to clarify the expected transition from galactic to extra-galactic cosmic ray origins and the comparison of the data with Monte Carlo (MC) simulation that takes into account the results of the latest LHC experiments. The TALE detector is located north of the TA site (at around the MD FD station). The TALE FD station consists of 10 refurbished HiRes telescopes. The TALE FD views 31° -

59° in elevation angle. The TALE detectors are located at the northern corner of the TA detectors. The TALE FD operation was commenced in the spring of 2013. The TALE SD array consists of 80 SDs (40 SDs with 400-meter spacing and 40 SDs with 600-meter spacing). The TALE SD array was completed in February 2018 and is in stable operation. The mode energy of TALE hybrid events is $10^{16.8}$ eV. There is a plan to install additional 50 SDs with 100-meter spacing near the TALE FD station to observe even lower-energy cosmic rays, for which the mode energy is $10^{15.5}$ eV.

The Non-Imaging CHErenkov (NICHE) array is planned to have graded spacings, ranging from 100 meters to 400 meters. The NICHE Prototype Array consists of 14 counters each with a 3-inch PMT that collects non-imaging air-Cherenkov light, which started stable observation in May 2018 [2]. The array is situated 600-1000 m from the TALE FD. NICHE and TALE work together as a hybrid detector for cosmic rays with energies in the range between 10^{15} eV and $10^{18.5}$ eV.

Notable developments during JFY2022

TA, TAx4 and TALE SD arrays continued regular operations during recent three years even if various activities ceased due to the spread of COVID-19. On the other hand, FD observations that require on-site operations had been suspended. However, in June 2020, TA FDs and TAx4 FDs at the MD site resumed operations. In addition, the operation of TAx4 FDs at the BRM site, TALE FDs, and TA FDs at the BRM site resumed in July 2020, January 2021 and June 2022, respectively. The TA FDs at the LR site are not operational as of the end of JFY2022.

The north and south sites of the TAx4 experiment are each divided into three sub-arrays, which are operated as independent arrays. In 2022, a system for triggering air showers that fall on the boundaries of the independent sub-arrays, which we call "boundary trigger" was installed. This has roughly doubled the trigger frequency and increased detection efficiency by 60% for $10^{19.5}$. Fig. 15 show a footprint and related recorded waveforms of an typical TAx4 event boundary triggered.

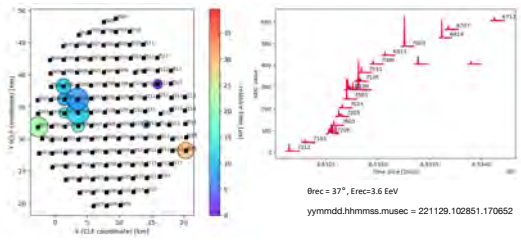

Fig. 15. A footprint and related recorded waveforms of an typical TAx4 event boundary triggered.

2. Publications in refereed journals

The follwing papers were published by the TA collaboration published in refereed journals in JFY 2022.

White paper for the "Snowmass" process

As part of the "Snowmass" process to inform the U.S. Department of Energy and National Science Foundation's long-term plan for high-energy physics, we have joined with other collaborators to submit a white paper [3]. The white paper summarizes discoveries in the field of ultra-high energy cosmic rays over the past two decades, contributions to particle physics, the potential for physics beyond the Standard Model and the search for dark matter, astrophysics in the highest energy regions, and research strategies and future plans for the next 20 years.

Search for Spatial Correlations of Neutrinos with Ultra-high-energy Cosmic Rays

A search for correlations between the arrival direction of high energy neutrinos and the UHECRs was examined [4]. Neutrino data were provided by ANTARES and IceCube, and UHECR data were provided by TA and Auger. The analysis was performed using three different approaches. First, we looked for clustering of neutrino events with respect to the arrival direction of UHECRs. Second, we searched for excesses of UHECRs in the direction of the highest energy neutrinos. Third, we looked for pairs of UHECRs and highest energy neutrinos on various angular scales. None of the analyses have found a significant excess.

3. Other physics results

Update of UHECR spectrum measured by the TA SD array

The TA SD array has been steadily collecting data since May 11, 2008. We have derived the energy spectrum using 14 years of TA SD data in 2022. The energy spectrum showed not only the previously known spectral features of ankle and cutoff, but also "instep" (softening) , at $10^{19.22}$ eV intermediate between ankle and cut off (see Fig. 16 [5]).

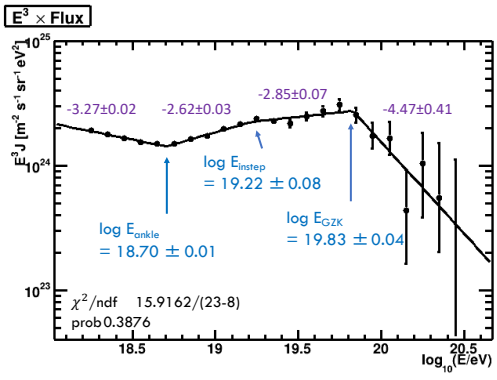

Fig. 16. Energy spectrum using 14-year SD data. The data is represented with the black points with error bars, and a fit to the broken power law having three break points is shown with the black solid line [5].

The differences in the energy spectra of the highest energy cosmic rays reported from the TA and Auger experiments were carefully examined by a working group made by members of the TA and Auger collaborations. It was found that the

two measurements agree well below 10^{19} eV, but at higher energies there are energy-dependent differences that exceed the systematic uncertainties on the energy scales. On the TA experiment side, efforts are underway to understand and resolve systematic differences in energy scales and to investigate the energy dependence of the energy scales themselves, for example, optimization of the energy estimator such as S(800), energy determination based on the equi-intensity cut method, which is an energy determination method that does not rely on Monte Carlo calculations, the use of common fluorescence yield and its wavelength dependence with the Auger experiment, and so on. (see Fig. 17 [6]).

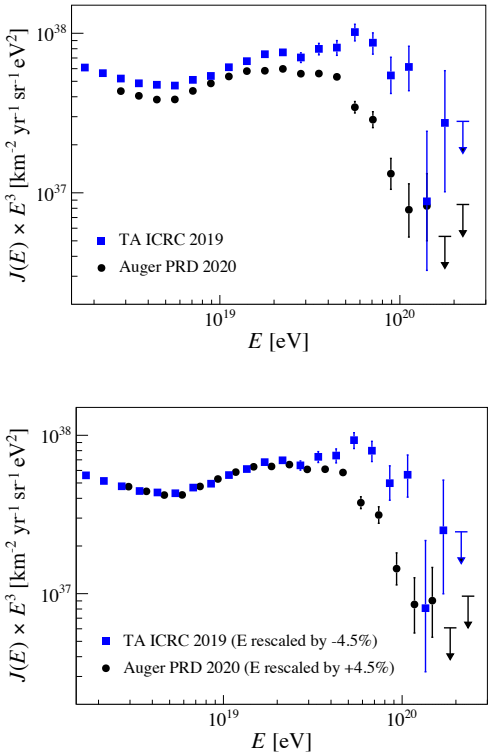

Fig. 17. Energy spectrum measured by Auger and TA in the full declination band (upper), in the full band after a rescaling of the energy by an overall 9% (4.5% for TA and +4.5% for Auger) factor (lower). In the lower panel we show how the spectra can be put in agreement up to about 10^{19} eV introducing an overall energy independent energy shift of 9%. The discrepancy that persist at the highest energies can only be recovered by introducing energy-dependent energy shifts. However, interpreting the spectral differences only as a matter of energy scale may not be entirely correct. This is because the two detectors observe different parts of the sky, and at the highest energies, where cosmic ray deflections due to galactic and extra-galactic magnetic fields are not expected to be as large, the energy spectrum can differ depending on sources in the detector's field of view.

UHECR spectrum measured by the TAx4 SD array

The TAx4 SD array began operation in 2019 as an air shower array of 257 SDs and has been collecting data steadily since then. In 2022 we reported an UHECR energy spectrum based on TAx4 SD data obtained from October 2019 to October 2022 (see Fig. 18).

It is known from the TA experiment that the primary energy, $E_{\rm SD}$ determined by the SD data reconstruction is different from the energy, $E_{\rm FD}$ calorimetrically determined by the FD observations. The energy scale factor for converting $E_{\rm SD}$ to $E_{\rm FD}$ was determined to be 1/1.27 in the TA experiment, but since TAx4 does not have enough statistics for the number of hybrid events detected in both SD and FD, the energy scale factor was determined based on the number of events observed as follows. First, the number of events observed at TAx4 expected from the energy spectrum was calculated using MC simulations with different energy scale factors. The energy scale factor with the smallest difference between the expected number of events calculated in MC and the number of events actually observed was selected, resulting in an energy scale factor of 1/1.36.

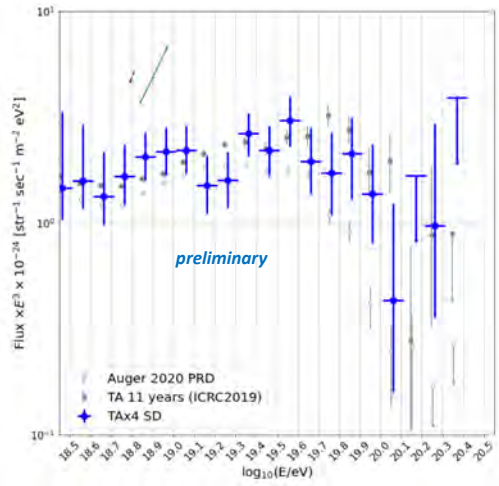

Fig. 18. Energy spectrum based on TAx4 SD data obtained from October 2019 to October 2022.

Averaged $X_{\rm max}$ measured by TALE hybrid

The TA Low energy Extension (TALE) experiment is designed to expand the low energy limit of 10^{18} eV of the TA experiment and measure the cosmic ray flux, anisotropy, and nuclear mass composition over a wide energy range, in order to separate the contribution of heavy and low energy, *i.e.* galactic, cosmic rays and light and high energy, *i.e.* extra galactic, cosmic rays, and to reveal their respective energy spectra to study the physics of cosmic ray sources and cosmic ray propagation. For this purpose, we have installed 10 FDs and 80 SDs in the TA experiment as the TALE hybrid detector, which has been in regular operation since September 2018.

We reported on the preliminary result of the mass composition measurement by using 4 years of TALE hybrid data in the energy range of $10^{16.5}$ - $10^{18.4}$ eV. The $\langle$Xmax$\rangle$ elongation rate has changed from 16 ± 5 g/cm^2/decade to 97 ± 4 g/cm^2/decade at the energy just above 10^{17} eV. This break in the elongation rate is likely correlated with the observed break in the cosmic ray energy spectrum know as the 2nd knee. From the $\langle$Xmax$\rangle$, the mean ln$A$ can be calculated and shown in Fig. 19.

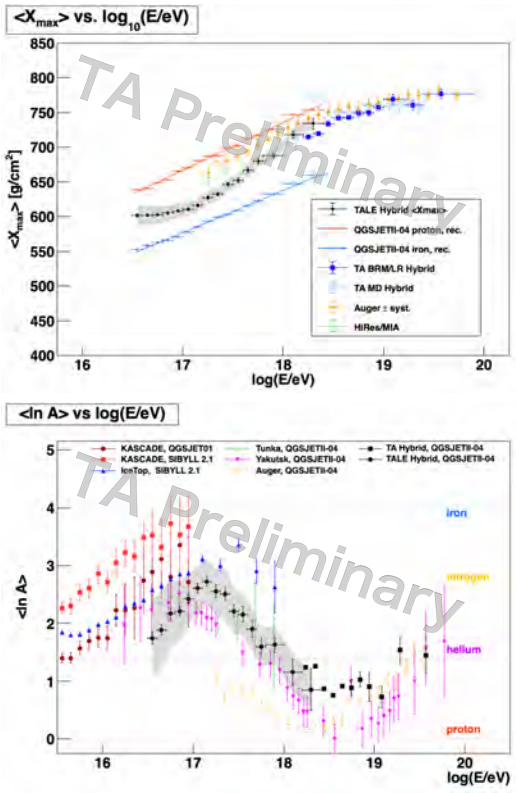

Fig. 19. Upper: ⟨Xmax⟩ as a function of shower energy, measured by using 4 years of the TALE hybrid data. Lower: Comparison of ⟨lnA⟩ as a function of energy with various measurements. For comparison, two interpretations by KASCADE, IceTop, Tunka, Yakutsk, Auger, and 8.5 yrs TA BRM/LR hybrid results are shown. The gray band in both figures represents the systematic uncertainty on Xmax measurement.

A machine learning approach for mass composition analysis

Mass composition is one of the characteristics of cosmic rays that is not only related to the propagation of UHECRs, but also to the cosmic ray acceleration mechanism at the sources and source population. It can be measured from extensive air showers observed on the Earth. The most widely used method is FD observation to derive the depth of the shower maximum, Xmax, as a composition-sensitive observable. However, FD observations are limited in their statistics by small duty cycles. Therefore, we are conducting study on the determination of mass composition using only SD array observations.

In 2019, we developed and used a classifier to determine the 'proton likeness' of primaries for each event by multivariate analysis using a Boosted Decision Tree [8]. Subsequently in 2021, a machine-learning classifier was developed using more "raw" information, such as the characteristics of the spatial and temporal distribution of showers from all triggered detector waveforms and the maximum signal waveform itself [9].

In 2022, a binary classification model for proton and iron nuclei has also been studied for the TALE SD array, using as input the 27 air shower reconstruction parameters plus the waveforms recorded in the SD that showed the maximum signal (128 bins in each of the upper and lower layers) themselves, as deep machine-learning NN. The model achieves a classification accuracy of 72.3% [10][11] (Fig. 20).

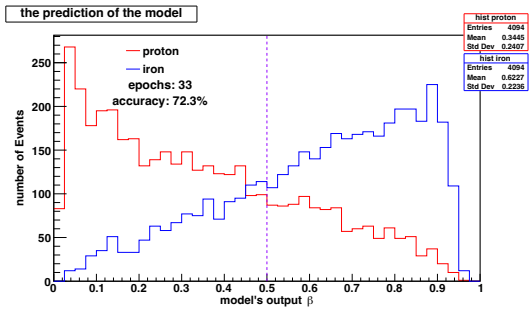

Fig. 20. The response distribution of the test data to the machine learning model studied in [11]. The purple dashed line is drawn at $\beta = 0.5$.

4. Other activities

Other research results and activities reported at UHECR2022, JPS meetings and/or other conferences are listed and introduced below.

- Measurement of energy spectrum with TALE in hybrid mode [12]
- Measurement of energy spectrum with the TALE SD array [13]
- Updates on the Hotspot and the Perseus-Pisces supercluster excess [14]
- Constraints on the starburst galaxy source model [15]
- Study on reconstruction method for large zenith angle air showers [16]
- Calibration of FDs using a UAV-mounted light source [17]
- Joint analysis of the energy spectrum measured at Pierre Auger observatory (PAO) and TA [6]
- Joint study of the Xmax and the mass composition measured at PAO and TA [18]
- Joint study of the arrival directions of UHECRs observed by PAO and TA [19]
- Auger@TA: an independent PAO SD micro-array at the TA site [20]

5. Future Plans

TALE infill SD array

The TALE infill experiment is a further extension of TA-TALE detectors to observe low-energy cosmic rays down to the PeV region. TALE infill uses existing TALE-FD detectors and newly developed "infill" surface detectors with 100m spacing.

Fig. 21. Photographs showing the production of detectors for the TALE infill SD array at Akeno observatory of ICRR, taken in October 2021.

50 SDs used in the TALE infill array were manufactured at the Akeno observatory of ICRR in October 2021(Fig. 21).

In the summer of 2022, these detectors were transported to the TA site in Utah, U.S.A., where they were installed with solar panels, batteries and other power-related equipment on mounts at the Cosmic Ray Center in Delta. They were then installed in the area between the TALE FD station and the TALE SD array in October 2022. Once the SDs were moved to a staging area, they were finally confirmed to be in normal operation there. Each SD was then deployed by helicopter on a pre-determined installation point(Fig. 22).

Fig. 22. Photographs of detectors being installed for the TALE infill experiment, taken in October 2022. Once the SDs were moved to the staging area (upper-left), they were finally confirmed to be in normal operation there (upper-right). Each SD was then transported by helicopter to a pre-determined installation point (lower).

The 50 SDs were placed within 2 km of the TALE FD station with 100 m interval. A map of the installation site is shown in Fig. 23. The SD array covers 0.36 km^2.

The performance of the hybrid observation with the TALE infill detectors was evaluated [21][22]. Some of the results are shown in Fig. 24. The energy threshold was found to fall to $10^{15.2}$ eV. The accuracy of the shower parameter determination depends on the energy and, as expected, is better at higher energies. At 10^{16} eV, the energy resolution is found to be 21% and the Xmax resolution is 38 g/cm^2.

Observations with the TALE infill are scheduled to begin in September 2023.

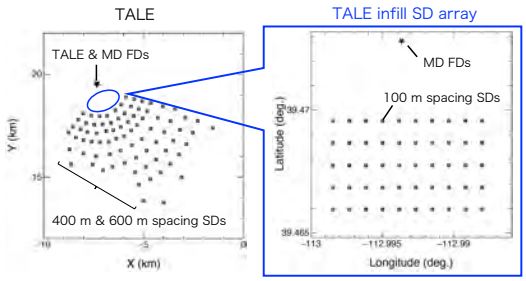

Fig. 23. The layout of TALE FD, TALE SDs and TALE infill SDs.

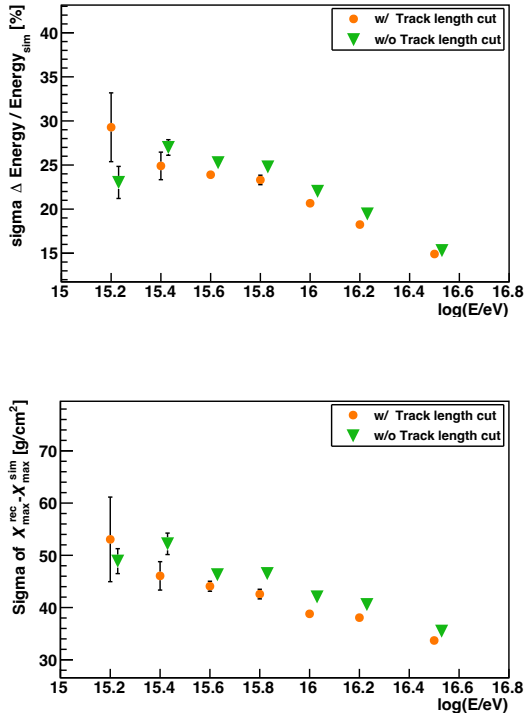

Fig. 24. Upper: Energy resolution of TALE infill hybrid. Lower: Xmax resolution of TALE infill hybrid.

Research and development of next-generation detectors

The TA experiment site is also a facility for the development of next-generation detectors, and prototype detectors for EUSO [23][24], FAST [25] and CRAFFT [26] have been installed and are being used for joint observations with the TA experiment. With the calm down of COVID-19, the research activity has recovered, and the on-site activities by these research groups have been resumed from 2022.

Discussions are also underway for the next-generation observatories, to measure the properties of the highest-energy cosmic rays with unprecedented accuracy in the future such as TA2 and GCOS (The Global Cosmic Ray Observatory). In May 2021, the first international workshop of GCOS was held [27]. In 2022, GCOS is also included in the Snowmass process as a future plan for this field [3]. In addition, a second workshop was held in 2022 [28], and the group has spoken

at several international conferences to increase its visibility in the community.

Bibliography

[1] R. Abbasi, *et al.*, "Current status and prospects of surface detector of the TAx4 experiment", PoS(ICRC2021), 203, 2021.

[2] Y. Omura, *et al.*, "TA experiment 381: jNICHE - Energy spectrum and composition analysis of cosmic rays measured with the NICHE detectors at the TA site", 2022 Annual JPS Meeting.

[3] A. Coleman, *et al.*, "Ultra high energy cosmic rays: The intersection of the Cosmic and Energy Frontiers", Astropart. Phys. 149, 102819, 2023.

[4] A. Albert, *et al.*, "Search for Spatial Correlations of Neutrinos with Ultra-high-energy Cosmic Rays", Ap. J. 934, 162, 2022.

[5] J.H. Kim, *et al.*, "Energy Spectrum Measured by the Telescope Array Surface Detectors", EPJ Web of Conferences, 283, 02005, 2023.

[6] D.R. Bergman, *et al.*, "The energy spectrum of ultra-high energy cosmic rays measured at the Pierre Auger Observatory and the Telescope Array", EPJ Web of Conferences, 283, 02003, 2023.

[7] K. Fujita, *et al.*, "Cosmic ray mass composition measurement with the TALE hybrid detector", EPJ Web of Conferences, 283, 02009, 2023.

[8] R.U. Abbasi, *et al*, "Mass composition of ultra high-energy cosmic rays with the Telescope Array Surface Detector data", Phys. Rev. D 99, 022002, 2019

[9] O. Kakashev, *et al.*, "Deep learning method for identifying mass composition of ultra-high-energy cosmic rays", JINST, 17, P05008, 2022

[10] R. Arimura, *et al.*, "A machine learning approach for mass composition analysis with TALE-SD data", EPJ Web of Conferences, 283, 02011, 2023.

[11] R. Arimura, "Measurement of cosmic ray mass-composition at the 2nd knee region with the TALE surface detectors", Master thesis, Osaka City University, 2023.

[12] H. Oshima, *et al.*, "Measurement of Cosmic-ray Energy Spectrum with the TALE Detector in Hybrid Mode", EPJ Web of Conferences, 283, 02006, 2023.

[13] I. Komae, *et al.*, "TA experiment 395: Report on the TALE experiment 9", JPS meeting, Online, 2023.

[14] J.H. Kim, *et al.*, "Updates on the Hotspot and the Perseus-Pisces supercluster Excess Observed by the Telescope Array Experiment", EPJ Web of Conferences, 283, 03005, 2023.

[15] R. Higuchi, *et al.*, "Constraints on the starburst galaxy source model by UHECR anisotropy and the galactic magnetic field model", JPS meeting, Okayama, 2022.

[16] K. Takahashi, *et al.*, "TA experiment 397: TA SD reconstruction method for large zenith angle air showers", JPS meeting, Online, 2023.

[17] R. Hibi, *et al.*, "TA experiment 398: Improving Observation Efficiency in Measuring Optical Properties of TA FD Using UAV-Mounted Light Sources", JPS meeting, Online, 2023.

[18] D.R. Bergman, *et al.*, "Testing the Compatibility of the Depth of the Shower Maximum Measurements performed at Telescope Array and the Pierre Auger Observatory - Auger-TA Mass Composition Working Group Report", EPJ Web of Conferences, 283, 02008, 2023.

[19] A. di Matteo, *et al.*, "2022 report from the Auger-TA working group on UHECR arrival directions", EPJ Web of Conferences, 283, 03002, 2023.

[20] S. Mayotte, *et al.*, "Auger@TA: Deploying an independent Pierre Auger Observatory SD micro-array at the Telescope Array Project - Auger@TA Working Group Report", EPJ Web of Conferences, 283, 06005, 2023.

[21] A. Iwasaki, *et al.*, "Performance of the TALE infill experiment as a TA-TALE extension down to the PeV region", EPJ Web of Conferences, 283, 06015, 2023.

[22] A. Iwasaki, "TALE infill experiment : Detector performance evaluation and optimization for PeV-EeV cosmic ray observations", Master thesis, Osaka City University, 2023.

[23] Z. Plebaniak *et al.*, "Study of the calibration method using the stars measured by the EUSO-TA telescope", PoS(ICRC2021), 240, 2021.

[24] M. Bertaina "An overview of the JEM-EUSO program and results", PoS(ICRC2021), 406, 2021.

[25] T. Fujii, "Recent results from prototypes of the Fluorescence detector Array of Single-pixel Telescopes (FAST) in both hemispheres", EPJ Web of Conferences, 283, 06010, 2023.

[26] Y. Tameda *et al.*, "Progress and future prospect of the CRAFFT project for the next generation UHECR observatory", EPJ Web of Conferences, 283, 06011, 2023.

[27] GCOS workshop, May 17-21, online, 2021; https://agenda.astro.ru.nl/event/18/

[28] GCOS 2nd workshop, July 13-15, Wuppertal, 2022; https://agenda.astro.ru.nl/event/21/

Tibet ASγ Experiment

[Spokesperson: M. Takita]
ICRR, The Univ. of Tokyo, Kashiwa, Chiba 277-8582

1. Experiment

The Tibet air shower experiment has been successfully operated at Yangbajing (90°31′ E, 30°06′ N; 4300 m above sea level) in Tibet, China since 1990. It has continuously made a wide field-of-view (approximately 2 steradian) observation of cosmic rays and gamma rays in the northern sky.

The Tibet I array was constructed in 1990 and it was gradually upgraded to the Tibet II by 1994 which consisted of 185 fast-timing (FT) scintillation counters placed on a 15 m square grid covering 36,900 m^2, and 36 density (D) counters around the FT-counter array. Each counter has a plastic scintillator plate of 0.5 m^2 in area and 3 cm in thickness. All the FT counters are equipped with a fast-timing 2-inch-in-diameter photomultiplier tube (FT-PMT), and 52 out of 185 FT counters are also equipped with a wide dynamic range 1.5-inch-in-diameter PMT (D-PMT) by which we measure up to 500 particles which saturates FT-PMT output, and all the D-counters have a D-PMT. A 0.5 cm thick lead plate is put on the top of each counter in order to increase the counter sensitivity by converting gamma rays into electron-positron pairs in an electromagnetic shower. The mode energy of the triggered events in Tibet II is 10 TeV.

In 1996, we added 77 FT counters with a 7.5 m lattice interval to a 5,200 m^2 area inside the northern part of the Tibet II array. We called this high-density array Tibet HD. The mode energy of the triggered events in Tibet HD is a few TeV.

In the late fall of 1999, the array was further upgraded by adding 235 FT-counters so as to enlarge the high-density area from 5,200 m^2 to 22,050 m^2, and we call this array and further upgraded one Tibet III. In 2002, all of the 36,900 m^2 area was covered by the high-density array by adding 200 FT-counters more. Finally we set up 56 FT-counters around the 36,900 m^2 high density array and equipped 8 D-counters with FT-PMT in 2003. At present, the Tibet air shower array consists of 761 FT-counters (249 of which have a D-PMT) and 28 D-counters as in Fig. 1.

The performance of the Tibet air shower array has been well examined by observing the Moon's shadow (approximately 0.5 degrees in diameter) in cosmic rays. The deficit map of cosmic rays around the Moon demonstrates the angular resolution to be around 0.9° at a few TeV for the Tibet III array. The pointing error is estimated to be better than $\sim$0.01°, as shown in Fig. 2, by displacement of the shadow center from the apparent center in the north-south direction, as the east-west component of the geomagnetic field is very small at the experimental site. On the other hand, the shadow center displacement in the east-west direction due to the geomagnetic field enables us to spectroscopically estimate the energy scale uncertainty at $\pm$12 % level, as shown in Fig. 3. Thus, the Tibet air shower experiment introduces a new method for energy scale calibration other than the conventional estimation by the difference between the measured cosmic-ray flux by an air shower experiment and the higher-energy extrapolation of cosmic-ray flux measured by direct measurements by balloon-borne or satellite experiments.

In 2007, a prototype 100-m^2 underground water

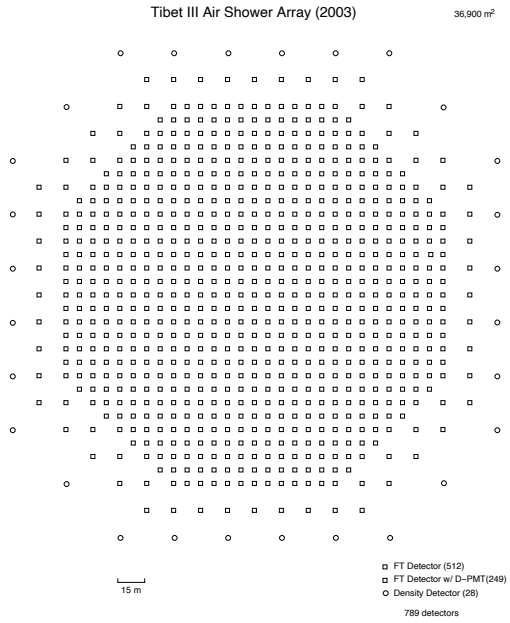

Fig. 1. Schematic view of Tibet III.

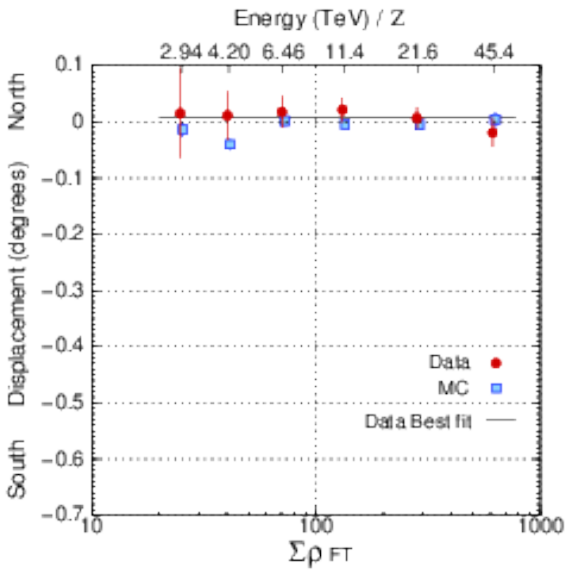

Fig. 2. From [1]. The Moon's shadow center displacement from the apparent position in the north-south direction as a function of energy, observed by Tibet III.

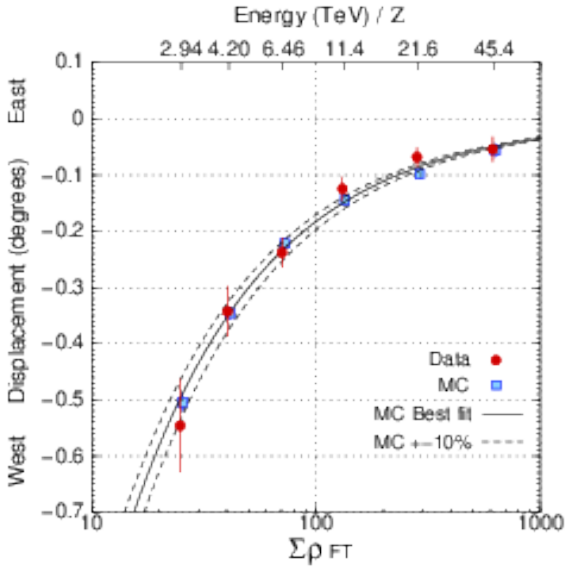

Fig. 3. From [1]. The Moon's shadow center displacement from the apparent position in the east-west direction as a function of energy, observed by Tibet III.

Cherenkov muon detector was successfully constructed in Tibet to demonstrate the technical feasibility, cost estimate, validity of our Monte Carlo simulation. Data analyses demonstrate that our MC simulation reproduces real data quite reasonably.

After the success of the prototype underground muon detector, we added a large underground muon detector (MD) array and the experimental configuration was changed starting from February 2014. The current array consists of 597 plastic scintillation detectors with an area of 0.5 m^2 as shown by small dots in Fig. 4, covering an area of 65,700 m^2. The Tibet MD array (3,400 m^2 in total area) consists of 64 water-Cherenkov-type detectors located at 2.4 m underground of the AS array as shown by open squares in Fig. 4. Each detector is a waterproof concrete cell filled up with water of 1.5 m in depth, 7.35 m $\times$ 7.35 m in area, equipped with a 20-inch-diameter downward-facing photomultiplier tube (PMT) on the ceiling. The inner walls and floor have a white Tyvek sheet lining to efficiently gather catoptric water Cherenkov light. The electromagnetic component is shielded by the soil overburden which corresponds to $\sim$19 radiation lengths. The energy threshold for muons is approximately 1 GeV. A photon induced air shower has much less muons compared with a cosmic-ray induced one. The Tibet MD array enables us to significantly discriminate a cosmic-ray background event from a photon signal by means of counting the number of muons in an air shower.

2. Physics Results

Our current research theme is classified into 4 categories:

(1) TeV celestial gamma-ray point/diffuse sources,

(2) Chemical composition and energy spectrum of primary cosmic rays in the knee energy region,

(3) Cosmic-ray anisotropy in the multi-TeV region with high precision,

(4) Global 3-dimensional structure of the solar and interplanetary magnetic fields by observing the Sun's shadow in cosmic rays.

We will introduce a part of the results obtained in this fiscal year[2].

We successfully detected gamma-rays in the 100 TeV region from Cygnus OB1 and OB2 regions.

A photon induced air shower contains much less muons compared with a cosmic-ray induced air shower. Therefore, the MD array enables us to distinguish a photon signal event from a cosmic-ray induce background event. Using the AS and MD arrays, we analyzed the air shower data and muon data during 719 live days from February 2014 to May 2017.

Figure 4 (a) and (b) show the event display and the lateral distribution, respectively, of a typical photon-like event observed with $E = 251$ TeV from the Crab nebula[5]. The total uncertainty of the energy ΔE is defined as the quadratic sum of the absolute energy-scale error (12%) [1] and the energy resolution estimated by using MC events with the same θ and core distance from the array center (R). The ΔE of the 251 TeV photon-like event is estimated to be $^{+45}_{-43}$ TeV.

We reconstruct the arrival direction of an air shower by means of the relative timing information recorded at each scintillation detector. The color scale and circle size in Fig. 4 (a) stand for the relative timing (t) and the number of particle density (ρ) in an air shower. In the first place, we estimate the air shower core location weighted by ρ. The arrow head position and direction in the figure indicate the estimated core position and azimuthal direction. The t's in the air shower front are fitted by a conical shape, and its cone angle is optimized by the MC simulation depending on the air shower size. The angular resolutions (50% containment) are estimated to be approximately 0.5° and 0.2° for 10 TeV and 100 TeV photon, respectively.

The secondary particles in an air shower deposit energy, which is proportional to ρ, in a scintillator. The ρ at each detecto r is defined as the PMT output charge divided by the single particle peak which is monitored every 20 minutes to correct temperature dependence of each detector gain. The energy of each air shower is reconstructed using the lateral distribution of ρ, above 10 TeV. Figure 4 (b) shows an example of the lateral distribution of ρ. As an energy estimator, we use $S50$[6], which is defined as ρ at a distance of 50 m from the air shower axis in the best-fit Nishimura-Kamata-Greisen (NKG) function. The energy resolutions with $S50$, which depend on air shower core location and zenith angle, are roughly estimated to be 40% at 10 TeV and 20% at 100 TeV. On the other hand, the energy below 10 TeV was estimated directly from $\Sigma\rho$ corresponding to the sum of of the particle density measured by each scintillatoin detector, as the number of hit

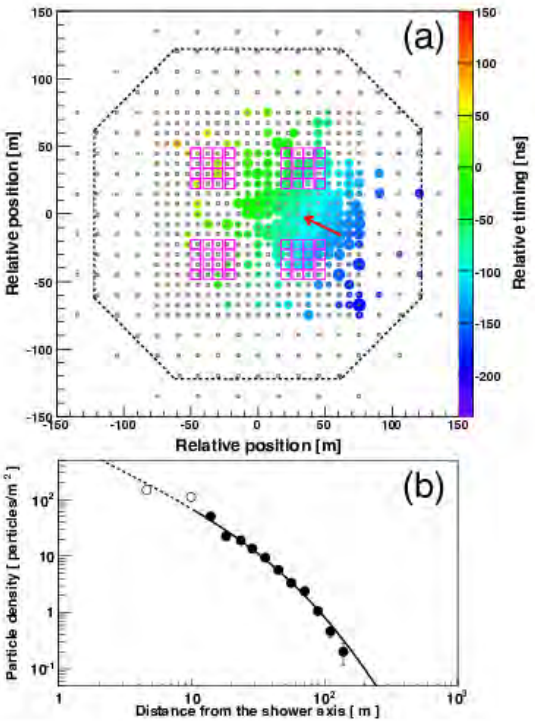

Fig. 4. From Ref.[5], references therein. (a) An event display of the observed photon-like AS of energy 251 TeV. The size and color of each circle represent the logarithmic particle density and the relative timing in each detector, respectively. The arrow head and direction indicate the AS core location and incident direction, respectively. Dots and open squares denote scintillation detectors and underground MDs, respectively. The enclosed area by the dashed line indicates the fiducial area of the AS array. (b) Lateral distribution of the photon-like shower event in panel (a). The solid circles and curve show the experimental data and fitting result by the Nishimura-Kamata-Greisen (NKG) function to the data recorded by detectors more than 10 m apart from the AS axis. The dashed curve and open circles are an extrapolation of the NKG function fitting and the unused data within 10 m from the AS axis.

detectors is too low to fit $S50$. The absolute energy scale uncertainty is estimated to be 12 by the westward displacement of the Moon shadow position.

The electromagnetic cascade in the air shower is strongly suppressed by the bremsstrahlung process in the overburden, while muons and a part of hadronic components penetrate into the underground MD array. The number of detected particles at an MD (N_μ) is defined as the output charge divided by the single muon peak which is monitored every 20 minutes. The sum of detected particles in all MDs (ΣN_μ) is used as a parameter to separate between photon and cosmic-ray induced air showers.

An event trigger is issued at any 4-fold coincidence with detectors recording more than 0.6 particles within the area enclosed by the dashed lines in Fig. 4. At air shower energies smaller than 10 TeV, we employ the same selection criteria and estimate the event energy as in the previous work[1], except for the MD selection criterion. At air shower energies greater than 10 TeV, we employ the following event selections: (1) zenith angle of arrival direction (θ) should be $\theta < 40^\circ$; (2) number of available detectors for the air shower reconstruction should be ≥ 16; (3) among 6 detectors recorded with the largest ρ's, 5 should be contained in the fiducial area enclosed by the dashed lines in Fig. 4; (4) $\log(S50)$ should be > -1.2; (5) age parameter (s) in the best-fit NKG function should be $0.3 < s < 1.3$. (6) ΣN_μ should be $\Sigma N_\mu < 0.15(\Sigma\rho)^{2.8}$ or $\Sigma N_\mu < 3.6\times10^{-4}(\Sigma\rho)^{1.4}$, where $\Sigma\rho$ is the sum of particle density measured by the AS array. The MD cut is optimized for photon detection by our MC simulation.

To estimate the background contribution from cosmic rays, we adopt the Equi-Zenith Angle method which is the same as in our previous works [1]. The background counts are estimated from the number of events averaged over 20 off-source bins of the same size as the on-source bin located at the equi-zenith angle. The radius of the on/off-source bin is set to $R_{\rm sw}(\Sigma\rho) = 6.9/\sqrt{\Sigma\rho}$ (deg.). In order to efficiently extract signals in the higher energy region at low background level, the lower limit of $R_{\rm sw}$ is set to 0.5°, which corresponds to $\sim 90\%$ containment of photons above 100 TeV.

To generate air shower events in the atmosphere, Employed are the CORSIKA code v7.4000 with EPOS-LHC for the high-energy hadronic interaction model and FLUKA code v2011.2b for the low-energy hadronic interaction model. The very-high-energy photons at the top of atmosphere are inputted, assuming the power-law spectrum with a differential index -2.9 above 0.3 TeV. The generated secondary particles in an air shower are fed into the detector response simulation for the AS array developed based on the GEANT4 code v4.10.00. The MC simulation for the MD array considering the overburden has been developed based on the GEANT4 code. The electromagnetic and hadronic cascades by the secondary particles in the overburden, as well as the ray tracing of Cherenkov lights emitted in the water cells are simulated by the GEANT4 code. The number of photoelectrons detected in the 20-inch PMT is converted to N_μ referring to the single muon peakin each cell. The muon cut is determined to maximize the figure of merit $N_\gamma^{\rm MC}/\sqrt{N_\gamma^{\rm MC}+N_{\rm CR}^{\rm DATA}}$, where $N_\gamma^{\rm MC}$ and $N_{\rm CR}^{\rm DATA}$ denote the expected number of photons by the MC and the number of background events in the data after the muon cut. The photon-like events are defined as the remaining events after the muon cut.

We detect a gamma-ray source above 25 TeV near HESS J1843-033 with a statistical significance of $6.2\,\sigma$, as is shown in Fig. 5. A two-dimensional maximum likelihood analysis is applied to estimate the source centroid assuming an axisymmetric Gaussian distribution for the distribution of the gamma rays. The resultant center is $(\alpha, \delta) = (281.^\circ09 \pm 0.^\circ10, -3.^\circ76 \pm 0.^\circ09)$ in the J2000 equatorial coordinates. We name the source TASG J1844-038. The position of TASG J1844-038 is statistically consistent with those of HESS J1843-033, eHWC J1842-035, and LHAASO J1843-0338. On the other hand, TASG J1844-038 deviates from HESS J1844-030 and HESS J1846-029 at the $3.2\,\sigma$ and $4.5\,\sigma$ levels, respectively, making its associations with these sources unlikely.

HESS J1843-033 is an unidentified gamma-ray source discovered by the H.E.S.S. Galactic plane survey. The energy spectrum was measured up to 30 TeV, described by a

power-law function with an spectral index of $\simeq -2.2$. HAWC reported on the detection of 2HWC J1844-032 and eHWC J1842-035 near HESS J1843-033, and for the latter, HAWC estimated the integral gamma-ray flux above 56 TeV[3]. Recently, LHAASO detected LHAASO J1843-0338 and provided a gamma-ray flux point at 100 TeV [4]. This is the first observational result of the energy spectrum of gamma rays beyond 100 TeV in the direction of the HESS J1843-033 region and discusses the origin of the gamma-ray emission in view of its associations with celestial bodies around it.

Figure 6 shows the angular distribution of the events observed above 25 TeV around the centroid of TASG J1844-038. The horizontal axis ϕ^2 represents the square of the angle between the centroid of TASG J1844-038 and the direction of events. The blue histograms are made from background events in the OFF regions and Monte Carlo gamma-ray events from a point source normalized to the number of excess counts in the ON-source region. The source extension is estimated by fitting the following Gaussian function to the observed number of events:

$$G(\phi^2; A, \sigma_{\rm ext}) = A \exp\left(-\frac{\phi^2}{2(\sigma^2{}_{\rm ext} + \sigma^2_{\rm psf})} \right) + N_{\rm bg} \qquad (1)$$

where A is a normalization constant, $\sigma_{\rm ext}$ the extension of TASG J1844-038, $\sigma_{\rm psf} = 0.^\circ 28$ the radius of the point-spread function for gamma rays above 25 TeV that follow a power-law energy spectrum with an index of 3.0, and $N_{\rm bg} = 29.4$ the number of background events. The best-fit result is shown by the black curve in Fig. 6, leading to $\sigma_{\rm ext} = 0.^\circ 34 \pm 0.^\circ 12$ with a reduced chi-square of $\chi^2/{\rm d.o.f.} = 39.5/38$.

Figure 7 shows the differential gamma-ray energy spectrum of TASG J1844-038. A gamma-ray flux is calculated when the statistical significance of gamma-ray detection in each energy bin exceeds $2\,\sigma$, and otherwise, the 95% flux upper limit is calculated. Our results in 25 TeV $< E <$ 130 TeV is fitted with a power-law function of $dN/dE = (9.70 \pm 1.89) \times 10^{-16} (E/40\,{\rm TeV})^{-3.\,26\pm0.30}\,{\rm TeV}^{-1}{\rm cm}^{-2}{\rm s}^{-1}$ with $\chi^2/{\rm d.o.f.} = 2.1/2$. As a conceivable systematic uncertainty, the source extension $\sigma_{\rm ext}$ affects the flux normalization by 19% and the spectral index by 0.02. The absolute energy-scale uncertainty of 12% [1] causes the flux normalization by 39% as well. Adding these two uncertainties in quadrature, the total systematic uncertainty in the flux normalization is estimated to be 43%. The energy spectrum of TASG J1844-038 smoothly connects to that of HESS J1843-033 and is consistent with the fluxes of eHWC J1842-035 and LHAASO J1843-0338, supporting the common origin for gamma rays from these sources. Fitting a simple power-law function to the combined spectra of HESS J1843-033, LHAASO J1843-0338, and TASG J1844-038 is disfavored at the $5.0\,\sigma$ C.L., and the spectrum can be better fitted with the power-law function with an exponential cutoff as follows:

$$\frac{dN}{dE} = N_0 \left(\frac{E}{\rm TeV} \right)^{-\Gamma} \exp\left(-\frac{E}{E_{\rm cut}} \right) \qquad (2)$$

where the best-fit parameters are $N_0 = (3.57 \pm 0.26) \times 10^{-12}\,{\rm TeV}^{-1}{\rm cm}^{-2}\,{\rm s}^{-1}$, $\Gamma = 2.02 \pm 0.06$ and $E_{\rm cut} = 49.5 \pm 9.0$ TeV with $\chi^2/{\rm d.o.f.} = 10.4/8$. The contribution from eHWC J1842-035 is not taken into account in the combined fit, since the integral flux above 56 TeV is only given[3] (the differential flux of eHWC J1842-035 shown in Fig. 7 is estimated from the integral flux with a spectral index of -2.7 assumed in the HAWC paper).

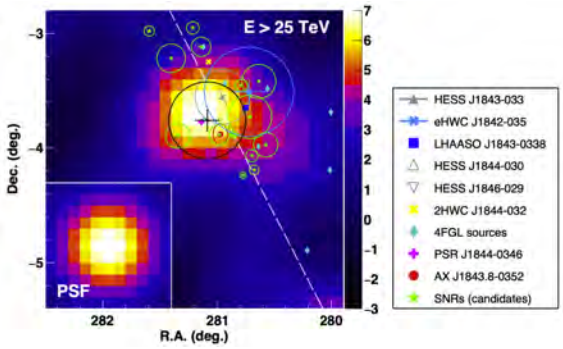

Fig. 5. From Ref.[2], references therein. Significance map of TASG J1844-038 above 25 TeV smoothed with the point-spread function (PSF). The black cross shows the source center and its statistical errors in the right ascension and declination, and the source extension ($\sigma_{\rm ext}$, see the text) is denoted by the black circle. The Galactic plane is drawn by the white dashed line. The lower-left inset denotes the PSF above 25 TeV. Positions and extensions of nearby sources listed in the right legend are indicated in the same way as for TASG J1844-038. For HESS J1843-033 and eHWC J1842-035, the statistical errors on their positions are also shown.

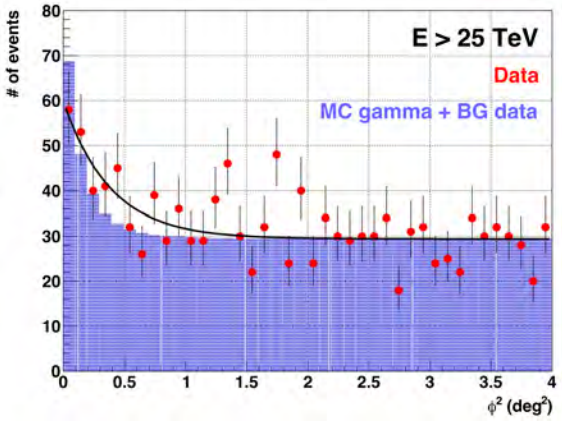

Fig. 6. From Ref.[2], references therein. Distribution of events above 25 TeV around the center of TASG J1844-038. The horizontal axis ϕ^2 denotes the square of the angle between the center of TASG J1844-038 and the incoming direction of events. The blue histograms are constructed from background events in OFF regions plus Monte Carlo gamma-ray events from a point source normalized to the number of excess counts in the ON-source region. The solid black curve shows the best-fit function to the data formulated as Equation (1).

For more details on the gamma rays in the 100 TeV region from HESS J1843-033, see [2].

3. Other Activities

The emulsion-pouring facilities can meet the demands for making any kind of nuclear emulsion plates which are used

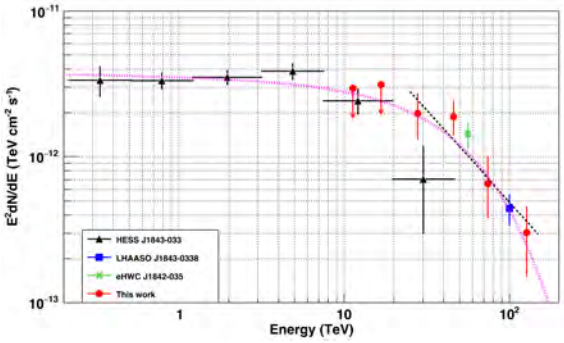

Fig. 7. From Ref.[2], references therein. Differential gamma-ray energy spectrum measured in this work (red). Vertical bars and downward arrows denote 1σ statistical errors and the 95% upper limits, respectively. The black dashed line shows the best-fit power-law function to our results in $25\,\mathrm{TeV} < E < 130\,\mathrm{TeV}$. Also shown are the flux points of HESS J1843-033 (black), eHWC J1842-035 (light green), and LHAASO J1843-0338 (blue). The flux of eHWC J1842-035 is calculated from the integral flux above $56\,\mathrm{TeV}$ assuming a differential spectral index of -2.7. The magenta dotted curve shows the best-fit power-law function with an exponential cutoff fitted to the combined spectra of HESS J1843-033, LHAASO J1843-0338, and TASG J1844-038.

for cosmic ray or accelerator experiments. The thermostatic emulsion-processing facilities are operated in order to develop nuclear emulsion plates or X-ray films. Using these facilities, it is also possible to make and develop emulsion pellicle in 600-micron thickness each. In this way, these facilities have been open to all the qualified scientists who want to carry out joint research programs successfully. Of recent, however, the shrinking demand for the facilities let us decide that we should suspend calls for joint research programs to utilize the emulsion-pouring facilities, starting from 2012.

4. Ongoing Research Plans with MD

(1) Chemical composition of primary cosmic rays making the knee in the all-particle energy spectrum

We have measured the energy spectra of primary cosmic-ray protons, helium, all particles around the knee energy region. The main component responsible for making the knee structure in the all particle energy spectrum is heavier nuclei than helium. The next step is to identify the chemical component making the knee in the all particle energy spectrum. We have a plan to install an Yangbajing Air shower Core detector array (YAC) near the center of Tibet III to distinguish the chemical component making the knee. We completed construction of YAC2 (124 detectors over $\sim$500m^2 in area), as is shown in Fig. 8, and started data-taking in 2014. YAC2 aims at mainly studying the energy spectra of proton and helium components in the knee energy region.

(2) Gamma-ray astronomy in the 100 TeV region

For the purpose of detecting high-energy cosmic gamma rays with an air shower array, a large underground muon

Fig. 8. YAC2 set up at Yangbajing.

detecter[7] is very effective to reduce cosmic-ray background. We added a large ($\sim$3,400 m^2) underground water Cherenkov muon detector (Tibet-MD) array under the present Tibet air shower array (Tibet AS $\sim$65,700 m^2). By Tibet AS + MD, we aim at background-free detection of celestial point-source gamma rays around 100 TeV with the world-best sensitivity and at locating the origins (PeVatrons) of cosmic rays accelerated up to the knee (PeV) energy region in the northern sky. The measurement of cut off energies in the energy spectra of such gamma rays in the 100 TeV region may contribute significantly to understanding of the cosmic- ray acceleration limit at the acceleration sites. Above 100 TeV, the angular resolution of Tibet AS with 2-steradian wide field of view is 0.2° and the hadron rejection power of Tibet MD is typically 1/1000 for a point-like source.

Development of Monte Carlo simulation is under way for comparison with real data. Various analysis tools are also extensively being developed.

As is described in the text, we succeeded in the first detection of photons with energies above 100 TeV from Crab in the world, opening a new energy (sub-PeV) window in astronomy. We have also succeeded in detection of gamma rays in the 100 TeV region from G106.3+2.7, Cygnus OB1 and OB2 regions, HESS J1843-033 as well as sub-PeV diffuse gamma rays from the galactic disk. Analyses are under way in search of other sub-PeV gamma-ray sources.

Bibliography

Papers in refereed journals

[1] "Multi-TeV Gamma-Ray Observation from the Crab Nebula Using the Tibet-III Air Shower Array Finely Tuned by the Cosmic-Ray Moon's Shadow", M. Amenomori *et al.*, Astrophysical Journal, **692** , 61-72 (2009).

[2] "Measurement of the Gamma-Ray Energy Spectrum beyond 100 TeV from the HESS J1843-033 Region", M. Amenomori. *et al.*, Astrophy. J. **932**, 120 (2022).

[3] A. U. Abeysekara *et al.*, Physical Review Letters, **124**:021102, (2020).

[4] Z. Cao *et al.*, Nature **594** 33 (2021).

[5] "First Detection of Photons with Energies beyond 100 TeV from an Astrophysical Source", M. Amenomori*et al.*, Physical Review Letters, **123** :051101-1-6 (2019).

[6] "Energy determination of gamma-ray induced air showers observed by an extensive air shower array", K. Kawata *et al.*, Experimental Astronomy, **44** 1-9 (2017).

[7] "Exploration of a 100 TeV gamma-ray northern sky using the Tibet air-shower array combined with an underground water-Cherenkov muon-detector array", T.K. Sako *et al.*, Astroparticle Physics, **32** , 177-184 (2009).

The Tibet ASγ Collaboration

M. Amenomori[1], S. Asano[2], Y. W. Bao[3], X. J. Bi[4], D. Chen[5], T. L. Chen[6], W. Y. Chen[4], Xu Chen[4,5], Y. Chen[3], Cirennima[6], S. W. Cui[7], Danzengluobu[6], L. K. Ding[4], J. H. Fang[4,8], K. Fang[4], C. F. Feng[9], Zhaoyang Feng[4], Z. Y. Feng[10], Qi Gao[6], A. Gomi[11], Q. B. Gou[4], Y. Q. Guo[4], Y. Y. Guo[4], H. H. He[4], Z. T. He[7], K. Hibino[12], N. Hotta[13], Haibing Hu[6], H. B. Hu[4], K. Y. Hu[4,8], J. Huang[4], H. Y. Jia[10], L. Jiang[4], P. Jiang[5], H. B. Jin[5], K. Kasahara[14], Y. Katayose[11], C. Kato[2], S. Kato[15], T. Kawashima[15], K. Kawata[15], M. Kozai[16], D. Kurashige[11], Labaciren[6], G. M. Le[17], A. F. Li[18,9,4], H. J. Li[6], W. J. Li[4,10], Y. Li[5], Y. H. Lin[4,8], B. Liu[19], C. Liu[4], J. S. Liu[4], L. Y. Liu[5], M. Y. Liu[6], W. Liu[4], X. L. Liu[5], Y.-Q. Lou[20,21,22], H. Lu[4], X. R. Meng[6], Y. Meng[4,8], K. Munakata[2], K. Nagaya[11], Y. Nakamura[15], Y. Nakazawa[23], H. Nanjo[1], C. C. Ning[6], M. Nishizawa[24], M. Ohnishi[15], S. Okukawa[11], S. Ozawa[25], L. Qian[5], X. Qian[5], X. L. Qian[26], X. B. Qu[27], T. Saito[28], Y. Sakakibara[11], M. Sakata[29], T. Sako[15], T. K. Sako[15], J. Shao[4,9], M. Shibata[11], A. Shiomi[23], H. Sugimoto[30], W. Takano[12], M. Takita[15], Y. H. Tan[4], N. Tateyama[12], S. Torii[31], H. Tsuchiya[32], S. Udo[12], H. Wang[4], Y. P. Wang[6], Wangdui[6], H. R. Wu[4], Q. Wu[6], J. L. Xu[5], L. Xue[9], Z. Yang[4], Y. Q. Yao[5], J. Yin[5], Y. Yokoe[15], N. P. Yu[5], A. F. Yuan[6], L. M. Zhai[5], C. P. Zhang[5], H. M. Zhang[4], J. L. Zhang[4], X. Zhang[3], X. Y. Zhang[9], Y. Zhang[4], Yi Zhang[33], Ying Zhang[4], S. P. Zhao[4], Zhaxisangzhu[6] and X. X. Zhou[10]

[1]Department of Physics, Hirosaki University, Hirosaki 036-8561, Japan.
[2]Department of Physics, Shinshu University, Matsumoto 390-8621, Japan.
[3]School of Astronomy and Space Science, Nanjing University, Nanjing 210093, China.
[4]Key Laboratory of Particle Astrophysics, Institute of High Energy Physics, Chinese Academy of Sciences, Beijing 100049, China.
[5]National Astronomical Observatories, Chinese Academy of Sciences, Beijing 100012, China.
[6]Department of Mathematics and Physics, Tibet University, Lhasa 850000, China.
[7]Department of Physics, Hebei Normal University, Shijiazhuang 050016, China.
[8]University of Chinese Academy of Sciences, Beijing 100049, China.
[9]Institute of Frontier and Interdisciplinary Science and Key Laboratory of Particle Physics and Particle Irradiation (MOE), Shandong University, Qingdao 266237, China.
[10]Institute of Modern Physics, SouthWest Jiaotong University, Chengdu 610031, China.
[11]Faculty of Engineering, Yokohama National University, Yokohama 240-8501, Japan.
[12]Faculty of Engineering, Kanagawa University, Yokohama 221-8686, Japan.
[13]Faculty of Education, Utsunomiya University, Utsunomiya 321-8505, Japan.
[14]Faculty of Systems Engineering, Shibaura Institute of Technology, Omiya 330-8570, Japan.
[15]Institute for Cosmic Ray Research, University of Tokyo, Kashiwa 277-8582, Japan.
[16]Institute of Space and Astronautical Science, Japan Aerospace Exploration Agency (ISAS/JAXA), Sagamihara 252-5210, Japan.
[17]National Center for Space Weather, China Meteorological Administration, Beijing 100081, China.
[18]School of Information Science and Engineering, Shandong Agriculture University, Taian 271018, China.
[19]Department of Astronomy, School of Physical Sciences, University of Science and Technology of China, Hefei 230026, China.
[20]Department of Physics and Tsinghua Centre for Astrophysics (THCA), Tsinghua University, Beijing 100084, China.
[21]Tsinghua University-National Astronomical Observatories of China (NAOC) Joint Research Center for Astrophysics, Tsinghua University, Beijing 100084, China.
[22]Department of Astronomy, Tsinghua University, Beijing 100084, China.
[23]College of Industrial Technology, Nihon University, Narashino 275-8576, Japan.
[24]National Institute of Informatics, Tokyo 101-8430, Japan.
[25]National Institute of Information and Communications Technology, Tokyo 184-8795, Japan.
[26]Department of Mechanical and Electrical Engineering, Shangdong Management University, Jinan 250357, China.
[27]College of Science, China University of Petroleum, Qingdao 266555, China.
[28]Tokyo Metropolitan College of Industrial Technology, Tokyo 116-8523, Japan.
[29]Department of Physics, Konan University, Kobe 658-8501, Japan.
[30]Shonan Institute of Technology, Fujisawa 251-8511, Japan.
[31]Research Institute for Science and Engineering, Waseda University, Tokyo 162-0044, Japan.
[32]Japan Atomic Energy Agency, Tokai-mura 319-1195, Japan.
[33]Key Laboratory of Dark Matter and Space Astronomy, Purple Mountain Observatory, Chinese Academy of Sciences, Nanjing 210034, China.

(The Tibet ASγ Collaboration as of 2021)

ALPACA Project

[Spokesperson: M. Takita]
ICRR, The Univ. of Tokyo, Kashiwa, Chiba 277-8582

Cosmic rays are supposed to be accelerated up to the knee energy (PeV) region at supernova remnants (SNRs), star formation regions and PWNe in our galaxy. Therefore, we naturally expect gamma rays at 100 TeV energies, which originate in π^0 decays produced by the accelerated cosmic rays interacting with matter surrounding the acceleration sites. The gamma-ray emission of electron origin might be highly suppressed above 10 TeV due to rapid decrease of inverse-Compton cross section by the Klein-Nishina effect as well as synchrotron radiation energy loss in the strong magnetic field around the acceleration sites. The detection and spectral measurement of gamma rays in the 100 TeV region from their celestial sources, together with multi-wavelength (radio, X-ray, gamma-ray) observations, will be an important experiment enabling us to discriminate between the two processes (cosmic-ray/electron origins), to locate the acceleration site (PeVatron which accelerate cosmic rays up to PeV energies) of cosmic rays and to verify the standard acceleration model of cosmic rays. Furthermore, diffuse gamma rays from the Fermi bubbles recently reported by the Fermi-LAT group and sub-PeV neutrino events[1] detected by IceCube suggests that the Fermi bubbles be a PeVatron candidate. Similarly, the energy spectrum of diffuse gamma rays from the extended region around the galactic center marginally measured by HESS up to approximately 10 TeV also strongly indicates existence of PeVatron[2], from which we expect to detect gamma rays at 100 TeV energies. In 2021, the Tibet ASγ experiment succeeded in the first detection of sub-PeV diffuse gamma rays from the glactic disk. The natural interpretation is that the sub-PeV gamma rays are of cosmic ray origin. Therefore, this is the first experimental evidence that PeVatrons exist in our galaxy. However, there has been no agreed-upon PeVatron in the northern sky so far. Thus, a wide field-of-view gamma-ray imaging at 100 TeV energies in the southern sky, where the HESS sources[3], the Fermi bubbles and the galactic center are located within field of view, will be a key experiment.

5. Experiment

The ALPACA[4],[5] (Andes Large area PArticle detector for Cosmic ray physics and Astrophysics) is a cosmic-ray experiment with a large surface air shower array with a large underground muon detector array The experimental site (approximately 500 m$\times$500 m $\sim$250,000 m^2 in total area) is located on a flat high land called Chacaltaya Plateau (4,740 m above sea level, 16°23' S, 68°08' W), as shown in Fig. 1,

Fig. 1. From Ref.[4]. Experimental site for the ALPACA experiment, Chacaltaya Plateau ia (4,740 m above see level, 16°23' S, 68°08' W), near Mount Chacaltaya, in Bolivia.

around Mount Chacaltaya, near La Paz, Bolivia. In some part in this area, our detectors will be constructed.

We plan to set up a 3,600 m^2 underground (approximately one to a few meters) muon detector array (MD) and an 83,000 m^2 air shower array (AS). MD of water Cherenkov type is composed of eight pools with each pool (approximately 1 m deep) containing twelve 56 m^2 unit detectors. AS is made up of 401 1 m^2 plastic scintillation counters at 15 m spacing.

The AS field of view is roughly 2 steradian. The expected angular resolution of AS is approximately 1 degree at 5 TeV and 0.2 degrees around 100 TeV for gamma rays. For 100 TeV gamma rays, the AS energy resolution is estimated to be $\sim$20-25 %. The hadron rejection power of MD is more than 99.9 % at 100 TeV, while keeping most of gamma-ray events. Long-term detector stability, angular resolution, pointing accuracy and energy scale can be calibrated by the cosmic-ray shadow in the Moon as well as by some of the bright stable TeV gamma ray sources in the southern sky.

6. Covered Physics

Our reserch target is divided into four in ALPACA:

1. Measurement of high-energy (5 TeV – 1 PeV) cosmic gamma rays.

2. Measurement of cosmic ray energy spectra around the Knee energy region (100 TeV – 100 PeV).

3. Measurement of cosmic ray anisotropy $>$ 5 TeV at sidereal time frame.

4. Measurement of the Sun shadow in cosmic rays $>$ 5 TeV.

We aim at low-background detection of celestial gamma rays in the 100 TeV region with the world-best sensitivity (an order of magnitude better than any previous/existing experiments) and at locating the origins of cosmic rays accelerated up to the knee energy region in the southern sky. Presuming a

Crab-like gamma-ray source extending up with power-law index -2.6 located in the southern sky, the ALPACA experiment is sensitive to the source with ∼15 % Crab intensity during one calendar year, as is demonstrated in Fig. 2.

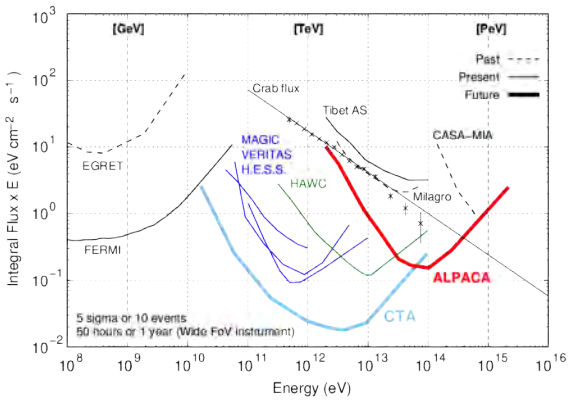

Fig. 2. Sensitivity of ALPACA to high-energy gamma-ray point source. Experimental data points are from HEGRA. The ALPACA sensitivity is evaluated from Ref.[6].

The AS + MD in the southern hemisphere will be a unique/complementary experiment to on-going experiments (FERMI, CALET, DAMPE, HESS, VERITAS, MAGIC, Tibet ASγ, HAWC, LHAASO) and future projects (CTA, SWGO) in this field, which are either located in the northern hemisphere or aiming at gamma-ray astronomy below 10 TeV region, or having narrow field-of-view, or not expected to start operation in the near future (within 5 to 10 years). Thus, the new energy window in the 100 TeV region observing gamma rays with wide field-of-view will be opened first in the southern sky by the ALPACA experiment. We expect to detect established more than a dozen of sources, i.e., young SNRs (SN1006, RX J1713.7-3946, RX J0852.0-4622), Pulsar Wind Nebulae, the galactic center, etc) in the 100 TeV region, some of which may be cosmic-ray PeVatron candidates. Furthermore, our wide field-of-view sensitivity to diffuse gamma rays allows us to study extremely diffuse gamma-ray sources which are difficult to detect by IACTs. The diffuse gamma rays from the Fermi bubbles recently reported by the Fermi-LAT group may be clearly detected, if they extend up to the 100 TeV region. Similarly, detection of diffuse gamma rays above 100 TeV from extended region from the galactic center is promising, where the gamma-ray energy spectrum strongly suggests existence of PeVatron. The sub-PeV diffuse gamma rays along the galactic disk in the southern sky are an interesting target to understand the PeV cosmic-ray propagation in our galaxy. Detection and spectral measurement of gamma rays in the 100 TeV region from these celestial sources, together with multi-wavelength (radio, X-ray, gamma-ray) observations, are key points enabling us to discriminate between the two processes (cosmic-ray/electron origins), to locate the acceleration site of cosmic rays and to examine the standard acceleration and propagation model of cosmic rays. In astronomical point of view, we will open the ultra-high-energy (above 100 TeV) window in gamma-ray astronomy in the southern sky. Besides, gamma-ray emission from near-by extragalactic sources, e.g. M87, Cen A, gamma rays of dark matter origin, those from the Sun disk recently obseved by Fermi[9] may be interesting subjects.

We also aim at measuring energy spectra of proton, helium and iron components separately around the knee energy region with the new AS + MD. The standard cosmic-ray acceleration model at SNR predicts the knee energy of each nucleus component being proportional to Z (atomic number). We can discriminate proton and iron components by MD, as an iron nucleus produces approximately 2 times more muons than a proton with the same energy. Thus, the cosmic-ray acceleration scenario (SNR shock acceleration) will be verified by observing the linearly Z(atomic number)-dependent knee(=bent) positions of proton, helium, iron components around the knee energy region.

Precise cosmic-ray anisotropy measurement at sidereal time frame in the TeV energy region in the southern sky provides unique data for the community to understand the magnetic field structure in the heliosphere. The ALPACA experiment gives complementary data in the TeV region to those from IceCube above a few tens of TeV.

Furthermore, measurement of the Sun shadow in cosmic rays above the TeV energy region in the southern hemisphere also helps understand the modeling of the magnetic fields between the Sun and the Earth, complementary to the observations in the northern hemisphere.

7. ALPAQUITA

As a proto-type experiment, the ALPAQUITA[7] air shower array which is ∼25 % of the ALPACA air shower array in area is being constructed at the experimental site, Chacaltaya Plateau. The containers including materials and equipments necessary to construct the ALPAQUITA air shower array arrived at La Paz, Bolivia in early 2019. The main infrastructures including electricity, experimental hut, fence, cable guide drains are ready in 2021. Due to COVID19 problems, the construction of ALPAQUITA air shower array in the central part of ALPACA, as shown in a black octagon in Fig. 3 was delayed, but was completed in 2022, as is seen in Fig. 4. We will expand the ALPAQUITA air shower array, as shown in a red octagon in Fig. 3, under which we will add a ∼900-m^2 muon detector array in 2023.

The ALPAQUITA sensitivity to gamma rays from a point source is estimated by a Monte Carlo simulation[7], as is shown in Fig. 5. Even with the ALPAQUI TA air shower array with a 900 m^2 MD, we expect to detect several bright 100 TeV gamma-ray sources.

We estimate the dependence of the gamma-ray detection efficiency on hadronic interaction models[8], assuming the ALPAQUITA air shower array with a 900 m^2 underground muon detector array. Traditionally, in the case of gamma-ray detection efficiency, such dependence has been neglected as it may be very small. We estimate the dependence quantitatively for the first time. As is demonstrated in Fig. 6, we evaluate the model dependence on hadronic interactions as less than 3.6in the typical gamma-ray flux estimation performed by ALPAQUITA, where the 3.6 % is dominated by

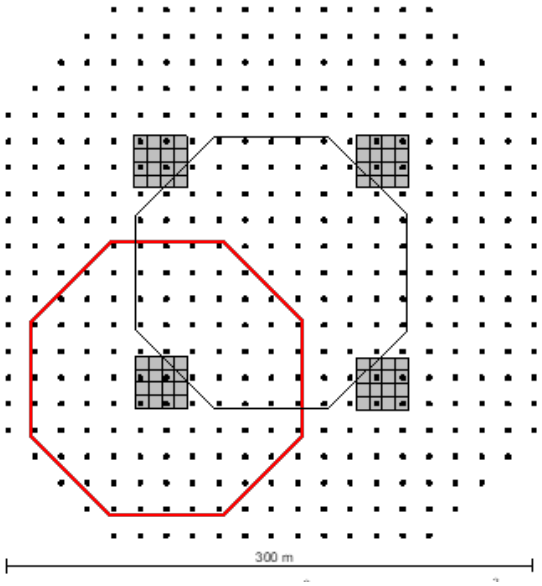

Fig. 3. ALPAQUITA air shower array configuration.

Fig. 4. Completed ALPAQUITA air shower array in 2022.

Monte Carlo statistics. Anyway,this is negligible compared with other uncertainties such as energy scale uncertainty in the energy range from 6 to 300 TeV.

8. ALPACA

The budget which affords to construct ALPACA was funded in 2022. We will set up ALPACA, a 3,600 m^2 underground muon detector array (MD) and an 83,000 m^2 air shower array (AS), shown in Fig. 7. MD of water Cherenkov type is composed of four pools with each pool containing sixteen 56 m^2 unit detectors. AS is made up of 401 1 m^2 plastic scintillation counters at 15 m spacing.

We will finish construction of ALPACA in 2024.

Bibliography

Papers and references

[1] C. Lunardini et al., PRD, **92**, 021301-1-5 (2015).

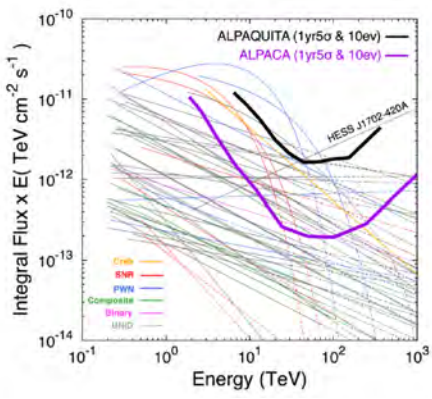

Fig. 5. From [7]. Sensitivity of the ALPAQUITA air shower array with a 900 m^2 MD (black curve) to point-like gamma-ray sources. The measured energy spectra of the H.E.S.S. sources are represented by solid curves, while the dashed curves represent the extrapolations of the measured spectra.

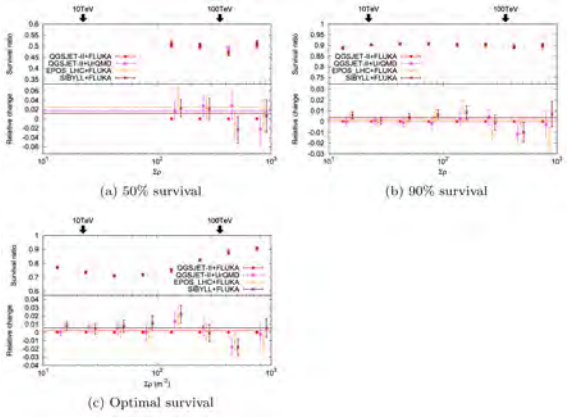

Fig. 6. From [8]. Expected survival ratio of gamma-ray events after applying the $\Sigma N\mu$ selection criterion (see the black lines shown in Fig. 5 in Ref.[8]) and R (the survival ratio relative to the QGSJET-II + FLUKA model) as a function of $\Sigma\rho$, assuming (a) the 50 %survival line, (b) the 90 %survival line, and (c) the optimal survival line in Fig. 5 in Ref.[8] in ALPAQUITA. All symbols are the same as those used in the Fig. 1 in Ref.[8]. Each horizontal straight line results from fitting the R to a constant value for each model (QGSJET-II + UrQMD, EPOS LHC + FLUKA, and SIBYLL + FLUKA). The arrows over the upper horizontal axis show the corresponding gamma-ray energies, 10TeV and 100TeV.

[2] A. Abramoswski et al., Nature, **531**, 476 (2016).

[3] H. Abdalla et al., A&A **612**, A1 (2018).

[4] M. Takita for the ALPACA Collaboration, THE EUROPEAN PHYSICAL JOURNAL, **145**, 01002-1-3, (2017).

[5] F. Aceves de la Cruz et al. (The ALPACA Collaboration), Proc. of ICRC2021, POS(ICRC2021)733, Online, July 12-23, (2021).

[6] T. K. Sako et al., Astroparticle Physics, **32**, 177 (2009).

[7] S. Kato et al (The ALPACA Collaboration), Experimental Astronomy, **52**, 85-107 (2021).

[8] S. Okukawa et al (The ALPACA Collaboration), Experimental Astronomy, **55**, 325-342 (2023).

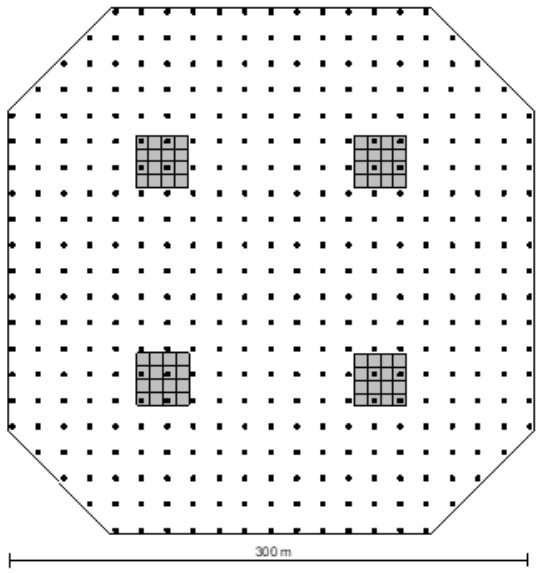

Fig. 7. Schematic view of the ALPACA experiment. The small black squares indicate 401 1 m^2 plastic scintillation detectors at 15 m spacing, forming an air shower array with 83,000 m^2 in area.The black large rectangles indicate four underground muon detector pools, each of which contains sixteen 56 m^2 muon detector units. The total area of the underground muon detector array is 3,600 m^2.

[9] C. Y. Kenny et al., arXiv:1508.06276v1.

The ALPACA Collaboration, as of 2022

M. Anzorena[10], S. Asano[2], C. A. H. Condori[3], E. de la Fuente[1,4], J. L. Garcia-Luna[1], A. Gomi[5], K. Hibino[6], N. Hotta[7], A. Jimenez-Meza[8], Y. Katayose[9], C. Kato[2], S. Kato[10], T. Kawashima[10], K. Kawata[10], T. Koi[11], H. Kojima[12], D. Kurashige[5], J. Lozoya[13], R. Mayta[14,15], P. Miranda[3], K. Munakata[2], K. Nagaya[5], Y. Nakamura[10], Y. Nakazawa[16], C. Nina[3], M. Nishizawa[17], S. Ogio[10], M. Ohnishi[10], S. Okukawa[5], A. Oshima[11], M. Raljevich[3], H. Rivera[3], T. Saito[18], Y. Sakakibara[5], T. Sako[10], T. K. Sako[10], S. Shibata[12], A. Shiomi[16], M. Subieta[3], N. Tajima[19], W. Takano[6], M. Takita[10], Y. Tameda[20], K. Tanaka[21], R. Ticona[3], I. Toledano-Juarez[22,23], H. Tsuchiya[24], Y. Tsunesada[14,15], S. Udo[6], K. Yamazaki[11] and Y. Yokoe[10]

[1]Departamento de Física, CUCEI, Universidad de Guadalajara, Guadalajara, Jalisc o, Mexico.
[2]Department of Physics, Shinshu University, Matsumoto, Nagano 390-8621, Japan.
[3]Instituto de Investigaciones Físicas, Universidad Mayor de San Andrés, La Paz 8635, Bolivia.
[4]Doctorado en Tecnologías de la Información, CUCEA, Universidad de Guadalaj ara, Zapopan, Jalisco, Mexico.
[5]Graduate School of Engineering Science, Yokohama National University, Yokohama, Ka nagawa 240-8501, Japan.
[6]Faculty of Engineering, Kanagawa University, Yokohama, Kanagawa 221-8686, Japan.
[7]Utsunomiya University, Utsunomiya, Tochigi 321-8505, Japan.
[8]Departamento de Tecnologíias de la Información, CUCEA, Universidad de Guad alajara, Zapopan, Jalisco, Mexico.
[9]Faculty of Engineering, Yokohama National University, Yokohama, Kanagawa 240-8501, Japan.
[10]Institute for Cosmic Ray Research, University of Tokyo, Kashiwa, Chiba 277-8582 , Japan.
[11]College of Engineering, Chubu University, Kasugai, Aichi 487-8501, Japan.
[12]Chubu Innovative Astronomical Observatory, Chubu University, Kasugai, Aichi 487 -8501, Japan.
[13]Departamento de Ciencias de la Información y Desarrollo Tecnológico, Cu tonala, Universidad de Guadalajara, Tonalá, Jalisco, Mexico.
[14]Graduate School of Science, Osaka City University, Osaka, Osaka 558-8585, Japan .
[15]Nambu Yoichiro Institute for Theoretical and Experimental Physics, Osaka City U niversity, Osaka, Osaka 558-8585, Japan.
[16]College of Industrial Technology, Nihon University, Narashino, Chiba 275-8576, Japan.
[17]National Institute of Informatics, Chiyoda, Tokyo 101-8430, Japan.
[18]Tokyo Metropolitan College of Industrial Technology, Arakawa, Tokyo 116-8523, J apan.
[19]RIKEN, Wako, Saitama 351-0198, Japan.
[20]Faculty of Engineering, Osaka Electro-Communication University, Neyagawa, Osaka 572-8530, Japan.
[21]Graduate School of Information Sciences, Hiroshima City University, Hiroshima, Hiroshima 731-3194, Japan.
[22]Doctorado en Ciencias Físicas, CUCEI, Universidad de Guadalajara, Guadalaja ra, Jalisco, Mexico.
[23]Maestría en Ciencia de Datos, Departamento de Métodos Cuantitativos, CU CEA, Universidad de Guadalajara, Zapopan, Jalisco, Mexico.
[24]Japan Atomic Energy Agency, Tokai-mura, Ibaraki 319-1195, Japan.

High Energy Astrophysics Group

[Spokesperson: K. Asano]

ICRR, The Univ. of Tokyo, Kashiwa, Chiba 277-8582

Overview

The high energy astrophysics group has been making theoretical studies of violent astrophysical phenomena, in which nonthermal cosmic-ray particles are being accelerated. Targets of the group's study include high energy astrophysical objects such as supernova remnants/explosions, pulsars, pulsar wind nebulae, black hole/neutron star mergers, jets from active galactic nuclei (AGNs), and gamma-ray bursts (GRBs). We especially study the formation of relativistic outflows, particle acceleration in jets, emission mechanisms of electromagnetic waves or neutrinos, and electromagnetic counterparts for compact binary mergers. Our research carries the multi-messenger astronomy forward, which probes astronomical phenomena through collaborating observations of elec-

tromagnetic waves, cosmic rays, neutrinos, and gravitational waves. Gravitational-wave astronomy is also our target. We have been probing the formation history of massive stars from the early universe to the present time with the observation results by gravitational-wave detectors.

Research Topic 1: Origin of Cosmic Ray Electrons in Clusters of Galaxies

One of the most promising mechanisms for producing radio halos (RHs) in galaxy clusters is the reacceleration of cosmic-ray electrons by turbulence. However, the origin of the seed electrons for reacceleration is still poorly constrained. In the secondary scenario, most of the seed electrons are injected via collision of proton cosmic-rays, while nonthermal electrons are directly injected in the primary scenario.

We examine the two scenarios for seed electrons with the observed statistical properties of RHs by combining two methods: by following the temporal evolutions of the electron energy and the radial distributions in a cluster, as well as the merger history of clusters. We find that the RH lifetime largely depends on the seed origin, as it could be longer than the cosmological timescale in the secondary scenario. We study the condition for the onset of RHs with the observed RH fraction and the RH lifetime we obtained and find that long-lived RHs in the secondary scenario should originate from major mergers with a mass ratio of ~ 0.1, while the short lifetime in the primary scenario requires more frequent onsets from minor mergers with a mass ratio of ~ 0.01. Our simple model of the turbulence acceleration can reproduce the observed radio luminosity–mass relation. The RH luminosity functions we obtained suggest that the expected RH number count with the ASKAP survey will detect $\sim 10^3$ RHs in both scenarios.

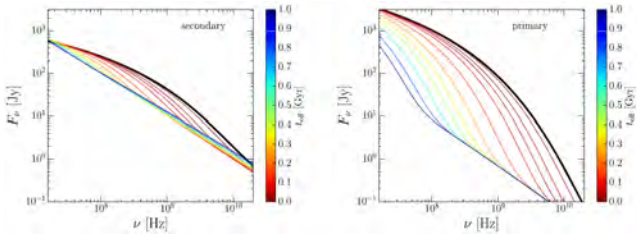

Fig. 1. Time evolutions of the synchrotron flux of a Coma-like RH at the cooling phase in the secondary (left) and primary (right) scenarios. The elapsed time (distinguished with different colors) is measured from the peak time, which corresponds to the time when the reacceleration ends. The thick black line shows the spectrum at the peak time.

Research Topic 2: Emission Mechanism of Gamma-Ray Bursts

The typical spectrum of the prompt emission of gamma-ray bursts (GRBs) indicates that the electron cooling is suppressed in spite of the strong magnetic field in the standard synchrotron model. Recent particle-in-cell simulations show that the particle acceleration by magnetic reconnection in a magnetically dominated plasma can lead to small pitch angles, especially in a low-energy region. Such a small pitch angle prevents electrons from cooling via synchrotron radiation.

Taking into account the effects of synchrotron cooling and adiabatic cooling, we numerically calculate the synchrotron spectra with anisotropic electron distributions. If we require a Poynting flux larger than 10^{50} erg s^{-1} as the model is motivated by magnetic reconnection, the bulk Lorentz factor of ~ 1000 and the electron minimum Lorentz factor of $\sim 10^4$ are required to reproduce the typical GRB spectrum.

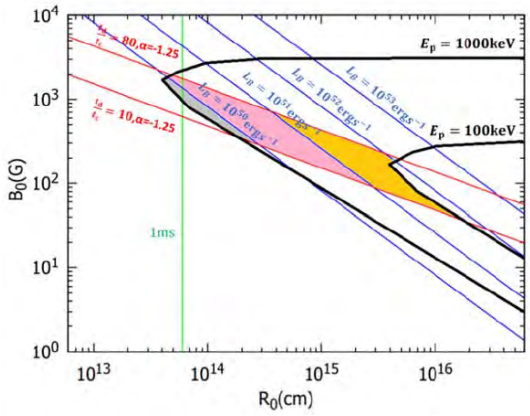

Fig. 2. The allowed parameter regions for the bulk Lorentz factor $\Gamma = 1000$ and the electron minimum Lorentz factor $\gamma_{\rm min} = 10^4$ are shown. The two red lines enclose the region for the photon spectral index $\alpha > -1.25$ and the two black lines enclose the region for the spectral peak energy 100 keV$< E_{\rm p} <$ 1 MeV. In the allowed regions, 10^{50} erg s$^{-1} < L_B < 10^{51}$ erg s^{-1}, and 10^{51} erg s$^{-1} < L_B < 10^{52}$ erg s^{-1} are shown by magenta, and orange areas, respectively. The region for $L_B < 10^{50}$ erg s^{-1} is shown by gray areas. The green vertical line at a radius $R_0 = 6 \times 10^{13}$ cm corresponds to a variability timescale $\delta t = R_0/(2c\Gamma^2) = 1$ ms.

Research Topic 3: Theoretical Interpretation of the Sgr A* Images Observed by EHT

The Event Horizon Telescope (EHT) has been observed the radio images of the region in the vicinity of the nearby supermassive black holes. We analyzed the EHT 2017 observation data of Sagittarius A* (Sgr A*), which is a black hole candidate in the Galactic center, and obtained the ring-like images.

In order to interpret the observed images, we have carried out general relativistic magnetohydrodynamic (GRMHD) simulations and the subsequent general relativistic radiative transfer (GRRT) calculations by post-processing the GRMHD simulation data. By comparing the time-dependent theoretical images and spectral energy distributions (SEDs) with the observed data, it was found that the observed images are consistent with the expected appearance of a Kerr black hole with mass $\sim 4 \times 10^6 M_\odot$, where $M_\odot$ is the solar mass. The viewing angle $i > 50^\circ$ is disfavored, where i is the angle between the rotation axis of the black hole and the line of sight. It was also found that accretion flows with stronger magnetic field (so called Magnetically Arrested Disks, i.e., MADs) are preferred to explain the observed ring-like images at 230 GHz (i.e., EHT photon frequency band) and the image sized at lower frequency band (86 GHz) and so on.

It should be emphasized that the MADs cannot explain the time variability of the observed light curve of Sgr A* by EHT. In order to fully explain the EHT observation data of Sgr A*, we may have to consider some physical processes which were missed in this collaboration paper, e.g., viscosity, thermal conduction, and so on. More sophisticated models of the nonthermal electrons, i.e., cosmic-ray electrons, may be also required.

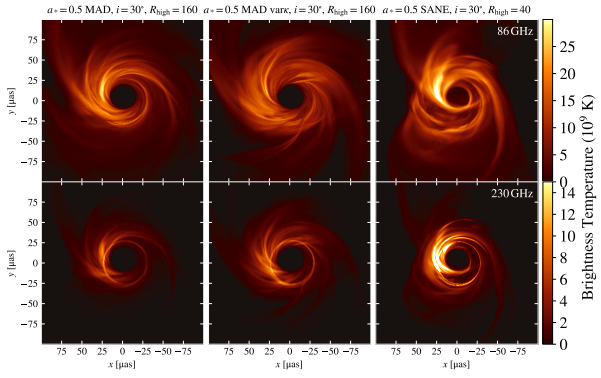

Fig. 3. Examples of the theoretical Sgr A* images obtained by GRRT computations by post-processing GRMHD simulations. The top and bottom panels display the images at the observing photon frequency 86 GHz and 230 GHz (EHT), respectively. The left, middle, and right panels represent the images of MAD with thermal electron model, MAD with thermal and nonthermal electron models based on κ-distribution, and SANE (Standard And Normal Evolution, i.e., weakly magnetized accretion flow model) with thermal electron model, respectively. The MADs are preferred to explain the thickness of the EHT ring images and also the emission region size at 86 GHz.

The non-Kerr black holes (e.g., Johannsen–Psaltis metric and solution from Einstein–Maxwell-dilaton-axion theories) and compact objects with their surface (i.e., objects without event horizons, e.g., boson stars) are also examined. It is found that the compact objects with thermal surfaces and the black holes whose metric remarkably differs form the Kerr, can be ruled out.

Research Topic 4: Magnetar Bursts and Fast Radio Bursts

Fast Radio Bursts (FRBs) are bright radio transients whose duration is about a few milliseconds. Their high brightness temperature implies that the radio wave is emitted by a coherent radiation process although the concrete emission mechanism and the origin are still unclear. Most FRBs have extragalactic origin except one FRB, FRB 20200428A. FRB 20200428A is emitted from a Galactic magnetar, SGR1935+2154, and is associated with hard bursts in X-ray band. This event implies that other FRBs are also produced in magnetars and they may be associated with hard X-ray short bursts. One of the models that explain the hard X-ray short bust and the FRB from the magnetar is an expanding fireball model.

We analytically study this expanding fireball model and apply it to the hard X-ray short burst and FRB 20200428A. A fireball of radiation plasma created near the surface of a neutron star (NS) expands under its own pressure along magnetic field lines, and produces photon emission and relativistic matter outflow. The photon emission produces the observed hard X-ray short burst, and the relativistic matter outflow may trigger the observed FRB. We comprehensively classify the expanding fireball evolution into five cases and obtain the photospheric luminosity and the kinetic energy of the outflow (Figure 4), taking into account key processes; lateral diffusion of photons escaping from a magnetic flux tube, effects of strong magnetic field, baryon loading from the NS surface, and radiative acceleration via cyclotron resonant scattering, some of which have not been considered in the context of gamma-ray bursts. Applying our model to magnetar bursts with FRBs, in particular the X-ray short bursts from SGR 1935+2154 associated with the Galactic FRB 20200428A, we show that the burst radiation can accelerate the outflow to high Lorentz factor with sufficient energy to power FRBs.

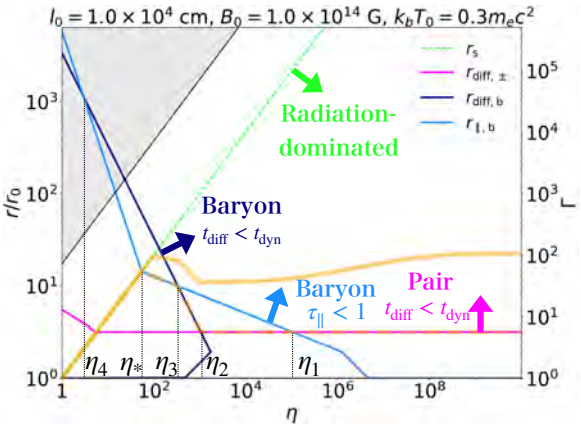

Fig. 4. Classification of the fireball evolution based on the initial dimensionless entropy. The horizontal axis is the initial dimensionless entropy and the vertical axis is the radius normalized by the NS radius (left axis) and the final Lorentz factor of the relativistic outflow (right axis). The minimum of the pink, navy, and light blue lines shows the radius where the X-ray photons escape from the fireball (scale on the left axis). The yellow line shows the terminal Lorentz factor of the relativistic outflow (scale on the right axis).

Research Topic 5: Neutron Star Merger Ejecta and Kilonova Emission

We predicted the kilonova lightcurve models in various setups based on the latest numerical relativity simulations and radiative transfer simulations, and discussed the property of the progenitor employing our kilonova lightcurve models.

We explored the electromagnetic counterparts that will associate with binary neutron star mergers for the case that remnant massive neutron stars survive for > 0.5 s after the merger. For this study, we employed the outflow profiles obtained by long-term general-relativistic neutrino-radiation magnetohydrodynamics simulations with a mean field dynamo effect. We showed that a synchrotron afterglow with high luminosity can be associated with the merger event if the magnetic fields of the remnant neutron stars are significantly amplified by the dynamo effect. We also performed a radiative transfer calculation for kilonovae and find that for the highly amplified

magnetic field cases, the kilonovae can be bright in the early epoch, while it shows the optical emission rapid declining in a few days and the long-lasting (~ 10 d) emission very bright in the near-infrared wavelength. All these features have not been found in GW170817, indicating that the merger remnant neutron star formed in GW170817 might have collapsed to a black hole within several hundreds of ms or magnetic-field amplification might be a minor effect.

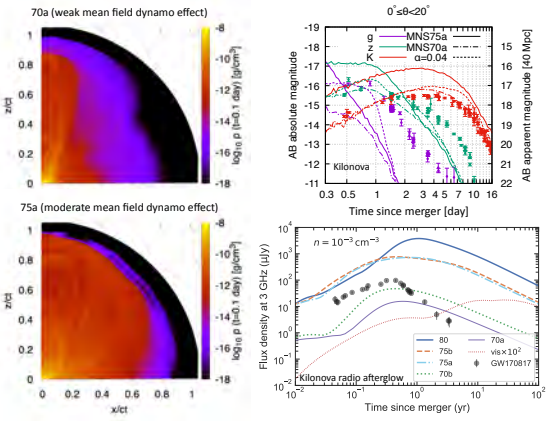

Fig. 5. The left top and bottom panels denote the rest-mass density for the binary neutron star merger in the cases that a mean field dynamo effect is moderately significant and less significant, respectively. The right top panel denotes the kilonova gzK-band lightcurves. The right bottom panel denotes the synchrotron radio emission lightcurves rises due to the interaction between merger ejecta and inter-stellar medium.

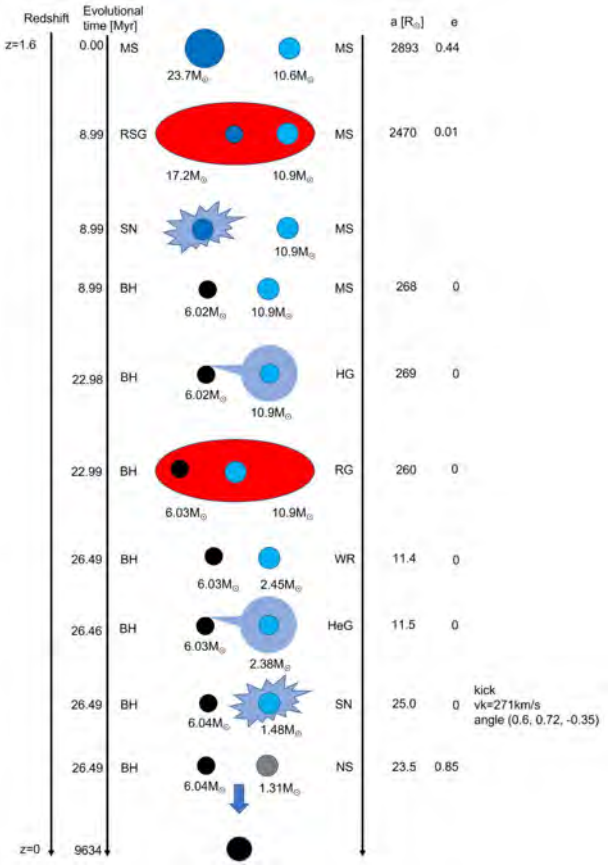

Fig. 6. The formation of a NS-BH with $m_1 = 6.04 M_\odot$ and $m_2 = 1.31 M_\odot$ which looks like GW200115. The pulsar kick velocity is 271 km/s with kick angle $(0.6, 0.72, -0.35)$ where the kick angle. RSG, RG, WR, and HeG mean a red super giant, a red giant, a Wolf-Rayet star, and a Helium giant, respectively.

Research Topic 6: Development of a Higher Order Monte-Carlo based Radiative Hydrodynamics Code

Neutrino radiation plays an important role in the post-merger phase of neutron star mergers. It is crucial to take the energy and angular dependence of neutrino radiation into account for the quantitative prediction of merger outcomes, while solving radiative transfer is for many cases computationally expensive due to its large dimensionality of the phase space dependence. For this purpose, we developed a new relativistic radiation hydrodynamics code based on the Monte-Carlo algorithm. In this work, we developed a new scheme for the first time to achieve the second-order accuracy in time in the limit of a large packet number for solving the interaction between matter and radiation. This higher-order time integration scheme is implemented in the manner to guarantee the energy-momentum conservation to the precision of the geodesic integrator. We demonstrated that our new method reproduces physically appropriate results with reasonable accuracy and that the second-order accuracy in time and space is indeed achieved with our implementation for one-zone and one-dimensional problems.

Research Topic 7: Gravitational Wave Astronomy

Two neutron star (NS)–black hole (BH) binaries, GW200105 and GW200115 found in the LIGO/Virgo O3b run have smaller BH mass of 6–9 $M_\odot$ which is consistent with Population I and II origin. We calculate 10^6 Population I and II binaries with appropriate initial parameters. Our calculation shows consistent binary mass, event rate, and no detection of radio pulsar (PSR) and BH binaries in our galaxy so far. Especially, we found possible progenitors of GW200105 and GW200115 which were formed at redshift $z = 0.15$ and $z = 1.6$ with binary mass of $(34M_\odot, 9.2M_\odot)$ and $(23.7M_\odot, 10.6M_\odot)$, respectively. The final masses of these binaries are $(6.85M_\odot, 2.14M_\odot)$ and $(6.04M_\odot, 1.31M_\odot)$ which look like $(9.0^{+1.7}_{-1.7}M_\odot, 1.91^{+0.33}_{-0.24}M_\odot)$ of GW200105 and $(5.9^{+2.0}_{-2.5}M_\odot, 1.44^{+0.85}_{-0.29}M_\odot)$ of GW200115, respectively (see Fig. 6). We also estimate that 2.68-19.7 PSR-BH binaries in our galaxy will be observed by SKA. The existence of NS-BHs in our galaxy can be confirmed in future SKA era. Using the GW observation of NS-BH mergers and the radio observation of PSR-BHs in future, we can get more severe constraints on the NS-BH formation process.

We also consider the merger of a binary white dwarf for future gravitational wave detectors. It is generally believed that Type Ia supernovae are thermonuclear explosions of carbon-oxygen white dwarfs (WDs). However, there is currently no consensus regarding the events leading to the explo-

sion. A binary WD (WD-WD) merger is a possible progenitor of Type Ia supernovae. Space-based gravitational wave (GW) detectors with considerable sensitivity in the deci-Hz range such as the DECi-hertz Interferometer Gravitational wave Observatory (DECIGO) can observe WD-WD mergers directly. Therefore, access to the deci-Hz band of GWs would enable multi-messenger observations of Type Ia supernovae to determine their progenitor and explosion mechanism. In this paper, we consider the event rate of WD-WD mergers and minimum detection range to observe one WD-WD merger per year, using a nearby galaxy catalog and the relation between the Ia supernova and host galaxy. Furthermore, we calculate DECIGO's ability to localize WD-WD mergers and to determine the masses of binary mergers. We estimate that the deci-Hz GW observatory can detect GWs with amplitudes $h \sim 10^{-20}[\mathrm{Hz}^{-1/2}]$ at 0.01-0.1 Hz, which is 1000 times higher than the detection limit of DECIGO. Assuming progenitors of Ia supernovae are merging WD-WD ($1M_{\odot} - 0.8M_{\odot}$), DECIGO is expected to detect 6600 WD-WD mergers within $z = 0.08$, and identify the host galaxy of such WD-WD mergers within $z \sim 0.065$ using GW detection alone.

Research Topic 8: Observation of Radio Relics in a Galaxy Cluster

In merging clusters, arc-shaped diffuse radio emission, which exhibits strong polarization up to $\sim 60\%$, has been observed at the cluster periphery. We study a galaxy cluster A3376 using high angular resolution and high sensitivity images taken by the MeerKAT telescope. We detected West and East relics, and radio galaxies, which have been observed in previous studies. The improved images revealed faint, extending radio arcs for relics, and a connection between the East relic and radio galaxies. It is probable that (at least some of) the re-accelerated electrons of the East relic are supplied by the jets of the radio galaxies.

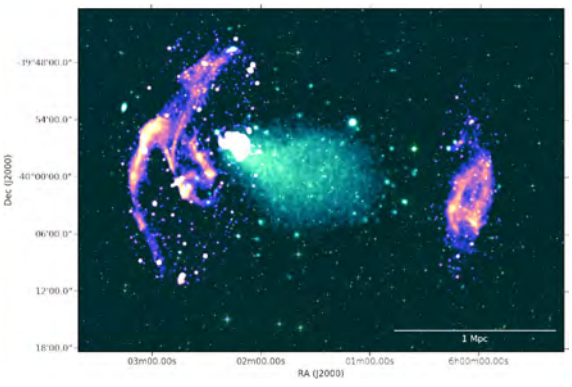

Fig. 7. Composite image of Abell 3376. The full-band, 1283 MHz MeerKAT image is shown in color, while DSS and XMM-Newton (0.3–2.0 keV) images are both shown in cyan. The synthesized beam of the MeerKAT image is $5'' \times 5''$ and the rms noise level is 4.2 μJy beam^{-1}. To illustrate the remarkable features of A3376, the color scale is optimized for radio relics/shocks.

Research Topic 9: CALET Project

We have joined CALET, CALorimetric Electron Telescope, which is a mission for the Japanese Experiment Module-Exposed Facility (JEM-EF) on the International Space Station. The CALET mission aims at revealing unsolved problems in high energy phenomena of the Universe by carrying out accurate measurements of high energy spectra of electrons, gamma-rays and nuclei.

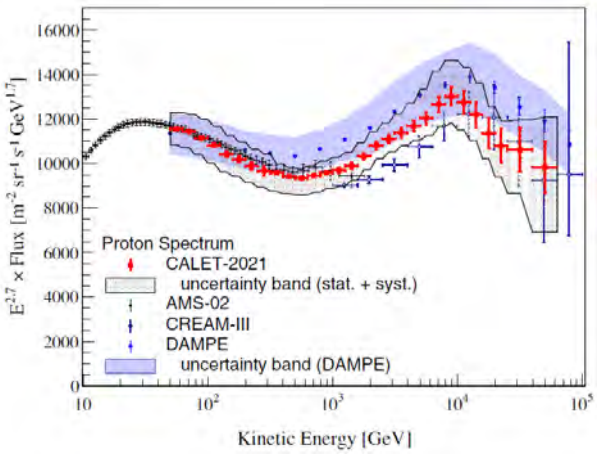

Fig. 8. Proton spectrum measured by CALET (red circles).

Figure 8 shows the cosmic-ray proton spectrum measured with CALET in the energy interval from 50 GeV to 60 TeV. We find a softening of the spectrum above 10 TeV. The analysis is based on the data collected during ~ 6.2 years of smooth operations and covers a broader energy range with respect to the previous proton flux measurement by CALET, with an increase of the available statistics by a factor of ~ 2.2. Above a few hundred GeV we confirm our previous observation of a progressive spectral hardening with a higher significance (more than 20 σ). In the multi-TeV region we observe a second spectral feature with a softening around 10 TeV and a spectral index change from -2.6 to -2.9 consistently, within the errors, with the shape of the spectrum reported by DAMPE.

We also report the measurement of the energy dependence of the boron flux in cosmic rays and its ratio to the carbon flux in an energy interval from 8.4 GeV/n to 3.8 TeV/n. The observed boron flux shows a spectral hardening at the same transition energy $E_0 \sim 200$ GeV/n of the C spectrum, though B and C fluxes have different energy dependences. The B/C flux ratio is compatible with a hardening of 0.09 ± 0.05, though a single power-law energy dependence cannot be ruled out given the current statistical uncertainties. A break in the B/C ratio energy dependence would support the recent AMS-02 observations that secondary cosmic rays exhibit a stronger hardening than primary ones.

Bibliography

Papers in refereed journals

1. Ignacio Botella, Shin Mineshige, Takaaki Kitaki, Ken Ohsuga, Tomohisa Kawashima "Structure of the super-Eddington outflow and its impact on the cosmological scale", Pub. Astron. Soc. J., 74, 384-397 (2022).

2. O. Adriani, Y. Akaike, K. Asano, et al. “Direct Measurement of the Nickel Spectrum in Cosmic Rays in the Energy Range from 8.8 GeV/n to 240 GeV/n with CALET on the International Space Station”, Phys. Rev. Lett., 128, 131103(8pp) (2022).

3. EHT Collaboration “First Sagittarius A Event Horizon Telescope Results. I. The Shadow of the Supermassive Black Hole in the Center of the Milky Way”, Astrophys. J. Lett., 930, L12(21pp) (2022).

4. EHT Collaboration “First Sagittarius A Event Horizon Telescope Results. II. EHT and Multiwavelength Observations, Data Processing, and Calibration”, Astrophys. J. Lett., 930, L13(31pp) (2022).

5. EHT Collaboration “First Sagittarius A Event Horizon Telescope Results. III. Imaging of the Galactic Center Supermassive Black Hole”, Astrophys. J. Lett., 930, L14(64pp) (2022).

6. EHT Collaboration “First Sagittarius A Event Horizon Telescope Results. IV. Variability, Morphology, and Black Hole Mass”, Astrophys. J. Lett., 930, L15(52pp) (2022).

7. EHT Collaboration “First Sagittarius A Event Horizon Telescope Results. V. Testing Astrophysical Models of the Galactic Center Black Hole”, Astrophys. J. Lett., 930, L16(49pp) (2022).

8. EHT Collaboration “First Sagittarius A Event Horizon Telescope Results. VI. Testing the Black Hole Metric”, Astrophys. J. Lett., 930, L17(44pp) (2022).

9. J. Farah, P. Galison, K. Akiyama, et al. “Selective Dynamical Imaging of Interferometric Data”, Astrophys. J. Lett., 930, L18(21pp) (2022).

10. M. Wielgus, N. Marchili, I. Marti-Vidal, et al. “Millimeter Light Curves of Sagittarius A Observed during the 2017 Event Horizon Telescope Campaign”, Astrophys. J. Lett., 930, L19(32pp) (2022).

11. B. Georgiev, D. W. Pesce, A. E. Broderick, et al. “A Universal Power-Law Prescription for Variability from Synthetic Images of Black Hole Accretion Flows”, Astrophys. J. Lett., 930, L20(32pp) (2022).

12. A. E. Broderick, R. Gold, B. Georgiev, et al. “Characterizing and Mitigating Intraday Variability: Reconstructing Source Structure in Accreting Black Holes with mm-VLBI”, Astrophys. J. Lett., 930, L21(30pp) (2022).

13. Yuh Tsunetoe, Shin Mineshige, Tomohisa Kawashima, Ken Ohsuga, Kazunori Akiyama, Hiroyuki R. Takahashi “Investigating the Disk–Jet Structure in M87 through Flux Separation in the Linear and Circular Polarization Images”, Astrophys. J., 931, 25(26pp) (2022).

14. Ryota Hayakawa, Shinya Yamada, Hirotaka Suda, Yuto Ichinohe, Ryota Higurashi, Haruka Sakemi, Mami Machida, Takumi Ohmura, Satoru Katsuda, Hideki Uchiyama, Toshiki Sato, Hiroki Akamatsu, Magnus Axelsson “X-Ray Hot Spots in the Eastern Ear of the Supernova Remnant W 50 and the Microquasar SS 433 System”, Pub. Astron. Soc. J., 74, 510-520 (2022).

15. Ataru Tanikawa, Gen Chiaki, Tomoya Kinugawa, Yudai Suwa, Nozomu Tominaga “Can Population III Stars be Major Origins of both Merging Binary Black Holes and Extremely Metal Poor Stars?”, Pub. Astron. Soc. J., 74, 521-532 (2022).

16. V. A. Acciari, S. Ansoldi, L. A. Antonelli, A. Arbet Engels, M. Artero, K. Asano, et al. “Proton Acceleration in Thermonuclear Novae Explosions Revealed by Gamma Rays”, Nature Astron., 6, 689-697 (2022).

17. C. B. Adams, P. Batista, W. Benbow, et al. “Multiwavelength Observations of the Blazar VER J0521+211 during an Elevated TeV Gamma-Ray State”, Astrophys. J., 932, 129(17pp) (2022).

18. Ryota Goto, Katsuaki Asano “GRB Prompt Emission with Anisotropic Electron Distribution”, Astrophys. J., 933, 18(9pp) (2022).

19. Kyohei Kawaguchi, Sho Fujibayashi, Kenta Hotokezaka, Masaru Shibata, Shinya Wanajo “Electromagnetic Counterparts of Binary-Neutron-Star Mergers Leading to a Strongly Magnetized Long-Lived Remnant Neutron Star”, Astrophys. J., 933, 22(18pp) (2022).

20. O. Adriani, Y. Akaike, K. Asano, et al. “CALET Search for Electromagnetic Counterparts of Gravitational Waves during the LIGO/Virgo O3 Run”, Astrophys. J., 933, 85(16pp) (2022).

21. Smaranika Banerjee, Masaomi Tanaka, Daiji Kato, Gediminas Gaigalas, Kyohei Kawaguchi, Nanae Domoto “Opacity of the Highly Ionized Lanthanides and the Effect on the Early Kilonova”, Astrophys. J., 934, 117(13pp) (2022).

22. S. Issaoun, M. Wielgus, S. Jorstad, et al. “Resolving the Inner Parsec of the Blazar J1924–2914 with the Event Horizon Telescope”, Astrophys. J., 934, 145(21pp) (2022).

23. Kosuke Nishiwaki, Katsuaki Asano “Statistical Properties of Radio Halos in Galaxy Clusters and the Origin of Seed Electrons for Reacceleration”, Astrophys. J., 934, 182(23pp) (2022).

24. O. Adriani, Y. Akaike, K. Asano, et al. “Observation of Spectral Structures in the Flux of Cosmic-Ray Protons from 50 GeV to 60 TeV with the Calorimetric Electron Telescope on the International Space Station”, Phys. Rev. Lett., 129, 101102(8pp) (2022).

25. Tomoya Kinugawa, Takashi Nakamura, Hiroyuki Nakano "Constraints on Population /II Neutron Star-Black Hole Binary Formation by Gravitational Wave and Radio Observations", Mon. Not. Roy. Astro. Soc., 515, L78-L83 (2022).

26. Reetika Dudi, Ananya Adhikari, Bernd Brügmann, Tim Dietrich, Kota Hayashi, Kyohei Kawaguchi, Kenta Kiuchi, Koutarou Kyutoku, Masaru Shibata, Wolfgang Tichy "Investigating GW190425 with Numerical-Relativity Simulations", Phys. Rev. D, 106, 084039(11pp) (2022).

27. Yuh Tsunetoe, Shin Mineshige, Tomohisa Kawashima, Ken Ohsuga, Kazunori Akiyama, Hiroyuki R. Takahashi "Diverse Polarimetric Features of AGN Jets from Various Viewing Angles: Towards a Unified View", Galaxies, 10, 103(11pp) (2022).

28. Tomoya Kinugawa, Hiroki Takeda, Ataru Tanikawa, Hiroya Yamaguchi "Probe for Type Ia Supernova Progenitor in Decihertz Gravitational Wave Astronomy", Astrophys. J., 938, 52(9pp) (2022).

29. Nanae Domoto, Masaomi Tanaka, Daiji Kato, Kyohei Kawaguchi, Kenta Hotokezaka, Shinya Wanajo "Lanthanide Features in Near-Infrared Spectra of Kilonovae", Astrophys. J., 939, 8(18pp) (2022).

30. Motoki Kino, Masaaki Takahashi, Tomohisa Kawashima, Jongho Park, Kazuhiro Hada, Hyunwook Ro, Yuzhu Cui "Implications from the Velocity Profile of the M87 Jet: A Possibility of a Slowly Rotating Black Hole Magnetosphere", Astrophys. J., 939, 83(16pp) (2022).

31. Shogo Yoshioka, Shin Mineshige, Ken Ohsuga, Tomohisa Kawashima, Takaaki Kitaki "Large-Scale Outflow Structure and Radiation Properties of Super-Eddington Flow: Dependence on the Accretion Rates", Pub. Astron. Soc. J., 74, 1378-1395 (2022).

32. O. Adriani, Y. Akaike, K. Asano, et al. "Cosmic-Ray Boron Flux Measured from 8.4 GeV/n to 3.8 TeV/n with the Calorimetric Electron Telescope on the International Space Station", Phys. Rev. Lett., 129, 251103(7pp) (2022).

33. H. Abe, S. Abe, V. A. Acciari, T. Aniello, S. Ansoldi, L. A. Antonelli, A. Arbet Engels, C. Arcaro, M. Artero, K. Asano, et al. "Gamma-Ray Observations of MAXI J1820+070 during the 2018 Outburst", Mon. Not. Roy. Astro. Soc., 517, 4736-4751 (2022).

34. G. Giacinti, T. Abounnasr, A. Neronov, D. Semikoz "Signatures of Anisotropic Diffusion around PeVatrons in 100 TeV Gamma-Ray Data", Phys. Rev. D, 106, 123029(7pp) (2022).

35. Kyohei Kawaguchi, Sho Fujibayashi, Masaru Shibata "Monte Carlo-Based Relativistic Radiation Hydrodynamics Code with a Higher-Order Scheme", Phys. Rev. D, 107, 023026(25pp) (2023).

36. S. Jorstad, M. Wielgus, R. Lico, et al. "The Event Horizon Telescope Image of the Quasar NRAO 530", Astrophys. J., 943, 170(19pp) (2023).

37. James O. Chibueze, Hiroki Akamatsu, Viral Parekh, Haruka Sakemi, Takumi Ohmura, Ruby van Rooyen, Takuya Akahori, Hiroyuki Nakanishi, Mami Machida, Tsutomu T Takeuchi, Oleg Smirnov, Dane Kleiner, Filippo M. Maccagni "MeerKAT's View of Double Radio Relic Galaxy Cluster Abell 3376", Pub. Astron. Soc. J., 75, S97-S107 (2023).

38. Yuta Tashima, Takumi Ohmura, Mami Machida "Pseudo-Observation of Spiral Galaxies in the Radio Band to Verify Depolarization Models", Pub. Astron. Soc. J., 75, S123-S137 (2023).

39. V. A. Acciari, T. Aniello, S. Ansoldi, L. A. Antonelli, A. Arbet Engels, C. Arcaro, M. Artero, K. Asano, et al. "Long-Term Multi-Wavelength Study of 1ES 0647+250", Astron. Astrophys., 670, A49(20pp) (2023).

40. V. A. Acciari, I. Agudo, T. Aniello, S. Ansoldi, L. A. Antonelli, A. Arbet Engels, M. Artero, K. Asano, et al. "A Lower Bound on Intergalactic Magnetic Fields from Time Variability of 1ES 0229+200 from MAGIC and Fermi/LAT Observations", Astron. Astrophys., 670, A145(8pp) (2023).

41. H. Abe, S. Abe, V. A. Acciari, T. Aniello, S. Ansoldi, L. A. Antonelli, A. Arbet Engels, C. Arcaro, M. Artero, K. Asano, et al. "Search for Gamma-Ray Spectral Lines from Dark Matter Annihilation up to 100 TeV toward the Galactic Center with MAGIC", Phys. Rev. Lett., 130, 061002(8pp) (2023).

42. Hyunwook Ro, Kunwoo Yi, Yuzhu Cui, Motoki Kino, Kazuhiro Hada, Tomohisa Kawashima, Yosuke Mizuno, Bong Won Sohn, Fumie Tazaki "Transverse Oscillations of the M87 Jet Revealed by KaVA Observations", Galaxies, 11, 33(13pp) (2023).

43. Tomoki Wada, Kunihito Ioka "Expanding Fireball in Magnetar Bursts and Fast Radio Bursts", Mon. Not. Roy. Astro. Soc., 519, 4094–4109 (2023)

44. H. Abe, S. Abe, V. A. Acciari, I. Agudo, T. Aniello, S. Ansoldi, L. A. Antonelli, A. Arbet Engels, C. Arcaro, M. Artero, K. Asano, et al. "MAGIC Observations Provide Compelling Evidence of Hadronic Multi-TeV Emission from the Putative PeVatron SNR G106.3+2.7", Astron. Astrophys., 671, A12(12pp) (2023).

Other Activities

Ashra NTA

[Spokesperson : M. Sasaki]

Collaboration list:
ICRR, The University of Tokyo, Chiba, Japan: **M. Sasaki, T. Aoki**; Physics Department, Toho University, Chiba, Japan: **S. Ogawa**; Academia Sinica, Taipei, Taiwan: **S. Haino**; Institute for Interdisciplinary Science, Okayama University, Okayama, Japan: **K. Yoshimura**; IPNS, KEK, Ibaraki, Japan: **M. Tanaka**; et al.

VHE Physics and Astronomy

Probing for VHE elementary particles will enable the discovery of VHE celestial objects and the elucidation of their phenomena. VHE neutrinos and photons can also probe super heavy dark matter and dark energy. Neutrino oscillations cause neutrino fluxes to homogenize between generations during propagation. VHE tau neutrinos skim the earth, are converted to tau, and after decaying in air become an upward air shower at a shallow elevation angle, emitting Cherenkov light and fluorescence. Thus, the tau neutrino observation can necessarily be a clear-cut tau appearance experiment. The NTA unit is a unique wide-angle, high-precision optical system with a light-branching trigger imaging system. This detection scheme is particularly powerful for the simultaneous observation of Cherenkov light and fluorescence from VHE tau and photons.

NTA for VHE Tau and Photon probes

NTA will radially observe air-shower light in a vast amount of night-time air on the mountain within more than π sr field of view (FoV) covered with 1 minute square pixels (Fig.9) [1]. Earth-skimming or mountain-hitting tau neutrino is converted to tau in the rock, and tau decays make upward air shower. The upward tau shower signal is very clear and there are almost no background events. Downward coming photon showers are observed in both Cherenkov and fluorescence light. The Cherenkov light coming from a large zenith angle earns a large effective detection area. The lookout layout allows Cherenkov and fluorescence observations over a wide energy range. Fluorescence arriving from behind is advantageous for low-energy tau showers compared to Cherenkovs, which require more distance to achieve a large effective area due to their directional nature. The X_{max} of the fluorescent air shower is about 1 km from the detector, which is sufficient to detect 1-PeV class tau. This is a benefit of the lookout layout of NTA.

The geo-propagation of tau by GEANT and ALLM simulations revealed emergent tau remembers the tau neutrino direction above 1 PeV with much better than 1 minute of accuracy. We also confirmed shower reconstruction with CORSIKA simulation, resulting in the point-back resolution of $0.1^\circ/\sqrt{E_{sh}/PeV}$ where E_{sh} is the shower energy. The emergent tau energy is deformed from the parent tau neutrino energy due to the inelastic nature of the charge current interaction and energy loss in the rock. It still allows for a relatively good energy reconstruction of ν_τ with the energy around 1 PeV. We confirmed energy resolution of nu-tau with ANIS simulation, resulting in 20 or 40 % around 1 PeV depending on the elevation angle.

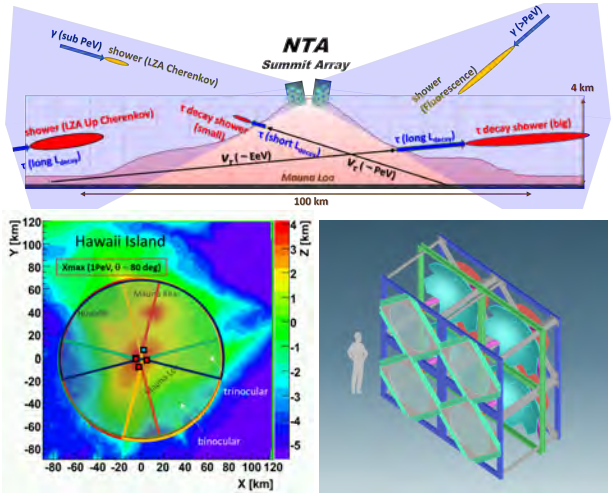

Fig. 9. Schematics of "lookout layout" for imaging tau and photon showers with NTA [1] (*top*). Contour map of the island of Hawaii (*left*) as input for the MC simulation. The radius of the wheel represents the distance to Xmax of the 1PeV shower coming toward NTA at 80° zenith. One of four stations on the mountainside is responsible for 210° azimuth range indicated by four fans. The basic design is a 1.5-fold scaled-up version of the Ashra-1 light collector, and four of these collectors are stacked together to form one NTA detector unit with the same FoV (*right*).

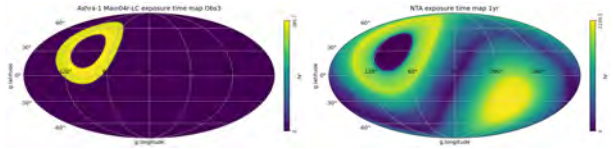

Fig. 10. Ashra-1 exposure time map for Cherenkov taus in Obs03 with one of the light collectors toward Mauna Kea mountain (*left*). NTA annual exposure time map for tau neutrinos (*right*).

Regarding the NTA's view of the southern sky, NTA can always cover the Galactic bulge of the nigh/t sky. The NTA detector unit's FoV center should be aligned with this arc, considering a high multi-eye observation ratio. NTA Galactic bulge monitor with viewing radius of 20° has a good advantage of including 12 % of total mass of the dark matter halo, assuming the Einasto profile. The effective detection area of the surface detector decreases rapidly depending on the cosine of the zenith angle. In the case of a surface detector at 16.4° south latitude and a 45° zenith angle cut, the observation time must be less than 2300 hours per year even if 100 % duty cycle. In the case of the NTA, the galactic center is in the moonless night sky for 980 hours per year, a ratio of only 2.3 to the surface detector above.

NTA proto-project, Ashra-1, was placed in 2008 at the north side (Fig.9 *left*). It allows for binocular and trinocular observation, resulting in a high multi-eye observation rate. The basic design is a 1.5-fold scaled-up version of the Ashra-1 light collector, and four of these collectors are stacked together to form one NTA detector unit with the same FoV

(Fig.9 *right*). The effective pupil diameter is 3 m, providing good light gathering power. It can also facilitate background muon rejection, transport and construction.

Fig.10 compares the NTA annual exposure map to that by one light collector of Ashra-1, which actually searched for mountain-hitting tau from Mauna Loa to Mauna Kea for 14 months (Obs03). The sensitivity of NTA to search for vast neutrino sources can be seen. Notably, NTA is able to search for tau neutrinos in the central region of the Galaxy for more than 400 hours per year, as well as throughout the extragalactic region.

NTA Diffuse Neutrino Sensitivity

Fig.11 shows a comparison of diffuse neutrino sensitivity from various VHE neutrino detectors. NTA has the best sensitivity from a few PeV to 100 PeV. Trinity observes Earth skimming neu-tau as well as NTA but only with Cherenkov light. The sensitivity of its higher energy part is determined by the large zenith angle shower, which is consistent with NTA. The NTA sensitivity at lower energy is superior to that of Trinity due to the tau shower fluorescence observed near the mountain surface as mentioned earlier.

NTA Dark Matter Sensitivity

As shown Fig.12, NTA's powerful wide-angle view of air-shower morphology from tau and photons with high precision shows that it has unparalleled sensitivity to neutrinos and photons from annihilation and decay of super heavy dark matter WIMP particles, especially near the unitarity bound.

Conclusions

Simultaneous wide-field, high-precision observations of Cherenkov and fluorescence showers from both tau and photon probes by NTA are strongly expected to be a key to VHE physics and VHE astronomy using multiple elementary particles.

Bibliography

[1] NTA LOI (look-in layout array), M. Sasaki and G. W.-S. Hou,ArXiv:1408.6244 (2014). NTA look-out layout summit array, M. Sasaki, PoS (ICRC2017) 941. M. Sasaki, ICHEP2022.

[2] J. Álvarez-Muñiz,et al.,Mechanics and Astronomy 63, 219501 (2019).

[3] J. F. Krizmanic,et al.,UHECR2018 (Paris).

[4] C. R. Persichilli,Thesis,Univ. California (2018).

[5] P. Allison,et al.,Phys. Rev. D93, 082003 (2016).

[6] R. A. Batista,et al.,J. Cosmol. Astropart. Phys.,01,002, (2019).

[7] M. Aartsen,et al.,Phys. Rev. D98,062003 (2018).

[8] A. Aab,et al.,arXiv:1708.06592.

[9] P. Gorham,et al.,arXiv:1902.04005.

[10] A. M. Otte,Phys. Rev. D99, 083012 (2019).

[11] M. Sasaki,PoS (ICRC2019) 1003.

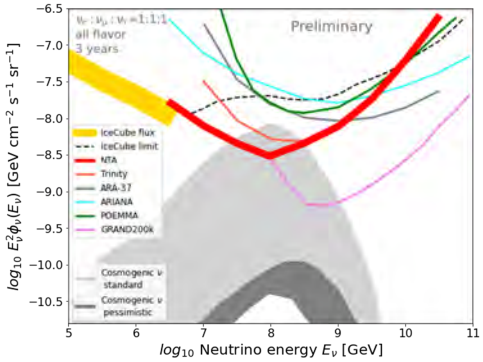

Fig. 11. A comparison of diffuse neutrino sensitivity from various VHE neutrino detectors. NTA has the best sensitivity from a few PeV to 100 PeV [2]-[11].

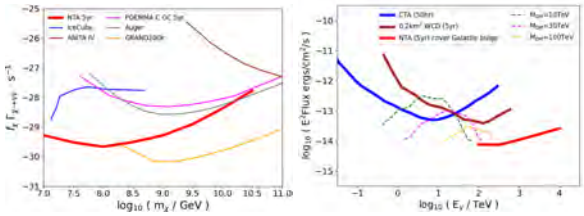

Fig. 12. 5-year sensitivities of NTA to DM decay width ($f_\chi \Gamma_\chi$) for $\nu\bar{\nu}$ channels and those of other experiments. NTA has the highest sensitivity in the 10 PeV to sub-EeV region (*left*). Figure adapted from [12]. Flux sensitivities of NTA for 5 yr, of a possible 2D observatory (0.2 km^2 WCD) for 5 yr and of CTA for 50 hr observation of the Galactic halo. The predicted DM annihilation rates into τ pairs are indicated. Figure is adopted from [13].

[12] C. Guépin, et al., arXiv:2112.04801.

[13] A. Viana, et al., Astro2020 Science White Paper.

γI Group

γI Project

γI Consortium

[Spokesperson : R.Enomoto]

Collaboration list:

ICRR, The University of Tokyo, Chiba, Japan: **R. Enomoto**; National Institute of Technology, Sendai College, Miyagi, Japan: **M. Kagaya**; College of Science, Ibaraki University, Ibaraki, Japan: **H. Katagiri, K. Yoshida**; Faculty of Medical Engineering and Technology, Kitasato University, Kanagawa, Japan: **H. Muraishi, S. Ishikawa, H. Tsukamoto**; IPNS, High Energy Accelerator Research Organization, Ibaraki, Japan: **M. M. Tanaka**; National Cancer Center Hospital East, Chiba, Japan: **D. Kano, T. Watanabe**

Overview

The Compton camera method is as a technique capable of imaging sub-MeV gamma-ray sources. Several types

of Compton cameras have been proposed and developed for applications in gamma-ray astronomy [1][2][3][4][5], environmental radiation imaging [6][7], and medical diagnostics [8][9]. However, most of these developments have primarily focused on achieving high angular resolution, and there has been a paucity of research targeting sensitivity and versatility of these cameras.

The γI group has conducted cutting-edge research on the development of Compton camera technology that excels in both sensitivity and versatility [10]. Our approach involves the use of multiple independent scintillation detectors (Figure 13) to measure the energy deposit information for each coincidence event in two counters. Using this information, we calculated the Compton scattering angle, θ, and back-projected it onto the projection plane as a smeared ring shape with a radius of θ for each event to perform image reconstruction. However, due to the limitations imposed by Compton kinematics, events with scattering angles above a certain threshold (e.g., $\theta > 60$ degrees for 511-keV gamma rays and $\theta > 45$ degrees for 662-keV gamma rays) cannot determine the order of hits based on energy deposit information alone. Consequently, conventional methods have excluded many of these events from image reconstruction (except for gamma rays below 250 keV, for which the hit order is known).

In contrast, we have demonstrated that we can easily achieve gamma-ray imaging with enhanced sharpness, ghost image reduction, and higher sensitivity by adopting the following techniques [11][12][13][14]: (1) Utilizing events with unknown hit orders in image reconstruction (by back-projecting two rings representing true and false rings), (2)Rotating the Compton camera during measurements to increase back-projection ring patterns (Figure 13), and (3) Applying image sharpening techniques based on the filtered back-projection algorithm used in computed tomography (Figure 14).

In this study, we developed a practical portable Compton camera [15] by improving the sensitivity and angular resolution of the system developed in previous research [12]. We also conducted experimental investigations into the possibility of detecting the diffusion of radioactive gases in indoor environments by performing environmental radiation visualization measurements in nuclear medicine facilities [16].

1 Development of a portable high-sensitivity omnidirectional Compton camera with the rotation function [15]

The counters of the detector were constructed using scintillators and photomultiplier tubes (PMTs). In previous studies [12], PMTs (H11432-100) with a length of 12.8 cm were used. In this study, we reduced the size of the six detectors by using metal package type PMTs (H13543-100) with a length of 5 cm, which is less than half of the previous PMTs. The scintillator employed in this study was a 3.5cm CsI(Tl) cube, similar to the one used in previous studies. The six scintillators were arranged such that their coordinates corresponded to the vertices of a regular octahedron with a side length of 10 cm. This value of 10 cm was chosen to achieve an angular resolution of $\sigma \sim 10$ degrees, which is equivalent to 30 cm at a distance of 1.5 m. The arrangement of the PMTs in previous studies was in a vertical orientation; however, in this study, we changed it to a tilted configuration in the horizontal direction. As a result, the height of the detector portion decreased from 43 cm to 23 cm.

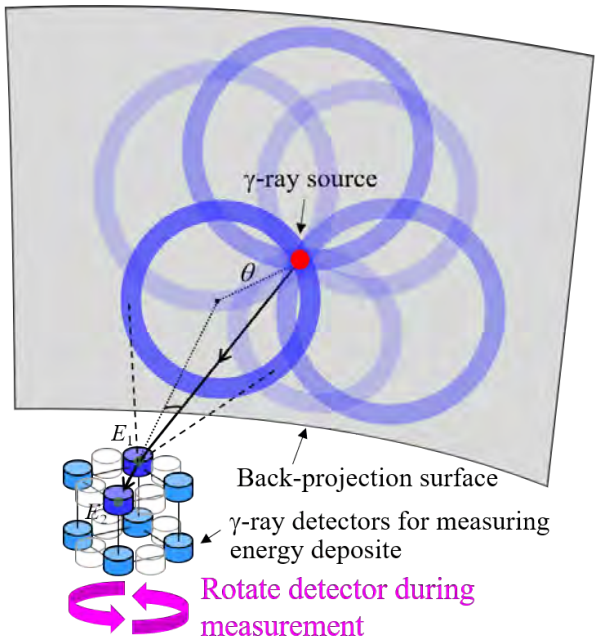

Fig. 13. Schematic diagram of Compton image reconstruction of the data measured while rotating the detector.

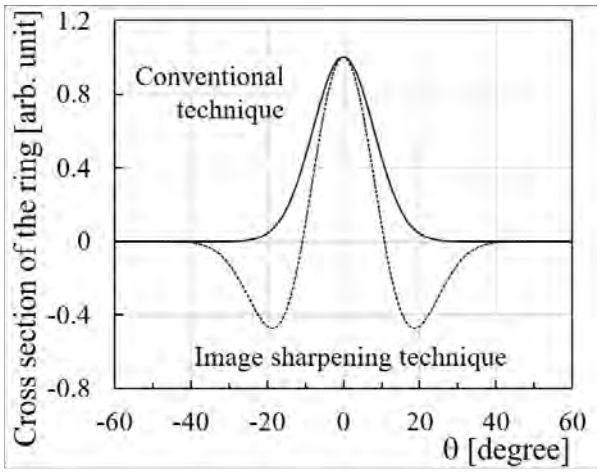

Fig. 14. Cross-section of the smeared ring used in the Compton image reconstruction. The solid and dotted lines represent the cross-sections in the conventional technique (a Gaussian profile) and the image-sharpening technique based on the principle of a filtered back-projection algorithm (a multiple-Gaussian profile), respectively.

In a previous study, each of the six detectors was connected to a separate preamplifier. In this study, we consolidated the six preamplifiers onto a single board. Furthermore, we integrated the power supply, which provides power to the preamplifiers, PMTs, and flash ADC board (40 MHz sampling) equipped with the SiTCP protocol, into a single integrated power source board. This board configuration al-

lowed for the stacking of the ADC board and the power supply board together. Additionally, the utilization of a lithium battery meant there was no longer a need for an AC power outlet. The lithium battery used in this study had a capacity of 50,000 mAh and provided a total current of 1 A, allowing the system to operate for approximately 6.5 hours. Moreover, the installation of Wi-Fi connectivity between the ADC board and the stage controller enabled remote operations from a PC. Furthermore, we reevaluated the storage box design. A sturdy aluminum case was used in the previous study, while an acrylic box with a polycarbonate bottom was employed in this one. As a result, the weight of the system, excluding the stage controller (0.5 kg), decreased from 7.4 kg in the previous study to 5.8 kg (including the stage controller and Wi-Fi-related devices but excluding the lithium battery) in this one. These miniaturization and organization efforts resulted in a reduction in the dimensions of the Compton camera from 72 × 26 × 28 cm to 51 × 21 × 23 cm.

The rotational function in the previous study was a discrete rotation system that rotated by one degree at specified intervals and stopped once it completed a full 360-degree rotation. In this study, we modified the system to operate in a continuous rotation mode, rotating at a constant speed of 350 degrees per minute. Additionally, we implemented a continuous back-and-forth motion where the rotation angle starts from zero degrees, reaches 350 degrees, returns toward zero degrees, and repeats the cycle upon getting there again. Due to the specifications of the stage controller, it is not possible to perform reverse rotation from angles greater than 350 degrees; however, this limitation does not affect the image quality. As a result, there is no longer a need to determine the measurement time considering the rotation beforehand.

2 Measurements in Nuclear Medicine Facilities [16]

We conducted environmental radiation visualization measurements at the Nuclear Medicine Facility of the National Cancer Center Hospital East using the portable rotating Compton camera described in the previous section. Here, we describe the measurements performed in the hot laboratory, where the preparation of radiopharmaceuticals for PET (positron emission tomography) is carried out. The room is equipped with multiple hot cells where synthesis devices for adjusting PET radiopharmaceuticals are installed along the wall, and the area in front of the hot cells serves as the workspace (including a partial cleanroom) (Figure 15). During this study, the installation of a new synthesis device for PET radiopharmaceuticals using ^{11}C was carried out in hot cell 3. As part of the testing process to ensure that no gas containing radioactive isotopes leaks from the synthesis device into the cleanroom and workspace, a test was conducted to transfer gas containing ^{11}C into the synthesis device. In parallel with this test, we conducted environmental radiation visualization measurements using the Compton camera developed in this study to investigate the temporal ambient dose variation and visualize any leakage of gamma radiation from the synthesis device.

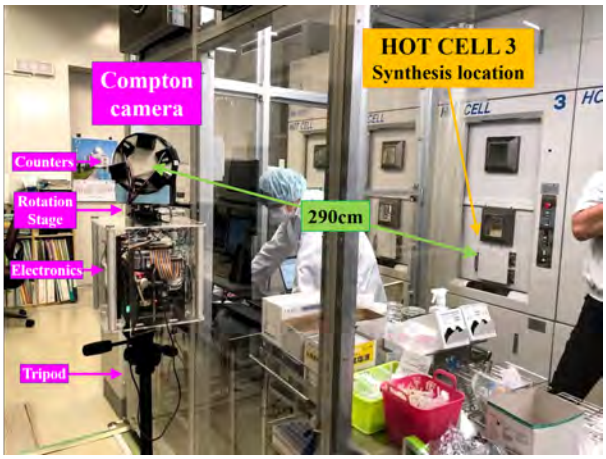

Fig. 15. Measurement in front of a hot cell.

2.1 Before the improvement of the synthesis apparatus

The radioactivity of the ^{11}C used for the synthesis was approximately 2 GBq. The measured ambient dose rate near the detector before the start of synthesis, using a NaI(Tl) survey meter, was 0.07 μSv/h, the background level. From the start of measurement until 300 seconds, the ambient dose rate at the detector position remained constant. However, after the initiation of $^{11}CO_2$ transfer at 300 seconds, the rate started to increase, peaking at around 350 seconds when the transfer was completed; thereafter, it showed a decreasing trend. Figure 16(a) represents the composite omnidirectional image (511 keV gamma rays) obtained using the conventional back-projection method, while Figure 16(b) shows an enlarged view of the image using the image sharpening technique. From these images, a distribution extending upward in the cleanroom was observed, and the gamma-ray sources in the direction of Hot Cell 3 were relatively small. This suggests the possibility of a slight leakage of $^{11}CO_2$ from the synthesis apparatus into the cleanroom. On the other hand, the ambient dose rate near the detector remained sufficiently low, reaching a maximum of approximately 0.26 μSv/h. Additionally, since the measurement target was a gas, variations in the position of the radiation source over time could be considered. However, due to the limited statistics available for short-time analyses, it was not possible to make conclusive interpretations based on the reconstructed images.

2.2 After the improvement of the synthesis apparatus

Following the measurement results obtained before the improvement, a review of the gas containment process was conducted in the synthesis apparatus. After the improvement, similar synthesis experiments were performed, and measurements were carried out with the Compton camera placed in the same location. Figure 17(a) represents the composite image obtained using the conventional back-projection method, while Figure 17(b) shows an enlarged view of the image using the image-sharpening technique. From these results, it can be observed that the distribution appears as point sources mainly in the direction of Hot Cell 3, indicating an improvement in the leakage of $^{11}CO_2$ into the cleanroom, at least.

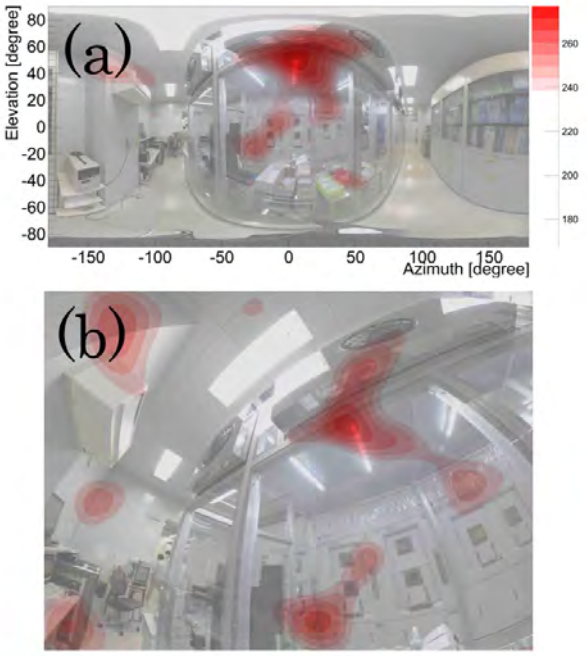

Fig. 16. (a) Composite image of the measurement before upgrading (with conventional back-projection); (b) Enlarged composite image (with the image-sharpening technique, air purifier direction) [16].

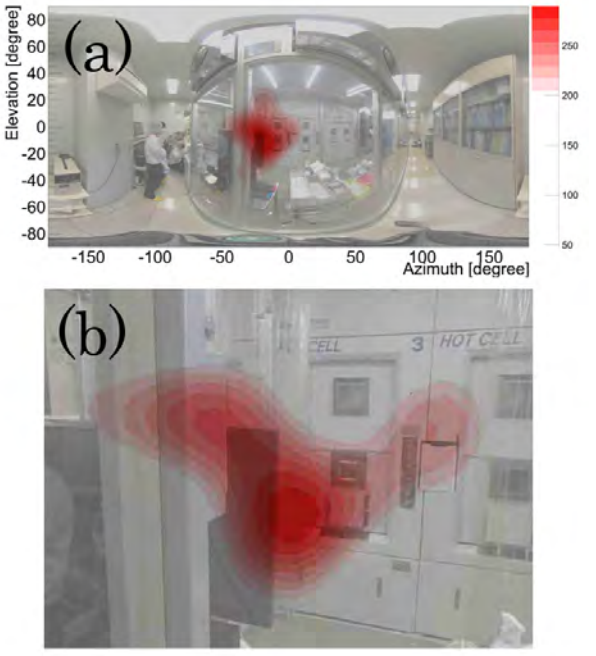

Fig. 17. (a) Composite image of the measurement after upgrading (with conventional back projection); (b) Enlarged composite image (with the image-sharpening technique, compositor orientation) [16].

Therefore, our system has demonstrated the potential to detect not only the visualization of gamma-ray leakage from the Hot Cell but also the diffusion of radioactive gases. In April 2021, Japan's Ministry of Health, Labour and Welfare in Japan revised the Ionizing Radiation Hazards Prevention Regulations, including a significant reduction in the dose limit for the crystalline lens of radiation workers [17]. Recently, there has been a growing concern about occupational exposure to radiation both domestically and internationally. The proposed method is expected to be utilized in the field of health physics and applied physics as an unprecedented environmental radiation visualization device that enables the efficient visualization of low-dose gamma-ray sources in a short period.

Acknowledgments

This study was supported by JSPS KAKENHI Grant Number JP19H04492 and Special Research Grants of the School of Allied Health Sciences, Kitasato University (Nos. 2021-1004, 2022-1003). We would like to thank the open-source consortium of instrumentation (Open-It), Japan, for its support.

Bibliography

[1] A new method to measure energy, direction, and polarization of gamma rays, Kamae T., Enomoto R., and Hanada N., Nucl. Instrum. Methods Phys. Res. A 260, 254-257 (1987)

[2] Instrument description and performance of the imaging gamma-ray telescope COMPTEL aboard the Compton gamma-ray observatory, Schoenfelder V., Aarts H., Bennett K. et al., Astrophy. J. Suppl. 86, 657-692 (1993)

[3] The Si/CdTe semiconductor Compton camera of the ASTRO-H Soft Gamma-ray Detector (SGD), Watanabe S., Tajima H., Fukazawa Y. et al., Nucl. Instrum. Methods Phys. Res. A 765, 192-201 (2014)

[4] Readout Test of Plastic Scintillator with MPPC for the Development of Gamma-Ray Burst Polarimeter, Gunji S., Saito Y., Yonetoku D. et al., JPS Conf. Proc. 24, 011009 (6pp) (2019)

[5] First Observation of the MeV Gamma-Ray Universe with Bijective Imaging Spectroscopy Using the Electron-tracking Compton Telescope on Board SMILE-2+, Takada A., Takemura T., Yoshikawa K. et al., Astrophys. J. 930, 6 (13pp) (2022)

[6] The Polaris-H imaging spectrometer, Wahl C., Kaye W., Wang W. et al, Nucl. Instrum. Methods Phys. Res. A 784, 377-381 (2015)

[7] Ultracompact Compton camera for innovative gamma-ray imaging, Kataoka J., Kishimoto A., Taya T. et al., Nucl. Instrum. Methods Phys. Res. A 912, 1-5 (2018)

[8] Development of simultaneous PET and Compton imaging using GAGG-SiPM based pixel detectors, Shimazoe K., Yoshino M., Ohshima Y. et al., Nucl. Instrum. Methods Phys. Res. A 954, 161499 (6pp) (2020)

[9] Whole gamma imaging: a new concept of PET combined with Compton imaging, Yoshida E., Tashima H., Nagatsu K. et al., Phys. Med. Biol. 65, 125013 (14pp) (2020)

[10] Development of a low-cost-high-sensitivity Compton camera using CsI(Tl) scintillators (γI), Kagaya M., Katagiri H., Enomoto R. et al., Nucl. Instrum. Methods Phys. Res. A 804, 25-32 (2015)

[11] Development of an omnidirectional gamma-ray imaging Compton camera for low-radiation-level environmental monitoring, Watanabe T., Enomoto R., Muraishi H. et al., Jpn. J. Appl. Phys. 57, 026401 (5pp) (2018)

[12] Shift-invariant gamma-ray imaging by adding a detector rotation function to a high-sensitivity omnidirectional Compton camera, Muraishi H., Enomoto R., Katagiri H. et al., Jpn. J. Appl. Phys. 59, 090911 (6pp) (2020)

[13] Development of an omnidirectional Compton camera using CaF_2(Eu) scintillators to visualize gamma rays with energy below 250 keV for radioactive environmental monitoring in nuclear medicine facilities, Katagiri H., Narita N., Enomoto R. et al., Nucl. Instrum. Methods Phys. Res. A 996, 165133 (10pp) (2021)

[14] Muraishi H., Japanese Patent Application, 7014423 (2022)

[15] Development of a compact and portable high-sensitivity omnidirectional Compton camera with detector rotation function, S. Ishikawa, H. Muraishi, R. Enomoto et al, Conference Record of IEEE Nuclear Science Symposium and Medical Imaging Conference 2021 (3pp) (2022)

[16] γ-ray imaging in a nuclear medicine facility using a compact and portable high-sensitivity omnidirectional Compton camera with detector rotation function, S. Ishikawa, H. Muraishi, R. Enomoto et al., Ionizing Radiation (in Japanese), 47(3), 80-88 (2022)

[17] https://www.mhlw.go.jp/stf/seisakunitsuite/bunya/koyou_roudou/roudoukijun/anzen/0000186714_00003.html

ASTROPHYSICS AND GRAVITY DIVISION

Overview

Astrophysics and Gravity Division consists of Gravitational Wave Group, The Observational Cosmology Group, Primary Cosmic Ray Group and Theory Group.

The Gravitational Wave Group conducts experimental research of gravitational waves with researchers of gravitational wave experiments and theory in Japan. The main items are the construction of the large-scale cryogenic interferometer (KAGRA) at Kamioka underground and the operation of CLIO. For this purpose, KAGRA observatory was established at the beginning of the fiscal year of 2016 to assist the construction of KAGRA gravitational wave telescope.

The Observational Cosmology Group studies cosmic history based on deep multi-wavelength observations in collaboration with worldwide researchers. This group has started a new optical deep survey project with the wide-field imager of Hyper Suprime-Cam mounted on the Subaru telescope.

Theory Group conducts both theoretical studies of the Universe and astroparticle physics.

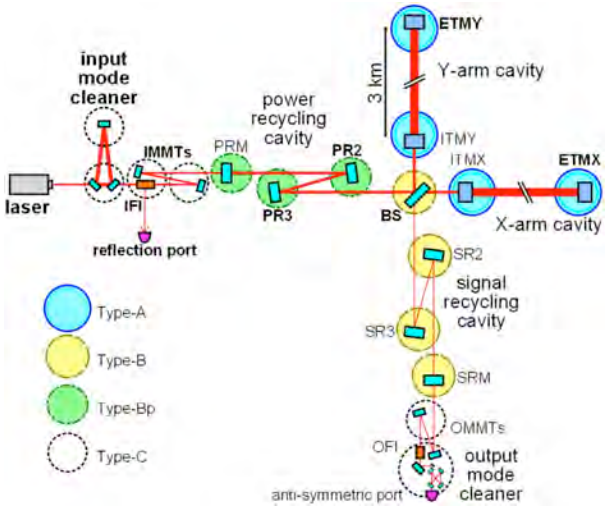

Fig. 1. Schematic view of the bKAGRA interferometer[3]. Type-A, Type-B, Type-Bp, and Type-C are the names of vibration isolation systems for each mirror.

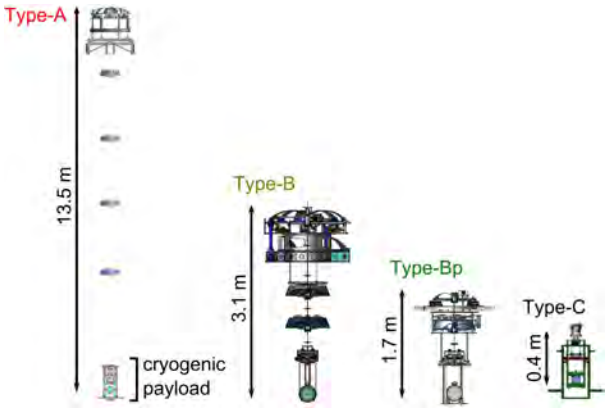

Fig. 2. KAGRA vibration isolation systems[3]. KAGRA equips four kinds of vibration isolation systems as Type-A, Type-B, Type-Bp, and Type-C.

Gravitational Wave Group

KAGRA Project Status

[Spokesperson : Takashi UCHIYAMA]
ICRR, The Univ. of Tokyo, Hida, Gifu 506-1205

Overview

KAGRA, Large-scale Cryogenic Gravitational wave Telescope, aims at detecting gravitational waves and developing gravitational wave astronomy, which was established by the first detection of gravitational waves by LIGO. KAGRA employs a 3 km L-shaped laser interferometer with a cryogenic mirror system placed underground at Kamioka[1]. The KAGRA development is divided into two stages: the initial KAGRA (iKAGRA) and baseline KAGRA (bKAGRA). The iKAGRA interferometer is a simple Michelson interferometer with a 2-Watt laser, room-temperature mirrors, and a simple vibration isolation system. We completed the iKAGRA interferometer with a test run in April 2016[2]. Then we proceeded to bKAGRA.

Figures 1 and 2 show a schematic view of the optical layout of the bKAGRA interferometer and the KAGRA vibration isolation systems. Table 1 shows the design parameter of the bKAGRA interferometer[3]. The bKAGRA interferometer will employ a Resonant Sideband Extraction (RSE) interferometer with a 180-Watt laser, cryogenic Sapphire mirrors, and several kinds of vibration isolation systems. The bKAGRA interferometer should attain a sensitivity high enough for the detection of gravitational waves with the help of the high-power laser and RSE interferometer to reduce the quantum noise, the cryogenic Sapphire mirrors to reduce the thermal noise, and the vibration isolation systems to reduce the seismic noise. Figure 3 shows designed sensitivities of bKAGRA in the cases of Broadband RSE (BRSE) and of Detuned RSE (DRSE), where the incoherent sum of the fundamental noise sources is assumed. The observation range for an inspiral and merger of neutron-star binary reaches 135 Mpc in BRSE and 153 Mpc in DRSE with the same definition of the observation range as LIGO and Virgo.

The KAGRA observatory signed the three documents between LIGO and VIRGO in order to realize international joint

Table 1. The design parameters of the bKAGRA interferometer[3].

Arm cavity length	3000 m	Test mass size	$\phi 22\,\mathrm{cm} \times 15\,\mathrm{cm}$
Laser wave length	1064 nm	Mass of test mass	22.8 kg
Input power at PRM	67W	Temperature of test mass	22 K
Arm intra-cavity power	340 kW	Beam radius at test mass	3.5 cm
ITM transmittance	0.4 %	PRC/SRC lengths	66.6 m
PRM transmittance	10 %	Detuning angle	3.5 deg
SRM transmittance	15 %	Homodyne angle	135.1 deg

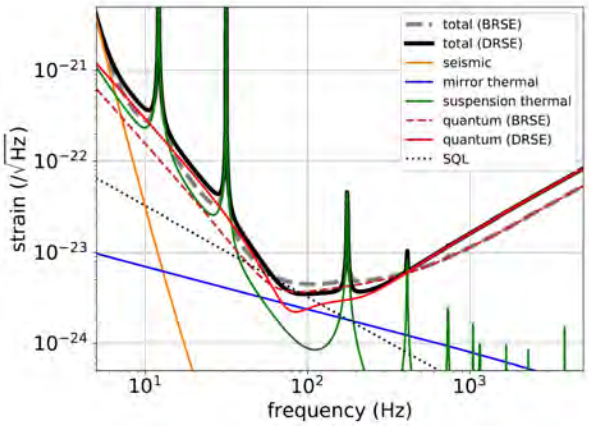

Fig. 3. The designed sensitivity of the bKAGRA interferometer[3]. "total", "seismic", "mirror thermal", "suspension thermal", "quantum", and "SQL" mean total sum of fundamental noise sources shown in this figure, seismic noise including gravity gradient noise, mirror thermal noise, suspension thermal noise, quantum noise, and standard quantum limit, respectively. The figure shows "total" and "quantum noise" in both Broadband RSE (BRSE) and Detuned RSE (DRSE) cases. Observation range for an in-spiral and merger of neutron-star binary reaches 135 Mpc in BRSE and 153 Mpc in DRSE with the same definition of the observation range as LIGO and Virgo.

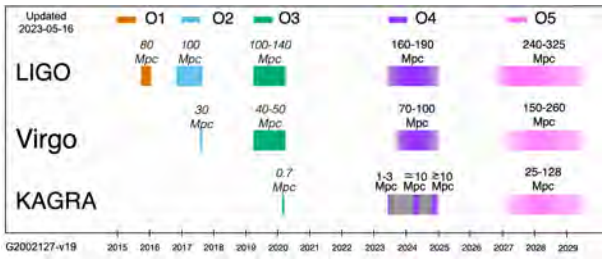

Fig. 4. International observation scenario[7]. The next international collaborative observation called O4 has already started on May 24, 2023. O4 will last 20 months including up to 2 months of commissioning breaks for maintenance. KAGRA performed the observation from March 24 to June 21, 2023 and resumed commissioning works. KAGRA will rejoin the observation in the next spring.

observation on October 4, 2019. The documents are the Memorandum of Agreement between VIRGO, KAGRA, and LIGO (main part)[4], Memorandum of Agreement between VIRGO, KAGRA, and LIGO (Attachment A)[5], and Letter of Intent for KAGRA to Join the O3 Run[6]. On the same day, the KAGRA observatory held a completion ceremony.

Figure 4 shows the international collaborative observation scenario[7] as of June 15, 2023. LIGO conducted Observation 1 (O1) from September 12, 2015, to January 19, 2016, and Observation 2 (O2) from November 30, 2016, to August 25, 2017. Virgo joined O2 on August 1, 2017. LIGO and Virgo started Observation 3 (O3) on April 1, 2019. Initially, O3 was planned to continue until the end of April 2020, but it was suspended on March 27, 2020, due to the influence of COVID-19[8]. The next international collaborative observation called O4 has already been started on March 24, 2023, and it will last 20 months including up to 2 months of commissioning breaks for maintenance[7]. KAGRA performed the observation from March 24 to June 21, 2023 and resumed commissioning works. KAGRA will rejoin the observation in the next spring.

In FY2019 we started interferometer commissioning works to reach the sensitivity required to join O3. The required sensitivity of 1 Mpc was defined as an observation range of neutron star binary coalescences[6]. KAGRA reached the required sensitivity almost at the end of March 2020. Along with the commissioning works the KAGRA observatory carried out several engineering runs and two Observation runs by the end of April 2020. The first observation run was carried out only by KAGRA with the observation range of 0.5 Mpc from February 25 to March 7, 2020. The second observation run was carried out with GEO600 from April 7 to 21, 2020. This observation called O3GK is regarded as an official joint observation with GEO600 by LIGO, VIRGO, and KAGRA. KAGRA was operated in O3GK with the observation range of almost 0.7 Mpc, and a duty factor of 53 % achieved.

After the O3GK observation, we restricted activities by the end of May 2020 to prevent the spread of COVID-19. Searching for transient gravitational-wave signals in observation data obtained in O3GK has been performed. Dedicated searches for binary coalescence signals and generic transients associated with gamma-ray burst events observed during O3GK have been also performed. No gravitational wave events were identified[9]. In order to improve the sensitivity towards O4, we evaluated the contribution of a lot of noise sources to the sensitivity and the results have been published[10].

In FY2022, we have done several upgrades and refurbishment works before closing the vacuum chambers. Control noise of mirror suspension systems was one of the sensitivity-

limiting noise sources in the low-frequency band (lower than 100 Hz) in the O3GK period[10]. We have successfully reduced the noise by one order of magnitude. In the middle-frequency band (100 Hz to 400 Hz) of the sensitivity, scattering light noise was thought of as a major noise source. To mitigate the scattering light noise, we have installed optical baffles in vacuum chambers. In the high-frequency band which is higher than 400 Hz, laser shot noise and laser intensity noise were serious noise sources. We introduced a higher-power laser source to reduce the laser shot noise and upgraded the laser intensity stabilization servo. Finally, vacuum chambers for the central part of the interferometer, the Y-arm cavity, and the Output Mode Cleaner have been closed and pumped down. Careful vacuum leak tests also have been done after the pumping down to avoid surface condensation on cooled mirrors. And then, commissioning works toward O4 has been started and KAGRA achieved the sensitivity of 1.3 Mpc at the beginning of O4. Details of the commissioning works are explained in the section on "commissioning".

We also enhanced the international collaborations with the Einstein Telescope (ET) project, LIGO, Virgo, Korean, and other Asian groups mainly based on the JSPS core-to-core program.

The rapidly progressing status of KAGRA was presented in many international conferences. Many papers about the progress of KAGRA were also published [11], [12], [13], [14], [15], [16], [18], [19], [20], [21], [22]. We also presented activities on our web page.[23]

Bibliography

[1] "KAGRA: 2.5 generation interferometric gravitational wave detector", KAGRA collaboration, Nature Astronomy, Vol. 3, January 2019, 35-40

[2] "Construction of KAGRA: an underground gravitational-wave observatory", KAGRA collaboration, Prog. Theor. Exp. Phys. 2018, 013F01 (2018)

[3] "First cryogenic test operation of underground km-scale gravitational-wave observatory KAGRA", KAGRA collaboration, Class. Quantum Grav. 36 165008 (2019)

[4] https://gwdoc.icrr.u-tokyo.ac.jp/cgi-bin/DocDB/ShowDocument?docid=10663

[5] https://gwdoc.icrr.u-tokyo.ac.jp/cgi-bin/DocDB/ShowDocument?docid=10664

[6] https://gwdoc.icrr.u-tokyo.ac.jp/cgi-bin/DocDB/ShowDocument?docid=10813

[7] https://observing.docs.ligo.org/plan/

[8] https://www.ligo.caltech.edu/news/ligo20200326

[9] "First joint observation by the underground gravitational-wave detector KAGRA with GEO 600", The LIGO Scientific Collaboration, the Virgo Collaboration, and the KAGRA Collaboration, Prog. Theor. Exp. Phys. 2022 063F01(37 pages)

[10] "Performance of the KAGRA detector during the first joint observation with GEO 600 (O3GK)", The KAGRA Collaboration, Progress of Theoretical and Experimental Physics, 2022;, ptac093

[11] "Unsupervised learning architecture for classifying the transient noise of interferometric gravitational-wave detectors", Sakai, Y., Itoh, Y., Jung, P. et al., Sci Rep 12, 9935 (2022)

[12] "Response of the underground environment of the KAGRA observatory against the air pressure disturbance from the Tonga volcanic eruption on January 15, 2022,", Tatsuki Washimi and others, Progress of Theoretical and Experimental Physics, Volume 2022, Issue 11, November 2022, 113H02

[13] "A laser interferometer accelerometer for vibration sensitive cryogenic experiments", R Bajpai et al., 2022 Meas. Sci. Technol. 33 085902

[14] "Vibration analysis of KAGRA cryostat at cryogenic temperature", R Bajpai et al., 2022 Class. Quantum Grav. 39 165004

[15] "Input optics systems of the KAGRA detector during O3GK", T Akutsu and others, Progress of Theoretical and Experimental Physics, Volume 2023, Issue 2, February 2023, 023F01

[16] "Estimation of Newtonian noise from the KAGRA cooling system", Rishabh Bajpai, Takayuki Tomaru, Toshikazu Suzuki, Kazuhiro Yamamoto, Takafumi Ushiba, and Tohru Honda, Phys. Rev. D 107, 042001

[17] "Noise subtraction from KAGRA O3GK data using Independent Component Analysis", H Abe et al., 2023 Class. Quantum Grav. 40 085015

[18] "Search for continuous gravitational wave emission from the Milky Way center in O3 LIGO-Virgo data", R. Abbott et al. (LIGO Scientific Collaboration, Virgo Collaboration, and KAGRA Collaboration), Phys. Rev. D 106, 042003

[19] "The Current Status and Future Prospects of KAGRA, the Large-Scale Cryogenic Gravitational Wave Telescope Built in the Kamioka Underground", Abe, H.; Akutsu, T.; Ando, M.; Araya, A.; Aritomi N.; Asada, H.; Aso, Y.; Bae, S.; Bajpai R.; Cannon K.; et. al., Galaxies 2022, 10, 63

[20] "Model-based Cross-correlation Search for Gravitational Waves from the Low-mass X-Ray Binary Scorpius X-1 in LIGO O3 Data", R. Abbott et al., 2022 ApJL 941 L30

[21] "Search for subsolar-mass black hole binaries in the second part of Advanced LIGO's and Advanced Virgo's third observing run", R. Abbott et al., Monthly Notices of the Royal Astronomical Society, stad588

[22] ”Open data from the third observing run of LIGO, Virgo, KAGRA and GEO”, The LIGO Scientific Collaboration, the Virgo Collaboration, the KAGRA Collaboration, Accepted by ApJS

[23] http://gwcenter.icrr.u-tokyo.ac.jp/en/

Commissioning

[Spokesperson : Takafumi USHIBA]

ICRR, The Univ. of Tokyo, Hida, Gifu 506-1205

In FY2022, one of the major achievements of KAGRA was success of stable lock of a Power Recycling Fabry Pérot Michelson Interferometer (PRFPMI). After the previous observing run in 2020, optical and suspension systems were upgraded for improving sensitivity and stability of the interferometer. In the former half of FY2022, commissioning for vibration isolation system (VIS) was mainly performed while commissioning for the interferometer control was performed in latter half of this fiscal year. As a result of the commissioning, KAGRA joins the 4th international joint observing run (O4) with better stability and sensitivity compared with the one in the previous run.

On August 2022, Fabry Pérot Michelson Interferometer (FPMI) was locked with better low-frequency sensitivity owing to the upgraded VIS. In the following three months, Power Recycling Michelson Interferometer (PRMI) commissioning was performed and stable lock of PRMI was achieved. On January 2023, PRFPMI was successfully locked with RF signals, and DC readout was achieved in the following month. After the achievement of PRFPMI lock with DC readout, noise hunting was started and several noises were reduced. Then, Alignment Sensing and Control (ASC) was implemented for improving the sensitivity and stability of the interferometer.

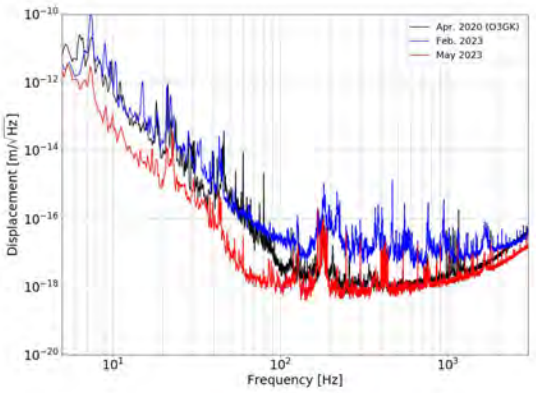

Fig. 5. PRFPMI sensitivities during O3GK and before and after the commissioning for O4. Black line shows the sensitivity on April 2020 (O3GK). Blue and red line shows the sensitivity on February and May 2023, respectively. On February, the sensitivity was worse than O3GK because the tuning of interferometer had not been performed sufficiently while the sensitivity was improved in entire frequency band with three months

Figure.5 shows the improvement in sensitivity over a period of about three months from the first lock of PRFPMI DC readout with the reference sensitivity during O3GK. At low frequency region below 100 Hz, control noise of VIS and auxiliary controls of the interferometer were limited and successfully reduced by optimizing their controls. In the middle frequencies from 100 Hz to 1 kHz, environmental noise such as vibration and sound affected sufficiently and could be mitigated by turning off several instruments of their sources. In addition, ASC plays a important role for improving at this middle frequency region by keeping interferometer alignment in the good condition. At high frequency region above 1 kHz, frequency noise and some electrical noises, which was reduced by optimizing controls and filters of signal taking, limited the sensitivity.

Finally, we achieved the sensitivity of 1.3 Mpc and stable lock for more than 20 hours, and then, KAGRA joins O4 with two LIGO detectors. However, current sensitivity is still not sufficiently good for detecting gravitational wave events with high expectation, we will once stop observing run and restart commissioning for further improvement of the sensitivity after one month observation.

Input and Output Optics

[Spokesperson : Osamu MIYAKAWA]

ICRR, The Univ. of Tokyo, Hida, Gifu 506-1205

The input and output optics (IOO) of KAGRA consists of the pre-stabilization laser (PSL), auxiliary locking system (ALS), input optics chain, output optics chain. PSL includes the intensity stabilization servo (ISS), pre-mode cleaner (PMC), and modulation system for the main interferometer. ALS includes the phase-locking system for the green beam each for X and Y arms, the fiber system, and the locking system for the arm cavities. The input optics chain includes the input mode cleaner (IMC), input Faraday isolator (IFI), and two input mode matching telescopes (MMT). The output optics chain includes the output mode matching telescopes (OMT), output Faraday isolator (OFI), and output mode cleaner (OMC).

In the summer of 2022, a high-power laser that had been developed at the University of Toyama was installed into the KAGRA well. The new laser was temporarily replaced with the existing high-power laser and locked to PMC and IMC. The new laser showed similar performance to the existing laser, including the control bandwidth for frequency stabilization. Since the replacement of the existing laser was a little uncertain before the observation, the new laser was switched again to the original laser after confirming stable operation. It is planned that the new laser will be replaced with the existing laser after the O4a observation and will be used permanently.

The most significant development in IOO is the Intensity Stabilization Servo (ISS). The ISS, which is a completely new design from the optical table, has been developed at the University of Toyama for a long time and was finally installed in KAGRA in the summer of 2022. Especially, it was shown that centering to the photo diode is very important, which had not been considered until the O3GK observation. By properly

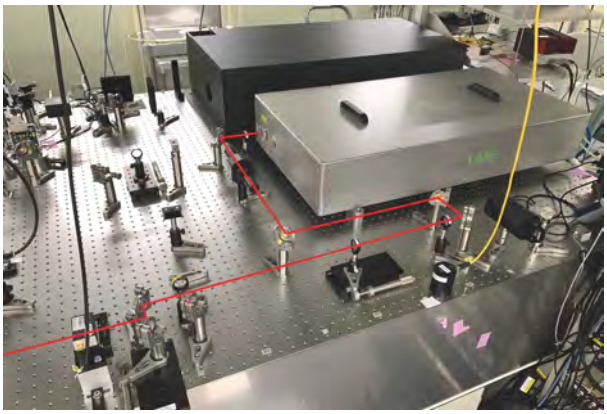

Fig. 6. 60W High power laser installed into KAGRA.

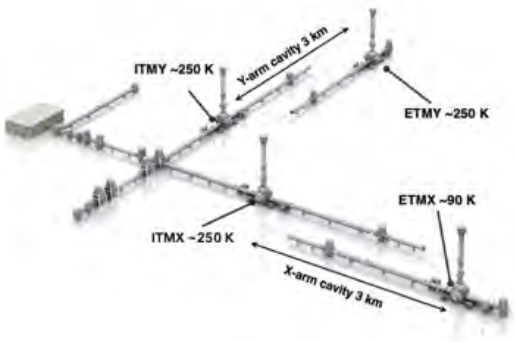

Fig. 7. Cryogenic mirrors for O4.

centering the photo diode, we have achieved excellent results in reaching the shot noise limit from 7Hz to about 1.5kHz. We will introduce a servo for beam centering, and we can expect long-term stability in the future.

ALS, IMC, IFI, etc. have been tuned in preparation for the observation, but basically they are working stably with no major changes. If necessary for observation in the future, alignment control and frequency stability will be investigated and improved.

We are preparing the whole IOO system working stably for O4 that will start in FY2022.

Cryogenic system

[Spokesperson : Nobuhiro KIMURA]
ICRR, The Univ. of Tokyo, Hida, Gifu 506-1205

One of the unique features of KAGRA is the use of cryogenic sapphire mirrors in the 3 km arm cavities. In FY2022, improvements were made to the cryogenic operation problems identified during the O3GK observation period. Based on these improvements, the commissioning of the cryogenic system for the O4 observation was started.

Improved the cryogenic system The loss of finesse due to surface condensation on the cryogenic mirror of ETMX during the O3GK observations was one of the serious problems for the stable operation of the KAGRA cryogenic interferometer.

After the O3GK observation, the KAGRA cryogenic group conducted R&D on mirror cooling and component analysis of the residual gas in the vacuum vessel containing the mirror. The results of this analysis suggested that moisture and nitrogen in the residual gas components were the sources of surface condensation on the mirrors.

With the aim to reduce the total amount of residual gases in the vacuum vessel and to operate the cryogenic interferometer continuously, the following measures were taken during the preparation period of the O4 observations.

1. Vacuum leak tests were performed on all vacuum vessels and duct connections that were opened to the atmosphere. The total number of vacuum connections subjected to this testing was over 1500.
2. The allowable vacuum leakage value was changed from "no leakage greater than $1 \times 10^{-10}\,\mathrm{Pa \cdot m^3 s^{-1}}$ to "no leakage greater than $1 \times 10^{-11}\,\mathrm{Pa \cdot m^3 s^{-1}}$.
3. If a vacuum leak exceeding the allowable value is found, it is repaired, and no more than $1 \times 10^{-11}\,\mathrm{Pa \cdot m^3 s^{-1}}$ leak is found. As a result, the vacuum leakage at the vacuum connection subject to the leak test was less than $1 \times 10^{-12}\,\mathrm{Pa \cdot m^3 s^{-1}}$.
4. The five-step cooling proposed and demonstrated in Cooling R&D was adopted as the cooling method for the cryo-mirror. In this cooling method, the surface of the radiation shield surrounding the cryocooler is cooled in stages to adsorb residual gas components, and then cooling of the cryocooler is initiated.
5. The partial pressure of the residual gas component in the cryostat during the cooling process is periodically measured to determine the adsorption condition on the surface of the radiation shield.

Cryogenic operation Figure7 shows the setup of KAGRA's cryogenic mirrors before the start of O4 observations, along with the positional relationship of the vacuum vessel.

After confirming the function of the hardware update of the cryogenic payloads and the vacuum leak test of the vacuum vessels containing the cryogenic mirror, the cryocoolers of the duct shields of ITMX turned on in February 2022 among the four cryogenic mirrors. Subsequently, the cryocoolers of the duct shields were turned on in the order of ETMX, ITMY, and ETMY. For ETMX, the cooling of the radiation shield surrounding the cryo-mirror was has been done, and ETMX was cooled to about 90 K by radiation cooling.

Although the KAGRA cryogenic mirrors are at the intermediate stage of the design cooling temperature, the KAGRA interferometers have continued to operate at low temperatures for more than one year since the start of cooling without a decrease in finesse.

Control optimization of cryogenic payload The sensitivity at low frequencies below 50 Hz during the previous observing run was limited by noises coming from local damping controls of cryogenic payloads. So, control optimization was performed to reduce the low-frequency noise in FY 2022.

The controls are separated into 2 stages: lock-acquisition and observation stages. The lock-acquisition stage engages strong damping controls to reduce the vibration as quickly as possible. The observation stage engages minimal damping controls to reduce noises induced at the observation band while keeping a stable lock of the interferometer. This control optimization reduces low-frequency noises by a factor of 10 from the previous observing run.

Master thesis One master thesis, "Characterization and Control of Cryogenic Suspension in KAGRA", was accepted in FY 2022.

Acknowledgement The Vacuum Group of the Accelerator Laboratory of KEK made support vacuum leak repair techniques. We would like to express our appreciation to them.

Digital system

[Spokesperson : Shoichi OSHINO]

ICRR, The Univ. of Tokyo, Hida, Gifu 506-1205

We plan to upgrade the digital system after the fourth phase of international joint observations. We have started to build a test bench system for this purpose. As a first step, we are building a system consisting of a boot server, data concentrator, frame writer, and real-time front-end. We will install the latest version of software developed at LIGO to build a system that will facilitate future collaborative observations.

The workstations used to control the interferometers and display various data had become obsolete and needed updating. We replaced 18 workstations with new ones. We have also updated several servers with newer operating systems that are no longer supported. As commissioning support, we prepared a network for picomoter and function generator and laid LAN cables. This work enabled the stable operation of these equipments. The previous half-wave plate had a problem in that the angle at which the plate was rotated was unknown, making it difficult to determine the appropriate angle. The installation of a half-wave plate with encoder and a dedicated PC has enabled more precise interferometer control.

Analog ELectronic circuits

[Spokesperson : Osamu MIYAKAWA]

ICRR, The Univ. of Tokyo, Hida, Gifu 506-1205

The Analog Electronics Group (AEL) has been continuously manufacturing the circuits that are necessary for KAGRA. We have produced several hundred different types of circuits, about a thousand as units, and several thousand as boards. In FY2022, KAGRA is in a situation to be ready for observation, so we do not need so many new circuits already. We have been replacing them for malfunctions, preparing spare circuits for redundancy, and manufacturing circuits that will be necessary for the future. The circuits we have actually fabricated in FY2022 are 10 units of anti-aliasing filters, 5 units of IO chassis, 4 sets of photon calibration drivers, 100 boards of generic power supplies, and so on.

Over the past several years, the procurement of circuit components has been extremely difficult due to the COVID-19. We had planned to produce 10 units of coil drivers and 10 units of whitening filters in FY2022, but decided to purchase circuit components over several years and produce the circuit boards when all the components were collected. Although many of the electronic parts were obtained in FY2022, we will continue to procure parts and plan to manufacture the circuit boards in FY2023.

In FY2022 we produced several hundred units of specially designed D-SUB cables to connect between the KAGRA circuits and subsystems. The actual order was in FY2021 however, due to worldwide unavailability of parts, especially for the connectors, it was completed in FY2022 when the parts were available. Some of these cables have already been used in KAGRA.

The circuits built into the main body of KAGRA sometimes have only a few minor problems or failures, we have made a good system to minimize downtime by replacing circuits that have problems immediately, using the spares we have. Since KAGRA is preparing for observation, we have been no major changes to the circuits in KAGRA, basically we can say that the circuits are running stable.

It is important to provide circuits for KAGRA to be able to carry out observations and commissioning stably in the future. On the other hand, our members are getting older and I am a little concerned about our AEL group after 5 years. We will take responsibility for the KAGRA circuits-related things considering the possibility of new members.

Detector Charcterization

[Spokesperson : Hirotaka Yuzurihara]

ICRR, The Univ. of Tokyo, Hida, Gifu 506-1205

Updates of data quality evaluation for O4 One of the most important roles of detector characterization (DetChar) is to prevent the false detection of gravitational waves. Gravitational waves (GWs) are very weak signals and are buried by various disturbances such as vibration of the mirrors that constitute an interferometer and instability of the laser power and frequency. Such disturbances can also be detected as false GWs events. In order to separate GWs from such false events, it is necessary to understand the behavior and statistics of the detector noise.

Customarily, in GW searches, the observational data which contains a lot of known disturbances is tagged named as Data Quality (DQ) flags and data category flags. Tagged data is removed from the data set for searching gravitational waves to reduce the false event rate.

In fiscal year 2022, DQ flags were updated from ones provided in the 3rd observing run with GEO600 and KAGRA

in 2020 called O3GK. In O3GK, only basic operating status of the interferometer was shared as an online process that cadence is o(10s) and another information about noise behavior were served as an offline process that cadence is o(month). As one of DetChar's activities, optimization of criteria of DQ flags and update of the softwares for providing DQ flags with more shorter cadence. The optimization of criteria was conducted based on knowledge about the hardware problem which were obviously during the hardware upgrade and reinstallation of the interferometer. DQ flags which have been set based on knowledge during installation phase are contained not only disturbances due to the environmental noise but also noise transients coming from electrical glitches of instruments, operational errors of human activities, etc. As the results, a part of flags which had served as the offline process in O3GK will be served as the online process in more detailed than O3GK.

Data sharing with LIGO and Virgo To access the physics related to the neutron star merger or the supernovae, it is important to perform follow-up observation by electromagnetic telescopes just after the discovery of the GW candidate. The data from GW observatories (LIGO, Virgo, and KAGRA) are collected to the cluster at California Institute of Technology (CIT). The low-latency search pipelines analyze the data set and provide the GW alert with the latency of a few seconds. The information such as the mass of the binary star, the merger time, the estimated sky map, and the signal-to-noise ratio are registered in the database (called GraceDB) to share with the collaborators.

The task of DetChar is to provide the data quality report (called DQR) of the data around the time of GW candidate. In the past observation run (O3), the DQR was organized by LIGO and Virgo. The DQR played an important role to a number of retracted candidates and increased the confidence of candidates for astronomers of the electromagnetic telescopes.

Toward next observation run, LVK DetChar plans to provide the tool standardized across collaborations and to launch the DQR processes automatically triggered by the GW alert. KAGRA DetChar members have participated in the development of the DQR tools and have contributed to the operation test with LIGO and Virgo DetChar members.

Environment Monitors

[Spokesperson : Takaaki YOKOZAWA]

ICRR, The Univ. of Tokyo, Hida, Gifu 506-1205

Because the amplitude of the GW is extremely small, vibration from essential instruments, sound from outside of the experimental area and so on, can produce noise source contamination that limits KAGRA sensitivity. To evaluate the noise sources, many sensors are installed at the KAGRA site, Examples include seismometers, microphones, magnetometers, and accelerometers. The main purposes of physical environmental monitoring are as follows:

The first is to characterize underground and cryogenic environments. KAGRA detector has two unique features, underground and cryogenic environment, and These features are essential for next-generation detectors.

One homework from O3GK is the identification of narrow peak noise, which is called line noise. The origin of the line noise is colorful, power supplying related line, resonant frequencies of the suspension system and/or instruments inside the chamber, and environmental noise. As a first step, we measured the resonant frequency for the instruments inside the vacuum chamber before closing the vacuum chambers and taking 360 °pictures. Measurement of the vibration amplitude inside the chamber is also important. For the future filter cavity installation, we evaluated the vibration amplitude inside and outside of the OMC vacuum chamber for both air and vacuum conditions. Next, we improved the voltage monitors for the ground level of the chamber and optical tables, for the DC power supplying and AC power monitors. As you know, the KAGRA experimental area is operated at an AC power of 60 Hz. So there are possibility to appear the 60 Hz noise in the KAGRA sensitivity. To identify the noise path for AC noise, we prepared the following monitors: Now the data analysis is performed using the coherence and correlation method [1].

On January 15, 2022, the undersea volcano of the Hunga Tonga-Funga Ha'apai erupted. The global seismic wave, shock waves, and electromagnetic waves generated by the recent eruption in Tonga reached KAGRA experimental area, which is more than 8,000 km away, and their signals were clearly seen in various environmental monitors and a geophysics interferometer. Unfortunately, the KAGRA interferometer has been upgraded. Two papers were published[2], one is focusing the evaluating the KAGRA Facility, second is the result of the geophysics interferometer[3]. This volcanic eruption induced multiple lightning strikes, , and electromagnetic waves were emitted. These lightning strikes excited Schumann resonance. A twice-larger magnetic field around the 7.5 Hz frequency region was detected soon after the Tonga volcano. After several tens minutes after the Tonga volcano, the p-wave and s-wave ground motion was detected in the seismometers in the KAGRA experimental area, respectively. The arrival times were consistent with those of the iasp91 model. After about seven hours after the Tonga volcano, the air pressure signal and ground motion induced by air pressure was detected in the seismometer, infrasound microphone, and barometers. Using the combination of their detector, we characterized the facility of KAGRA experimental area, for example, transfer function of the air pressure from outside area to inside area, and the ground motion between the center area and each end-station area.

Water drain systems exist in the KAGRA experimental area. In the snow melting season, a large amount of water appears. Therefore, the water drain system played an important role in maintaining the experimental area. One of the water pipes was placed near a sapphire mirror. So we need to evaluate the effect of the Newtonian noise from water flow system. To measure the water flow continuously, we placed the water flow measurement system at the end of the Y-end area. Also, using the results of the water flow measurement system, we tried to investigate the Newtonian noise using 3D simulation and theoretical calculations. We evaluated Newto-

nian noise at the KAGRA site using a seismometer and microphone. We used FLOW3D software for the water flow simulation. It is known from theoretical calculations that the surface microstructure largely affects Newtonian noise. Both evaluate the Newtonian noise with straight and KAGRA realistic shapes of pipes with various water flows. The conclusion is that the NN is under the KAGRA design sensitivity but appears in the ET design sensitivity. This result is interesting for future detectors[4].

Microseismic waves are ground motions excited by ocean waves. The frequency was approximately 0.1 Hz. Even at an underground site, microseismic motion cannot be ignored. During the O3GK, due to the stormy days, implied the large micro seismic motion, it became difficult to keep the observation state in several days. Qualitatively, we know the effect of the ocean wave to KAGRA site, we would like to quantify them by creating simple approximation equations for ocean waves and ground velocity at the KAGRA. In addition, we evaluated the characteristics of the ocean waves around the KAGRA site. Ocean wave data are published from the NOWPHAS(The Nationwide Ocean Wave information network for Ports and HArbourS) By the correlation analysis for the ocean wave data in each bays, we can categorize to three part, Sea of Japan, Pacific east area, and Pacific south area. From the 12 ocean wave data of near bay, we performed the principal component analysis to extract the typical ocean wave data for the upper three areas, and then fitting the result with a nonlinear function. Finally, we succeeded in explaining the ground motion from ocean wave data with high precision. By inputting wave forecast data into the established model, we can also forecast future microseismic motions. This contributes to the commissioning work at the KAGRA observatory, particularly for scheduling.

Measuring and evaluating the Schumann resonance inside and outside the mountain. The Schumann resonances are a set of spectrum peaks in the extremely low frequency (ELF) portion of Earth's electromagnetic field spectrum. This would be a noise source for stochastic gravitational wave background search. From the past measurement at the KAGRA site, the amplitude of the Schumann resonance inside the KAGRA experimental area is larger than the outside, but remains a mystery of the amplification. The amplitude of the Schumann resonance was measured using a magnetic field with various areas. Then, we concluded that the amplitude increased near the 3 km beam duct. The results are summarized as follows: We also measured the magnetic field at the CLIO site; however, no amplification was detected. Next, we set the magnetometer outside the KAGRA experimental area and measured the long-term variation. With assuming the theoretical model with

$$P_{\mathrm{SF}}(f) = A\left(\frac{f}{10\mathrm{Hz}}\right)^{-\alpha}\Sigma_l \frac{[f_l^{'}/(2Q))]^2}{(f-f_l^{'})^2+[f_l/(2Q)]^2}, \qquad (1)$$

where the fitting parameters are A(amplitude), α(power exponent), Q(Q value), and s(discrepancy from typical resonance frequency). We measured the Schumann resonance from August to December 2022, and calculated the time variance of each parameter. After them, we tried to evaluate the effect ot Schumann resonance with time variation to the search for the stochastic gravitational wave background by using a fissure matrix. This result will soon be reported [5].

The second aim is to understand interferometer noise using environmental monitors. To achieve better sensitivity, understanding the main contribution of noise is essential, which is called the noise budget. Environmental noise is one of the candidates to limit the interferometer sensitivity

We installed various PEMs including accelerometers, microphones, magnetometers, thermometers, and weather stations. After the O3GK observation, we reinstalled several PEMs to optimize their position and cabling. Easy access to measure using the portable PEMs Generate a new PEM management tool using the KAGRA data-acquisition system.

The study of offline noise subtraction is also ongoing, not only for independent component analysis[6], but also for the DeepClean method. We are trying to establish the power line noise subtraction algorithm (60 Hz and its harmonics, already established in LIGO) with online system.

Bibliography

[1] Taiseki Kiyota, master thesis (Osaka Metropolitan University)

[2] T.Washimi et al, Prog. Theor. and Exp. Phys. volume 2022, issue 11, 113H02 (2022)

[3] A. Takamori et al, Earth, Planets and Space 75:98 (2023)

[4] Takanori Suzuki, master thesis (Tokyo Institute of Technology)

[5] Isamu Fukunaga, master thesis (Osaka Metropolitan University)

[6] Class. Quan. Grav. volume 40, number 8 (2023)

Data Analysis, Computing environment

[Spokesperson : Hideyuki Tagoshi]

ICRR, The Univ. of Tokyo, Kashiwa, Chiba, 277-8582

Data Analysis

The data analysis of KAGRA is now performed jointly with LIGO and Virgo under the LIGO-Virgo-KAGRA Memorandum of Agreement (MoA). The MoA defines the policy of the joint data analysis and the data sharing. In the LIGO-Virgo-KAGRA (LVK) Collaboration, there is a Data Analysis Council (DAC) which is a committee managing data analysis activities in LVK. Under DAC, there are four working groups regarding gravitational wave signal search, Compact Binary Coalescence working group (CBC), Burst working group (Burst), Continuous Wave Working group (CW), and Stochastic background working group (Stochastic). In LVK, there is also Operations group which manages various data related activities. From ICRR, Hideyuki Tagoshi is serving as a co-chair of DAC and CBC, and Soichiro Morisaki is serving as a co-chair of the Low Latency group in the Operations division.

LVK Collaboration has continued the analysis of O3 data. We published 14 observational science papers in 2022 as full LVK Collaboration papers.

Various activities related to the data analysis were also done during FY2022.

Detailed Bayesian parameter estimation of compact binary coalescence signals is computationally time-consuming, so speeding up the process is a very important issue. Since one of the reasons for the time-consuming process is the nontrivial correlation of mass and spin parameters, we tried to speed up the process by taking a new combination of mass and spin parameters with small correlations. As a result, we succeeded in increasing the efficiency of Markov chain Monte Carlo sampling by a factor of 10 to 100 [Eunsub Lee, Soichiro Morisaki, Hideyuki Tagoshi, PRD105, 124057 (2022)].

One of the main goals of rapid parameter estimation is to provide accurate source localization of compact binary coalescence signal in low latency. In preparation for O4, we developed a rapid parameter estimation framework, which enables optimal source localization of binary neutron star signal within several minutes. Our framework is based on the reduced order quadrature technique, which approximates gravitational-wave waveform as linear combination of basis elements, and resolves its short comings by utilizing multiple reduced order quadrature bases in a single parameter estimation run. Our technique has been implemented in one of the LIGO-Virgo-KAGRA parameter estimation engines, Bilby, and being employed to circulate estimates on source locations of detected signals in O4.

We also investigated the possibility to perform the rapid source localization by using a machine learning, one-dimensional residual neural network. We used whitened GW strain data directly, and produce the probability sky map from the neural network. We train two models, one is the GW waveform with simulated detector noise, and the other is GW waveform with real detector noise. Both models show high localization ability on GW data. We demonstrate the accuracy of our model by an third observation run event, and the result is comparable with LALInference and BAYESTAR, which are the pipelines used in the usual GW analysis, showing that our analysis method is reliable. The project was done by Bin-Hua Hsieh as his Doctor Thesis.

Using the two binary neutron star merger signal data that have been detected so far, we compared waveform models including tidal deformation rates based on the post-Newtonian approximations and waveform models based on numerical relativity. The results show that the post-Newtonian approximation model has a larger error in the tidal deformability than the numerical relativity model, and that it is difficult to determine the superiority of the different numerical relativity models compared to the post-Newtonian model [Tatsuya Narikawa, Nami Uchikata, PRD106, 103006 (2022)].

The significance of the tidal effects on observed gravitational-wave signal depends on the equation of state (EoS) of matter with supra-nuclear densities, and measuring them can constrain the nuclear EoS, which remains to be uncertain. On the other hand, calculating the constraints on the nuclear EoS from the measurements from multiple binary neutron star signals requires computationally costly hierarchical Bayesian analysis. To solve this issue, we developed an efficient algorithm to perform that hierarchical Bayesian analysis, based on the source parameter combinations which can be precisely measured from gravitational-wave data [A. Ray, M. Camilo, J. Creighton, S. Ghosh and S. Morisaki, PRD107, 043035 (2023)].

We searched for ultralight scalar dark matter, whose mass is in the range $[10^{-13}$–$10^{-11}]$ eV, using data from LIGO detectors. Since they are precise measurement tools, they can be used to detect an undiscovered scalar dark matter particle with a tiny coupling with the Standard Model particles, as well as gravitational waves. We employed an analysis method calculating the cross correlation of data between the two LIGO detectors, a method similar to what is used to for stochastic gravitational-wave background. We did not find any significant signal candidates, and hence obtained the upper limits on the coupling between the hypothetical scalar field and the standard model particles. While the constraints are weaker than the current best constraints from the tests of weak equivalence principle, the difference is less than ~ 5, demonstrating gravitational-wave experiments are starting to bring us meaningful information about the nature of dark matter [K. Fukusumi, S. Morisaki and T. Suyama, [arXiv:2303.13088 [hep-ph]].].

We also conducted dark matter search using data from a bow-tie cavity. The idea is that if a hypothetical scalar particle coupling with photon, axion, behaves as dark matter, it induces oscillatory modulations in the left/right-handed laser light, and those modulations can be observed with a bow-tie cavity. The experiment is referred to as Dark matter Axion search with riNg Cavity Experiment (DANCE). We conducted a search using data from the prototype cavity. Although the bounds did not exceed the current best limits, this work is the first demonstration of axion dark matter search with an optical cavity [Y. Oshima, H. Fujimoto, J. Kume, S. Morisaki, K. Nagano, T. Fujita, I. Obata, A. Nishizawa, Y. Michimura and M. Ando, [arXiv:2303.03594 [hep-ex]].]. In either search, the main contribution of our work is to develop data analysis software to search for signal and calculating upper limits on the coupling.

Computing environment

As one of the main computing resources in KAGRA, the main data server of KAGRA is located at ICRR Kashiwa. It has a 2.5PiB data storage. In June 2022, an additional KAGRA main data server (System B) was introduced at ICRR Kashiwa. It has 4PiB data storage and computing nodes with 512 cores.

All KAGRA data taken at Kamioka are packed into one file for every 32 seconds, and are transferred continuously to the main data server at Kashiwa. Beside this, low latency data transfer is also done by packing only the gravitational wave channel and a few other channels into one file for every 1 seconds. For low latency data transfer, the latency of about 3 seconds is achieved from Kamioka to Kashiwa (this time includes the time necessary for calibration). In order to share the low latency data file among LIGO-Virgo-KAGRA, the low latency data files are also transferred to a server at LIGO Caltech. On the other hand, low latency data files of LIGO and

Virgo detectors are transferred from Caltech to the main data server at Kashiwa.

Observational Cosmology Group

[Spokesperson : Yoshiaki Ono]
ICRR, The Univ. of Tokyo, Kashiwa, Chiba 277-8582

A Comprehensive Study on Galaxies at $z \sim 9-16$ Found in the Early JWST Data: UV Luminosity Functions and Cosmic Star-Formation History at the Pre-Reionization Epoch [1]

In collaboration with the members of Chiba University, and National Astronomical Observatory of Japan.

We conduct a comprehensive study on dropout galaxy candidates at $z \sim 9-16$ using the first 90 arcmin^2 JWST/NIRCam images taken by the early release observations (ERO) and early release science (ERS) programs. With the JWST simulation images, we find that a number of foreground interlopers are selected with a weak photo-z determination ($\Delta\chi^2 > 4$). We thus carefully apply a secure photo-z selection criterion ($\Delta\chi^2 > 9$) and conventional color criteria with confirmations of the ERO NIRSpec spectroscopic redshifts, and obtain a total of 23 dropout galaxies at $z \sim 9-16$, including two candidates at $z_{\rm phot} = 16.25^{+0.24}_{-0.46}$ and $16.41^{+0.66}_{-0.55}$. We perform thorough comparisons of dropout galaxies found in our work with recent JWST studies, and conclude that our galaxy sample is reliable enough for statistical analyses. We derive the UV luminosity functions at $z \sim 9-16$, and confirm that our UV luminosity functions at $z \sim 9$ and 12 agree with those determined by other HST and JWST studies. The cosmic star-formation rate density decreases from $z \sim 9$ to 12, and perhaps to 16, but the densities at $z \sim 12-16$ are higher than the constant star formation efficiency model. Interestingly, there are six bright galaxy candidates at $z \sim 10-16$ with $M_{\rm UV} < -19.5$ mag and $M_* \sim 10^{8-9} M_\odot$. Because a majority ($\sim 80\%$) of these galaxies show no signatures of AGNs in their morphologies, the high cosmic star-formation rate densities and the existence of these UV-luminous galaxies are explained by no suppression of star-formation by the UV background radiation at the pre-reionization epoch and/or an efficient UV radiation production by a top-heavy IMF with Population III-like star formation (Figure 8).

Bibliography

[1] Harikane, Y., Ouchi, M., Oguri, M., Ono, Y., Nakajima, K., Isobe, Y., Umeda, H., Mawatari, K., Zhang, Y., 2023, The Astrophysical Journal Supplement Series, 265, 5

EMPRESS. V. Metallicity Diagnostics of Galaxies over $12+\log({\rm O/H}) \simeq 6.9-8.9$ Established by a Local Galaxy Census: Preparing for JWST Spectroscopy [2]

In collaboration with the members of National Astronomical Observatory of Japan, Observatories of the Carnegie Institution for Science, The Graduate University for Advanced Studies (SOKENDAI), University of Geneva, Ehime University, Waseda University, Seoul National University, Hosei University, and NSF's National Optical-Infrared Astronomy Research Laboratory.

We present optical-line gas metallicity diagnostics established by the combination of local SDSS galaxies and the largest compilation of extremely metal-poor galaxies (EMPGs) including new EMPGs identified by the Subaru EMPRESS survey. A total of 103 EMPGs are included that cover a large parameter space of magnitude ($M_i = -19$ to -7) and Hβ equivalent width ($10-600$ Å), i.e., wide ranges of stellar mass and star-formation rate. Using reliable metallicity measurements of the direct method for these galaxies, we derive the relationships between strong optical-line ratios and gas-phase metallicity over the range of $12+\log({\rm O/H}) \simeq 6.9-8.9$ corresponding to $0.02-2$ solar metallicity $Z_\odot$ (Figure 9). We confirm that R23-index, ([O III]+[O III])/Hβ, is the most accurate metallicity indicator with the metallicity uncertainty of 0.14 dex over the range among various popular metallicity indicators. The other metallicity indicators show large scatters in the metal-poor range ($\lesssim 0.1\,Z_\odot$). It is explained by our `CLOUDY` photoionization modeling that, unlike R23-index, the other metallicity indicators do not use a sum of singly and doubly ionized lines and cannot trace both low and high ionization gas. We find that the accuracy of the metallicity indicators is significantly improved, if one uses Hβ equivalent width measurements that tightly correlate with ionization states. In this work, we also present the relation of physical properties with UV-continuum slope β and ionization production rate $\xi_{\rm ion}$ derived with GALEX data for the EMPGs, and provide local anchors of galaxy properties together with the optical-line metallicity indicators that are available in the form of ASCII table and useful for forthcoming JWST spectroscopic studies.

Bibliography

[2] Nakajima, K., Ouchi, M., Xu, Y., Rauch, M., Harikane, Y., Nishigaki, M., Isobe, Y., Kusakabe, H., Nagao, T., Ono, Y., Onodera, M., Sugahara, Y., Kim, J. H., Komiyama, Y., Lee, C.-H., Zahedy, F. S., 2022, The Astrophysical Journal Supplement Series, 262, 3

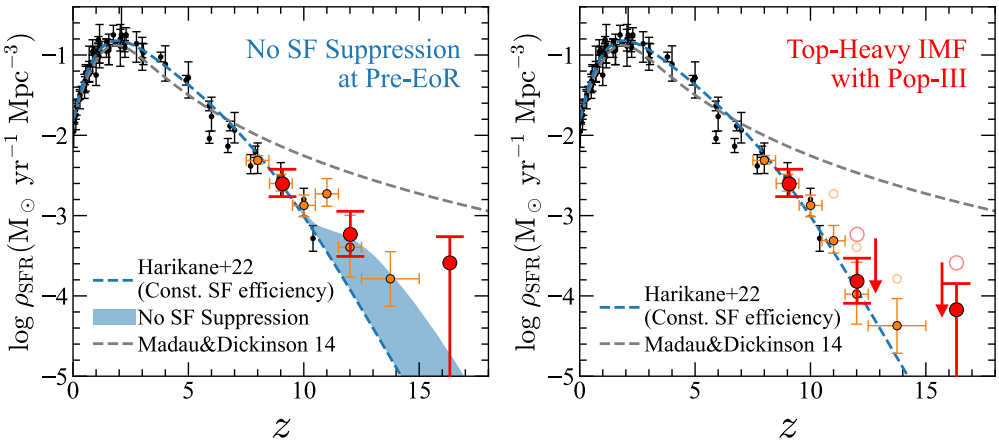

Fig. 8. Possible scenarios to explain the observed SFR densities at $z > 10$. (Left:) Scenario of no star formation suppression at pre-reionization epoch. At the reionization epoch and after that, star formation in low-mass halos is suppressed by strong UV background radiation, while before the reionization epoch such a suppression of star formation activity does not occur. The upper edge of the blue shaded region indicates the enhancement of the star formation by this effect, which explains the observed SFR densities. (Right:) Scenario of Pop III star formation. Pop III stellar populations with a top-heavy IMF produces a significant amount of UV photons at a given SFR, resulting in the overestimates of the SFR densities if we use the canonical UV-SFR conversion factor. The red and orange filled circles at $z > 10.5$ are SFR densities calculated based on the conversion factor for a Pop III stellar population with a top-heavy IMF, which agree well with the constant star formation efficiency model in the literature. The open circles are SFR densities based on the canonical conversion factor.

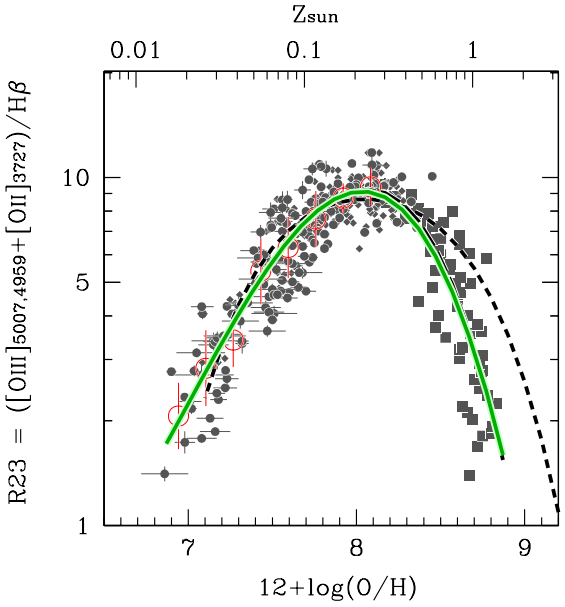

Fig. 9. Relationship between metallicity and the strong line ratio of R23-index. Our compiled (E)MPGs are shown with gray filled circles (individual) and red open circles (binned average, with the standard deviation of the binned distribution as the error). Gray filled squares denote stacked SDSS spectra in the high-metallicity regime. Small gray diamonds are metal-poor galaxies compiled in the literature just for a reference (i.e., not used for the following best-fit function). All the measurements of metallicity are done in a consistent manner based on the direct T_e method. Green curve presents our best-fit function, whereas the black short-dashed and long-dashed curve illustrates the function obtained in the literature.

EMPRESS. VI. Outflows Investigated in Low-Mass Galaxies with $M_* = 10^4 - 10^7$ $M_\odot$: Weak Feedback in Low-Mass Galaxies? [3]

In collaboration with the members of Carnegie Observatories, National Astronomical Observatory of Japan, Waseda University, Hosei University, University of Geneva, Cosmic Dawn Center (DAWN), and University of Copenhagen.

We study emission line profiles of 21 nearby low-mass ($M_* = 10^4 - 10^7$ $M_\odot$) galaxies in deep medium-high resolution spectra taken with Magellan/MagE. These low-mass galaxies are actively star-forming systems with high specific star-formation rates of sSFR $\sim 100 - 1000$ Gyr^{-1} that are well above the star-formation main sequence and its extrapolation. We identify broad-line components of Hα and [OIII]λ5007 emission in 14 out of the 21 galaxies that cannot be explained by the MagE instrumental profile or the natural broadening of line emission. We conduct double Gaussian profile fitting to the emission of the 14 galaxies, and find that the broad-line components have line widths significantly larger than those of the narrow-line components, indicative of galactic outflows. The board-line components have moderately large line widths of ~ 100 km s^{-1}. We estimate the maximum outflow velocities $v_{\rm max}$ and obtain values of $\simeq 60 - 200$ km s^{-1}, which are found to be comparable to or slightly larger than the escape velocities. Positive correlations of $v_{\rm max}$ with star-formation rates, stellar masses, and circular velocities, extend down into this low-mass regime. Broad- to narrow-line flux ratios BNRs are generally found to be smaller than those of massive galaxies. The small $v_{\rm max}$ and BNRs suggest that the mass loading factors η can be as small as 0.1 - 1 or below, in contrast to the large η of energy-driven outflows predicted by numerical simulations (Figure 10).

Bibliography

[3] Xu, Y., Ouchi, M., Rauch, M., Nakajima, K., Harikane, Y., Sugahara, Y., Komiyama, Y., Kusakabe, H., Fujimoto, S., Isobe, Y., Kim, J. H., Ono, Y., Zahedy, F. S., 2022, The Astrophysical Journal, 929, 134

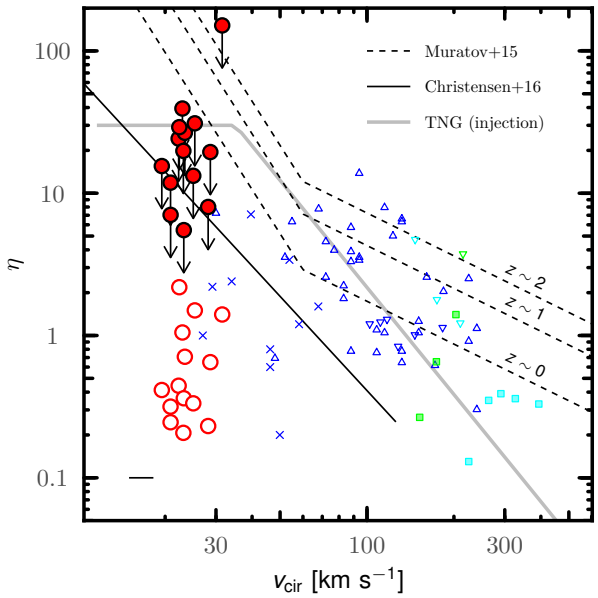

Fig. 10. Mass loading factor (η) and its dependence on $v_{\rm cir}$. We estimate η with fiducial parameters and extreme parameters, shown as the open and close solid circles, respectively. The solid line in the left-bottom corner indicates the typical error of $v_{\rm cir}$ for our galaxies. We include the predictions of two 'zoom' simulations and the prescription used at injection by IllustrisTNG.

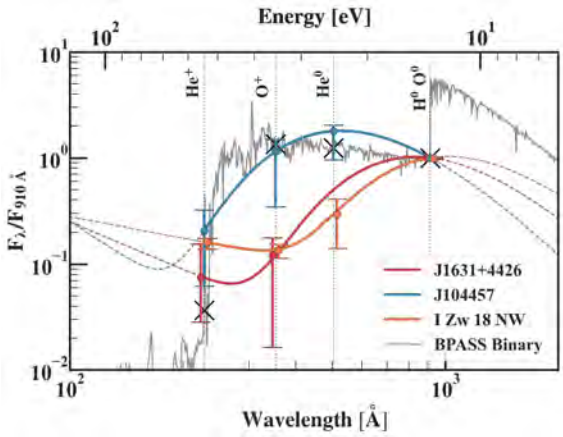

Fig. 11. Ionizing spectrum shapes reproduced for J1631+4426 (red line), J104457 (blue line), and I Zw 18 NW (orange line) with our MCMC methods. The grey line is an example ionizing spectrum from the BPASS binary model (Age = 10 Myr, $Z_* = 0.05Z_\odot$). The vertical dotted lines mark the ionization energies of H^0, O^0, He^0, O^+, and He^+. The colored dot (bar) represents the value of flux (the range of uncertainty) at each ionization energy for the best-fit ionizing spectra. The black cross represents the value of flux at each ionization energy for the BPASS binary model. All ionizing spectra are normalized at 910 Å

EMPRESS. VII. Ionizing Spectrum Shapes of Extremely Metal-Poor Galaxies: Uncovering the Origins of Strong* He II *and the Impact on Cosmic Reionization [4]

In collaboration with the members of National Astronomical Observatory of Japan, and University College London.

Strong high-ionization lines such as He II of young galaxies are puzzling at high and low redshift. Although recent studies suggest the existence of non-thermal sources, whether their ionizing spectra can consistently explain multiple major emission lines remains a question. Here we derive the general shapes of the ionizing spectra for three local extremely metal-poor galaxies (EMPGs) that show strong He IIλ4686. We parameterize the ionizing spectra composed of a blackbody and power-law radiation mimicking various stellar and non-thermal sources. We use photoionization models for nebulae, and determine seven parameters of the ionizing spectra and nebulae by Markov Chain Monte Carlo methods, carefully avoiding systematics of abundance ratios. We obtain the general shapes of ionizing spectra explaining ~ 10 major emission lines within observational errors with smooth connections from observed X-ray and optical continua. We find that an ionizing spectrum of one EMPG has a blackbody-dominated shape, while the others have convex downward shapes at > 13.6 eV, which indicate a diversity of the ionizing spectrum shapes (Figure 11). We confirm that the convex downward shapes are fundamentally different from ordinary stellar spectrum shapes, and that the spectrum shapes of these galaxies are generally explained by the combination of the stellar and ultra-luminous X-ray sources. Comparisons with stellar synthesis models suggest that the diversity of the spectrum shapes arises from differences in the stellar age. If galaxies at $z \gtrsim 6$ are similar to the EMPGs, high energy (> 54.4 eV) photons of the non-stellar sources negligibly contribute to cosmic reionization due to relatively weak radiation.

Bibliography

[4] Umeda, H., Ouchi, M., Nakajima, K., Isobe, Y., Aoyama, S., Harikane, Y., Ono, Y., Matsumoto, A., 2022, The Astrophysical Journal, 930, 37

EMPRESS. VIII. A New Determination of Primordial He Abundance with Extremely Metal-Poor Galaxies: A Suggestion of the Lepton Asymmetry and Implications for the Hubble Tension [5]

In collaboration with the members of National Astronomical Observatory of Japan, Kavli Institute for the Physics and Mathematics of the Universe, University College London, Waseda University, The Graduate University for Advanced Studies (SOKENDAI), Osaka University, University of Nevada, University of Geneva, University of Notre Dame, Tohoku University, Monash University, Kitami Institute of Technology, Cosmic Dawn Center (DAWN), University of Copenhagen, Ichinoseki College, Osaka Sangyo University, Ehime University, Carnegie Observatories, University of Hyogo, Nagoya University, University of Tsukuba, and University of Arizona.

The primordial He abundance $Y_{\rm P}$ is a powerful probe of cosmology. Currently, $Y_{\rm P}$ is best determined by observations of metal-poor galaxies, while there are only a few known local extremely metal-poor ($< 0.1Z_\odot$) galaxies (EMPGs) having

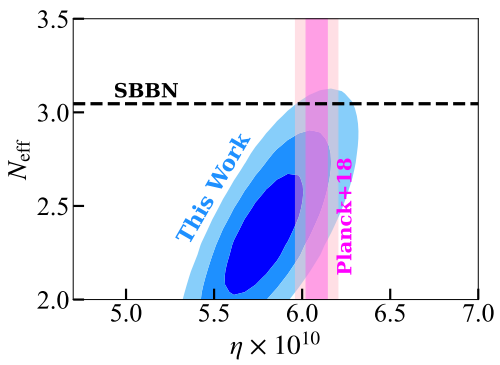

Fig. 12. Observational constrains on η and $N_{\rm eff}$. The blue contours show the 1σ, 2σ, and 3σ levels determined by this work. The black dashed line shows the standard model value of $N_{\rm eff} = 3.046$. The magenta and light magenta bands represent the Planck constraint on η at the 1σ and 2σ levels, respectively.

reliable He/H measurements with HeIλ10830 near-infrared (NIR) emission. Here we present deep Subaru NIR spectroscopy for 10 EMPGs. Combining the existing optical data, He/H values of 5 out of the 10 EMPGs are reliably derived by the Markov chain Monte Carlo algorithm. Adding the existing 3 EMPGs and 51 moderately metal-poor ($0.1-0.4Z_\odot$) galaxies with reliable He/H estimates, we obtain $Y_{\rm P} = 0.2370^{+0.0034}_{-0.0033}$ by linear regression in the $({\rm He/H})-({\rm O/H})$ plane, where we increase the number of EMPGs from 3 to 8 anchoring He/H of the most metal-poor gas in galaxies. Although our $Y_{\rm P}$ measurement and previous measurements are consistent, our result is slightly ($\sim 1\sigma$) smaller due to our EMPGs. Including the existing primordial deuterium $D_{\rm P}$ measurement, we constrain the effective number of neutrino species $N_{\rm eff}$ and the baryon-to-photon ratio η showing $\gtrsim 1-2\sigma$ tensions with the Standard Model and Planck Collaboration et al. (Figure 12). Motivated by the tensions, we allow the degeneracy parameter of electron-neutrino ξ_e to vary as well as $N_{\rm eff}$ and η. We obtain $\xi_e = 0.05^{+0.03}_{-0.02}$, $N_{\rm eff} = 3.11^{+0.34}_{-0.31}$, and $\eta \times 10^{10} = 6.08^{+0.06}_{-0.06}$ from the $Y_{\rm P}$ and $D_{\rm P}$ measurements with a prior of η taken from the literature. Our constraints suggest a lepton asymmetry and allow for a high value of $N_{\rm eff}$ within the 1σ level, which could mitigate the Hubble tension.

Bibliography

[5] Matsumoto, A., Ouchi, M., Nakajima, K., Kawasaki, M., Murai, K., Motohara, K., Harikane, Y., Ono, Y., Kushibiki, K., Koyama, S., Aoyama, S., Konishi, M., Takahashi, H., Isobe, Y., Umeda, H., Sugahara, Y., Onodera, M., Nagamine, K., Kusakabe, H., Hirai, Y., Moriya, T. J., Shibuya, T., Komiyama, Y., Fukushima, K., Fujimoto, S., Hattori, T., Hayashi, K., Inoue, A. K., Kikuchihara, S., Kojima, T., Koyama, Y., Lee, C.-H., Mawatari, K., Miyata, T., Nagao, T., Ozaki, S., Rauch, M., Saito, T., Suzuki, A., Takeuchi, T. T., Umemura, M., Xu, Y., Yabe, K., Zhang, Y., Yoshii, Y., 2022, The Astrophysical Journal, 941, 167

Theory Group

Overview

The theory group is active in elementary particle physics focusing on particle phenomenology, and in astroparticle physics focusing on particle cosmology. In particle physics, the main topics are theoretical studies of dark matter, inflation and extensions of the standard model. In astroparticle physics, the main topics are theoretical studies of inflation, thermal history of the early universe, dark matter, baryogenesis and big-bang nucleosynthesis.

After the discovery of the Higgs boson, the LHC has shown no strong hints on new physics. In this situation, we need to reconsider many ideas of new physics models as well as conventional strategies to search for them. Accordingly, our studies on beyond the Standard Model physics becomes more and more diverse.

Since the LIGO detectors detected the first confirmed gravitational waves (GWs) from colliding black holes on September 14, 2015, new era of GW astronomy began. So far, six GW events were detected by LIGO. Among them is the first detection of GW from binary neutron star. The discovery suggested strongly the existence of kilonova which can produce r-process elements. If they continue to find GW events from black holes and neutron stars, their origin becomes one of the most interesting topics.

The supersymmetric (SUSY) extension of the standard model (SM) in the particle physics is considered to be one of the most promising models beyond the standard model. It solves the naturalness problem for the Higgs boson mass term in the standard model, and it is also compatible with the grand unified theories (GUTs). Although no hints of the superparticles have been indicated from the LHC yet, the SUSY models are the most attractive candidates beyond the Standard Model. Our group has been studying phenomenological and cosmological aspects of the SUSY models.

Recent cosmological observations including the Planck data determine precisely the mean densities of matter and baryon in the Universe, and existence of non-baryonic dark matter is established. Weakly interacting massive particles (WIMPs) are considered to be good candidates of the dark matter. They act as the cold dark matter in the structure formation of the universe. Our group has been studying model building for dark matter and detectability in direct and indirect search experiments.

For understanding of the early universe, a role of the elementary particle physics is crucial. Recent progress in the particle physics such as grand unification theories and supersymmetry leads us to a more deeper insight into the fundamental aspects of the early universe. In the inflationary universe, the quantum fluctuations of the scalar field which drives the inflation become the density fluctuations and lead to formation of the structure observed in the present universe. On the other hand cosmology and astrophysics are used to test new theories in particle physics. Such particle cosmology is one of main subjects of our group.

Big Bang Nucleosynthesis (BBN) is one of the most important subjects in modern cosmology. Predicted abundances

of the light elements are very sensitive to the cosmological scenario. On the other hand, physics beyond the standard model predicts the new particles which would have existed at the BBN epoch. Such particles may spoil the success of BBN, which leads to constraints on the new particles and the particle physics models.

The grand unified theories predict that our universe undergoes several vacuum phase transitions. In the course of phase transitions topological defects (monopoles, cosmic strings and domain walls) are generally produced depending on symmetries of the vacua. Our group has studied evolution of various topological defects.

Particle Phenomenology

[Spokesperson : M. Ibe]
ICRR, The Univ. of Tokyo, Kashiwa, Chiba 277-8582

Beyond Standard Model

• More on fake GUT [1]

In collaboration with the members of ICRR, Kavli IPMU, KEK, Tsung-Dao Lee Inst.

It is remarkable that the matter fields in the Standard Model (SM) are apparently unified into the $\mathrm{SU}(5)$ representations. A straightforward explanation of this fact is to embed all the SM gauge groups into a simple group containing $\mathrm{SU}(5)$, i.e., the grand unified theory (GUT). Recently, however, a new framework "fake GUT" has been proposed. In this new framework, the apparent matter unification can be explained by a chiral gauge group G, $G \supset \mathrm{SU}(5)$. We emphasize that the SM matter fields are not necessarily embedded into the chiral representations to explain the apparent unification. In this paper, we discuss details of concrete realizations of the fake GUT model. We first study the model based on $\mathrm{SU}(5) \times \mathrm{U}(2)_H$, where $\mathrm{SU}(3)_c$ in the SM is from $\mathrm{SU}(5)$ while $\mathrm{SU}(2)_L \times \mathrm{U}(1)_Y$ are from the diagonal subgroups of $\mathrm{SU}(5) \times \mathrm{U}(2)_H$. We also extend this model to the one based on a semi-simple group, $\mathrm{SU}(5) \times \mathrm{SU}(3)_H$, so that $\mathrm{U}(2)_H$ is embedded in $\mathrm{SU}(3)_H$. We also show that this framework predicts rather different decay patterns of the proton, compared to the conventional GUT.

• Chiral Z' in FASER, FASER2, DUNE, and ILC beam dump experiments [2]

In collaboration with the members of ICRR, Yokohama National Univ., Hokkaido Univ., Sichuan Univ.

The origin of neutrino mass is a big unsolved problem of the Standard Model (SM) that motivate us to consider beyond the SM (BSM) scenarios where SM-singlet right-handed neutrinos (RHNs) are introduced to explain the origin of the light neutrino masses through the seesaw mechanism. There is a variety of ways which could lead us to this goal and one of them is a general $\mathrm{U}(1)$ extension of the SM. In this scenario, three SM-singlet RHNs are introduced to cancel the gauge and mixed gauge gravity anomalies. After anomaly cancellation, we notice that the left- and right-handed charged fermions are differently charged under the general $\mathrm{U}(1)$ gauge group evolving a chiral scenario. After the breaking of the general $\mathrm{U}(1)$ symmetry, a neutral BSM gauge boson (Z') acquires mass and it is a free parameter. Such Z', being lighter than 5 GeV, could be probed at the intensity and lifetime frontiers like FASER, FASER2, DUNE, and ILC beam dump experiments. The estimated bounds are needed to be compared with the existing bounds. We find that existing constraints from Orsay, Nomad, PS191, KEK, LSND, CHARM experiments, and cosmological scenario like SN1987A can be compared in our case once estimated for chiral scenarios. Finally, we compare the parameter spaces showing viable ones that could be probed by FASER, FASER2, DUNE, and ILC beam dump experiments and already excluded regions from Orsay, Nomad, PS191, KEK, LSND, CHARM, and SN1987A for a chiral scenario.

• Search for Lepton Flavor Violating Decay at FASER [3]

In collaboration with the members of Ohu Univ., ICRR, Yokohama National Univ., Saitama Univ., Kyushu Univ., Miyazaki Univ., KEK

FASER is one of the promising experiments which search for long-lived particles beyond the Standard Model. In this paper, we consider charged lepton flavor violation (CLFV) via a light and weakly interacting boson and discuss the detectability by FASER. We focus on four types of CLFV interactions, i.e., the scalar-, pseudoscalar-, vector-, and dipole-type interaction, and calculate the sensitivity of FASER to each CLFV interaction. We show that, with the setup of FASER2, a wide region of the parameter space can be explored. Particularly, it is found that FASER2 has a sensitivity to very small coupling regions in which the rare muon decays, such as $\mu \to e\gamma$, cannot place bounds, and that there is a possibility to detect CLFV decays of the new light bosons.

• Muon $g-2$ and non-thermal leptogenesis in $U(1)_{L_\mu - L_\tau}$ model [4]

In collaboration with the members of ICRR, Kavli IPMU

The gauged $U(1)_{L_\mu - L_\tau}$ symmetry is the simplest possibility to explain the observed muon $g-2$, while being consistent with the neutrino oscillations through the seesaw mechanism. In this paper, we investigate if leptogenesis can work at the same time. At first glance, leptogenesis seems challenging because the right-handed neutrino masses are related to the $U(1)_{L_\mu - L_\tau}$ breaking scale of 10 - 100 GeV as required from the muon $g-2$. Contrary to this expectation, we find that non-thermal leptogenesis with the right-handed neutrino masses of $\mathcal{O}(10^7)$ GeV is possible. The successful scenario results in strict predictions on the neutrino oscillation parameters, which will be tested in future experiments.

Bibliography

[1] M. Ibe, S. Shirai, M. Suzuki, K. Watanabe and T. T. Yanagida, JHEP **07** (2022), 087

doi:10.1007/JHEP07(2022)087 [arXiv:2205.01336 [hep-ph]].

[2] K. Asai, A. Das, J. Li, T. Nomura and O. Seto, Phys. Rev. D **106** (2022) no.9, 095033 doi:10.1103/PhysRevD.106.095033 [arXiv:2206.12676 [hep-ph]].

[3] T. Araki, K. Asai, H. Otono, T. Shimomura and Y. Takubo, doi:10.1007/JHEP01(2023)145 [arXiv:2210.12730 [hep-ph]].

[4] S. Eijima, M. Ibe and K. Murai, [arXiv:2303.09751 [hep-ph]].

Supersymmetric Model

• Precise estimate of charged Wino decay rate [1]

In collaboration with the members of ICRR, Kavli IPMU

The Wino is an $\mathrm{SU}(2)_L$ triplet Majorana fermion and a well-motivated dark matter candidate. The mass difference between the charged and the neutral Winos is small thanks to the $\mathrm{SU}(2)_L$ symmetry. The small mass difference makes the charged Wino meta-stable, which provides disappearing charged track signatures at collider experiments. The constraint on the Wino dark matter at the LHC strongly depends on the Wino lifetime. We compute the next-to-leading order (NLO) correction of the charged Wino decay and make the most precise estimate of the decay rate. We find that the NLO decay rate is determined by the mass difference and scarcely depend on the Wino mass itself in the heavy Wino limit. As a result, we find the NLO correction gives a minor impact on the lifetime of $2-4\%$ increase.

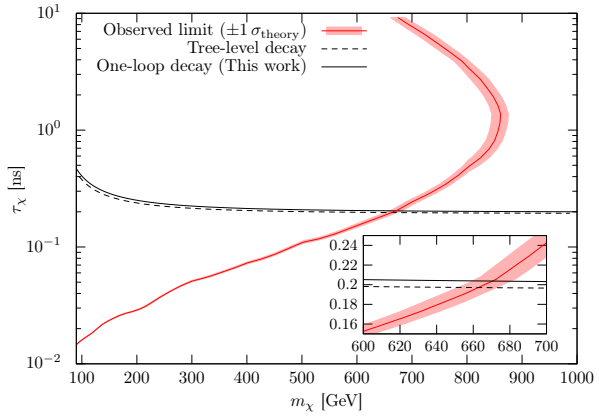

Fig. 13. The LHC constraint on the charged Wino mass and lifetime based on the disappearing charged track search. The red solid line shows the 95% CL limit by the ATLAS with data of $\int \mathscr{L} dt = 136$ fb^{-1} and $\sqrt{s} = 13$ TeV. The red band shows $\pm1\sigma$ uncertainty of the production cross section of the Wino. The black solid line is the prediction with the two-loop mass difference and the one-loop decay rate, whereas the dashed line shows the result of the tree-level calculation.

Bibliography

[1] M. Ibe, M. Mishima, Y. Nakayama and S. Shirai, JHEP **01** (2023), 017 doi:10.1007/JHEP01(2023)017 [arXiv:2210.16035 [hep-ph]].

Dark Matter

• Revisiting sterile neutrino dark matter in gauged $U(1)_{L_\mu - L_\tau}$ model [1]

In collaboration with the members of ICRR, Hokkaido Univ., Miyazaki Univ., Kyushu Univ.

We reexamine sterile neutrino dark matter in gauged $U(1)_{B-L}$ model. Improvements have been made by tracing and careful evaluation of the evolution of the number densities of sterile neutrinos N and extra neutral gauge bosons Z'. As a result, the cosmologically-interesting gauge coupling of $U(1)_{B-L}$ for freeze-in sterile neutrinos turns out to be smaller than the values reported in the literature. This avoids the overproduction of Z' so that it is consistent with the big bang nucleosynthesis and the cosmic microwave background constraints on the effective number of neutrino species. Similarly, the free-streaming length constraints exclude a large parameter space derived in previous studies. In addition to known freeze-in pair production of N from the standard model fermion pairs, we find the case that N is dominantly produced from a pair of Z' at the temperature characterized by the $B-L$ breaking scalar mass. Thus, the naive truncation of the $U(1)_{B-L}$ scalar contribution made in the literature is not valid.

• Asymmetric mediator in scotogenic model [2]

In collaboration with the members of ICRR, Yokohama National Univ., Saitama Univ.

The scotogenic model is the Standard Model (SM) with Z_2 symmetry and the addition of Z_2 odd right-handed Majorana neutrinos and $\mathrm{SU}(2)_L$ doublet scalar fields. We have extended the original scotogenic model by an additional Z_2 odd singlet scalar field that plays a role in dark matter. In our model, the asymmetries of the lepton and Z_2 odd doublet scalar are simultaneously produced through CP-violating right-handed neutrino decays. While the former is converted into baryon asymmetry through the sphaleron process, the latter is relaid to the DM density through the decay of $\mathrm{SU}(2)_L$ doublet scalar that is named "asymmetric mediator". In this way, we provide an extended scotogenic model that predicts the energy densities of baryon and dark matter being in the same order of magnitude, and also explains the low-energy neutrino masses and mixing angles.

• Sub-GeV dark matter search at ILC beam dumps [3]

In collaboration with the members of ICRR, Yokohama National Univ., ELTE, Cornell Univ., KEK, SOKENDAI, Peking Univ.

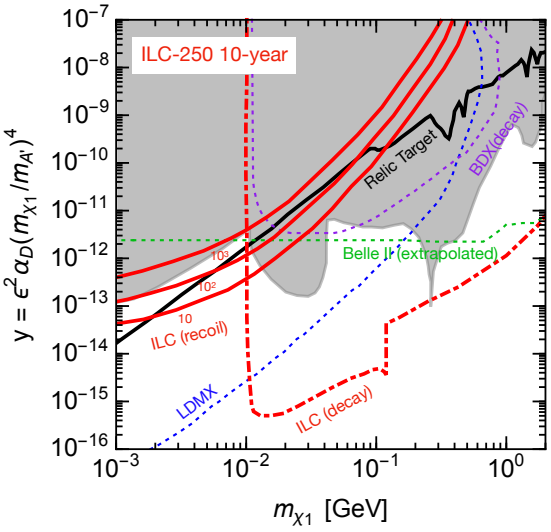

Fig. 14. Projected sensitivity reach of the ILC positron beam dump experiment in a 10-year ILC-250 run in the pseudo-Dirac DM model with a large mass-splitting, $\Delta = 0.1 m_{\chi_1}$. It is assumed that $\alpha_D = 0.5$ and $m_{A'} = 3m_\chi$. The three red solid lines show the sensitivity of the ILC-BDX recoil-electron search, corresponding to $10, 10^2$, and 10^3 signal events, and the dot-dashed lines show the sensitivity of the ILC-BDX decay-signal search (95% C.L. exclusion). The black solid line shows DM relic targets. The shaded grey region is excluded by the past experiments. Also shown are expected sensitivities of the BDX visible-decay search (purple-dashed lines), the LDMX (blue), and Belle II (green).

Light dark matter particles may be produced in electron and positron beam dumps of the International Linear Collider (ILC). We propose an experimental setup to search for such events, the Beam-Dump eXperiment at the ILC (ILC-BDX). The setup consists of a muon shield placed behind the beam dump, followed by a multi-layer tracker and an electromagnetic calorimeter. The calorimeter can detect electron recoils due to elastic scattering of dark matter particles produced in the dump, while the tracker is sensitive to decays of excited dark-sector states into the dark matter particle. We study the production, decay and scattering of sub-GeV dark matter particles in this setup in several models with a dark photon mediator. Taking into account beam-related backgrounds due to neutrinos produced in the beam dump as well as the cosmic-ray background, we evaluate the sensitivity reach of the ILC-BDX experiment. We find that the ILC-BDX will be able to probe interesting regions of the model parameter space and, in many cases, reach well below the relic target.

Bibliography

[1] S. Eijima, O. Seto and T. Shimomura, Phys. Rev. D **106** (2022) no.10, 103513 doi:10.1103/PhysRevD.106.103513 [arXiv:2207.01775 [hep-ph]].

[2] K. Asai, Y. Sakai, J. Sato, Y. Takanishi and M. Yamanaka, Phys. Lett. B **836** (2023), 137627 doi:10.1016/j.physletb.2022.137627 [arXiv:2209.08257 [hep-ph]].

[3] K. Asai, S. Iwamoto, M. Perelstein, Y. Sakaki and D. Ueda, [arXiv:2301.03816 [hep-ph]].

Topological Defect

• More on Dark Topological Defects [1]

In collaboration with the members of ICRR

We consider a model of dark photon which appears as a result of the successive symmetry breaking $\mathrm{SU}(2) \to \mathrm{U}(1) \to \mathbb{Z}_2$, where various types of topological defects appear in the dark sector. In this paper, we study the interactions between QED charges and the dark topological defects through mixing between QED photon and dark photon. In particular, we extend our previous analysis by incorporating the magnetic mixing and θ-terms. We also consider the dyons and dyonic beads in the dark sector. Notably, dark magnetic/dyonic beads are found to induce a QED Coulomb potential through the magnetic mixing despite finite mass of the dark photon.

Bibliography

[1] A. Chitose and M. Ibe, [arXiv:2303.10861 [hep-ph]].

Particle Cosmology

[Spokesperson : M. Kawasaki]
ICRR, The Univ. of Tokyo, Kashiwa, Chiba 277-8582

Gravitational Wave

• Enhancement of second-order gravitational waves at Q-ball decay [1]

In collaboration with the members of Kanagawa Univ., ICRR, Kavli IPMU

The recent observation of ^{4}He favors a large lepton asymmetry at the big bang nucleosynthesis. If Q-balls with a lepton charge decay after the electroweak phase transition, such a large lepton asymmetry can be generated without producing too large baryon asymmetry. In this scenario, Q-balls dominate the universe before the decay and induces the sharp transition from the early matter-dominated era to the radiation-dominated era. In this transition, the gravitational waves (GWs) are enhanced through a second-order effect of the scalar perturbations. We evaluate the density of the produced GWs and show that pulsar timing array observations can probe this scenario depending on the amplitude of the scalar perturbations.

Bibliography

[1] S. Kasuya, M. Kawasaki and K. Murai, [arXiv:2212.13370 [astro-ph.CO]].

Primordial Black Holes

• Revisiting the Affleck-Dine mechanism for primordial black hole formation [1]

In collaboration with the members of ICRR, Kavli IPMU

We study a primordial black hole (PBH) formation scenario based on the Affleck-Dine (AD) mechanism and investigate two PBH mass regions: $M \sim 30M_\odot$ motivated by the LIGO-Virgo observations of the binary black hole mergers and $M \gtrsim 10^4 M_\odot$ motivated by the observations of supermassive black holes at the center of galaxies. In the previous studies, it has been considered that the inhomogeneous AD baryogenesis generates regions with a large baryon asymmetry, some of which collapse into PBHs. In this paper, we show that this scenario is severely constrained due to the baryon asymmetry remaining outside PBHs, which would spoil the success of the big bang nucleosynthesis. Then, we propose an alternative scenario where the AD leptogenesis results in the inhomogeneous formation of Q-balls with lepton charges, which collapse into PBHs. As a result, we find that our scenario can explain the favorable PBH abundance without conflicting with the observational constraints.

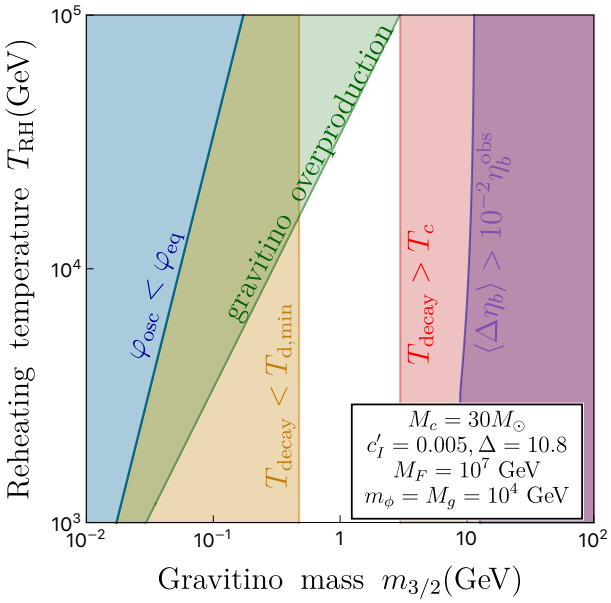

Fig. 15. Constraints on $m_{3/2}$ and $T_{\rm RH}$ in the delayed-type L-ball scenario for $M_F = 10^7$ GeV and $m_\phi = 10^4$ GeV. We take $(c_I', \Delta, f_{\rm PBH}) = (0.005, 10.8, 1.1 \times 10^{-3})$ for $M_c = 30M_\odot$. The green regions are excluded from the gravitino problem. The orange regions are excluded from the observation of $N_{\rm eff}$, and the red regions are excluded because the L-balls decay before the PBH formation. In the blue regions, our assumption $\varphi_{\rm osc} > \varphi_{\rm eq}$ is not satisfied. In the purple regions, the baryon asymmetry from L-balls can spoil the success of the standard BBN.

Bibliography

[1] K. Kasai, M. Kawasaki and K. Murai, JCAP **10** (2022), 048 doi:10.1088/1475-7516/2022/10/048 [arXiv:2205.10148 [astro-ph.CO]].

Dark Matter

• Stochastic effects on observation of ultralight bosonic dark matter [1]

In collaboration with the members of ICRR, Univ. of Wisconsin-Milwaukee, Waseda Univ., RESCEU, Univ. of Tokyo, JST, JAXA, Max Planck Inst.

Ultralight bosonic particles are fascinating candidates of dark matter (DM). It behaves as classical waves in our Galaxy due to its large number density. There have been various methods proposed to search for the wave-like DM, such as methods utilizing interferometric gravitational-wave detectors. Understanding the characteristics of DM signals is crucial to extract the properties of DM from data. While the DM signal is nearly monochromatic with the angular frequency of its mass, the amplitude and phase are gradually changing due to the velocity dispersion of DMs in our Galaxy halo. The stochastic amplitude and phase should be properly taken into account to accurately constrain the coupling constant of DM from data. Previous works formulated a method to obtain the upper bound on the coupling constant incorporating the stochastic effects. One of these works compared the upper bound with and without the stochastic effect in a measurement time that is much shorter than the variation time scale of the amplitude and phase. In this paper, we extend their formulation to arbitrary measurement time and evaluate the stochastic effects. Moreover, we investigate the velocity-dependent signal for dark photon DM including an uncertainly of the velocity. We demonstrate that our method accurately estimates the upper bound on the coupling constant with numerical simulations. We also estimate the expected upper bound of the coupling constant of axion DM and dark photon DM from future experiments in a semi-analytic way. The stochasticity especially affects constraints on a small mass region. Our formulation offers a generic treatment of the ultralight bosonic DM signal with the stochastic effect.

Bibliography

[1] H. Nakatsuka, S. Morisaki, T. Fujita, J. Kume, Y. Michimura, K. Nagano and I. Obata, [arXiv:2205.02960 [astro-ph.CO]].

CMB

• Isotropic cosmic birefringence from early dark energy [1]

In collaboration with the members of ICRR, Kavli IPMU, Univ. of Tokyo, RESCEU, Max Planck Inst.

A tantalizing hint of isotropic cosmic birefringence has been found in the *EB* cross-power spectrum of the cosmic microwave background (CMB) polarization data with a statistical significance of 3σ. A pseudoscalar field coupled to the CMB photons via the Chern-Simons term can explain this

observation. The same field may also be responsible for early dark energy (EDE), which alleviates the so-called Hubble tension. Since the EDE field evolves significantly during the recombination epoch, the conventional formula that relates EB to the difference between the E- and B-mode auto-power spectra is no longer valid. Solving the Boltzmann equation for polarized photons and the dynamics of the EDE field consistently, we find that currently favored parameter space of the EDE model yields a variety of shapes of the EB spectrum, which can be tested by CMB experiments.

• Constraint on Early Dark Energy from Isotropic Cosmic Birefringence [2]

In collaboration with the members of Univ. of Oslo, Imperial College London, Max Planck Inst., Kavli IPMU, ICRR, Univ. of Tokyo, RESCEU

Polarization of the cosmic microwave background (CMB) is sensitive to new physics violating parity symmetry, such as the presence of a pseudoscalar "axionlike" field. Such a field may be responsible for early dark energy (EDE), which is active prior to recombination and provides a solution to the so-called Hubble tension. The EDE field coupled to photons in a parity-violating manner would rotate the plane of linear polarization of the CMB and produce a cross-correlation power spectrum of E- and B-mode polarization fields with opposite parities. In this paper, we fit the EB power spectrum predicted by the photon-axion coupling of the EDE model with a potential $V(\phi) \propto [1-\cos(\phi/f)]^3$ to polarization data from Planck. We find that the unique shape of the predicted EB power spectrum is not favored by the data and obtain a first constraint on the photon-axion coupling constant, $g = (0.04 \pm 0.16) M_{\rm Pl}^{-1}$ (68% CL), for the EDE model that best fits the CMB and galaxy clustering data. This constraint is independent of the miscalibration of polarization angles of the instrument or the polarized Galactic foreground emission. Our limit on g may have important implications for embedding EDE in fundamental physics, such as string theory.

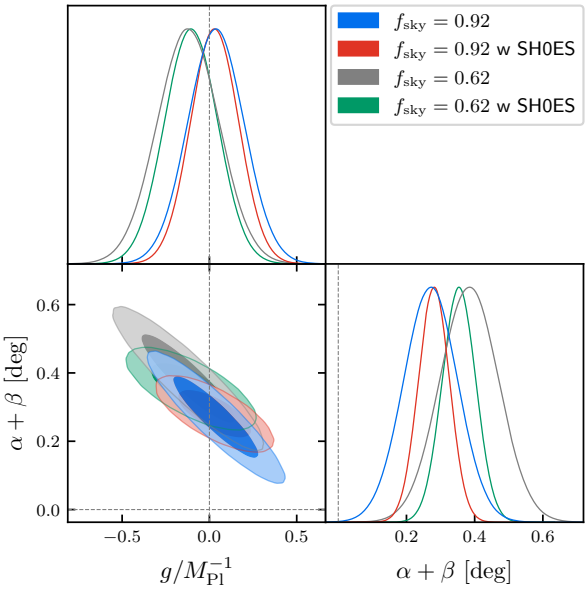

Fig. 16. Posterior distributions of $g/M_{\rm Pl}^{-1}$ and $\alpha+\beta$ for the best-fitting EDE parameters under the base and base+SH0ES data sets, and two Galactic masks.

Bibliography

[1] K. Murai, F. Naokawa, T. Namikawa and E. Komatsu, Phys. Rev. D **107** (2023) no.4, L041302 doi:10.1103/PhysRevD.107.L041302 [arXiv:2209.07804 [astro-ph.CO]].

[2] J. R. Eskilt, L. Herold, E. Komatsu, K. Murai, T. Namikawa and F. Naokawa, [arXiv:2303.15369 [astro-ph.CO]].

OBSERVATORIES and A RESEARCH CENTER

Location of the Institute and the Observatories

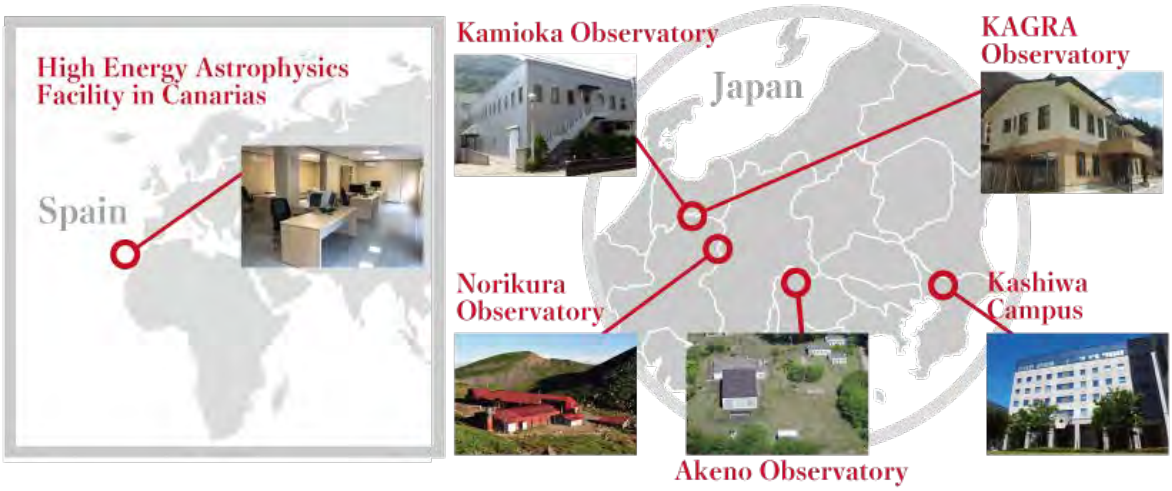

Norikura Observatory

Location:	Norikuradake, Nyukawa-cho, Takayama-shi, Gifu Prefecture 506-2100
Telephone (Fax):	+81-50-3730-3809
Telephone (satellite):	+81-90-7721-5674
Telephone (car):	+81-90-7408-6224

Akeno Observatory

Location:	5259 Asao, Akeno-machi, Hokuto-shi, Yamanashi Prefecture 408-0201
Telephone / Fax:	+81-551-25-2301 / +81-551-25-2303

Kamioka Observatory

Location:	456 Higashi-mozumi, Kamioka-cho, Hida-shi, Gifu Prefecture 506-1205
Telephone / Fax:	+81-578-85-2116 / +81-578-85-2121

KAGRA Observatory

Location:	238 Higashi-mozumi, Kamioka-cho, Hida-shi, Gifu Prefecture 506-1205
Telephone / Fax:	+81-578-85-2343 / +81-578-85-2346

Research Center for Cosmic Neutrinos

Location:	5-1-5 Kashiwanoha, Kashiwa, Chiba Prefecture 277-8582
Telephone / Fax:	+81-4-7136-3138 / +81-4-7136-3115

High Energy Astrophysics Facility in Canarias

Location:	C/Via Lactea, s/n E-38205 La Lagua - Tenerife Espana

NORIKURA OBSERVATORY

Introduction

Norikura Observatory (36.10°N and 137.55°E) was founded in 1953 and attached to ICRR in 1976. It is located at 2770 m above sea level, and is the highest altitude manned laboratory in Japan (Fig. 1). Experimental facilities of the laboratory are made available to all the qualified scientists in the field of cosmic ray research and associated subjects. The AC electric power is generated by the dynamo and supplied throughout the observatory. The observatory can be accessed easily by car and public bus in summer (July-September). The 60th anniversary of Norikura Observatory was celebrated in 2013.

Fig. 1. Norikura Observatory

Norikura Observatory gave manned operation to the observations by the qualified scientists all the year until the year 2003. However, the feasibility of the automatic operation of Norikura Observatory during winter period has been tested since winter 2004 in order to study the possibilities to reduce maintenance and labor costs without causing serious inconveniences for the researches. A long-distance (∼40km) wireless LAN system (11M bps) was set up in 2003. Two new easy-to-handle and easy-to-maintain dynamos of 115 KVA each, as shown in Fig. 2 were installed in 2004 as well. The unmanned operation of Norikura Observatory has been mostly successful in winter, during which the battery backed-up solar panels and/or wind power generators kept supplying the electricity to the wireless LAN and on-going cosmic-ray experiments.

Present major scientific interests of the laboratory is focused on the modulation of high energy cosmic rays in the interplanetary space associated with the solar activity, the generation of energetic particles by the solar flares, and the particle acceleration mechanism in thunderclouds, all of which require long-term observation. These researches have been carried out by the group of user universities, where ICRR provides them with laboratory facility. A part of the facility has been open for the environmental study at high altitude such as aerosol-related mechanism in the atmosphere, observation of total ozone and UV solar radiation, for botanical study in the high-altitude environment, etc..

Fig. 2. A dynamo of 115KV.

Cosmic Ray Physics

Space weather observation

Space weather observation is actively made by a 25 m^2 muon hodoscope at Norikura Observatory[1],[2],[3],[4],[5],[6],[7],[8],[9],[10]. Mt. Norikura muon hodoscope has started operation in May, 1998 and successfully observed a clear precursory signature of the interplanetary shock arrival at Earth. With its improved angular resolution of muon incident direction, the detector succeeded for the first time to observe a loss-cone signature which is an intensity deficit within a narrow cone around the interplanetary magnetic field (IMF). The observation of the loss-cone precursor gives us unique information for the space weather forecast and for understanding the interplanetary disturbances in near Earth space.

Following this successful observation, we installed a small muon hodoscope in Kuwait City, Kuwait as the fourth detector in our Global Muon Detector Network (GMDN) with other three multidirectional muon detectors in Nagoya (Japan), Hobart (Australia), and São Martinho (Brazil). The GMDN has started operation in March, 2006 monitoring the intensity of $\sim$ 50 GeV cosmic rays over an entire sky around Earth. The cosmic ray observations using muon detector are complementary to observations with neutron monitors monitoring a lower energy range below $\sim$ 10 GeV and the observations with GMDN have a great advantage particularly in precise measurement of the cosmic ray anisotropy, i.e. the dependence of intensity on incident direction in space, which gives us valuable information of the spatial distribution of the cosmic ray density in three dimensions. The Mt. Norikura muon hodoscope and GMDN have revealed the dynamic variations of the anisotropy which give us important information of the space weather. It has been already confirmed that the GMDN can measure the rapid variation of the anisotropy in the “cos-

mic ray burst" observed in June 2015 in 10 minute time resolution. The Kuwait muon hodoscope was enlarged three times in March 2016 and one minute data are now available from all of four detectors in the GMDN enabling us to analyze the anisotropy in 1 minute time resolution.

Recently, we also developed the method of the correction of the atmospheric temperature effect on muon count rate by using the GMDN data. This is a significant step, because it makes possible for the first time the analysis of the long-term variation of ~ 50 GeV cosmic ray density (i.e. isotropic intensity) which was possible so far only for cosmic ray below ~ 10 GeV using the neutron monitor data nearly free from the temperature effect. We have already published the long-term variation of the anisotropy observed by Nagoya muon detector.

Solar neutron observation

Observation of solar neutrons in solar cycle 24 has continued at Norikura Observatory of ICRR since fiscal 2007 to understand the acceleration mechanism of high energy ($>$100 MeV) ions associated with solar flares[11]. These neutrons are produced by the interaction between accelerated ions and the solar atmosphere. Neutrons are not reflected by the interplanetary magnetic field, and thought to be more informative than accelerated ions themselves to study the acceleration mechanism at the solar surface. Solar neutron events detected on the ground are rare, and about 10 events were reported before solar cycle 24. The group led by Institute for Space-Earth Environmental Research, Nagoya University has operated a world-wide network of 7 solar neutron telescopes in the world. The solar neutron telescope operated at Norikura Observatory has an area of 64 m^2, which is largest among the 7 stations. The solar neutron telescope at Norikura consists of plastic scintillation detector and proportional counters. The neutron is detected when a recoil proton is produced in the scintillator, and the energy of the recoil proton is measures. Proportional counters are used both to veto charged particles and measure the direction of recoil protons. The telescope is operated by solar power during the winter period when the Norikura observatory is closed.

Solar cycle 24 was its maximum in February 2014 and has decreased its activity since then. We searched for solar neutron signals from the world-wide network of the solar neutron telescopes between January 2010 and December 2014 when the large ($\geq$X1.0 class) solar flare occurred. No solar neutron event was detected by this search. We statistically studied the relation between upper limits of the neutron flux and the energy of soft X-rays during the solar flare. This comparison was also made for the successful detections of solar neutrons before solar cycle 24. The conclusion from this study is that the total energy obtained by neutrons during solar flare does not exceed 0.1 % of the total energy of soft X-rays.

Relativistic electron acceleration in thunderstorm electric field and high-energy atmospheric phenomena at lightning

The Gamma-Ray Observation of Winter THundercloud (GROWTH) collaboration is aiming at revealing high-energy atmospheric phenomena occurring at lightning and in thunderstorms[12],[13],[14],[15],[16]. The project started in 2006 and has detected bremsstrahlung gamma rays from relativistic electrons accelerated by strong electric fields in winter thunderstorms. This gamma-ray radiation events were named "long burst" by our group (as known as gamma-ray glow), which lasts for a minute time-scale corresponding with passage of a thundercloud above our detectors. Winter thunderstorms observed along the Japan sea are ideal targets for our observation campaigns thanks to its low altitude of the cloud base and frequent energetic lightning, while observations of summer thunderclouds at mountain tops are also important to measure the phenomena very close to or even inside thunderstorms. Our collaboration has used the Mount Norikura cosmic ray observatory to study the long bursts, and successfully recorded events.

The GROWTH collaboration newly launched multi-point mapping observation campaigns in 2015. The primary purpose is to study life cycle of the electron acceleration sites in thunderstorms comparing with weather-monitoring data. Another purpose of the project is to reveal mysterious "short burst" events, which have been sometimes detected in our past observations, associated with lightning discharges with its duration shorter than a second. Financially supported by the ICRR joint research programme, academic crowdfunding "academist", and JSPS/MEXT KAKENHI grant, we have developed portable and high-performance radiation detectors. In FY2016 and FY2017, the collaboration deployed radiation detectors at the Mt. Norikura cosmic ray observatory. So far, there is no detection of "long burst" nor "short burst" events from summer thunderclouds during the two years. However, we successfully used these summer campaigns as pilot observations toward the winter campaigns to check our operation and capability of the detectors. The Norikura observations are also educationally important as a training yard for Ph.D students in the team. In 2017 winter, our new mapping system at Kashiwazaki, Niigata, provided us a chance to solve the mystery of the short burst. This phenomena is revealed to be photonuclear reaction triggered by gamma rays from a lightning discharge. This discovery was selected, by the Physics World, as one of the top 10 breakthrough in the physics field in 2017. We are now trying to develop the "high-energy atmospheric physics" of lightning and thunderstorms, a new interdisciplinary field combining the gamma-ray and radio observations.

Study of Secondary Cosmic Rays from Thundercloud at Mt. Norikura

In order to study the relativistic electron acceleration mechanism by thundercloud-derived electric field and the relation between thunder and cosmic-ray air shower, we started an experiment in 2015, mainly using gamma-ray detectors at Norikura Observatory of Institute for Cosnic Ray Research, the University of Tokyo. This experiment consists of gamma-ray detectors, a lightning sensor, an electric field meter, a weather monitor, and an air shower array. Gamma-ray detectors using three crystals, NaI, CsI, and BGO respectively, cover the energy range over 3 orders of magnitude from 70 keV to 120 MeV as a whole.

Observation period: 22 days from August 24 to September 14, 2015
During this time, the thundercloud did not pass, and no gamma-ray burst derived from thundercloud was detected. However, the gamma ray detector was able to observe gamma rays derived from radon of less than 3 MeV as expected during rainfall. Also, gamma ray detectors using CsI and BGO for detecting gamma rays of 3 MeV or more did not observe an increase in gamma rays of 3 MeV or more. This means that gamma rays from radon can be distinguished from contributions from other gamma rays not derived from radon, and it can be expected that these detectors can operate normally even when they are installed at an altitude about 4000 m for a certain future project.

Observation period: 30 days from July 19 to September 16, 2016 (excluding the summer season)
No direct lightning strike event occurred during the observation period, but 6 atmospheric electric field fluctuations exceeding 30 kV/m, which seemed to be an influence of thunder cloud passage, were observed. In one of the events, it seems there was a lightning strike in the vicinity.

Observation period: 41 days from July 31 to September 9, 2017
Unfortunately, during this observation period there was no lightning strike nearby, but it was observed that the thundercloud passed several times. Currently, the data at the time of the thundercloud passing is being analyzed in detail (Fig. 3).

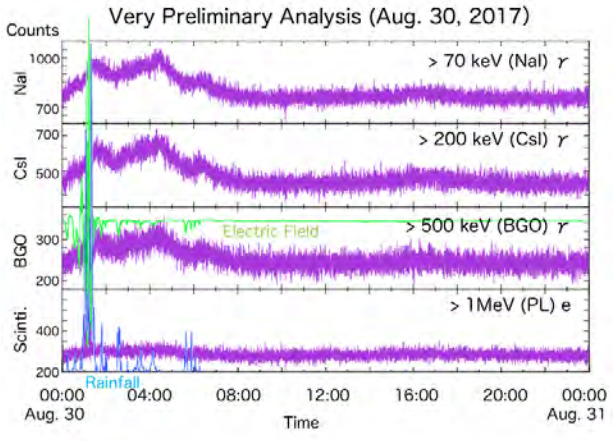

Fig. 3. Electric field (green), rainfall (blue), count value (purple) of each detector at the time of thundercloud passing.

Study of gamma ray bursts from mountain-top thunderclouds

We observed gamma ray bursts that arise in relation to thunderclouds at the Norikura Observatory of ICRR(2,770 m above sea level)[17],[18],[19],[20]. Measurement was carried out by placing PANDA64 detector outdoors of the observatory. The detector is made of 64-module plastic scintillators(total mass about 640 kg) developed for reactor operation monitoring. Our measurement has unprecedented features including high statistics, good energy response, direction sensitivity and neutron identification.

Long-duration persistent bursts were observed 12 times in 54 days from July to September 2014 and their energy spectrum extended up to 25 MeV in the largest burst. The duration of the bursts ranged from a few to ten minutes. Since these bursts were found in the energy range higher than 3 MeV, they were not attributed to the rain fallout of radon and its daughter nuclei.

According to the thundercloud information provided by the Japan Meteorological Agency, the bursts were observed when there was thunder activity near the observatory. The observation is qualitatively in good agreement with thundercloud radiation bursts previously observed in mountain areas or coastal areas of the Sea of Japan.

Monte Carlo simulation showed that the bremsstrahlung γ-rays by source electrons with monochromatic energy of 40–80 MeV falling downwards from altitude of 400–1000 m produced the observed total energy spectra of the bursts well. It is supposed that secondary cosmic ray electrons, which act as seed, were accelerated in electric field of thunderclouds and multiplied by relativistic runaway electron avalanche.

The estimated energy of the source electrons was higher than that of the bursts we previously observed at Ohi Power Station at sea level. Additionally, estimated electron flux at the estimated source height was remarkably lower than that of the Ohi site. These results give new restrictions to the model of electron acceleration and multiplication process in electric field of thunderclouds.

Development of high energy proton irradiation technique for devices used in spaceship

Space exploration is presently interesting in business field. Ion beam irradiation verification for devices to be mounted on spaceships is required to simulate cosmic rays expected in the universe to estimate lifetime of these devices[21],[22],[23],[24].

Flux estimation technique of primary ion beam in wide range from an accelerator is needed In this kind of cosmic ray simulation field. The desired flux of the ion beam for this kind of field is between 10^2 and 10^6 protons·cm^{-2} ·s^{-1} in typical proton cases. Plastic scintillators can be used in lower intense region to count direct primary ions, while ionization chambers can be used in higher intense region to count ionization caused by primary ions. But there have been no definite modalities available to measure throughout this whole intensity region.

One of the candidate techniques is to measure secondary γ-ray intensity emitted through a beam transport, which has nearly a maximum energy of the primary ion beam around 100 MeV for this kind of simulation field. This technique has a feature that detector components do not occupy the beam path and the presence of the detector do not influence the main simulation field at all.

NaI(Tl) scintillator system for high energetic γ-ray measurement which had been used in previous thunder lightning γ-ray measurement was used. This system has a 5-inch NaI(Tl) scintillator with NT100GPS pulse hight analysis system of Laboratory Equipment. Ion beam accelerator exper-

iments using 100 MeV proton beam were carried out at the Wakasa Wan Energy Research Center (WERC). Background measurements were carried out at Norikura Observatory of ICRR in summer, where one can expect high energetic γ-ray, which has the similar energy region compared to the accelerator field of this study. EFM100 atmospheric electric field monitor system of Boltek was added at Norikura to measure accidental high energetic γ-rays caused by thunder lightning.

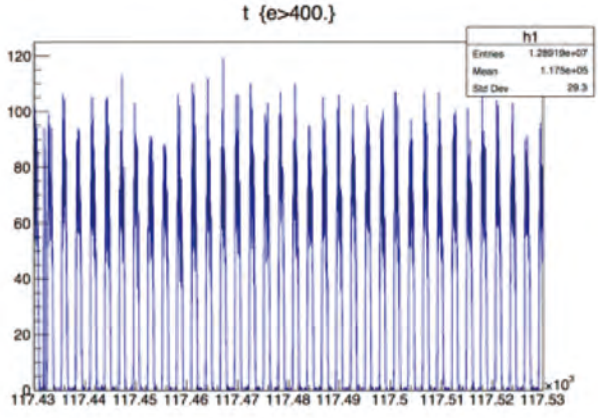

Fig. 4. Time structure of γ-ray above 3 MeV at WERC 100 MeV proton beam delivery. Vertical axis shows γ intensity (events/ms) while horizontal shows time after beginning of the operation (s).

As shown in Fig.4 of a time structure of γ-ray during 100 MeV proton beam delivery duration obtained at WERC, the result clearly shows that this measurement system can distinguish the beam ON/Off, while this system is still in verification for a quantitative discussion. The dead time of the system should be defined.

In the meantime, thunder lightning events were searched using data obtained at Norikura. No events have been distinguished. The whole data at Norikura show a stable condition of the whole system for a couple of months.

With the help of this study, the trial to carry out cosmic ray simulation at the ion beam accelerator facility (WERC) has been successfully carried out. One will keep trying to estimate the quantitative property of the system in ion beam environment.

Development of high energy proton irradiation technique for devices used in spaceship

Aircraft crew are exposed to elevated levels of cosmic rays at aviation since the dose rate of cosmic rays increases with altitude. The occupational doses of aircraft crew have generally been evaluated by model calculation. It is necessary to verify the calculation with measurements to maintain accuracy and credibility of dose assessment. The purposes of this study were to construct a compact and inexpensive cosmic-ray neutron monitoring system which was based on a rem-counter at Norikura Observatory (2770 m above sea level), and to examine the feasibility of it. The monitoring system was installed in the Norikura Observatory in 2014. It consisted of an extended-energy neutron rem counter with wide energy range from 25 meV to 5 GeV, a custom-made data logger connected to LAN, and a battery power unit. The measured data was received in National Institute of Radiological Science in Chiba-city via the ICRR network. This monitoring system succeeded in continuous monitoring more than ten months twice during 2014 to 2016. The averaged counting rate was about 1 count per minute, which was equivalent to neutron ambient dose equivalent rate of about 15 nSv/h by the preliminary evaluation. It is a future problem to reveal the cause of the reduction in counting rate seen over from November to April.

Evaluation of Response to the Gamma-ray of the Emulsion Telescope (2007, 2013)

GRAINE project (Gamma-Ray Astro-Imager with Nuclear Emulsion) has been developing the observation of cosmic γ-ray in the energy range 10 MeV–100 GeV with precise (0.08° at 1–2 GeV), polarization-sensitive, large-aperture-area ($\sim$10 m^2) balloon-borne telescope using nuclear emulsion film[25],[26],[27],[28],[29],[30],[31]. Under the development of the telescope, we performed test observation at Norikura Observatory (2770 m a.s.l.) in 2007 and 2013 using prototype emulsion telescope in order to confirm detection performance using atmospheric γ-ray.

2007 test was the first trial of the detection to the γ-ray spread wide incoming angle. We established configuration of the telescope and its analysis scheme. Based on this experience, we finalized the design of the first balloon-borne emulsion telescope and performed 1st balloon experiment (GRAINE 2011) at the Taiki Aerospace Research Field of JAXA in June 2011.

In 2013 test, we introduced self-produced nuclear emulsion gel film with higher volume occupancy of silver bromide crystals with respect to conventional ordinary gel in order to improve track finding efficiency as well as signal-to-noise ratio. We obtained high ($> 97\%$) track finding efficiency in a single film and confirmed γ-ray detection capability at 100 MeV energy region (Figure 5).

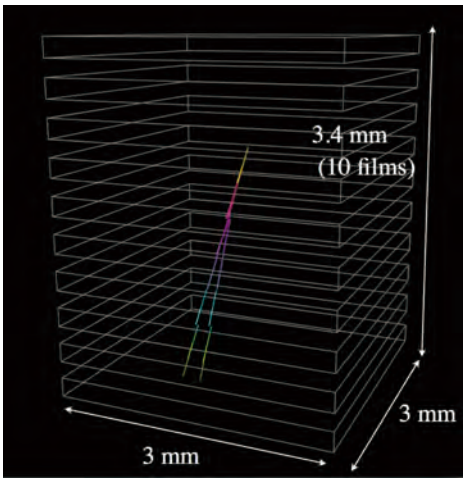

Fig. 5. 3-D view of $\gamma \to e^+ + e^-$ detected in the chamber employed in the obseration test at Norikura Observatory. The reconstructed energy of this event was 160 MeV.

Based on this experience, we performed 2nd balloon experi-

ment (obs/Norikura/GRAINE 2015) in Japan-Australia JAXA collaborative balloon experiment at the Alice Springs balloon-launching station in May 2015.

Environmental Study

Aerosol sampling at Mt. Norikura

Aerosol in the atmosphere has been sampled since 2013 at the Norikura observing site using air-samplers to investigate the production of cosmogenic nuclide ^{7}Be in a free troposphere above 2 km in the altitude. The aerosol size distribution of ^{7}Be was measured for the aerosols sampled by an Andersen sampler enable to separate aerosols to nine classes from 0.43 μm to 11 μm. The 81.7% of ^{7}Be was covered with the aerosol sizes less than 1.1 μm and the ^{7}Be with the aerosol sizes above 1.1 μm decrease with an exponential function. The ^{7}Be concentration at Mt. Norikura was approximately 9.4 times greater than that at the ground level in Yamagata-city (Fig.6.). Its ratio is almost consistent to a simulated ratio 8.8 of ^{7}Be productions due to secondary cosmic rays in the atmosphere by EXPACS. This experimental result is useful for an estimation of altitude distribution of cosmogenic nuclide.

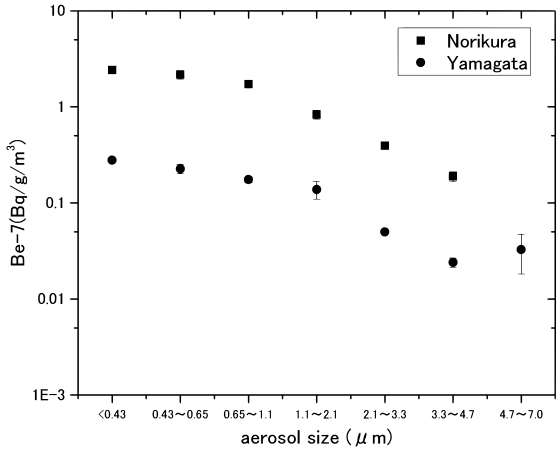

Fig. 6. ^{7}Be concentration as a function of aerosol size

Adaptation of alpine plants to severe environmental conditions

Trees in the alpine regions experience harsh conditions including strong winds, low temperatures, desiccation, and heavy snow. Thus, plants growing in such regions are predicted to have adaptations to these environmental stressors. Through the inter-university research of ICRR, we obtained an opportunity to intensively study plant responses to environmental factors. We identified several characteristics unique to alpine plants, some of which contradict conventional knowledges[32],[33],[34].

1. Adaptation of leaf cuticles in sub-alpine fir (Abies mariesii) at the alpine tree-line

Leaf browning and death are frequently observed in evergreen conifers at the alpine tree-line. These are thought to due to increased transpiration caused by a thinner cuticle and/or mechanical damage to the cuticle by wind-blown snow and ice particles. However, in the sub-alpine fir (Abies mariesii) at Mt. Norikura, mechanical damage was not observed, and the cuticle was rather thick, which may be an adaptation against overwintering at the alpine regions.

2. Embolism of sub-alpine fir (Abies mariessii) at the alpine tree-line

Trees at high altitudes experience severe embolism (loss of xylem conductivity for water) during winters, which is attributed to the entrapment of air in xylem conduits during frost-drought. However, in the sub-alpine fir (Abies mariessii) at Mt. Norikura, air-filled conduits were not observed even in severely-embolized (complete loss of conductivity) shoots. Rather, the pits (valves of partitions inter-conduits) closed before the severe frost-drought in mid-winter, thereby resulting in severe-embolism (complete loss of conductivity). Thus, by pit (valve) cloure, shoots could maintain water in the xylem throughout the winter, which is thought to be an adaptation against lethal filling of air in the conduits during severe frost-drought.

3. Photosynthesis of Haimatsu (Pinus pumila)

At wind-exposed sites on Mt. Norikura, photosynthesis in Haimatsu was suppressed by lower mesophyll CO_2 conductance, and not by stomatal closure.

Investigation of alpine plants on Mt. Norikura

We studied mainly the following three researches on Mt. Norikura after 2012[35],[36],[37],[38],[39],[40],[41],[42],[43],[44],[45],[46],[47],[48],[49].

1) Long-term monitoring and community assembly of alpine plants

We made 40 plots for long-term monitoring of alpine vegetation because climate change possibly affects distributions of alpine plants. We also examined the community assembly process of alpine plants at the 40 plots from the view points of habitat filtering and limiting similarity. Habitat filtering and limiting similarity relate environmental conditions and interspecific competition, respectively. It is suggested that habitat filtering is more important than limiting similarity for the community assembly of alpine plants.

2) Soil respiration rates along an altitudinal gradient

This study investigated seasonal changes of soil respiration rates from forest soil along an altitudinal gradient (1600 m to 2800 m above sea level). The soil respiration rate positively correlated with soil temperatures and forest biomass. It is suggested that forest productivity is an important factor for soil respiration rates.

3) Genetic differentiation of Solidago virgaurea complex

Plant species distributed along wide altitudinal or latitudinal gradients show phenotypic variation due to their heterogeneous habitats. This study investigated whether phenotypic variation in populations of the Solidago virgaurea complex along an altitudinal gradient is caused by genetic differentiation. Population genetic analyses with microsatellite markers were used to infer the genetic structure and levels of gene

flow between populations. However, the population genetic analysis suggested an extremely low level of genetic differentiation of neutral genes among the nine populations. This study suggests that genome regions responsible for adaptive traits may differ among the populations despite the existence of gene flow and that phenotypic variation of the S. virgaurea complex along the altitudinal gradient is maintained by strong selection pressure.

Bibliography

[1] " Solar neutron events in association with large solar flares in November 2003", Watanabe, K. *et al.*, Adv. Space Res., **38**, 425–430, 2006.

[2] K. Munakata, M. Kozai, P. Evenson, T. Kuwabara, C. Kato, M. Tokumaru, M. Rockenbach, A. Dal Lago, R. R. S. Mendonca, C. R. Braga, N. J. Schuch, H. K. Al Jassar, M. M. Sharma, M. L. Duldig, J. E. Humble, I. Sabbah, and J. Kota, "Cosmic Ray Short Burst Observed with the Global Muon Detector Network (GMDN) on June 22, 2015", Astrophys. J., 862:170 (9pp), 2018 (August 1).

[3] R. R. S. Mendonca, C. R. Braga, E. Echer, A. Dal Lago, M. Rockenbach, N. J. Schuch,, K. Munakata, "Deriving the solar activity cycle modulation on cosmic ray intensity observed by Nagoya muon detector from October 1970 until December 2012", Proc. IAU Sympo., 328, 1-4 (IAU-16-IAUS328-0453), 2016 (October 20).

[4] R. R. S. Mendonca, C. R. Braga, E. Echer, A. Dal Lago, K. Munakata, T. Kuwabara, M. Kozai, C. Kato, M. Rockenbach, N. J. Schuch, H. K. Al Jassar, M. M. Sharma, M. Tokumaru, M. L. Duldig, J. E. Humble, P. Evenson, I. Sabbah, "Temperature effect in secondary cosmic rays (muons) observed at ground: analysis of the global muon detector network data", Astrophys. J., 830:88 (25pp), 2016 (October 20). Cited by 2.

[5] M. Kozai, K. Munakata, C. Kato, T. Kuwabara, M. Rockenbach, A. Dal Lago, N. J. Schuch, C. R. Braga, R. R. S. Mendon, H. K. Al Jassar, M. M. Sharma, M. L. Duldig, J. E. Humble, P. Evenson, I. Sabbah, and M. Tokumaru, "Average spatial distribution of cosmic rays behind the interplanetary shock– Global Muon Detector Network observations", Astrophys. J., 825:100 (19pp), 2016 (July 10). Cited by 7.

[6] D. Ruffolo1, A. Saiz, P.-S. Mangeard, N. Kamyan, P. Muangha, T. Nutaro, S. Sumran, C. Chaiwattana, N. Gasiprong, C. Channok, C. Wuttiya, M. Rujiwarodom, P. Tooprakai, B. Asavapibhop, J. W. Bieber, J. Clem, P. Evenson, and K. Munakata, "Monitoring short-term cosmic-ray spectral variations using neutron monitor time-delay measurements", Astrophys. J., 817:38 (12pp), 2016 (January 20). Cited by 8.

[7] M. Kozai, K. Munakata, C. Kato, T. Kuwabara, J. W. Bieber, P. Evenson, M. Rockenbach, A. Dal Lago, N. J. Schuch, M. Tokumaru, M. L. Duldig, J. E. Humble, I. Sabbah, H. K. Al Jassar, M. M. Sharma, J. Kota, "The spatial density gradient of galactic cosmic rays and its solar cycle variation observed with the Global Muon Detector Network", Earth, Planets and Space, 66, 151-158, 2014 (November 14). Cited by 12.

[8] K. Munakata, M. Kozai, C. Kato, J. Kota, "Long term variation of the solar diurnal anisotropy of galactic cosmic rays observed with the Nagoya multi-directional muon detector", Astrophys. J., 791:22, 1-16, 2014 (August 10). Cited by 19.

[9] M. Rockenbach, A. Dal Lago, N. J. Schuch, K. Munakata, T. Kuwabara, A. G. Oliveira, E. Echer, C. R. Braga, R. R. S. Mendonca, C. Kato, M. Kozai, M. Tokumaru, J. W. Bieber, P. Evenson, M. L. Duldig, J. E. Humble, H. K. Al Jassar, M. M. Sharma, I. Sabbah, "Global muon detector network use d for space weather applications", Space Sci. Rev., 182, 1-18, 2014 (May 9). Cited by 18.

[10] K. Munakata, "For space weather applications", Space Sci. Rev., 182, 1-18, 2014 (May 9).

[11] D. Lopez et al., Estimates of the neutron emission during solar flares in the rising and maximum period of solar cycle 24, Astroparticle Physics, 76 (2016) 19-28.

[12] Enoto, T. and Wada, Y. and Furuta, Y. and Nakazawa, K. and Yuasa, T. and Okuda, K. and Makishima, K. and Sato, M. and Sato, Y. and Nakano, T. and Umemoto, D. and Tsuchiya, H, "Photonuclear reactions triggered by lightning discharge", Nature 551, (2017) 481-484.

[13] Dwyer, J. R. and Smith, D. M. and Cummer, S. A., "High-Energy Atmospheric Physics: Terrestrial Gamma-Ray Flashes and Related Phenomena", 173 (2012) 133-196.

[14] Tsuchiya, H. and Enoto, T. and Torii, T. and Nakazawa, K. and Yuasa, T. and Torii, S. and Fukuyama, T. and Yamaguchi, T. and Kato, H. and Okano, M. and Takita, M. and Makishima, K., "Observation of an Energetic Radiation Burst from Mountain-Top Thunderclouds", Physical Review Letters, 102, (2009) 255003.

[15] Wada, Y. and Bowers, G. S. and Enoto, T. and Kamogawa, M. and Nakamura, Y. and Morimoto, T. and Smith, D. M. and Furuta, Y. and Nakazawa, K. and Yuasa, T. and Matsuki, A. and Kubo, M. and Tamagawa, T. and Makishima, K. and Tsuchiya, H., "Termination of Electron Acceleration in Thundercloud by Intracloud/Intercloud Discharge", Geophysical Research Journal 45, (2018) 5700-5707.

[16] Tsuchiya, H. and Enoto, T. and Yamada, S. and Yuasa, T. and Kawaharada, M. and Kitaguchi, T. and Kokubun, M. and Kato, H. and Okano, M. and Nakamura, S. and Makishima, K., "Detection of High-Energy Gamma Rays from Winter Thunderclouds", Physical Review Letters, 99, (2007) 165002.

[17] Yo Kato, “Observational study of thundercloud radiation bursts using a segmented organic scintillator installed at a mounaintop”, Ph.D. thesis, The University of Tokyo, September, 2015.

[18] Y. Kato, “Thundercloud-related radiation bursts observed at a coastal area and a mountaintop using segmented organic scintillators”, Thunderstorms and Elementary Particle Acceleration (TEPA-2015), 5-9 October 2015, Yerevan, Armenia.

[19] Y. Kato, “Development of Plastic Anti-neutrino Detector Array (PANDA)”, Applied Antineutrino Physics(AAP) 2015, 7-8 December 2015, Virginia Tech Research Center, United States.

[20] Y. Kato “Observation of thundercloud radiation bursts using segmented plastic scintillators”, European Geosciences Union General Assembly (EGU), 8-13 April 2018, Austria Center Vienna, Austria.

[21] T. Torii *et al*., ”Gradual increase of energetic radiation associated with thunderstorm activity at the top of Mt. Fuji”, Geophys. Res. Lett 36(13) , 2009.

[22] T. Kuritai *et al*., ”The Status of the synchrotron of the Wakasa Wan Energy Research Center”, Proc. 12th Annual Meeting of the Particle Accelerator Societ of Japan, 288, 2015.

[23] K. Kume, T. Torii, M. Takita and T. Hasegawa, ”Development of a beam fluence measurement technique at atmosphere”, Igaku Butsuri, Vol.36 Suppl.3 178, 2016 (in Japanese).

[24] K. Kume, T. Hasegawa, S. Hatori, M. Takita and H. Tsuji, ”Space engineering application of therapeutic broad beam for cosmic rai simulation”, Igaku Butsuri, Vol.37 Suppl. 112, 2017 (in Japanese).

[25] Satoru Takahashi,Ph.D Thesis (2011) Nagoya University, http://hdl.handle.net/2237/14900.

[26] Hiroaki Kawahara, Master Thesis (2015), Nagoya University.

[27] “GRAINE project: gamma-ray observation with a balloon-borne emulsion telescope”, Hiroki Rokujo on behalf of GRAINE Collaboration, Proceeding of Science KMI2013 (2014) 042.

[28] “GRAINE project: The first balloon-borne, emulsion gamma-ray telescope experiment”, S. Takahashi, S. Aoki, K. Kamada, S. Mizutani, R. Nakagawa, K. Ozaki and H. Rokujo, PTEP 2015 (2015) no.4, 043H01.

[29] “Gamma-Ray Astro-Imager with Nuclear Emulsion, GRAINE (in Japanese)”, Satoru Takahashi, Shigeki Aoki for GRAINE collaboration, Journal of the SPSTJ, Vol,78(2015) No.4, pp.228-234.

[30] “GRAINE 2015, a balloon-borne emulsion γ-ray telescope experiment in Australia”, Satoru Takahashi et al. (GRAINE collaboration), PTEP 2016 (2016) no.7, 073F01.

[31] “GRAINE project, prospects for scientific balloon-borne experiments”, Satoru Takahashi, Shigeki Aoki for GRAINE collaboration, Advances in Space Research, Articles in press.

[32] Nakamoto A., Ikeda T., Maruta E. (2013) Needle browning and death in the flagged crown of Abies mariesii in the timberline ecotone of the alpine region in central Japan. Trees 27:815-825.

[33] Maruta E., Yazaki K.(submitted) Mechanism of embolism as induced by pit closure during winter in subalpine fir (Abies mariesii)on Mt. Norikura.

[34] Nagano S., Nakano T., Hikosaka K., Maruta E. (2013) Pinus pumila photosynthesis is suppressed by water stress in a wind-exposed mountain site. Arctic, Antarctic, and Alpine Research 45:229-237.

[35] Takahashi, K., Hirosawa, T. and Morishima, R. (2012) How the timberline formed: altitudinal changes in stand structure and dynamics around the timberline in central Japan. Annals of Botany 109: 1165-1174.

[36] Takahashi, K. and Okuhara, I. (2013) Forecasting the effects of global warming on radial growth of subalpine trees at the upper and lower distribution limits 3n central Japan. Climatic Change 117: 278-287.

[37] Takahashi, K. and Obata, Y. (2014) Growth, allometry and shade tolerance of understory saplings of four subalpine conifers in central Japan. Journal of Plant Research127: 329-338.

[38] Takahashi, K. (2014) Effects of wind and thermal conditions on timberline formation in central Japan: a lattice model. Ecological Research 29:121-131.

[39] Takahashi, K. and Koike, S. (2014) Altitudinal differences in bud burst and onset and cessation of cambial activity of four subalpine tree species. Landscape and Ecological Engineering 10:349-354.

[40] Takahashi, K. and Murayama, Y. (2014) Effects of topographic and edaphic conditions on alpine plant species distribution along a slope gradient on Mount Norikura, central Japan. Ecological Research 29: 823-833.

[41] Singh, D., Takahashi, K., Park, J. and Adams, J. M. (2016) Similarities and contrasts in the archaeal community of two Japanese mountains: Mt Norikura compared to Mt Fuji. Microbial Ecology 71: 428-441.

[42] Takahashi, K. and Furuhata, K. (2016) Shoot growth and seasonal changes of non-structural carbohydrate concentrations at the upper and lower distribution limits of three conifers. Landscape and Ecological Engineering 12: 239-245.

[43] Takahashi, K. and Tanaka, S. (2016) Relative importance of habitat filtering and limiting similarity on species assemblages of alpine and subalpine plant communities. Journal of Plant Research 129: 1041-1049.

[44] Takahashi, K. and Matsuki, S. (2017) Morphological variations of the Solidago virgaurea L. complex along an elevational gradient on Mt. Norikura, central Japan. Plant Species Biology 32: 238-246.

[45] Kerfahi, D., Tateno, R., Takahashi, K., Cho, H., Kim, H. and Adams, J. M. (2017) Development of soil bacterial communities on volcanic ash microcosms in a range of climates. Microbial Ecology 73: 775-790.

[46] Sakurai, A. and Takahashi, K. (2017) Flowering phenology and reproduction of the Solidago virgaurea L. complex along an elevational gradient on Mt. Norikura, central Japan. Plant Species Biology 32: 270-278.

[47] Dong, K., Moroenyane, I., Tripathi, B., Kerfahi, D., Takahashi, K., Yamamoto, N., An, C., Cho, H., and Adams, J. (2017) Soil nematodes show a mid-elevation diversity maximum and elevational zonation on Mt. Norikura, Japan. Scientific Reports 7: 3028.

[48] Hirano, M., Sakaguchi, S. and Takahashi, K. (2017) Phenotypic differentiation of the Solidago virgaurea complex along an elevational gradient: Insights from a common garden experiment and population genetics. Ecology and Evolution 7: 6949-6962.

[49] Takahashi, K., Otsubo, S. and Kobayashi, H. (2017) Comparison of photosynthetic traits of codominating subalpine conifers Abies veitchii and A. mariesii in central Japan. Landscape and Ecological Engineering 14: 91-97.

AKENO OBSERVATORY

Introduction

The Akeno Observatory is situated in Akeno of Hokuto-city, 20 km northwest of Kofu and 130 km west of metropolitan Tokyo. The location is at the longitude of 138.5°E and the latitude of 35.8°N. The altitude is ∼900 m above sea level. It was established in 1977 as a research center for air shower studies in the very high energy region, and it has been administered by the ICRR as a facility of joint-university-use.

The 40th anniversary of the Akeno Observatory was held in 2017.

Akeno Air Shower Experiments

The Akeno Air Shower Experiment started in 1979 with an array covering 1 km^2 area (the 1 km^2 array, see Fig.1). The array was enlarged to 20 km^2 in 1984 and was gradually expanded to the Akeno Giant Air Shower Array (AGASA) of approximately 100 km^2 area by 1990. The AGASA was built

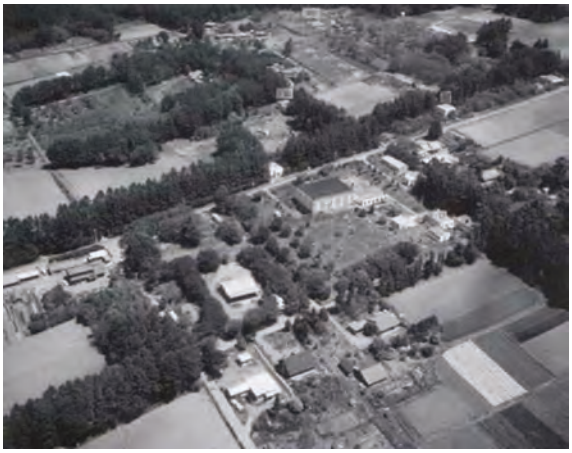

Fig. 1. Aerial View of Akeno Observatory and 1 km^2 Array Area

to detect Ultra-High Energy Cosmic Rays (UHECRs) in the energy range of 10^{20} eV.

One of the distinctive features of Akeno experiments is that the measurements were made over five decades of energies well covering 10^{15} eV - 10^{20} eV by using both the surface detector for electromagnetic component, and the shielded detector for muon component (Fig.2). The wide energy coverage was accomplished by the arrays of scintillation detectors of various inter-detector spacings from 3 m to 1 km and with different triggering conditions. This feature of Akeno air shower measurement is well demonstrated in Fig.3, in which the spectra from Akeno 1 km^2 array for $10^{14.5}$ eV - $10^{18.8}$ eV [1] and AGASA for $10^{18.5}$ eV - $10^{20.3}$ eV [2] are plotted.

*1 M. Nagano et al., J. Phys. **G10**, 1295 (1984); M. Nagano et al., J. Phys. **G18**, 423 (1992).

*2 M. Takeda et al., Astropart. Phys. **19**, 447 (2003).

Fig. 2. One of the muon detector housings with concrete shielding.

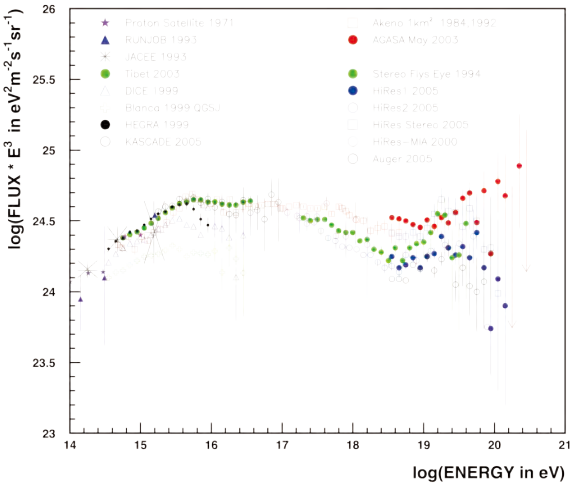

Fig. 3. Akeno energy spectrum measurements for 10^{15} eV - 10^{20} eV.

AGASA

The AGASA was composed of 111 surface detectors, each with plastic scintillator of 2.2 m^2 area and 5 cm thickness. The counters were deployed with ∼1 km spacing covering the ground area of approximately 100 km^2 in the suburban area of Akeno, outside of the observatory campus. The AGASA served as the largest air shower array in the world since its commissioning in 1990 until it stopped data taking in January 2004, when the construction of the succeeding experiment, Telescope Array (TA), started in Utah. The AGASA was dismantled in 2007 together with other Akeno air shower arrays.

An exposure of 5.8 × 10^{16} m^2 s sr above 10^{19} eV was accumulated by AGASA in 13 years of operation. Extensive air showers with zenith angles smaller than 45° and with core

locations inside the array area were used for the analysis. The AGASA reported an extension of the energy spectrum beyond the predicted Greisen-Zatsepin-Kuzmin (GZK) cutoff in 1998 [3] and a total of eleven UHECR events were observed above 10^{20} eV by 2003.

Measurement of UHECRs

Since the AGASA measurement in 1998, the High Resolution Fly's Eye (HiRes) [4], the Pierre Auger Observatory (PAO) [5], and the Telescope Array (TA) [6] measured the energy spectra of UHECRs with higher statistics.

The HiRes observed the UHECR using the fluorescence telescope. The PAO and the TA measure the energy spectra using the surface array consisting of either water tanks (PAO) or plastic scintillators (TA), but the energy scale of the array is determined by the fluorescence telescope using a subset of events observed by the fluorescence telescope and surface array at the same time. The adoption of the energy scale by the fluorescence telescopes is based on its small dependence on the air shower simulation.

The energy spectra above 10^{18} eV by AGASA and other experiments are compiled and compared by the working group represented by UHECR experiments in the UHECR2012 symposium held in 2012 [7]. The result is plotted in Fig.4 with the energy scale of each experiment adjusted to a reference energy, which is set halfway between PAO and TA/HiRes.

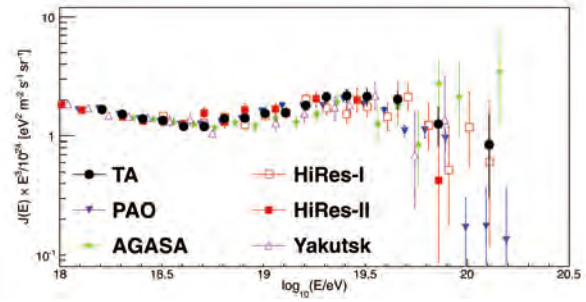

Fig. 4. Compilation of UHECR energy spectra (UHECR2012). The energy scales were adjusted as ×1.10 for PAO, ×0.91 for TA and HiRes, ×0.65 for AGASA and ×0.56 for Yakutsk.

The HiRes, PAO and TA confirmed a flux suppression above approximately $10^{19.7}$ eV. Although the AGASA spectrum does not demonstrate the cutoff structure, the number of events above 10^{20} eV became only two after the energy rescaling, making the claim of the extended spectrum statistically insignificant. The estimate of systematic uncertainty of the energy measurement is approximately 20% for all the experiments, and rescalings for the TA/HiRes and PAO are within this limit. Rescaling of the surface array energy for AGASA and Yaktsuk indicates that there exist larger systematic uncertainties than originally estimated by running the air shower simulation. This difference of energy scale obtained by the surface array and by the fluorescence telescope remains as a basic question in the understanding of the air shower phenomena.

Recent Research Activities

The study of UHECRs by AGASA in Akeno was succeeded by the TA experiment in Utah, USA since 2008. After the cessation of AGASA, the Akeno Observatory has been used for small scale cosmic ray experiments, astrophysical observations and as a test and maintenance facility by the ICRR and university researchers. Fig.5 shows a recent photograph of the main site of the Akeno Observatory.

Fig. 5. The main site of the Akeno Observatory. There are the movable tent for a small atmospheric Cherenkov telescope (A), the large experimental hall (B), the research building (C) and the lodging facility (D) from the left.

In 2020, as countermeasures against COVID-19 infection, an air conditioner and a heat-exchange ventilator were installed in the large room of the research building, and a heat-exchange ventilator was installed in the dining room of the lodging facility along with some other measures.

Observation by the multi-color imager for transients, survey and monstrous explosions (MITSuME) by N. Kawai (Tokyo Institute of Technology) et al.

One of the three MITSuME robotic telescopes was installed in the Akeno Observatory in 2003 (Fig. 6). The telescope has an aperture of 50 cm, an FOV of 28' × 28' and is equipped with a tricolor CCD camera capable of $g'R_CI_C$-bands photometry (g':400∼550 nm, Rc:570∼730 nm, Ic:730∼ 850 nm). It is operated remotely from the Tokyo Tech at the Ookayama Campus via a dedicated line. The operation of the telescope has continued in FY2021 as described below [8].

Upon receiving a GRB alert, it directs the telescope toward the GRB direction within two minutes, and makes a prompt observation of the GRB and its afterglow. The follow-up observation of GRBs was continued by the MITSuME telescope. Information about GRB events was reported to Gamma-Ray Burst (GRB) Coordinates Network Circular (GCNC).

In order to perform follow-up visible-light observations of gravitational wave objects, the MITSuME participated in

*3 M. Takeda et al., Phys. Rev. Lett. **81**, 1163 (1998).
*4 R.U. Abbasi et al., Phys. Rev. Lett. **100**, 101101 (2008).
*5 J. Abraham et al., Phys. Lett. **B685**, 239 (2010).
*6 T. Abu-Zayyad et al., Astrophys. J. **768**, L1 (2013).
*7 http://indico.cern.ch/conferenceDisplay.py?confId=152124
*8 N. Kawai et al., Research Result Presentations Meeting of the ICRR Inter-University Research Program 2021.

J-GEM (Japanese collaboration for Gravitational-wave ElectroMagnetic follow-up) and GROWTH(Global Relay of Observatories Watching Transients Happen) to establish worldwide observation network focusing on the electromagnetic identification of gravitational wave sources as one of scientific themes. In FY2021, the observation of gravitational wave by LIGO/Virgo was stopped. Therefore, the MITSuME participated in the follow-up observation of IceCube neutrino events that was derived from J-GEM.

The MITSuME team also conducted long-term monitoring observations of X-ray binary starts and blazars. The MITSuMe has also participated OISTER (Optical and Infrared Synergetic Telescopes for Education and Research).

Fig. 6. The dome in which the MITSuME telescope was installed in Akeno.

Observation of galactic cosmic rays by large area muon telescope by A. Oshima (Chubu University) et al.

Four layers of proportional counter telescopes, each with 25 m^2 area, were installed in three muon houses in Akeno and have been continuously measuring the cosmic ray muons since 2003. Fig. 2 shows one of the three muon houses (M1, M5, M8). The mode energy of the primary cosmic rays is approximately 2.5 GeV corresponding to 2m thick concrete ceiling of the muon house at the latitude of the Akeno Observatory. The measurement in Akeno is combined with a simultaneous measurement by the GRAPES-3 experiment at Ooty in India, and this telescope aims at measuring the modulation effects and anisotropy of galactic cosmic rays in the region of about 100 GeV and detecting trasient phenomena of cosmic rays. It is expected to understand cosmic-ray flow in the universe magnetic field and to obtain a clue to the solution of cosmic-ray propagation. And it is challenging to establish the method of a new space weather observation by simultaneous multi-directional observations with high statistical precision.

In FY2021, the data acquisition at M5 was restored in November and tuned in December. However, almost continuous observations have been made at M5 over the past 3.5 years except during power outages, etc [9].

*[9] A. Oshima et al., Research Result Presentation Meeting of the ICRR Inter-University Research Program 2021.

Research and development for a small atmospheric Cherenkov telescope at the Akeno Observatory by T. Yoshikoshi (ICRR) et al.

An alt-azimuth telescope with an aperture of three meters (Fig. 7) was setup in the Akeno Observatory for various prototype tests with atmospheric Cherenkov observations of gamma rays on the ground [10]. This telescope is the only telescope to observe atmospherice Cherenkov light emitted from air showers induced by TeV gamma rays in Japan.

In January 2021, the telescope was used to observe the Crab Pulsar in the visible light region for about ten hours. The collected data were analyzed in FY2021. The result was used to improve the signal-to-noise ratio of the Crab Pulsar observation and to study the removal of external noise.

Fig. 7. The Cherenkov telescope at the tour of the 40th anniversary of the Akeno Observatory in 2017.

Dark matter and Interstellar Meteoroid Study (DIMS) at the Akeno Observatory by F. Kajino (Konan University) et al.

The Dark Matter and Interstellar Meteoroid Study (DIMS) is a new experiment that aims at searching for macroscopic dark matter and interstellar meteoroids [11][12][13]. Nuclearites are nuggets of stable Strange Quark Matter (SQM), which are neutral in charge and hypothetical super-heavy macroscopic particles (macros), and may be important components of the dark matter in our universe. Nuclearites of galactic origins is expected to have a typical velocity of about 250 km/s in galactic frame. The DIMS team studies the possibility of searching for such fast moving particles using very high-sensitivity CMOS camera with a wide field of view. In the first stage, the DIMS system consists of 4 high-sensitivity CMOS camera stations. and is going to be constructed at the Telescope Array cosmic-ray experimental site in Utah, USA. Due to COVID-19 pandemic, the DIMS team did not transport the DIMS systems to Utah, and one of the systems was installed on the roof of the research building at the Akeno Observatory as shown in Fig. 8. The observed Geminids Meteor Shower taken by

*[10] M. Ohishi et al., 33rd ICRC, (Rio deJaneiro), 587 (2013).
*[11] D. Barghini et al., PoS(ICRC2021)500.
*[12] D. Shinto et al., PoS(ICRC2021)502.
*[13] F. Kajino et al., PoS(ICRC2021)554

the DIMS camera at the Akeno Observatory was shown in Fig. 9. The preliminary results on limiting magnitudes of stars and the number of meteors as a function of magnitude were reported [14]. Three camera systems are installed at the Kiso Observatory, Shinshu University and Akeno Observatory for stereoscopic observations.

Fig. 8. The DIMS camera installed on the roof of the research building at the Akeno Observatory in August 2021.

Fig. 9. Geminids Meteor Shower that was taken by DIMS camera at the Akeno Observatory on December 13th, 2021. Approximately 500 meteoroids are superimposed on the photograph.

Research and development for the Telescope Array observation in Utah by the TA collaboration and others

All the TA fluorescence imaging cameras and a part of the TA surface detectors were assembled in the Akeno Observatory by the TA collaboration team. All the unit mirrors of the TA fluorescence telescope were tested and the atmospheric monitoring lidar of TA using YAG laser was developed. In JFY 2015, the R&D of the surface detectors were performed for the TAx4 project that aims at quadrupling the TA surface detector array in Utah. In August in 2016, 2017 and 2018 the TAx4 and TALE (TA Low Energy extension) scintillator counters were assembled.

The assembly of the surface detectors for the TALE-infill array [15] that is described in the TA section was scheduled at the Akeno Observatory in 2020, but due to the COVID-19 epidemic, the assembly had to be postponed. The 50 surface detectors for the TALE-infill array were assembled at the Akeno Observatory from the middle of October to early November in 2021. Figure 10 shows one of the surface detectors that was being assembled.

Fig. 10. A surface detector for the TALE-infill array that was being assembled at the Akeno Observatory. The student was aligning the ends of bundled fibers.

*[14] F. Kajino et al., Research Result Presentation Meeting of the ICRR Inter-University Research Program 2021.

*[15] S. Ogio et al., "The status of the TALE surface detector array and a TALE infill project", PoS(ICRC2021)255.

KAMIOKA OBSERVATORY

Kamioka observatory is located at 1000 m underground (2700 m water equivalent) in the Kamioka Mine, Gifu prefecture, about 200 km west of Tokyo. The observatory was established in 1995 in order to operate Super-Kamiokande experiment (SK). The underground laboratories are located under Mt.Ikeno-yama and accessible to the experimental site through a 1.7 km horizontal tunnel. The observatory also has surface research buildings and a dormitory located at the distance of 15 minutes drive from the entrance of the underground laboratories.

The Super-Kamiokande experiment had discovered neutrino oscillations through the observations of atmospheric and solar neutrinos (see the section for Neutrino and Astroparticle Division). The atmospheric neutrino oscillation was confirmed by the long baseline neutrino oscillation experiment, K2K, using accelerator neutrino beam, which was conducted between 1999 and 2004. A new long baseline neutrino oscillation experiment (the T2K experiment) using a high intensity beam, 50 times of the K2K neutrino beam, by the J-PARC proton accelerator has started in 2009. In 2011, the experiment has observed 6 ν_e appearance events indicating non-zero θ_{13} which was as yet determined the last neutrino oscillation parameter. From 2014, T2K started taking data using an anti- neutrino beam, and confirmed the disappearance of muon antineutrinos through oscillations. Candidate events for the appearance of electron anti-neutrinos were also found. Additionally, T2K published in 2020 an indication that CP symmetry is not conserved in neutrino oscillations, with the probability of the observations being the results of a random fluctuation if CP symmetry was conserved being less than 5%.

The low cosmic ray flux and low seismic noise environment in the underground site enables us to conduct various researches. There is a 100 m long laser interferometer, which is a prototype of the 3 km gravitational wave antenna (KAGRA). Using the low radioactive background environment in the Kamioka Mine, a dark matter experiment, called XMASS was conducted in Lab-C. The XMASS group constructed a 800kg liquid xenon detector and data were taken from 2010 to 2019. Searches for dark matter interactions and rare phenomena in liquid xenon have been conducted using the obtained data. The R&D study of a tracking type detector for dark matter detection led by the Kobe University group (the NEWAGE experiment) has also been performed in Lab-B. A double beta decay experiment using ^{48}Ca (the CANDLES experiment) led by the Osaka University group has been running in Lab-D. The study to improve the neutrino detection sensitivity by adding gadolinium to Super-Kamiokande (called SK-Gd project) has been performed at Lab-E. A Low background Germanium detector and ICP-MS system are equipped in Lab-1 and Lab-A to measure extremely low radioactive backgrounds. Lab-G area was excavated in 2015 and the SK-Gd equipments which include a Gd dissolving system, a pretreatment system and a Gd-water circulation system were installed in 2016. Other preparations for Gd-loading have been performed including a tank open work to repair the water leak from the SK tank in 2018 and the test of the SK-Gd equipments in 2019. In 2020, SK added soluble Gd salt into the water. The next-generation neutrino experiment project, Hyper-Kamiokande, was started in 2020. The construction has been running underground the Kamioka mine, aiming to begin observations in 2027.

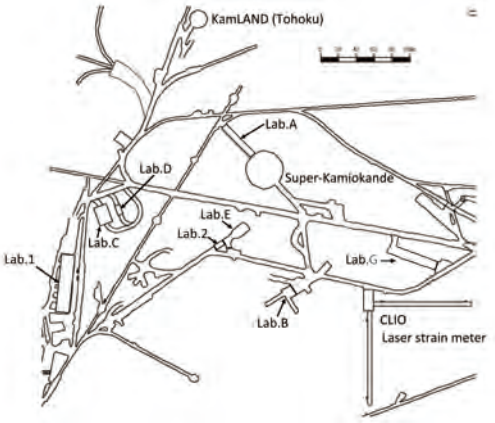

Fig. 1. Kamioka Underground Observatory.

Fig. 2. The surface buildings in Mozumi.

KAGRA OBSERVATORY

KAGRA observatory is located in the Ikenoyama-mountain on the border between Gifu and Toyama prefecture, about 35 km south of Toyama city in Japan. The observatory was established in 2016 in order to operate Large-scale Cryogenic Gravitational Wave Telescope "KAGRA". KAGRA itself has a L-shape tunnel facility, and it is located more than 200m under Mt.Ikeno-yama. The corner station of the L-shape tunnel is accessible through a 500-m horizontal access tunnel from Atotsu area. The observatory has its own surface research buildings and rental space in the community center of Hida city located about 5km away from the Atotsu entrance of KAGRA.

KAGRA aims to observe gravitational waves (GWs) as one of observatories of the world GW detection network including Advanced-LIGO, Advanced-Virgo and planned LIGO-India. KAGRA project (formerly named LCGT) was partially approved in 2010 as one of Leading-edge Research Infrastructure Program, and also supported by Program for Promoting Large-scale Science Projects, Subsidy for Facilities Expense and Grants-in-Aid for Scientific Research from Ministry of Education, Culture, Sports, Science and Technology (MEXT).

In the KAGRA project, Institute for Cosmic Ray Research plays a role of a host promoting institute, and National Astronomical Observatory of Japan (NAOJ) and High Energy Accelerator Research Organization (KEK) are the co-host institutions, then more than 454 researchers in 93 institutes and universities in the world are collaborating for construction and data analysis of KAGRA.

The tunnel excavation started in May 2012, and finished in March 2014. After that, the basic laboratory environment was prepared until September 2015. A Michelson interferometer with 3km arm (iKAGRA) was demonstrated in March 2016, and the first engineering run was performed until May 2016. In 2019, all the interferometer components had been installed to complete the KAGRA Observatory that adopts a power recycled Fabry-Perot Michelson type interferometer with the resonant sideband extraction. On February 25th, 2020, KAGRA started its first observation run. After performing the two week observation run "O3GK" with GEO600 on April 2020, KAGRA will be upgraded and prepared for the joint observation with LIGO and Virgo "O4" which is expected to start in May 2023.

Fig. 1. Surface Research Building.

Fig. 2. Atotsu Entrance of KAGRA.

RESEARCH CENTER FOR COSMIC NEUTRINOS

The Research Center for Cosmic Neutrinos (RCCN) was established in April 1999 to conduct research on neutrinos and related topics. The members of the Center participate in the Super-Kamiokande experiment, which is the neutrino research facility representing ICRR. We aim to maximize our knowledge of neutrinos by analyzing the observed neutrino data in Super-Kamiokande, as well as the long-baseline neutrino oscillation experiment T2K. We aim to explore the possibility of neutrino research by promoting the exchange of the research ideas between theoretical and experimental physicists. We are also participating in the Hyper-Kamiokande project, a next-generation large-scale experiment, where the development of the detector are being developed, produced, and prepared.

RCCN, in collaboration with with the computer committee, is responsible for overseeing the operation of the central computer system in ICRR (Fig 1). The computer facility is designed to handle high performance task and analyze large amounts of data. Since its upgrade in 2020, the facility has operated smoothly without encountering any significant issues.

Starting from 2004, RCCN has been involved in inter-university programs associated with activities in the low-background underground facility (see Fig 2). In FY2021, we accepted a total of 12 programs, including both domestic and international applications.

Since 2009, ICRR and Kavli Institute for the Physics and Mathematics of the Universe (Kavli IPMU) have held two public lectures a year, one in the spring and one in the summer. The lecture was broadcast in real time and archived on YouTube. The lecture titled ”Far Galaxies and Mysteries of the Universe” featured assistant professor Yuichi Harikane at ICRR and professor Naoki Yoshida at Kavli IPMU, who gave a talk on the study of early universe galaxies discovered through observations using the Subaru telescope and the results of large-scale computer simulation studies on the formation of cosmic structures. The two lecturers also cross-talked with the participants to answer their questions. In addition, there was a cross-talk session between the two speakers in which they answered questions from participants. About 100 people attended the event in person, and about 670 people watched it on YouTube, with approximately 1,400 views.

Fig. 1. Photo of the central computer facility in ICRR upgraded in 2014.

Fig. 2. Photo of the low-background underground facility in ICRR.

HIGH ENERGY ASTROPHYSICS FACILITY IN CANARIAS

High Energy Astrophysics Facility in Canarias, established on April 1, 2019 in La Palma, Canary Islands, Spain is the actual base of international collaborations on CTA (Cherenkov Telescope Array) project co-hosted by CTA group of ICRR.

The Cherenkov Telescope Array (CTA) is the next generation ground-based observatory for gamma-ray astronomy at very-high energies, participated by more than 1400 researchers from 25 countries. With more than 70 telescopes located in the northern and southern hemispheres, CTA will be the world's largest and most sensitive high-energy gamma-ray observatory. The CTA-Japan consortium is making a significant contribution to the construction of Large-sized Telescopes (LSTs), four telescopes of which are planned to construct at northern hemisphere site in La Palma. The first LST was completed and made the first light at the end of December of 2018.

Establishment of the local corporation assets were needed for daily activities such as local procurement and employment to manage and operate the site. High Energy Astrophysics Facility in Canarias was established as a room inside the building of CALP (The Centro de Astrofísica en La Palma), a branch of IAC (Instituto de Astrofisca de Canarias).

Fig. 1. High Energy Astrophysics Facility in Canarias.

APPENDICES

A. ICRR Workshops and Ceremonies

21st International Workshop on Next generation Nucleon Decay and Neutrino Detectors (NNN2022)

Date: September 28 - 30, 2022
Place : Hida City Cultural Communication Center in Hida City, Gifu Prefecture

Outline: Institute for Cosmic Ray Research, The University of Tokyo hosted the international workshop NNN2022 in Hida-Furukawa in person after the two-year postponement due to the COVID-19 pandemic.

From 28 to 30 September 2022, the 21st International Workshop on Next generation Nucleon Decay and Neutrino Detectors (NNN2022) was held in person in Hida-Furukawa, a neighboring town of Kamioka in Hida City, Gifu Prefecture. The NNN workshops have been held almost every year since 1999 in various parts of the world. NNN2022 is the fourth workshop of the NNN series held in Japan, following Hamamatsu, Toyama, and Kashiwa. It was originally planned to be held in 2020 but postponed due to the COVID-19 pandemic. ICRR hosted this workshop together with Hida City as a co-host. NNN2022 is the first international conference held in Hida City.

On the first day of the workshop, Prof. Masato Shiozawa, Director of the Kamioka Observatory, gave the opening address, followed by a welcome speech by Mr. Junya Tsuzuku, Mayor of Hida City. One hundred and eleven researchers from 10 countries participated in the conference, and 35 oral presentations and 32 poster presentations were made. The topics discussed include proton decay, high-intensity neutrino beams, supernova neutrinos, solar neutrinos, atmospheric neutrinos, reactor neutrinos, large detectors R&D, etc.

Participants: 111 participants including 2 attending online

Fig. 1. 21st International Workshop on Next generation Nucleon Decay and Neutrino Detectors (NNN2022)

B. ICRR Seminars

1. April, 27, 2022: Dr. Alicia López-Oramas (Instituto de Astrofísica de Canarias (IAC), JSPS visitor), “RS Ophiuchi: the first nova detected at very high energies”
2. May, 18, 2022: Dr. Yanis Liodakis (Gruber Fellow, Finnish Center for Astronomy with ESO, University of Turku and JSPS fellow visiting IPMU), “The Hunt for Extraterrestrial Neutrino Counterparts”
3. June, 8, 2022: Prof. Akitaka Ariga (Chiba University and University of Bern) (Switzerland), “Neutrinos and beyond with the LHC’s forward beam”
4. July, 27, 2022: Prof. Marcos López Moya (University Complutense of Madrid, Spain), “Unveiling gamma-ray emission from Pulsars”
5. August, 31, 2022: Dr. Zara Bagdasarian (Berkeley), “Studying the Earth with neutrinos – Borexino and Theia”
6. September, 14, 2022: Dr. Russell Neilson (Drexel), “Dark Matter and Neutrino Physics with Scintillating Bubble Chambers”
7. October, 12, 2022: Dr. Naoko Kurahashi Neilson (Drexel University), “Neutrino Astronomy with IceCube at the Earth’s South Pole
8. October, 26, 2022: Dr. Ralf Seidl (RIKEN BNL Center), “The physics of the electron-ion Collider (EIC)”
9. January, 11, 2023: Dr. Kazuhiro Terao, “Machines to Find Ghost Particles in Big Data”
10. January, 13, 2023: Dr. Glennys Farrar (New York University) visiting ICRR, “The seemingly-anomalous magnetic moment of the muon – a novel reconciliation with the Standard Model and connection with Dark Matter”
11. February, 1, 2023: Dr. Julian Sitarek (University of Lodz Poland), “Improving observations with Cherenkov telescopes: SiPM cameras and image corrections for cloud presence”
12. February, 27, 2023: Dr. Olaf Reimer (The university of Innsbruck), visiting professor of ICRR, “Challenges and chances for measuring diffuse emission with IACTs”
13. March, 30, 2023: Dr. Hiroyuki Sagawa (ICRR), “Ultra-high-energy cosmic rays – status and perspective”

C. List of Publications

(a) Papers Published in Journals

1. ”Search for neutrinoless quadruple beta decay of ^{136}Xe in XMASS-I”, XMASS Collaboration, Physics Letters B, volume **833** (2022) 137355, Oct. 2022.
2. ”Double-weak decays of ^{124}Xe and ^{136}Xe in the XENON1T and XENONnT experiments”, E. Aprile et al. (XENON Collaboration), Phys. Rev. C **106**, 024328, Aug. 2022.
3. ”Pre-supernova Alert System for Super-Kamiokande”, L. N. Machado et al. (The Super-Kamiokande Collaboration), 2022 ApJ **935** 40, Aug. 2022.
4. ”Search for proton decay via $p \to \mu^+ K^0$ in 0.37 megaton-years exposure of Super-Kamiokande”, R. Matsumoto et al. (Super-Kamiokande Collaboration), Phys. Rev. D **106**, 072003, Oct. 2022.
5. ”Searching for Supernova Bursts in Super-Kamiokande IV”, M. Mori et al. (The Super-Kamiokande Collaboration), 2022 ApJ **938** 35, Oct. 2022.
6. ”Neutron tagging following atmospheric neutrino events in a water Cherenkov detector”, The Super-Kamiokande Collaboration, 2022 JINST **17** P10029, Oct. 2022.
7. ”Search for Cosmic-Ray Boosted Sub-GeV Dark Matter Using Recoil Protons at Super-Kamiokande”, Super-Kamiokande Collaboration, Phys. Rev. Lett. **130**, 031802, Jan. 2023.

8. ”Scintillator ageing of the T2K near detectors fro 2010 to 2021”, T2K Collaboration, 2022 JINST **17** P10028, Oct. 2022.

9. ” Application and modeling of an online distillation method to reduce krypton and argon in XENON1T”, E. Aprile et al. (XENON Collaboration), PTEP **2022** 053H01 (2022) pp1-21, May 2022.

10. ”Emission of single and few electrons in XENON1T and limits on light dark matter”, E. Aprile et al. (XENON Collaboration), Phys. Rev. D **106** 022001 (2022) pp022001-1-022001-21, Jul. 2022.

11. ”Material radiopurity control in the XENONnT experiment”, E. Aprile et al. (XENON Collaboration), Eur. Phys. J. C **82**:599 (2022) pp1-10, Jul. 2022.

12. ”Search for New Physics in Electronic Recoil Data from XENONnT”, E. Aprile et al. (XENON Collaboration), Phys. Rev. Lett. **129**, 161805 (2022) pp161805-1-161805-1, Oct. 2022.

13. ”An approximate likelihood for nuclear recoil searches with XENON1T data”, E. Aprile et al. (XENON Collaboration), Eur. Phys. J. C **82**:989 (2022) pp1-10, Nov. 2022.

14. ”A next-generation liquid xenon observatory for dark matter and neutrino physics”, J. Aalbers et al., J. Phys. G: Nucl. Part. Phys. **50** 013001 (2023), Dec. 2022.

15. ”Development of ultra-pure gadolinium sulfate for the Super-Kamiokande gadolinium project”, K Hosokawa, M Ikeda, T Okada, H Sekiya, P Fernández, L Labarga, I Bandac, J Perez, S Ito, M Harada, , PTEP, 44907.

16. ”Proton acceleration in thermonuclear nova explosions revealed by gamma rays”, MAGIC Collaboration (V.A.Acciari, et al.), Nature Astronomy, **6** (2022) 689., Apr. 2022.

17. ”Multiwavelength Observations of the Blazar VER J0521+211 during an Elevated TeV Gamma-Ray State”, VERITAS Collaboration, MAGIC Collaboration, The Astrophysical Journal, **932** (2022) id.129, Jun. 2022.

18. ”Gamma-ray observations of MAXI J1820+070 during the 2018 outburst”, MAGIC Collaboration, H.E.S.S. Collaboration, VERITAS Collaboration, et al., MNRAS **517**, 4736-4751 (2022), Sep. 2022.

19. ”Study of the GeV to TeV morphology of the γ Cygni SNR (G 78.2+2.1) with MAGIC and Fermi-LAT. Evidence for cosmic ray escape”, MAGIC Collaboration, A&A **670**, A8 (2023), Jan. 2023.

20. ”Long-term multi-wavelength study of 1ES 0647+250”, MAGIC Collaboration, A&A **670**, A49 (2023), Feb. 2023.

21. ”A lower bound on intergalactic magnetic fields from time variability of 1ES 0229+200 from MAGIC and Fermi/LAT observations”, MAGIC Collaboration, et al., A&A **670**, A145 (2023), Feb. 2023.

22. ”Search for Gamma-Ray Spectral Lines from Dark Matter Annihilation up to 100 TeV toward the Galactic Center with MAGIC”, MAGIC Collaboration, Phys. Rev. Lett. **130**, 061002, Feb. 2023.

23. ”MAGIC observations provide compelling evidence of hadronic multi-TeV emission from the putative PeVatron SNR G106.3+2.7”, MAGIC Collaboration, A&A **671**, A12 (2023), Feb. 2023.

24. ”Search of the pair echo signatures in the high-energy light curve of GRB190114C”, Ievgen Vovk, Phys. Rev. D **107**, 043020, Feb. 2023

25. ”Simulation of solar neutron flux in the Earth’s atmosphere for three selected flares”, F. Monterde-Andrade et al., Astroparticle Physics **145** (2023) 102780, Mar. 2023.

26. ”Ultra high energy cosmic rays. The intersection of the Cosmic and Energy Frontiers”, A.Coleman, et al., Astroparticle Physics, Volume **149**, 102819, Feb. 2023.

27. ”Measurements of protons and charged pions emitted from $\nu\mu$ charged-current interactions on iron at a mean neutrino energy of 1.49 GeV using a nuclear emulsion detector”, H. Oshima, et al., Phys. Rev. D **106**, 032016, Aug. 2022.

28. ”Opacity of the Highly Ionized Lanthanides and the Effect on the Early Kilonova”, Smaranika Banerjee, Masaomi Tanaka, Daiji Kato, Gediminas Gaigalas, Kyohei Kawaguchi, and Nanae Domoto, 2022 ApJ **934** 117, Jul. 2022.

29. ”Direct Measurement of the Nickel Spectrum in Cosmic Rays in the Energy Range from 8.8 GeV/n to 240 GeV/n with CALET on the International Space Station”, O. Adriani, Y. Akaike, K. Asano, et al., PRL **128**, 131103(8pp), Apr. 2022.

30. ”Signatures of anisotropic diffusion around PeVatrons in 100 TeV gamma-ray data”, G. Giacinti, T. Abounnasr, A. Neronov, D. Semikoz,, Phys. Rev. D **106**, 123029, Dec. 2022.

31. ”Statistical Properties of Radio Halos in Galaxy Clusters and Origin of Seed Electrons for Reacceleration”, Kosuke Nishiwaki, and Katsuaki Asano, 2022 ApJ **934** 182, May 2022.

32. ”Electromagnetic Counterparts of Binary Neutron Star Mergers Leading to a Strongly Magnetized Long-Lived Remnant Neutron Star”, Kyohei Kawaguchi, Sho Fujibayashi, Kenta Hotokezaka, Masaru Shibata, and Shinya Wanajo, 2022 ApJ **933** 22, Jun. 2022.

33. ”Investigating the Disk-Jet Structure in M87 through Flux Separation in the Linear and Circular Polarization Images”, Yuh Tsunetoe, Shin Mineshige, Tomohisa Kawashima, Ken Ohsuga, Kazunori Akiyama, and Hiroyuki R. Takahashi, 2022 ApJ **931** 25, May 2022.

34. ”GRB Prompt Emission with Anisotropic Electron Distribution”, Ryota Goto, and Katsuaki Asano, 2022 ApJ **933** 18, Jun. 2022.

35. ”Constraints on population I/II neutron star-black hole binary formation by gravitational wave and radio observations ”, Tomoya Kinugawa, Takashi Nakamura, and Hiroyuki Nakano, MNRAS **515**, L78–L83 (2022), Jul. 2022.

36. ”Investigating GW190425 with Numerical-Relativity Simulations”, Reetika Dudi, Ananya Adhikari, Bernd Brügmann, Tim Dietrich, Kota Hayashi, Kyohei Kawaguchi, Kenta Kiuchi, Koutarou Kyutoku, Masaru Shibata, and Wolfgang Tichy, Phys. Rev. D **106**, 084039, Oct. 2022.

37. ”Selective Dynamical Imaging of Interferometric Data”, J. Farah, P. Galison, K. Akiyama, et al., ApJL **930**, L18(21pp), May 2022.

38. ”Millimeter Light Curves of Sagittarius A* Observed during the 2017 Event Horizon Telescope Campaign”, M. Wielgus, N. Marchili, I. Marti-Vidal, et al., ApJL **930**, L19(32pp), May 2022.

39. ”A Universal Power-Law Prescription for Variability from Synthetic Images of Black Hole Accretion Flows”, B. Georgiev, D. W. Pesce, A. E. Broderick, et al., ApJL **930**, L20(32pp), May 2022.

40. ”Characterizing and Mitigating Intraday Variability: Reconstructing Source Structure in Accreting Black Holes with mm-VLBI”, A. E. Broderick, R. Gold, B. Georgiev, et al., ApJL **930**, L21(30pp), May 2022.

41. ”Lanthanide Features in Near-infrared Spectra of Kilonovae”, Nanae Domoto, Masaomi Tanaka, Daiji Kato, Kyohei Kawaguchi, Kenta Hotokezaka, Shinya Wanajo, 2022 ApJ **939** 8, Oct. 2022.

42. ”CALET Search for Electromagnetic Counterparts of Gravitational Waves during the LIGO/Virgo O3 Run”, O. Adriani, Y. Akaike, K. Asano, et al., ApJ **933**, 85(16pp), Jul. 2022.

43. ”Resolving the Inner Parsec of the Blazar J1924-2914 with the Event Horizon Telescope”, S. Issaoun, M. Wielgus, S. Jorstad, et al., ApJ **934**, 145(21pp), Aug. 2022.

44. ”Expanding Fireball in Magnetar Bursts and Fast Radio Bursts”, Tomoki Wada, and Kunihito Ioka, MNRAS **519**, 4094–4109 (2023) , Dec. 2022.

45. ”Observation of Spectral Structures in the Flux of Cosmic-Ray Protons from 50 GeV to 60 TeV with the Calorimetric Electron Telescope on the International Space Station”, O. Adriani et al. (CALET Collaboration), PRL **129**, 101102(8pp), Sep. 2022.

46. ”Large-Scale Outflow Structure and Radiation Properties of Super-Eddington Flow: Dependence on the Accretion Rates”, Shogo Yoshioka, Shin Mineshige, Ken Ohsuga, Tomohisa Kawashima, and Takaaki Kitaki, Publ. Astron. Soc. Japan (2022) **74** (6), 1378–1395, Oct. 2022.

47. ”Implications from the Velocity Profile of the M87 Jet: A Possibility of a Slowly Rotating Black Hole Magnetosphere”, Motoki Kino et al, 2022 ApJ **939** 83, Nov. 2022.

48. ”A Monte-Carlo Based Relativistic Radiation Hydrodynamics Code with a Higher-Order Scheme”, Kyohei Kawaguchi, Sho Fujibayashi, and Masaru Shibata, Phys. Rev. D **107**, 023026, Jan. 2023.

49. ”Diverse Polarimetric Features of AGN Jets from Various Viewing Angles: Towards a Unified View”, Yuh Tsunetoe, Shin Mineshige, Tomohisa Kawashima, Ken Ohsuga, Kazunori Akiyama, and Hiroyuki R. Takahashi, Galaxies. 2022; **10**(5):103, Oct. 2022.

50. ”Probe for Type Ia Supernova Progenitor in Decihertz Gravitational Wave Astronomy”, Tomoya Kinugawa, Hiroki Takeda, Ataru Tanikawa, and Hiroya Yamaguchi, ApJ **938**, 52(9pp) (2022), Oct. 2022.

51. ”Cosmic-Ray Boron Flux Measured from 8.4 GeV/n to 3.8 TeV/n with the Calorimetric Electron Telescope on the International Space Station”, O. Adriani et al. (CALET Collaboration), Phys. Rev. Lett. **129**, 251103, Dec. 2022.

52. ”Pseudo-Observation of Spiral Galaxies in the Radio Band to Verify Depolarization Models”, Yuta Tashima, Takumi Ohmura, and Mami Machida, Publ. Astron. Soc. Japan (2023) **75** (SP1), S123–S137, Jan. 2023.

53. ”Structure of the Super-Eddington Outflow and its Impact on the Cosmological Scale”, Ignacio Botella, Shin Mineshige, Takaaki Kitaki, Ken Ohsuga, Tomohisa Kawashima, PASJ, **74**, 384-397, Apr. 2022.

54. ”First Sagittarius A Event Horizon Telescope Results.VI. Testing the Black Hole Metric”, K. Akiyama, A. Alberdi, W. Alef, et al., ApJL, **930**, L17(44pp), May 2022.

55. ”First Sagittarius A Event Horizon Telescope Results. V. Testing Astrophysical Models of the Galactic Center Black Hole”, K. Akiyama, A. Alberdi, W. Alef, et al., ApJL, **930**, L16(49pp), May 2022.

56. ”First Sagittarius A Event Horizon Telescope Results.IV. Variability, Morphology, and Black Hole Mass”, K. Akiyama, A. Alberdi, W. Alef, et al., ApJL, **930**, L15(52pp), May 2022.

57. ”First Sagittarius A Event Horizon Telescope Results.III. Imaging of the Galactic Center Supermassive Black Hole”, K. Akiyama, A. Alberdi, W. Alef, et al., ApJL, **930**, L14(64pp), May 2022.

58. ”First Sagittarius A Event Horizon Telescope Results.II. EHT and Multiwavelength Observations, Data Processing, and Calibration”, K. Akiyama, A. Alberdi, W. Alef, et al., ApJL, **930**, L13(31pp), May 2022.

59. ”First Sagittarius A Event Horizon Telescope Results. I. The Shadow of the Supermassive Black Hole in the Center of the Milky Way”, K. Akiyama, A. Alberdi, W. Alef, et al., ApJL, **930**, L12(21pp), May 2022.

60. ”X-Ray Hot Spots in the Eastern Ear of the Supernova Remnant W 50 and the Microquasar SS 433 System”, Ryota Hayakawa, et al., PASJ, **74**, 510-520, Jun. 2022.

61. ”Can Population III Stars be Major Origins of both Merging Binary Black Holes and Extremely Metal Poor Stars?”, Ataru Tanikawa, Gen Chiaki, Tomoya Kinugawa, Yudai Suwa, Nozomu Tominaga, PASJ, **74**, 521-532, Jun. 2022.

62. ”MeerKAT’s View of Double Radio Relic Galaxy Cluster Abell 3376”, James O. Chibueze, et al., PASJ, **75**, S97-S107, Feb. 2023.

63. ”Transverse Oscillations of the M87 Jet Revealed by KaVA Observations”, Hyunwook Ro, et al., Galax, **11**, 33(13pp), Feb. 2023.

64. ”Measurement of the Gamma-Ray Energy Spectrum beyond 100 TeV from the HESS J1843-033 Region”, M. Amenomori et al. (The Tibet ASgamma Collaboration), Astrophysical Journal, **932** (2022) 120, Jun. 2022.

65. ”Sensitivity of the large muon detector with the Tibet air-shower array to measure the primary proton spectrum between 40 and 630 TeV”, D. Kurashige et al., Prog. Theor. Exp. Phys. **2022** 093F01, Sep. 2022.

66. ”Hadronic interaction model dependence in cosmic Gamma-ray flux estimation using an extensive air shower array with a muon detector”, Okukawa, S. et al. (The ALPACA Collaboration), Exp Astron **55**, 325–342 (2023), Jan. 2023.

67. ”Gamma-ray imaging in a nuclear medicine facility using a compact and portable high-sensitivity omnidirectional Compton camera with detector rotation function(in Japanese)”, Saki Ishikawa;Hiroshi Muraishi;Ryoji Enomoto;Hideaki Katagiri;Mika Kagaya;Takara Watanabe;Daisuke Kano;Satoshi Nakamura;Yusuke Watanabe;Hiromichi Ishiyama,, Ionizing Radiation **47**,3, pp80-88, Oct. 2022.

68. ”Thermal Performance of a Cryogenic Parallel Heat Pipe System”, Ramnarong Wanison, Nobuhiro Kimura, Masahide Murakami, Hirotaka Nakai, and Suguru Takada, Cryogenics Vol.**128** (2022)103589, Dec. 2022.

69. ”Improving the stability of frequency-dependent squeezing with bichromatic control of filter cavity length, alignment, and incident beam pointing”, Yuhang Zhao, Eleonora Capocasa, Marc Eisenmann, Naoki Aritomi, Michael Page, Yuefan Guo, Eleonora Polini, Koji Arai, Yoichi Aso, Martin van Beuzekom, Yao-Chin Huang, Ray-Kuang Lee, Harald Lück, Osamu Miyakawa, Pierre Prat, Ayaka Shoda, Matteo Tacca, Ryutaro Takahashi, Henning Vahlbruch, Marco Vardaro, Chien-Ming Wu, Matteo Leonardi, Matteo Barsuglia, Raffaele Flaminio, Physical Review D **105**, Apr. 2022.

70. ”First joint observation by the underground gravitational-wave detector, KAGRA, with GEO 600”, The LIGO Scientific Collaboration, the Virgo Collaboration, the KAGRA Collaboration: R. Abbott, et al., Progress of Theoretical and Experimental Physics, Apr. 2022.

71. ”Follow-up analyses of the binary-neutron-star signals GW170817 and GW190425 by using post-Newtonian waveform models”, Tatsuya Narikawa, Nami Uchikata, Physical Review D, Nov. 2022.

72. ”Mass-spin reparametrization for a rapid parameter estimation of inspiral gravitational-wave signals”, Eunsub Lee, Soichiro Morisaki, and Hideyuki Tagoshi, Phys. Rev. D, Jun. 2022.

73. ”Noise subtraction from KAGRA O3GK data using Independent Component Analysis”, H Abe et al (KAGRA collaboratio), Classical and Quantum Gravity, Mar. 2023.

74. ”Search for Gravitational Waves Associated with Gamma-Ray Bursts Detected by Fermi and Swift during the LIGO-Virgo Run O3b”, Abbott R, Others (LIGO-Virgo-KAGRA collaboration), Astrophys. J., Apr. 2022.

75. ”The Current Status and Future Prospects of KAGRA, the Large-Scale Cryogenic Gravitational Wave Telescope Built in the Kamioka Underground”, H Abe et al (KAGRA collaboratio), Galaxies, Apr. 2022.

76. ”All-sky search for gravitational wave emission from scalar boson clouds around spinning black holes in LIGO O3 data”, Abbott R, Others (LIGO-Virgo-KAGRA collaboration), Phys. Rev. D, May. 2022.

77. ”Searches for Gravitational Waves from Known Pulsars at Two Harmonics in the Second and Third LIGO-Virgo Observing Runs”, Abbott R, Others (LIGO-Virgo-KAGRA collaboration), Astrophys. J., May. 2022.

78. ”A laser interferometer accelerometer for vibration sensitive cryogenic experiments”, Rishabh Bajpai, Takayuki Tomaru, Kazuhiro Yamamoto, Takfumi Ushiba, Nobuhiro Kimura, Toshikazu Suzuki, Tomohiro Yamada, Tohru Honda, Measurement Science and Technology, May. 2022.

79. ”Narrowband Searches for Continuous and Long-duration Transient Gravitational Waves from Known Pulsars in the LIGO-Virgo Third Observing Run”, Abbott R, Others (LIGO-Virgo-KAGRA collaboration), Astrophys. J., Jun. 2022.

80. ”All-sky, all-frequency directional search for persistent gravitational waves from Advanced LIGO’s and Advanced Virgo’s first three observing runs”, Abbott R,Others (LIGO-Virgo-KAGRA collaboration), Phys. Rev. D, Jun. 2022.

81. ”Unsupervised learning architecture for classifying the transient noise of interferometric gravitational-wave detectors”, Yusuke Sakai, Yousuke Itoh, Piljong Jung, Keiko Kokeyama, Chihiro Kozakai, Katsuko T. Nakahira, Shoichi Oshino, Yutaka Shikano, Hirotaka Takahashi, Takashi Uchiyama, Gen Ueshima, Tatsuki Washimi, Takahiro Yamamoto, and Takaaki Yokozawa, Scientific Reports, Jun. 2022.

82. ”Vibration analysis of KAGRA cryostat at cryogenic temperature”, Rishabh Bajpai, Takayuki Tomaru, Nobuhiro Kimura, Takafumi Ushiba, Kazuhiro Yamamoto, Toshikazu Suzuki, Tohru Honda, Classical and Quantum Gravity, Jul. 2022.

83. ”Search for continuous gravitational wave emission from the Milky Way center in O3 LIGO-Virgo data”, Abbott R, Others (LIGO-Virgo-KAGRA collaboration), Phys. Rev. D, Aug. 2022.

84. ”Search for Subsolar-Mass Binaries in the First Half of Advanced LIGO’s and Advanced Virgo’s Third Observing Run”, Abbott R, Others (LIGO-Virgo-KAGRA collaboration), Phys. Rev. Lett., Aug. 2022.

85. ”Search for gravitational waves from Scorpius X-1 with a hidden Markov model in O3 LIGO data”, Abbott R,Others (LIGO-Virgo-KAGRA collaboration), Phys. Rev. D, Sep. 2022.

86. ”Response of the underground environment of the KAGRA observatory against the air pressure disturbance from the Tonga volcano eruption on January 15th, 2022”, Tatsuki Washimi, Takaaki Yokozawa, Akiteru Takamori, Akito Araya, Sota Hoshino, Yousuke Itoh, Yuichiro Kobayashi, Jun’ya Kume, Kouseki Miyo, Masashi Ohkawa, Shoichi Oshino, Takayuki Tomaru, Jun’ichi Yokoyama, Hirotaka Yuzurihara, Progress of Theoretical and Experimental Physics, Sep. 2022.

87. ”All-sky search for continuous gravitational waves from isolated neutron stars using Advanced LIGO and Advanced Virgo O3 data”, Abbott R, Others (LIGO-Virgo-KAGRA collaboration), Phys. Rev. D, Nov. 2022.

88. ”Model-based Cross-correlation Search for Gravitational Waves from the Low-mass X-Ray Binary Scorpius X-1 in LIGO O3 Data”, Abbott R, Others (LIGO-Virgo-KAGRA collaboration), Astrophys. J. Lett., Dec. 2022.

89. ”Input optics systems of the KAGRA detector during O3GK”, T Akutsu et al (KAGRA collaboration), Progress of Theoretical and Experimental Physics, Dec. 2022.

90. ”A Search for H-Dropout Lyman Break Galaxies at z∼12-16”, Harikane, Yuichi; et al., 2022 ApJ **929** 1, Aug. 2022.

91. ”EMPRESS. VI. Outflows Investigated in Low-mass Galaxies with M_* = 104–107 $M_\odot$: Weak Feedback in Low-mass Galaxies?”, Xu, Y;, et al. , ApJ **929** 134, Apr. 2022.

92. ”EMPRESS. VII. Ionizing Spectrum Shapes of Extremely Metal-poor Galaxies: Uncovering the Origins of Strong He II and the Impact on Cosmic Reionization”, Umeda, Hiroya ; et al., 2022 ApJ **930** 37, May 2022.

93. ”Are the newly-discovered z$\sim$13 drop-out sources starburst galaxies or quasars?”, Pacucci, Fabio;et al., MNRAS **514**, L6–L10 (2022) , Apr. 2022.

94. ”SILVERRUSH. XII. Intensity Mapping for Lyα Emission Extending over 100-1000 Comoving Kpc around z$\sim$2-7 LAEs with Subaru HSC-SSP and CHORUS Data”, Kikuchihara, Shotaro; et al., 2022 ApJ **931** 97, May 2022.

95. ”CLASSY III. The Properties of Starburst-driven Warm Ionized Outflows”, Xu, Xinfeng; et al., 2022 ApJ **933** 222, Jul. 2022.

96. ”The COS Legacy Archive Spectroscopy Survey (CLASSY) Treasury Atlas”, Berg, Danielle A.; et al., 2022 ApJS **261** 31, Jul. 2022.

97. ”First Identification of a CMB Lensing Signal Produced by 1.5 Million Galaxies at z $\sim$4 : Constraints on Matter Density Fluctuations at High Redshift”, Miyatake, Hironao; et al., Phys. Rev. Lett. **129**, 061301, Aug. 2022.

98. ”EMPRESS. V. Metallicity Diagnostics of Galaxies over 12 + log(O/H)$\simeq$ 6.9-8.9 Established by a Local Galaxy Census: Preparing for JWST Spectroscopy”, Nakajima, Kimihiko; et al., 2022 ApJS **262** 3, Aug. 2022.

99. ”A Lower Bound of Star Formation Activity in Ultra-high-redshift Galaxies Detected with JWST: Implications for Stellar Populations and Radiation Sources”, Inayoshi, Kohei; Harikane, Yuichi; Inoue, Akio K.; Li, Wenxiu; Ho, Luis C., ApJL **938** L10, Oct. 2022.

100. ”CLASSY. II. A Technical Overview of the COS Legacy Archive Spectroscopic Survey”, James, Bethan L.;et al., 2022 ApJS **262** 37, Sep. 2022.

101. ”The discovery and characterization of (594913) ‘Ayló’chaxnim, a kilometre sized asteroid inside the orbit of Venus”, Bolin, Bryce T.; et ak., MNRAS **517**, L49–L54 (2022) , Aug. 2022.

102. ”Extreme value statistics of the halo and stellar mass distributions at high redshift: are JWST results in tension with λCDM?”, Lovell, Christopher C.et al., MNRAS **518**, 2511–2520 (2023), Nov. 2022.

103. ”JWST Imaging of Earendel, the Extremely Magnified Star at Redshift z = 6.2”, Welch, Brian ;et al., 2022 ApJL **940** L1, Nov. 2022.

104. ”Discovery of 24 radio-bright quasars at 4.9 $\leq$ z $\leq$ 6.6 using low-frequency radio observations”, Gloudemans, A. J. ; et al., A&A **668**, A27 (2022), Nov. 2022.

105. ”ALMA Lensing Cluster Survey: Hubble Space Telescope and Spitzer Photometry of 33 Lensed Fields Built with CHArGE”, Kokorev, V. ; et al., 2022 ApJS **263** 38, Dec. 2022.

106. ”A Wide and Deep Exploration of Radio Galaxies with Subaru HSC (WERGS). IX. The most overdense region at z$\sim$5 inhabited by a massive radio galaxy”, Uchiyama, Hisakazu ;et al., PASJ (2022) **74** (6), L27–L32, Sep. 2022.

107. ”ALMA Observations of CO Emission from Luminous Lyman-break Galaxies at z = 6.0293-6.2037”, Ono, Yoshiaki ; et al., 2022 ApJ **941** 74, Dec. 2022.

108. ”EMPRESS. VIII. A New Determination of Primordial He Abundance with Extremely Metal-poor Galaxies: A Suggestion of the Lepton Asymmetry and Implications for the Hubble Tension”, Matsumoto, Akinori ;et al., 2022 ApJ **941** 167, Dec. 2022.

109. ”HETDEX Public Source Catalog 1: 220 K Sources Including Over 50 K Lyα Emitters from an Untargeted Wide-area Spectroscopic Survey”, Mentuch Cooper, Erin ; et al., 2023 ApJ **943** 177, Feb. 2023.

110. ”The Gas and Stellar Content of a Metal-poor Galaxy at z = 8.496 as Revealed by JWST and ALMA”, Heintz, K. E. ; et al., 2023 ApJL **944** L30, Feb. 2023.

111. ”A Comprehensive Study of Galaxies at z$\sim$9-16 Found in the Early JWST Data: Ultraviolet Luminosity Functions and Cosmic Star Formation History at the Pre-reionization Epoch”, Harikane, Yuichi ;et al., 2023 ApJS **265** 5, Feb. 2023.

112. ”ALMA detection of 321 GHz water maser emission in the radio galaxy NGC 1052”, Kameno, Seiji ; et al., Publ. Astron. Soc. Japan (2023) **75** (2), L1–L, Feb. 2023.

113. "COSMOS2020: Discovery of a Protocluster of Massive Quiescent Galaxies at z = 2.77", Ito, Kei ;et al., 2023 ApJL **945** L9, Mar. 2023.

114. "A solar metallicity galaxy at z $>$ 7? Possible detection of the [N II] 122 μm and [O III] 52 μm lines", Killi, Meghana ;et al., MNRAS **521**, 2526–2534 (2023), Mar. 2023.

115. "Stellar Initial Mass Function (IMF) Probed with Supernova Rates and Neutrino Background: Cosmic-average IMF Slope Is $\simeq$2-3 Similar to the Salpeter IMF", Aoyama, Shohei ;et al., 2023 ApJ **946** 69, Mar. 2023.

116. "Freeze-in generation of lepton asymmetries after baryogenesis in the νMSM", Shintaro Eijima, Mikhail Shaposhnikov, Inar Timiryasov, JCAP04(**2022**)049, Apr. 2022.

117. "Gravitational waves detectable in laser interferometers from axion-SU(2) inflation", Tomohiro Fujita, Kaname Imagawa, Kai Murai, JCAP07(**2022**)046, Jul. 2022.

118. "Lepton Asymmetric Universe", Masahiro Kawasaki, Kai Murai, JCAP08(**2022**)041, Aug. 2022.

119. "Is cosmic birefringence due to dark energy or dark matter? A tomographic approach", Eiichiro Komatsu, Hiromasa Nakatsuka, Toshiya Namikawa, Phys. Rev. D **105**, 123509, Jun. 2022.

120. "Universality of linear perturbations in SU(N)-natural inflation", Tomohiro Fujita, Kai Murai, Ryo Namba, Phys. Rev. D **105**, 103518, May 2022.

121. "Inflation with two-form field: the production of primordial black holes and gravitational waves", Tomohiro Fujita, Hiromasa Nakatsuka, Ippei Obata, Sam Young, JCAP 09 (**2022**) 017, Sep. 2022.

122. "Anisotropies in Cosmological 21 cm Background by Oscillons/I-balls of Ultra-light Axion-like Particle", Masahiro Kawasaki, Kazuyoshi Miyazaki, Kai Murai, Hiromasa Nakatsuka, Eisuke Sonomoto, JCAP08(**2022**)066, Aug. 2022.

123. "Physics of star formation history and the luminosity function of galaxies therefrom", Masataka Fukugita and Masahiro Kawasaki, MNRAS **513**, 8–14 (2022) , Apr. 2022.

124. "Gauge Field Production and Schwinger Reheating in Runaway Axion Inflation", Soichiro Hashiba, Kohei Kamada, Hiromasa Nakatsuka, JCAP04(**2022**)058, Apr. 2022.

125. "Free Streaming Length of Axion-Like Particle After Oscillon/ I-ball Decays", Kaname Imagawa, Masahiro Kawasaki, Kai Murai, Hiromasa Nakatsuka, Eisuke Sonomoto, JCAP02(**2023**)024, Feb. 2023.

126. "SU(N)-natural inflation", Tomohiro Fujita, Kyohei Mukaida, Kai Murai, Hiromasa Nakatsuka, Phys. Rev. D **105**, 103519, May 2022.

127. "More on Fake GUT", Masahiro Ibe, Satoshi Shirai, Motoo Suzuki, Keiichi Watanabe, Tsutomu T. Yanagida, J. High Energ. Phys. **2022**, 87 (2022), Jul. 2022.

128. "Revisiting the Affleck-Dine mechanism for primordial black hole formation", Kentaro Kasai, Masahiro Kawasaki, Kai Murai, JCAP10(**2022**)048, Oct. 2022.

129. "Chiral Z' in FASER, FASER2, DUNE, and ILC beam dump experiments", Kento Asai, Arindam Das, Jinmian Li, Takaaki Nomura, Osamu Seto, Phys. Rev. D **106**, 095033, Nov. 2022.

130. "Revisiting sterile neutrino dark matter in gauged U(1)B-L model", Shintaro Eijima, Osamu Seto, Takashi Shimomura, PHYSICAL REVIEW D **106**, 103513 (2022), Nov. 2022.

131. "Isotropic cosmic birefringence from early dark energy", Eiichiro Komatsu, Kai Murai, Toshiya Namikawa, Fumihiro Naokawa, Phys. Rev. D **107**, L041302, Feb. 2023.

132. "Asymmetric Mediator in Scotogenic Model", Kento Asai, Yuhei Sakai, Joe Sato, Yasutaka Takanishi, Masato Yamanaka, Physics Letters B **836** (2023) 137627, Jan. 2023.

133. "Search for Lepton Flavor Violating Decay at FASER", Takeshi Araki, Kento Asai, Hidetoshi Otono, Takashi Shimomura, Yosuke Takubo, J. High Energ. Phys. **2023**, 145 (2023), Jan. 2023.

134. "Precise Estimate of Charged Wino Decay Rate", Masahiro Ibe, Masataka Mishima, Yuhei Nakayama, Satoshi Shirai, J. High Energ. Phys. **2023**, 17 (2023), Jan. 2023.

(b) Conference Papers (Proceedings)

1. ”GREX-PLUS: Galaxy Reionization EXplorer and PLanetary Universe Spectrometer”, Inoue, AK; Kaneda, H; Yamada, T; Harikane, Y; Ishihara, D; Kodama, T; Komiyama, Y; Moriya, T; Motohara, K; Nomura, H; Ouchi, M; Oyabu, S; Suzuki, T; Wada, T; Yamamura, I, Conference on Space Telescopes and Instrumentation - Optical, Infrared, and Millimeter Wave, JUL 17-22, 2022
2. ”NINJA: an LTAO assisted optical and near-infrared spectrograph of Subaru Telescope ”, Tokoku, Chihiro ; Ozaki, Shinobu ; Moriya, Takashi ; Yanagisawa, Kenshi ; Motohara, Kentaro ; Ouchi, Masami ; Tominaga, Nozomu ; Tanaka, Masaomi ; Ono, Yoshito ; Minowa, Yosuke ; Hayano, Yutaka ; Koyama, Yusei ; Ali, Sadman ; Tanaka, Masayuki ; Akiyama, Masayuki ; Nagao, Tohru ; Matsuoka, Yoshiki ; Kushibiki, Kosuke ; Homan, Shogo ; Yasuda, Akino ; Yoshida, Michitoshi , SPIE Astronomical Telescopes + Instrumentation, 2022, 44802
3. ”MAGIC observations of the putative PeVatron SNR G106.3+2.7 in the proximity of the Boomerang PWN”, Saito, T; Oka, T; Strzys, M;, Kubo, H;, 7th Heidelberg International Symposium on High-Energy Gamma-Ray Astronomy, Jul 4-8, 2022
4. ”The energy spectrum of ultra-high energy cosmic rays measured at the Pierre Auger Observatory and the Telescope Array”, D. R. Bergman, et al., Ultra High Energy Cosmic Rays (UHECR 2022), October 3-7, 2022
5. ”Energy Spectrum Measured by the Telescope Array Surface Detectors”, Jihyun Kim, et al., Ultra High Energy Cosmic Rays (UHECR 2022), October 3-7, 2022
6. ”Measurement of Cosmic-ray Energy Spectrum with the TALE Detector in Hybrid Mode”, H. Oshima, et al., Ultra High Energy Cosmic Rays (UHECR 2022), October 3-7, 2022
7. ”Testing the Compatibility of the Depth of the Shower Maximum Measurements performed at Telescope Array and the Pierre Auger Observatory”, D.R.Bergman, et al., Ultra High Energy Cosmic Rays (UHECR 2022), October 3-7, 2022
8. ”Cosmic ray mass composition measurement with the TALE hybrid detector”, K. Fujita, et al., Ultra High Energy Cosmic Rays (UHECR 2022), October 3-7, 2022
9. ”A machine learning approach for mass composition analysis with TALE-SD data”, R. Arimura, et al., Ultra High Energy Cosmic Rays (UHECR 2022), October 3-7, 2022
10. ”2022 report from the Auger-TA working group on UHECR arrival directions”, A. di Matteo, et al., Ultra High Energy Cosmic Rays (UHECR 2022), October 3-7, 2022
11. ”UHECR anisotropy and extragalactic magnetic fields with the Telescope Array”, M. Kuznetsov, et al., Ultra High Energy Cosmic Rays (UHECR 2022), October 3-7, 2022
12. ”Updates on the Hotspot and the Perseus-Pisces supercluster Excess Observed by the Telescope Array Experiment”, Jihyun Kim, et al., Ultra High Energy Cosmic Rays (UHECR 2022), October 3-7, 2022
13. ”Search for the large-scale cosmic-ray anisotropies using the TA and TALE surface detector arrays”, Y. Kimura, et al., Ultra High Energy Cosmic Rays (UHECR 2022), October 3-7, 2022
14. ”Current status of the TAx4 surface detectors ”, E. Kido, et al., Ultra High Energy Cosmic Rays (UHECR 2022), October 3-7, 2022
15. ”TAx4 surface detectors data analysis”, K. Fujisue, et al., Ultra High Energy Cosmic Rays (UHECR 2022), October 3-7, 2022
16. ”Performance of the TALE infill experiment as a TA-TALE extension down to the PeV region”, A. Iwasaki, et al., Ultra High Energy Cosmic Rays (UHECR 2022), October 3-7, 2022
17. ”The ALPACA experiment: The project of the first sub-PeV gamma-ray observation in the southern sky”, T. Kawashima et al., ISVHECRI2022, May 23-28
18. ”ALPACA experiment: A new air shower array to explore the sub-PeV gamma-ray sky in the southern hemisphere”, M. Anzorena et al. , ICHEP2022, July 25-29
19. ”Observation of multi-ten TeV to sub-PeV gamma rays from the HESS J1843-033 region with the Tibet air shower array”, M. Amenomori et al., ECRS2022, July 25-29
20. ”T2K-Super-Kamiokande Joint Neutrino Oscillation Sensitivity”, J. Xia, NOW2022, Sep 4 – 11, 2022

D. Doctoral Theses

1. Development of Rapid Sky Localization Methods of Gravitational Wave Signals using Machine Learning,
   HSIEH, Bin-Hua,
   Ph.D Thesis, Sep. 2022
2. Measurements of neutrino oscillation parameters from a joint analysis of SK atmospheric and T2K accelerator samples,
   XIA, JUNJIE,
   Ph.D Thesis, Sep. 2022
3. Study of VHE Gamma-ray Emission from Active Galactic Nucleus 1ES 1959+650 with the MAGIC Telescopes,
   SAKURAI, Shunsuke,
   Ph.D Thesis, Mar. 2023
4. First detection of the very-high-energy gamma rays from the recurrent nova RS Ophiuchi with the Large Size Telescope prototype of the Cherenkov Telescope Array,
   KOBAYASHI, Yukiho,
   Ph.D Thesis, Mar. 2023
5. Observation of Gamma Rays in the 100 TeV Region from Potential Galactic PeVatron Candidates with the Tibet Air Shower Array and the Muon Detector Array,
   KATO, Sei,
   Ph.D Thesis, Mar. 2023
6. Dynamics of axion and gauge fields during inflation,
   MURAI, Kai,
   Ph.D Thesis, Mar. 2023

E. Public Relations

(a) ICRR News

ICRR News is a quarterly publication written in Japanese about scientific and educational activities at ICRR.

Below lists the main topics in the issues published in FY 2022:

No.113 (2022 Spring)

- Features : Professor Masayuki Nakahata inaugurated as Director of ICRR
- Interview to Former Director, Professor Takaaki Kajita
- Features : Press Release 2022.4.7, Most Distant Galaxy Candidate Yet
- Features : Press Release 2022.2.2, The intrinsic structure of Sagittarius A*
- Reports : The 26th ICRR x IPMU Public Lecture ”Mystery of Distanct Galaxy and Universe” : Yuichi Harikane, ICRR Assistant Prof. and Naoki Yoshida, IPMU Prof. Talk about their Latest Research
- Reports : Commendation Ceremony and Commemorative Lecture Celebrating Associate Prof. Koji Noda’s Winning of the 18th JSPS Prize
- Reports : 2022 ICRR Spring School for Undergraduate Students Held online
- Topics : Prof. Kaita Elected as International Member of the National Academy of Sciences, USA
- Topics : ICRR Report on Japan and China Joint Research on Cosmic Rays (Edited by Dr. Itaru Ota) Published
- Information : Staff Reassignment
- Information : ICRR Seminar

No.114 (2022 Summer and Autumn)

- Features : Kashiwa Campus Open Days 2022 Held Online, About 1500 People Enjoy Online Events
- Features : Features : Super-Kamiokande and KAGRA Open Days Held Online
- Features : Press Release 2022.5.12, Astronomers reveal first image of the black hole at the heart of our galaxy
- Features : Press Release 2022.8.2, Scientists reveal distribution of dark matter around galaxies 12 billion years ago - further back than ever before
- Features : Press Release 2022. 7.22, First results from a Search for New Physics in Electronic Recoils from XENONnT
- Awards : Assitant Prof. Tomoya Kinugawa (belonged to High Energy Astrophysics Group) Awarded Kozai Yohihide Research Award 2021
- Awards : Dr. Tomohiro Inada (belonged to Cherenkov Cosmic Gamma Ray Group till 2021) Awarded 24th High Energy Physics Young Researcher's Award
- Awards : Assitant Prof. Kyohei Kawaguchi (belonging to both Gravitational Wave Group and High Energy Astrophysic Group) Awarded 17th Young Scientist Award of the Physical Society Japan
- Awards : Yosuke Nakatsuka (M3), Kai Murai (M1), Kosuke Nishiwaki Awarded Student Presentation Award of the Physical Society of Japan
- Topics : The Minisitry of Science and Innovation of the Kingdom of Spain, KEK and UTokyo Sign MoU to Promote Hyper-Kamiokande Project
- Topics : KAGRA Awarded Gakunin's IdP of the Year 2021
- Topics : Associate Prof. at the School of Science, the University of Tokyo Aya Bamba Talks online at Event for Female Students "Yappari Butsuriga Suki."
- Topics : The Schoold of Sicnce, the University of Tokyo Renovates Science Gallary
- Topics : Prof. Ogio Attends Joint Guidance for High School Students in Osaka
- Topics : ICRR Calls for Participation in Spring School 2023
- Topics : Informaion of ICRR's Recent Publications
- Topics : 21st International Workshop on Next Generation Nucleon Decay and Neutrion Detectors (NNN2022) Held in Gifu
- Topics : Super-Kamiokande Live Tour Held for UTokyo's Open Campus 2022 for High School Students
- Topics : The Hyper-Kamiokande tunnel excavation has reached the center of the cavern dome
- Information : Staff Reassignment
- Information : ICRR Seminar

No.115 (2022-2023 Winter)

- Features : ICRR Fellow Tomohisa Kawashima (High Energy Astrophysics Group) gives Talk at Science Café at Tamarokuto Science Center Titled "Black Hole Shadow and Multi-Messenger Astronomy"
- Message from Associate Prof. Katsuaki Asano
- Features : Press Release 2023.2.4, MAGIC Teleschopes scrutinize the center of our home Galaxy for fingerprints of dark matter
- Reports : The 27th ICRR x IPMU Public lecture "Cutting-edge Research of Dark Matter" : Shigetaka Moriyama, ICRR Prof. , Talks about his Latest Research
- Awards : Prof. Masato Takita in Tibet and ALPACA Experiment Awarded Koshiba Award from Foundation For High Energy Accelerator Science
- Awards : Ryota Kanashima (M2), Teruyoshi Kawashima (M2) Awarded Student Presentation Award of the Physical Society of Japan in 2022 Autumn Meeting

- Topics : Research Results Presentation Meeting of the ICRR Domestic and International Inter-University Research Program FY2022 Held with Hybrid Style
- Topics : 2022 ICRR Master and Doctor Thesis Workshop Held
- Topics : Nagaoka Minister of Education, Culture, Sports, Science and Technology visits Super-Kamiokande and KAGRA
- Topics : ICRR Report on electromagnetic interation of cosmic rays (Auther : Dr. Jun Nishimura, Emeritus Professor of UTokyo and JAXA) Published
- Topics : ICRR Calls for Participation in ICRR x IPMU Public Lecture on 22nd of April, 2023
- Information : Staff Reassignment
- Information : ICRR Seminar

(b) Public Lectures

- "Koukikai Symposium," Apr. 29, 2022, Korakuen Campus, Chuo University, Bunkyo-ku, Tokyo, Takaki Kajita (ICRR, The University of Tokyo).
- "Public Lecture commemorating the 50th Anniversary of Saitama Medical University," May. 14, 2022, Hidaka Campus, Saitama Medical University, Hidaka-City, Saitama, Takaki Kajita (ICRR, The University of Tokyo).
- "Public Lecuture commemorating the 10th Anniversary of the Japan Institution of Professional Engineers Japan, Saitama Branch," May. 28, 2022, CORSO Hall, Saitama-City, Saitama, Takaki Kajita (ICRR, The University of Tokyo).
- "Global Lecture Series for Tokyo Metropolitan University," Jul. 5, 2022, Online, Takaki Kajita (ICRR, The University of Tokyo).
- "The International Physics Olympaid (IPhO) 2022 in Japan," Jul. 15, 2022, National Olympics Memorial Youth Center, Shibuya-ku, Tokyo, Takaki Kajita (ICRR, The University of Tokyo).
- "KEK Summer Challenge 2022," Aug. 19, 2022, KEK Tsukuba-City, Ibaraki, Takaki Kajita (ICRR, The University of Tokyo).
- "Annual Meeting 2022 of the Japan Society of Mechanical Engineers," Sep. 13, 2022, Gofuku Campus, Toyama University, Toyama-City, Toyama, Takaki Kajita (ICRR, The University of Tokyo).
- "Advanced General Educaion in Doctoral WISE Program at Innovative Medicine Chiba ," Sep. 16, 2022, Inohana Campus, Chiba University, Chiba-City, Chiba, Takaki Kajita (ICRR, The University of Tokyo).
- "Omiya Kita High School SSH Special Lecture," Sep. 27, 2022, Omiya Kita High School, Saitama-City, Saitama, Takaki Kajita (ICRR, The University of Tokyo).
- "AEPSHEP 2022 School," Oct. 10, 2022, Online, Takaki Kajita (ICRR, The University of Tokyo).
- "National Private School Education," Oct. 20, 2022, Nagaragawa Convention Center, Gifu-City, Gifu, Takaki Kajita (ICRR, The University of Tokyo).
- "Public Lecture," Nov. 26, 2022, Lifelong Learning College Tonami Center, Oyabe-City, Toyama, Takaki Kajita (ICRR, The University of Tokyo).
- "JST's Sakura Science Exchange Program," Dec. 14, 2022, Tachikawa High School, Takaki Kajita (ICRR, The University of Tokyo).
- "Public Lecture for Junior High School Students in Higashimatsuyama City," Dec. 20, 2022, Higashimatsuyama Citizen's Culture Center, Higashimatsuyama-City, Saitama, Takaki Kajita (ICRR, The University of Tokyo).
- "30th Anniversary for the National Cancer Center Hospital East," Feb. 11, 2023, Kashiwanoha Conference Center, Kashiwa-City, Chiba, Takaki Kajita (ICRR, The University of Tokyo).
- "The 26th ICRR X IPMU Public Lecture," Apr. 9, 2022, Amuser Kashiwa, Kashiwa-City, Chiba, Yuichi Harikane (ICRR, The University of Tokyo).

- ""Let's Talk with Researchers" for Kashiwa Campus Open Day," Oct. 21, 2022, Onine, Masato Takita, Shoichi Ogio, Takashi Sako, Michiko Oishi, Shochi Oshino, Tatsuya Narikawa, Keitaro Fujita, Tomoki Wada, Kazuaki Hashiyama, Yo Kusafuka, Akinori Matsumoto, Masataka Mishima (ICRR, The University of Tokyo).
- "Public Lecture for Kashiwa Campus Open Day," Oct. 22, 2022, Onine, Masayuki Nakahata (ICRR, The University of Tokyo).
- "Public Lecture for Kashiwa Campus Open Day," Oct. 22, 2022, Onine, Kento Asai (ICRR, The University of Tokyo).
- ""Let's build up Cloud Chamber" for Kashiwa Campus Open Day," Oct. 23, 2022, Onine, Shintaro Miki, Kozo Fujisue (ICRR, The University of Tokyo)(Kamioka Observatory, ICRR, The University of Tokyo).
- "The 25th ICRR X IPMU Public Lecture," Nov. 28, 2021, Online, Kyohei Kawaguchi (ICRR, The University of Tokyo).
- "Science Café for Tamarokuto Science Center," Jan. 21, 2023, Tamarokuto Science Center, Nishi Tokyo-City, Tokyo, Tomohisa Kawashima (ICRR, The University of Tokyo).
- "Asahi Culture Cneter Yokohama," May. 21, 2022, LUMINE Yokohama, Yokohama-City, Kanagawa, Yuichi Harikane (ICRR, The University of Tokyo).
- "Toranomon Universe School," Jun. 5, 2022, Minato Science Museum, Minato-ku, Tokyo, Yuichi Harikane (ICRR, The University of Tokyo).
- "Sundai Gakuen Junior & Senior High School," Aug. 20, 2022, Sundai Gakuen Junior & Senior High School, Kita-ku, Tokyo, Yuichi Harikane (ICRR, The University of Tokyo).
- "Lecture for TOPPAN," Oct. 28, 2022, online, Yuichi Harikane (ICRR, The University of Tokyo).
- "UTalk," Nov. 12, 2022, UT Café, Fukutake Hall, Bunkyo-Ku, Tokyo, Yuichi Harikane (ICRR, The University of Tokyo).
- "Tokyo Municipal Musashi High School," Nov. 16, 2022, Musashi High School, Musashino-City, Tokyo, Yuichi Harikane (ICRR, The University of Tokyo).
- "Lecture for Fujitsu," Jan. 19, 2023, , Yuichi Harikane (ICRR, The University of Tokyo).
- "Adachi-ku Lifelong Learning Center," Feb. 19, 2023, Adachi-ku, Tokyo, Yuichi Harikane (ICRR, The University of Tokyo).
- "Niigata Prefectual Sado High School," Aug. 19, 2022, Niigata Prefectual Sado High School, Daniela Hadasch (ICRR, The University of Tokyo).
- "Lecture titled " High Energy Astrophysics to High-School Female Students"," Nov. 10, 2022, RYOZAN PARK Sugamo, Toshhima-Ku, Tokyo , Daniela Hadasch (ICRR, The University of Tokyo).
- "Ibaraki Prefectual Tsuchiura Daiichi High School," Nov. 12, 2022, Ibaraki Prefectual Tsuchiura Daiichi High School, Michiko Oishi (ICRR, The University of Tokyo).
- "Lecture titled "Communication Skills Workshop at The University of Tokyo's EMP (Excutive Management Program)," Dec. 2, 2022, Ito International Research Center, Bunkyo-Ku, Tokyo, Daniela Hadasch (ICRR, The University of Tokyo).
- "Public Lecture for the Institution of Professional Engineers, Japan," Apr. 18, 2022, Online, Katsuki Hiraide (Kamioka Observatory, ICRR, The University of Tokyo).
- "Science Café in Gifu," Apr. 23, 2022, Gifu Shimbun Sha, Gifu-City, Gifu, Masayuki Nakahata (Kamioka Observatory, ICRR, The University of Tokyo).
- "Kyoto Prefectural Rakuhoku High School," Jun. 9, 2022, Online, Ko Abe (Kamioka Observatory, ICRR, The University of Tokyo).
- "Researcher's Talk," Jun. 26, 2022, Kamioka Lab, Hida-City, Gifu, Jun Kameda (Kamioka Observatory, ICRR, The University of Tokyo).
- "Gifu Prefectural Yoshiki High School," Jul. 12, 2022, Kamioka Community Hall, Hida-City, Gifu, Hidekazu Tanaka (Kamioka Observatory, ICRR, The University of Tokyo).

- ”Yamanashi Prefectural Kofu Minami High School,” Jul. 26, 2022, Online, Kei Ieki (Kamioka Observatory, ICRR, The University of Tokyo).
- ”Nanao High School,” Jul. 26, 2022, Online, Guillaume Pronost (ILANCE, SK Collaborator).
- ”Toyama Prefectural Toyama Higashi High School,” Aug. 2, 2022, Kamioka Community Hall, Hida-City, Gifu, Yosuke, Kataoka (Kamioka Observatory, ICRR, The University of Tokyo).
- ”UTokyo’s Open Campus for High School Students 2022,” Aug. 3, 2022, Online, Yoshinari Hayato (Kamioka Observatory, ICRR, The University of Tokyo).
- ”Public Lecture,” Aug. 6, 2022, Akashina Community Hall, Azumino-City, Nagano, Masayuki Nakahata (Kamioka Observatory, ICRR, The University of Tokyo).
- ”Kyoto Prefectural Momoyama High School,” Aug. 9, 2022, Kamioka Community Hall, Hida-City, Gifu, Makoto Miura (Kamioka Observatory, ICRR, The University of Tokyo).
- ”Yamanashi Prefectural Nirasaki High School,” Sep. 14, 2022, Online, Atsushi Takeda (Kamioka Observatory, ICRR, The University of Tokyo).
- ”Science Café in Gifu,” Oct. 15, 2022, Gifu Shimbun Sha, Gifu-City, Gifu, Masato Shiozawa (Kamioka Observatory, ICRR, The University of Tokyo).
- ”Public Lecture for Gifu Association Radiological Technologists,” Oct. 16, 2022, Takayama City Cultural Hall, Takayama-City, Gifu, Masato Shiozawa (Kamioka Observatory, ICRR, The University of Tokyo).
- ”Technical Committee on Antennas and Propagation,” Oct. 20, 2022, Online, Motoyasu Ikeda (Kamioka Observatory, ICRR, The University of Tokyo).
- ””Let’s Talk with Researchers” for Kashiwa Campus Open Day,” Oct. 22, 2022, Online, Kimihiro Okumura (ICRR, The University of Tokyo).
- ””Let’s Talk with Researchers” for Kashiwa Campus Open Day,” Oct. 22, 2022, Online, Atsushi Takeda (Kamioka Observatory, ICRR, The University of Tokyo).
- ”Public Lecture for Kashiwa Campus Open Day,” Oct. 22, 2022, Online, Yohei Noguchi (Kamioka Observatory, ICRR, The University of Tokyo).
- ”JohokuSaitama High School,” Oct. 27, 2022, Kamioka Community Hall, Hida-City, Gifu, Jun Kameda (Kamioka Observatory, ICRR, The University of Tokyo).
- ”Researcher’s Talk,” Oct. 30, 2022, Kamioka Lab, Hida-City, Gifu, Keishi Hosokawa (Kamioka Observatory, ICRR, The University of Tokyo).
- ”Super-Kamiokande Open House,” Nov. 13, 2022, Funatsuza, Hida-City, Gifu and Online, Masato Shiozawa (Kamioka Observatory, ICRR, The University of Tokyo).
- ”Super-Kamiokande Open House,” Nov. 13, 2022, Funatsuza, Hida-City, Gifu and Online, Hiroyuki Sekiya (Kamioka Observatory, ICRR, The University of Tokyo).
- ”The 27th ICRR X IPMU Public Lecture,” Dec. 11, 2022, Online, Shigetaka Moriyama (Kamioka Observatory, ICRR, The University of Tokyo).
- ”UTokyo’s Lab Tour for High School Students,” Mar. 28, 2023, Online, Shoei Nakayama (Kamioka Observatory, ICRR, The University of Tokyo).
- ”Public Lecture for Optoelectronics Industry and Technology Development Associaion,” Jan. 27, 2023, L stay & Grow Harumi, Chuo-Ku, Tokyo, Hiroyuki Sekiya (Kamioka Observatory, ICRR, The University of Tokyo).
- ”Public Lecture for Okayama University of Science,” Oct. 26, 2022, Okayama University of Science, Okayama-City, Okayama, Takuya Tomiya (Kamioka Observatory, ICRR, The University of Tokyo).
- ”Science Cafe,” May. 15, 2022, Hybrid (Online + Kamioka Library), Masatake Ohashi (KAGRA Observatory, ICRR, The University of Tokyo).
- ”Researcher’s talk,” July. 3, 2022, Kamioka Laboratory, Hida-City, Gifu, Takahiro Yamamoto (KAGRA Observatory, ICRR, The University of Tokyo).

- ”Gifu Prefecutral Yoshiki Senior High School,” Jul. 12, 2022, Kamioka Community Center, Hida-City, Gifu, Osamu Miyakawa (KAGRA Observatory, ICRR, The University of Tokyo).
- ”Faculty of Science,Toyama University,” July. 14, 2022, Toyama-City, Toyama, Shoichi Oshino (KAGRA Observatory, ICRR, The University of Tokyo).
- ”Faculty of Science, Toyama University,” July. 30, 31, 2022, Toyama-City, Toyama, Shinji Miyoki (KAGRA Observatory, ICRR, The University of Tokyo).
- ”Hida Citizen College,” July. 31, 2022, Hida City Cultural Communication Center, Masatake Ohashi (KAGRA Observatory, ICRR, The University of Tokyo).
- ”Kyoto Prefecutral Momoyama High School,” Aug. 9, 2022, Kamioka Community Center, Hida-City, Gifu, Takafumi Ushiba (KAGRA Observatory, ICRR, The University of Tokyo).
- ”OHO’22 Lecture,” Sep. 9, 2022, Hybrid(Online+KEK), Nobuhiro Kimura (KAGRA Observatory, ICRR, The University of Tokyo).
- ”Yamanashi Prefectural Nirasaki High School,” Sep. 28, 2022, Online, Shinji Miyoki (KAGRA Observatory, ICRR, The University of Tokyo).
- ”Open College in Hida 2022,” Oct. 1, 2022, Hida Earth Wisdom Center, Masatake Ohashi (KAGRA Observatory, ICRR, The University of Tokyo).
- ”Hida Kamioka High School,” Oct. 11, 2022, Online, Takaaki Yokozawa (KAGRA Observatory, ICRR, The University of Tokyo).
- ”Public Lecture,” Oct. 15, 2022, Inotani Barrier Museum, Kazuhiro Yamamoto (KAGRA Collaborator)(Toyama University).
- ”Niigata University,” Oct. 18, 2022, Niigata-City, Niigata, Takaaki Yokozawa (KAGRA Observatory, ICRR, The University of Tokyo).
- ”KAGRA Open House Lecture,” Nov. 13, 2022, Hybrid(Online+Funatsuza), Masatake Ohashi (KAGRA Observatory, ICRR, The University of Tokyo).
- ”KAGRA Open House Q&A,” Nov. 13, 2022, Hybrid(Online+Funatsuza), Masatake Ohashi (KAGRA Observatory, ICRR, The University of Tokyo).
- ”Researcher’s talk,” Nov. 20, 2022, Kamioka Laboratory, Hida-City, Gifu, Hirotaka Yuzurihara (KAGRA Observatory, ICRR, The University of Tokyo).

(c) Visitors

Kashiwa Campus (Total: 19 groups, 576 people)

- Junior High and High schools: 3 group
- Universities and Graduate schools: 3 group
- Researchers: 5 group
- Inspections: 1 groups
- Press: 7 groups
- Others: 0 group

KAMIOKA Observatory (Total: 70 groups, 466 people)

- Junior High and High schools: 1 group
- Universities and Graduate schools: 15 groups
- Researchers: 14 groups
- Inspections: 0 groups
- Press: 9 groups
- Others: 31 groups

KAGRA Observatory (Total: 37 groups, 267 people)

- Junior High and High schools: 1 group
- Universities and Graduate schools: 11 groups
- Researchers: 2 groups
- Inspections: 20 groups
- Press: 2 groups
- Others: 1 group

F. Inter-University Research Activities

Numbers of Researchers

		Number of Applications	Number of Adoptions	Number of Researchers
Facility Usage				
Kamioka Observatory	Domestic	43	43	1,810
	International	9	9	153
Akeno Observatory	Domestic	12	12	266
	International	1	1	53
Norikura Observatory		9	9	84
Primary Cosmic rays, Kashiwa underground facility		5	5	30
KAGRA Observatory	Domestic	23	23	662
	International	3	3	33
High Energy Astrophysics Facility in Canarias	Domestic	10	10	261
Laboratorial Facilities in Kashiwa	Domestic	1	1	13
	International	3	3	18
Large-Scale Comping System in Kashiwa	Domestic	16	16	546
	International	6	6	141
Conference Facilities in Kashiwa	Domestic	5	5	75
Overseas Facilities (Utah, Tibet and Bolivia)	Domestic	9	9	114
	International	1	1	63
Annual Sums	Domestic	133	133	3,861
	International	23	23	461

Joint Research				
Neutrino and Astroparticle Research	Domestic	43	43	1,810
	International	9	9	153
High Energy Cosmic Ray Research	Domestic	56	56	1,263
	International	8	8	257
Astrophysics and Gravity Research	Domestic	25	25	710
	International	3	3	33
Research Center for Cosmic neutrinos	Domestic	9	9	78
	International	3	3	18
Annual Sums	Domestic	133	133	3,861
	International	23	23	461

Research Project Titles

1. Research and development of computer simulation of Super-Kamiokande detector
2. Study of atmospheric neutrino flux and neutrino oscillations
3. Study of simulation for atmospheric neutrino
4. Study of flavor identification of atmospheric and beam neutrinos
5. Study of solar neutrino energy spectrum
6. Precise measurement of Day/Night effect for B8 solar neutrinos
7. Study for Supernova monitor
8. Study of Supernova Relic Neutrinos
9. Search for proton decay via $e^+\pi^0$ mode

10. Study of proton decay p $\rightarrow \nu K^+$
11. Study in upward-going muons and high energy neutrinos
12. Sidereal daily variation of $\sim$10TeV galactic cosmic ray intensity observed by the Super Kamiokande
13. Neutrino search associated with astronominal transient events
14. Measurement of charge ratio and polarization of cosmic ray muon using undergraund particle physics experiments
15. Tokai to Kamioka Long Baseline Experiment T2K
16. Neutrino interaction study using accelerator data
17. Study for improvement of neutrino oscillation measurement in T2K expriment
18. Energy calibration for Super-Kamiokande
19. Astroparticle physics using the Super-Kamiokande detector
20. Development of low concentration radon detection system
21. Hyper-Kamiokande project
22. Development of the Large Aperture Photodetector for a next-generation neutrino detector
23. Development of software for the next generation neutrino detector
24. Measurement of radon in underground laboratoried and evaluate of effects from radon to experiments
25. Study for lowering backgrounds of radioisotopes in large volume detectors
26. Development of a radioactivity assay system for underground experiments
27. Measurement of neutron flux at the Kamioka underground laboratory
28. Trace level measurements of radioactive impurities for underground experiments, such as Super-Kamiokande with ICPMS
29. RI measurement for SK-Gd project with HPGe detector
30. Generation three direct dark matter search experiment
31. A Search for Dark Matter using Liquid Xenon Detector
32. Detector structure study for future direct dark matter search experiment
33. Improvement of ultra-low radioactivity molecular sieves and implementation in dark matter search experiment
34. Research and Development for XENONnT and future Dark Matter Searches
35. Direction-sensitive dark matter search
36. A study on the near-infrared emission of liquid xenon
37. Study of double beta decay of ^{48}Ca
38. Studies on the background evaluation using laser spectroscopy analysis
39. Integration of crustal activity observation around the Atotsugawa fault
40. Strain, tilt, seismic measurement in Kamioka-mine
41. Searches for neutrinoless double beta decay with high-pressure Xenon gas detector
42. Soft-error-rate estimation for semiconductor device at underground laboratory
43. Device activation and quantitative analysis for investigation of charged particle response of semiconductor quantum devices
44. R & D for a Small Atmospheric Cherenkov Telescope in Akeno Observatory

45. Development of new surface detector for observation
46. Multi-Color Imager for Transients, Survey and Monstrous Explosions
47. Observation of Galactic Cosmic Ray Intensities using Large Area Muon Telescopes
48. Observation of solar neutrons in solar cycle 25
49. Space weather observation using muon hodoscope at Mt. Norikura
50. Observation of cosmogenic nuclides concentrations at Mt. Norikura
51. Study of secondary cosmic rays from Thundercloud at Mt. Norikura
52. Investigation of alpine plants on Mt. Norikura
53. Atmospheric mercury speciation dynamics and mercury wet deposition monitoring at high-altitude
54. Patch dynamics of Pinus pumila and Vaccinium vitis-idaea at the ridge site of Mt. Norikura
55. Evaluation of atmospheric SO2 to cloud acidification at free troposhere through atmospheric observation at Mt. Norikura
56. Test experiment of the Fuel cell in Norikura
57. CTA Project
58. Development of Focal Plane Instruments for the CTA Large Sized Telescopes
59. Development of the readout system for the CTA large sized telescopes
60. Engineering runs of the first Large Size Telescope of CTA and construction of LST2-4 in La Palma Canary Islands, Spain
61. Commissioning and upgrade of the onsite data center for CTA North in La Palma, Spain
62. Localization of very high energy gamma-ray emission region in an active galactic nuclei
63. Development of SiPM modules for CTA-LST 2
64. Development of the CTA/LST telescope control system
65. maintenance and operation of the optical and power systems in CTA LST
66. CTA-Japan Physics Research
67. Development of analysis method and initial observation with CTA Large-Sized Telescope
68. Development of camera for CTA small-sized telescopes
69. CTA Monte Carlo Simulation
70. Search for neutrino sources with the Large-Aperture Atmospheric Cherenkov Telescope
71. The extreme Universe viewed in very-high-energy gamma rays 2022
72. Study of High Energy Gamma-ray Objects with the MAGIC telescope
73. Kashiwa Dark Matter symposium 2022
74. Study of Extremely-high Energy Cosmic Rays by Telescope Array
75. R&D of the measurement of atmospheric transparency at the Telescope Array site
76. Study of very high energy cosmic rays around 10^{17} eV with the TALE hybrid experiment
77. Evaluation of optical characteristics of atmospheric fluorescence telescope by standard light source mounted on drone
78. Development and analysis of night cloud observation by CCD camera for automatic observation of air fluorescence detector
79. Observing ultrahigh-energy cosmic rays with new fluorescence detectors at Telescope Array site

80. Research and development of a Fresnel lens air fluorescence telescope for the next generation UHECR observation
81. Cloud distance measurement for cosmic ray air shower observation with atmospheric fluorescence telescope
82. Experimental Study of High-energy Cosmic Rays in the Tibet ASγ experiment
83. Sidereal daily variation of $\sim$10TeV galactic cosmic ray intensity observed by the Tibet air shower array
84. Study of the composition of cosmic-rays at the Knee
85. A study on variation of interplanetary magnetic field with the cosmic-ray shadow by the sun.
86. Air shower observation for high-energy gamma ray and cosmic ray detections at the Chacaltaya Cosmic Ray Observatory
87. Study of High Energetic Radiation from Thundercloud in the Altiplano
88. Study of solar magnetic fields using the cosmic-ray Sun's shadow observed at the southern hemishpere
89. Study of high-energy cosmic-ray anisotropy at the Chacaltaya Cosmic Ray Observatory
90. Development of new trigger electronics for the ALPACA experiment
91. Development of an advanced Compton camera using SOI pixel semiconductor
92. Design study of a Compton camera for study of cosmic rays
93. Study of Fast Moving Dark Matters and Meteoroids using High Sensitivity CMOS Camera System
94. Study on High Energy Cosmic-ray Sources by Observations in Space with CALET
95. Comparative study of high energy astrophysical phenomena
96. Development of a new code for cosmic-ray air shower simulation
97. Cosmic ray interactions in the knee and the highest energy regions
98. Development of improvements and test observations for the elucidation of very-high energy particle emitting objects by NTA
99. Clear identification of very high energy particle sources by NTA
100. Research of Large-scale Gravitational wave Telescope(XII)
101. Study of Gravitational-wave by cryogenic laser interferometer CLIO in KAMIOKA Mine(VI)
102. Development of High Performance Cryogenic Mirror Control System
103. Research on cryogenic payload for KAGRA
104. Deveropment of conduction cooling schemes for KAGRA
105. R&D for the intensity stabilization of the laser system in KAGRA
106. Development of scattered light measurement technique and noise reduction for improving sensitivity in KAGRA III
107. Development of optical cavity for ultranarrow stable lasers
108. Study of Environmental Noise Reduction in KAGRA
109. Study of the environmental noise of KAGRA detector by environmental injection
110. Noise characteristics analysis using machine learning and deep learning and its application to interferometer diagnosis(II)
111. Development of glitch data analysis system for improving gravitational detection
112. Numerical Simulation of Electro-Magnetic Wave Propagation in Gravitational wave Detector X
113. Development of a high performance sapphire mirror suspension
114. Control and automatic operation for KAGRA

115. Construction of KAGRA data transfer and storage system(8)
116. Promotion of collaborative research to incorporate KAGRA data into the low latency international gravitational wave search network (2)
117. Construction of a diagnostic system for the gravitational wave detector
118. Search for poorly modeled gravitational wave signal using KAGRA
119. Test measurement of underground gravity measurement at micro-meter scale
120. Precise geophysical observation at the Kamioka underground site and modeling of crustal activities
121. Development of a noise source identification tool for improving the sensitivity of KAGRA telescope
122. Development of a new calibration method with thermal noise for a gravitational wave detector
123. Cosmic Reionization and Galaxy Formation Probed with Large Optical Near-Infrared Telescopes
124. Evolution of the universe and particle physics
125. Detection of time variations for cosmogenic nucleid Be-7
126. Time profile of radioactive Cs concentration and its aerosol size distribution in local area
127. Development of new analysis techniques for supernova neutrino observation by Super Kamiokande
128. Behavior of radionuclides in the marine environment
129. Frontier of the planetary material science
130. Measurement of the intrinsic radioisotopes in electron-tracking Compton telescopes for studying the radiation mechanism of extragalactic diffuse gamma-rays
131. Precise calculation of the atmospheric neutrino flux
132. CRC workshop for future plans in cosmic ray research
133. YMAP symposium 2022
134. Light scattering measurement in the water using the Super-Kamiokande detector
135. Search for the nucleon decay including multi pions in Super-Kamiokande
136. New Photogrammetry Calibration for Super-Kamiokande and Hyper-Kamiokande
137. Study of supernova neutrinos in Super-Kamiokande
138. Data Taking, Calibrations, Measurements and Analysis with Super-Kamiokande I - VI
139. Development and testing of cost-effective, high-performance PhotoDetector anti-implosion covers for Hyper-Kamiokande
140. Hyper-Kamiokande OD PMTs QA
141. Seal, mechanical and functional tests on the mPMT prototype for external vessel optimizzations
142. Towards a multiphysics liquid Xe TPC with scintillation and charge multiplication readouts
143. Neutrino Telescope Array (NTA) Prototype Test and Technical Design
144. Ultra-high-energy cosmic-ray origin studies with the Telescope Array and TAx4 surface detector
145. Study of Anisotropy of Ultra High Energy Cosmic Rays with Telescope Array and TAx4
146. Understanding the GeV-TeV signatures of star-forming galaxies in the extragalactic gamma-ray background with CTA
147. Study of high-energy cosmic rays at a high altitude in Tibet, China
148. Study for Galactic CR origin using the ALPACA air shower array in Bolivia

149. Constraining the nature of the emission in PeVatrons observed by Alpaca.
150. Bayesian analysis on the origin of ultra-high energy cosmic ray events collected by the telescope array experiment
151. Silicon steering stage for monolithic suspension for cryogenic detectors of gravitational waves
152. Filter cavity experiments for the frequency dependent squeezed light for KAGRA
153. Measuring the birefringence of the sapphire mirrors installed in the KAGRA detector
154. Water quality monitoring for precision neutrino detectors
155. Pressure Validation and Characterization of Underwater Detector Components
156. Constraining systematics at T2K and SuperKamiokande oscillation analyses using neutrino-nucleus interaction models

G. List of Committee Members

(a) Board of Councillors

NAKAHATA, Masayuki	ICRR, The University of Tokyo
MORIYAMA, Shigetaka	ICRR, The University of Tokyo
OGIO, Shoichi	ICRR, The University of Tokyo
KAWASAKI, Masahiro	ICRR, The University of Tokyo
HOSHINO, Masahiro	Graduate School of Science, The University of Tokyo
SAITO, Nobuhito	The University of Tokyo
SAITO, Naohito	Institute of Particle and Nuclear Studies, KEK
AOKI, Shinya	Yukawa Institute for Theoretical Physics, Kyoto University
TSUNETA, Saku	National Astronomical Observatory of Japan
KAJINO, Fumiyoshi	Faculty of Science and Engineering, Konan University
MORI, Masaki	College of Science and Engineering, Ritsumeikan University
YOKOYAMA, Junichi	Research Center for the Early Universe, The University of Tokyo
YAMADA, Toru	Institute of Space and Astronautical Science
ASAI, Shoji	International Center for Elementary Particle Physics, The University of Tokyo
KUSANO, Kanya	Institute for Space-Earth Environmental Research, Nagoya University
TAKITA, Masato	ICRR, The University of Tokyo

(b) Advisory Committee

NAKAHATA, Masayuki	ICRR, The University of Tokyo
KITANO, Ryuichiro	KEK Theory Center
YAMAZAKI, Ryo	College of Science and Engineering, Aoyama Gakuin University
SEIYA, Yoshihiro	Graduate School of Science, Osaka Metropolitan University
WADA, Michiharu	Wako Nuclear Science Center, Institute of Particle and Nuclear Studies, KEK
NAKAJIMA, Yasuhiro	Graduate School of Science, The University of Tokyo
TSURU, Takeshi	Graduate School of Science, Kyoto University
TAJIMA, Hiroyasu	Institute for Space-Earth Environmental Research, Nagoya University
ITOW, Yoshitaka	Institute for Space-Earth Environmental Research, Nagoya University
KANDA, Nobuyuki	Graduate School of Science, Osaka Metropolitan University
NISHIJIMA, Kyoshi	School of Science, Tokai University
TAKITA, Masato	ICRR, The University of Tokyo
MORIYAMA, Shigetaka	ICRR, The University of Tokyo
OGIO, Shoichi	ICRR, The University of Tokyo
KAWASAKI, Masahiro	ICRR, The University of Tokyo
SHIOZAWA, Masato	ICRR, The University of Tokyo
OHASHI, Masatake	ICRR, The University of Tokyo
KUBO, Hidetoshi	ICRR, The University of Tokyo

(c) Inter-University Research Advisory Committee

TSUNESADA, Yoshiki	Graduate School of Science, Osaka Metropolitan University
KANDA, Nobuyuki	Graduate School of Science, Osaka Metropolitan University
NISHIJIMA, Kyoshi	School of Scicnece, Tokai University
MORI, Masaki	College of Science and Engineering, Ritsumeikan University
NAKAMORI, Takeshi	Faculty of Science, Yamagata University
SHIOMI, Atsushi	College of Industrial Technology, Nihon University
ASO, Yoichi	National Astronomical Observatory of Japan
TAKEUCHI, Yasuo	Graduate School of Science, Kobe University
TAKITA, Masato	ICRR, The University of Tokyo
MIYOKI, Shinji	ICRR, The University of Tokyo
OKUMURA, Kimihiro	ICRR, The University of Tokyo
NODA, Koji	ICRR, The University of Tokyo
SEKIYA, Hiroyuki (Organizer)	ICRR, The University of Tokyo
NAKAHATA, Masayuki (Observer)	ICRR, The University of Tokyo

H. List of Personnel

Director NAKAHATA, Masayuki,

Vice-Director TAKITA, Masato

ICRR HQ in Kashiwa Campus

- High Energy Cosmic Ray Division

Scientific Staff	ASANO, Katsuaki,	ENOMOTO, Ryoji,	FIASSON, Armand,
	HADASCH, Daniela,	KAWAGUCHI, Kyohei	KAWATA, Kazumasa,
	KINUGAWA, Tomoya,	KUBO, Hidetoshi,	MAZIN, Daniel,
	NODA, Koji,	NONAKA, Toshiyuki,	OGIO, Shoichi,
	OHISHI, Michiko,	OHNISHI, Munehiro,	SAITO, Takayuki,
	SAKO, Takashi,	SAKO, Takashi,	SASAKI, Makoto,
	STRZYS, Marcel,	TAJIMA, Hiroyasu,	TAKEDA, Masahiro,
	TAKITA, Masato,	TESHIMA, Masahiro,	VOVK, Ievgen,
	YAMAMOTO, Tokonatsu,	YOSHIDA, Tatsuo,	YOSHIKOSHI, Takanori,
	OLAF, Reimer,	SITAREK, Julian,	LOPEZ MOYA, Marcos,
Technical Staff	AOKI, Toshifumi,	OHOKA, Hideyuki,	SEKINO, Koichi,
	TAMURA, Akiko,		
Research Fellow	ANZORENA, Marcos,	CERIBELLA, Giovanni,	COLOMBO, Eduardo,
	FUJITA, Keitaro	FUKAMI, Satoshi,	HUETTEN, Moritz,
	INADA, Tomohiro,	KAWASHIMA, Tomohisa,	LOPEZ ORAMAS, Alicia,
	OHMURA, Takumi,	OSHIMA, Hitoshi,	SHIN, Heungsu,
	TAKEISHI, Ryuji,	WADA, Tomoki,	
Secretary	IDOMURA, Takako,	SHIRAGA, Ryoko,	SUGAHARA, Midori,

- Astrophysics and Gravity Division

Scientific Staff	HARIKANE, Yuichi,	IBE, Masahiro,	KAWASAKI, Masahiro,
	ONO, Yoshiaki,	OUCHI, Masami,	
Research Fellow	AOYAMA, Shohei,	ASAI, Kento,	EIJIMA, Shintaro,
	LIANG, Yongming,	OTANI, Francis,	LOVELL, Christopher Cumminskey,

Kamioka Observatory

Director	SHIOZAWA, Masato,		
Scientific Staff	ABE, Ko,	ASAOKA, Yoichi,	BRONNER, Christophe,
	GONIN, Michel,	HAYATO, Yoshinari,	HIRAIDE, Katsuki,
	HOSOKAWA, Keishi,	IEKI, Kei,	IKEDA, Motoyasu,
	ITOW, Yoshitaka,	KAMEDA, Jun,	KATAOKA, Yosuke,
	MIURA, Makoto,	MORIYAMA, Shigetaka,	NAKAHATA, Masayuki,
	NAKANO, Yuki,	NAKAYA, Tsuyoshi,	NAKAYAMA, Shoei,
	NISHIMURA, Yasuhiro,	SATO, Kazufumi,	SEKIYA, Hiroyuki,
	TAKEDA, Atsushi,	TAKEMOTO, Yasuhiro,	TANAKA, Hidekazu,
	YANO, Takatomi,	DI LODOVICO, Francesca Romana	PLAYFER, Stephen Michael,
Administrative Staff	YOSHIDA, Takuto,		
Public Relations Staff	TAKENAGA, Yumiko,		
Technical Staff	HAMA, Satoshi,	HIGASHI, Tetsuji,	ISHITA, Katsumi,
	MINE, Shunichi,	ONOUE, Tatsuya,	
Research Administrator	KURACHI, Masafumi,		
Research Fellow	NOGUCHI,Yohei,	SONODA, Yutaro,	
Secretary	DOI, Kyoko,	KAMIKAWATO, Rie,	MAEDA, Yukari,
	NISHIDA, Hiromi,		

KAGRA Observatory

Director	OHASHI, Masatake,		
Scientific Staff	AONO, Yuri,	KIMURA, Nobuhiro,	MIO, Norikatsu,
	MIYAKAWA, Osamu,	MIYOKI, Shinji,	MORISAKI, Soichiro,
	NARIKAWA,Tatsuya,	OSHINO, Shoichi,	SAWADA,Takahiro,
	TAGOSHI, Hideyuki,	TAKAHASHI, Hirotaka,	TOMARU, Takayuki,
	UCHIYAMA, Takashi,	USHIBA, Takafumi,	YAMAMOTO, Kazuhiro,
	YAMAMOTO, Takahiro,	YOKOZAWA, Takaaki,	YUZURIHARA, Hirotaka,
	TROZZO, Lucia,		
Administrative Staff	KATO, Daichi,	OKINAKA, Mihoko,	
Technical Staff	AOUMI, Masakazu,	KAMIIZUMI, Masahiro,	MIYO, Koseki,
	NAKAGAKI, Koji,	NODE, Ayako,	OMAE, Akio,
	PENA ARELLANO, Fabian,	SAKAI, Akiko,	SAKAMOTO, Eri,
	SHIMODE, Katsuhiko,	TAKAHASHI, Masahiro,	TAKASE, Takashi,
	YAMAGUCHI, Hirokazu,	YASUI, Hiromi,	YOSHIMURA, Mitsuharu,
Research Fellow	TUYENBAHEV, Darkhan,	UCHIKATA, Nami,	ZHAO, Yuhang,
Secretary	KIKUCHI, Rie,	KUDO, Naomi,	NOJIRI, Midori,

High Energy Astrophysics Facility in Canarias

Director	KUBO, Hidetoshi,

Research Center for Cosmic Neutrinos

Director	OKUMURA, Kimihiro,		
Scientific Staff	KAJITA, Takaaki,	TASHIRO, Takuya,	TOKANAI, Fuyuki,
Technical Staff	SHINOHARA, Masanobu,		
Secretary	KITSUGI, Atsuko,	MASHIMA, Chieko,	

Norikura Observatory

Director	SAKO, Takashi,		
Technical Staff	AWAI, Kyosuke,	HAYAKAWA, Hideaki,	INOME, Yusuke,
	OKAZAKI, Nao,	SHIMODAIRA, Hideaki,	TOMURA, Tomonobu,
	USHIMARU, Tsukasa,		

Akeno Observatory

Director	OGIO, Shoichi,
Scietific Staff	SAGAWA, Hiroyuki,
Technical Staff	KOBAYASHI, Ryoichi,

Graduate Students

Doctor	ABE, Hyuga,	ABE, Shotaro,	BAXTER, Joshua Ryo,
	FUJISUE, Kozo,	GOTO, Ryota,	HAN, Seungho,
	HASHIYAMA, Kazuaki,	HIGUCHI, Ryo,	HSIEH, Bin-Hua,
	ISOBE, Yuki,	IWAYA,Masaki,	KANEMURA, Yuki,
	KATO, Nobuyuki,	KATO, Sei,	KATO, Takashi,
	KIKUCHIHARA, Shotaro,	KOBAYASHI, Shin,	KOBAYASHI, Yukiho,
	LEE, Eunsub,	MIKI, Shintaro,	MURAI, Kai,
	NAKATSUKA, Hiromasa,	NAKAYAMA, Yuhei,	NISHIWAKI, Kosuke,
	OHTANI, Yoshiki,	OKAMOTO, Kohei,	SAKURAI, Shunsuke,
	SUN, Dongsheng,	TANAKA, Kenta,	TANG, Shenli,
	WATANABE, Keiichi,	XIA, Junjie,	YOKOE, Yoshichika,
	ZHANG, Yechi,		

Master	ABOUNNASR-MARTINS, Théo,	CHIBA, Renichi,	CHITOSE, Akifumi,
	FUJII, Shingo,	GARG, Suyog,	IMAGAWA, Kaname,
	KAMINAGA, Yoshino,	KANAMORI, Shotaro,	KANESHIMA, Ryota,
	KASAI, Kentaro,	KASHIWAGI, Yuri	KAWASHIMA, Teruyoshi,
	KIBUKAWA, Hirofumi,	KOCHI,Hiroki,	KUSAFUKA, Yo,
	MATSUMOTO, Akinori,	MISHIMA, Masataka,	MIWA, Masataka,
	MIYAMOTO, Shinya,	MIYAZAKI, Kazuyoshi,	MURAKAMI, Yasuhiro,
	NEDA, Shunsuke,	OKIMOTO, Naoya,	SHIBA, Hayato,
	SHIMIZU, Kotaro,	SHIMODATE, Karin,	SUGIYAMA, Takumu,
	SUZUKI, Ryota,	TAKAHASHI, Kaoru,	TAMAKI, Masahide,
	TOMIYA, Takuya,	UMEDA, Hiroya,	USUI, Kazuki,
	WANG, Xubin,	WATANABE, Shuhei,	XU, Yi,
	YAMAMURA, Shunsei	YOSHIDA, Shunsuke,	ZHU, Chenghao,

Administrative Division

Administrative Staff	AKAIDA, Yohei,	AKASHI, Yoko,	AKIYAMA, Makiko,
	FUKUHARA, Nana,	IKEDA, Hiroshi,	MARUMORI, Yasuko,
	MATSUMOTO, Yasuo,	NAKAYA, Yukiko,	OKANO, Yuka,
	SAEKI, Yuya,	SAITO, Akiko,	SATO, Hiroki,
	TAKAMICHI, Ryo,	WATANABE, Taishi,	YAMAGISHI, Yukinao,
	YAMAGUCHI, Akiko,	YAMASUE, Akiko,	
Research Administrator	ITO, Michiru,	OTA, Ritsuko,	SATO, Ritsuko,
	SUGIMOTO, Kumiko,		
Public Relations Staff	ITO, Yoriko,	NAKAMURA, Makio,	
Archive Room	NAKAMURA, Kenzo,		

INSTITUTE FOR COSMIC RAY RESEARCH
THE UNIVERSITY OF TOKYO

Address 5-1-5, Kashiwanoha, Kashiwa-shi, Chiba, 277-8582 Japan
TEL +81-4-7136-3102
FAX +81-4-7136-3115
URL www.icrr.u-tokyo.ac.jp

ICRR
Institute for Cosmic Ray Research
University of Tokyo